Field Evaluation of the Caney Shale as an Emerging Unconventional Play, Southern Oklahoma

DOE Award No: DE-FE0031776

Final Report

Project Period (2019-2024)

Submitted by:

Mileva Radonjic

_____

Signature

Oklahoma State University
DUN's Number: 191510239

203 Whitehurst, Stillwater, OK 74078-1020
mileva.radonjic@okstate.edu

Prepared for:
United States Department of Energy
National Energy Technology Laboratory

Project Title: **FIELD EVALUATION OF THE CANEY SHALE AS AN EMERGING UNCONVENTIONAL PLAY, SOUTHERN OKLAHOMA**

Type of Report: **Final Scientific/Technical Report**

Reporting Period Start Date: October 2019

Reporting Period End Date: September 2024

Principal Author and Principal Investigator: Mileva Radonjic

Date Report was Issued: **November 08, 2024**

DOE Award Number: **DE-FE0031776**

Name and Address of Submitting Organizations:
Oklahoma State University

Mileva Radonjic

203 Whitehurst, Stillwater, OK 74078-1020

mileva.radonjic@okstate.edu

co-PIs and Contributors to the Final Report:

Oklahoma State University:
Jim Puckette, Geir Hareland, Michael Grammer, Jack Pashin, Prem Bikkina, Hunjoo Lee

Lawrence Berkeley National Laboratory:
Jonny Rutqvist, Christine Doughty

University of Pittsburgh:
Andrew Bunger

Oklahoma Geological Survey:
Nick Hayman, Abbas Seyedolali

Contents

List of Tables

List of Figures

1. Project Overview

1.1. Project Background

The Mississippian-age Caney Shale is an emerging unconventional oil and gas (UOG) resource play in the southern Midcontinent and is prospective in the Anadarko, Ardmore, Marietta and western Arkoma basins. This play is enigmatic in that time equivalent Fayetteville Shale in the eastern Arkoma basin and Barnett Shale in the Ft. Worth Basin are major unconventional plays, whereas Caney Shale production is sparse and unpredictable (Cardott, 2017). In the Anadarko, Ardmore and Marietta basins, the Caney Shale is in the oil window, but its resource potential has not been adequately assessed. The Caney reservoir is about 60-300 m thick, is rich in total organic carbon, contains a large oil resource base, and has a strong natural gas drive; however, development has been hampered by high clay content and reactivity of the formation with water. The main objective of this initial four-year research project was to address these issues by establishing a Caney Shale Field Laboratory in the Ardmore Basin of southern Oklahoma to (a) conduct a comprehensive field characterization (b) perform field experiments, and (c) validate cost-effective technologies that will lead to a comprehensive and efficient development strategy plan for Caney Shale.

The first step was the development of an open, collaborative, and integrated program to comprehensively characterize Caney Shale's geophysical, geological, petrophysical, geochemical, and geomechanical properties and further perform a baseline analysis of current well production performance and overall, well economics. The second step was to improve our understanding of hydraulic fracture propagation, fracture and proppant embedment, and fluid-rock interaction through detailed core and geophysical well-log analysis. The third step was validating the findings and recommendations from these analyses by drilling and stimulating a horizontal well. Based on the results of this research, a well development plan was developed for the Caney Shale, which helped facilitate accelerated development of the play and offer characterization, and completion practices applicable to similar clay-rich rocks. The integrated research findings presented in this report provide a comprehensive template on how to conduct the characterization of emerging UOG plays and accelerate the development of emerging UOG plays. The project was successfully completed 30th September 2024, with the Phase I (the first 24 months) focused primarily on field characterization as a result of a vertically drilled and retrieved Caney core (650ft), followed by Phase II (36 months) where the team focused on field relevant testing and modeling and preparation of the well development plan in collaboration with the industry partner.

All of the key objectives were achieved, and additional tasks performed during the five-year project (which included one year no-cost extension and substantially under budget). Below are some of the key objectives:

Key objectives from Phase I:

- Effective project management during COVID-19 enabled successful collaboration and productivity of all team members.
- Caney Core Workshop, OKC, February 2020, which brought all team members and enabled fast and effective confirmation of planned activities ahead.

- Coring and logging of the Caney Shale interval and additional CT imaging of entire 650ft Caney Shale rock core at NETL.
- Geological and petrophysical reservoir characterization
- Establishing geomechanical properties from geophysical well logs, cores and drilling data, applying reservoir conditions and both static and dynamic settings
- Determine an economic baseline for drilling and completion and identifying potential cost reduction
- Simulation of hydraulic fractures and flow to optimize stimulation design
- Investigate and optimize applicable fracturing options including fracturing fluids, proppant, and stage spacing/clustering in light of equipment requirements and limitations.
- STIM Lab Proppant Consortium Invitation to Join the group increased projects visibility and connectivity with industry nationally and internationally

Key objectives from Phase II:

- Drilling, logging and stimulating a horizontal well at the Caney Shale Field Laboratory was accomplished ahead of schedule, and new samples collected (cuttings were collected every 1000ft over the entire horizontal section, 20,000ft)
- Geological, geomechanical, petrophysical, and geochemical analysis of well cuttings an
- Field produced fluids were used in lab experiments to help further understand reservoir rock formations response to fracturing fluids, evaluating geochemical reactivity of rock matrix and how it may impact proppant embedment and fracture conductivity.
- Application of hydraulic fracture-flow simulators for optimizing stimulation of multistage-fractured horizontal wells.
- Finally, based on integrated research findings and the field data from the industry partner, the team was able to propose a field development plan, including optimized drilling and stimulation and various analysis of overall rate of returns (ROR) for the Caney shale.
- During phase two, with support from The Hamm Institute and the industry partner, all project team members, including students and staff who supported the project, the DOE PM and representatives as well as university and industry leadership attended the Caney Symposium in OKC, where each Task major research outcomes and accomplishments were presented and resulted in a comprehensive integration plan for the final year of the project.

1.2. Study Area and Geologic Setting of the Caney Formation

The Caney shale shown in Figure 1.1, located in the Arkoma basin, is stratigraphically comparable to the Barnett shale found in the Fort Worth Basin. In the aftermath of the significant success of the Barnett play, the formation has progressed to become a producer of gas and oil condensate (Maughan and Deming, 2006; Schad, 2004; Kamann, 2006; Andrews, 2007). The Caney shale is a large constituent composed of an organic-rich calcareous shale deposit that contains large concretions of carbonate (Radonjic et al., 2020). Over the past few years, it had become apparent that the way in which the Caney Shale is interpreted by geologists was based on the exposures in the Arbuckle Uplift (Andrews, 2007, 2012), while its name was derived from a location with little-known exposures. The Caney Shale was initially annotated and named by

Taff. (1901) and Taff. (1901). According to Maughan and Deming (2006), in the 1920's, some degree of confusion in terms of the stratigraphic nomenclature of rocks found in basins within Oklahoma was introduced by petroleum geologists. The Pennsylvanian Caney term was applied to an area above the Caney. This was later formally renamed the Goddard Shale. Andrews (2003) used an alternative term, the False Caney, to describe a Goddard section. According to Girty (1909), the Caney shale is formed from a variety of exposures that are located throughout the Arbuckle within the central areas of the Chickasaw & Choctaw nations. The thickness of the shale does not exceed 1000 ft, and it is formed of black and blue argillites that feature local sandy strata in the upper area. Although most of the Caney shale can be described as organically rich black shale, the beds found in the upper area are lighter in color and potentially have a different fauna. Girty (1909) also highlighted how some of the Caney goniatites are also found in the Batesville sandstone and Fayetteville shale. This indicates that the Caney shale correlates with both these formations and the Moorefield. Radonjic et al. (2020) microstructurally characterized the Caney Shale by evaluating an area of the Caney core spanning 200 ft that was extracted from a well drilled in 2007 located in southern Oklahoma. The outcomes of their analysis revealed that the Caney Shale is clay-rich dominated by illite. They also found matrix pores that ranged from nanometers to micrometers in scale. Unlike Barnett, Eagle Ford, Marcellus or even Fayetteville, no one has developed a standard completion process for the Caney that will generate reliable production. Given that every shale play is different and what works for Barnett, Fayetteville, Eagle Ford is not guaranteed to work for Caney or any other shale play. This is because important differences exist in deposition, mineralogy, microstructure, and petrophysics characteristics.

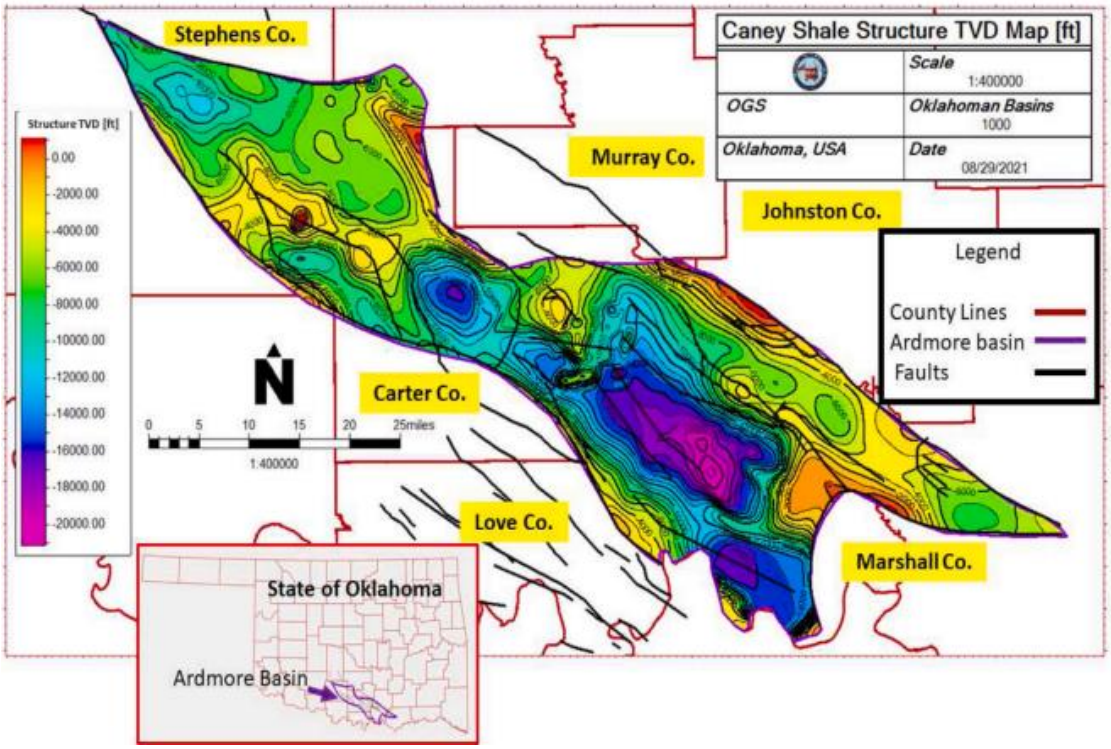

Figure 1.1.TVDSS structure map of the Caney Shale in the Ardmore and Marietta Basin, Oklahoma. The wells correspond to key locations and interpret cores. County names are highlighted in yellow.

2. Geological Structure and Rock Analysis

2.1.Geologic Structure and Burial and Thermal History

2.1.1. Approach

Regional analysis of the Ardmore Basin and Caney Shale focused on analysis of regional stratigraphy and geologic structure and the thermal and burial history of the basin to characterize exploration fairways for development of Caney Shale reservoirs. Techniques used include structural contour mapping, analysis of 2D reflection seismic profiles using Petrel software, and 1D burial modeling using PetroMod software. The stratigraphic section was analyzed using the available literature and geophysical well logs that were acquired through the industry partner and Enverus. Major stratigraphic units were identified, and well logs were correlated in well logs using standard geologic techniques.

Structural contour maps were made and gridded and contoured in showing the elevation of the top of the Woodford Shale and the Caney Shale, which are distinctive marker beds constituting the two most important unconventional hydrocarbon targets in the Ardmore Basin (Figure 2.1).

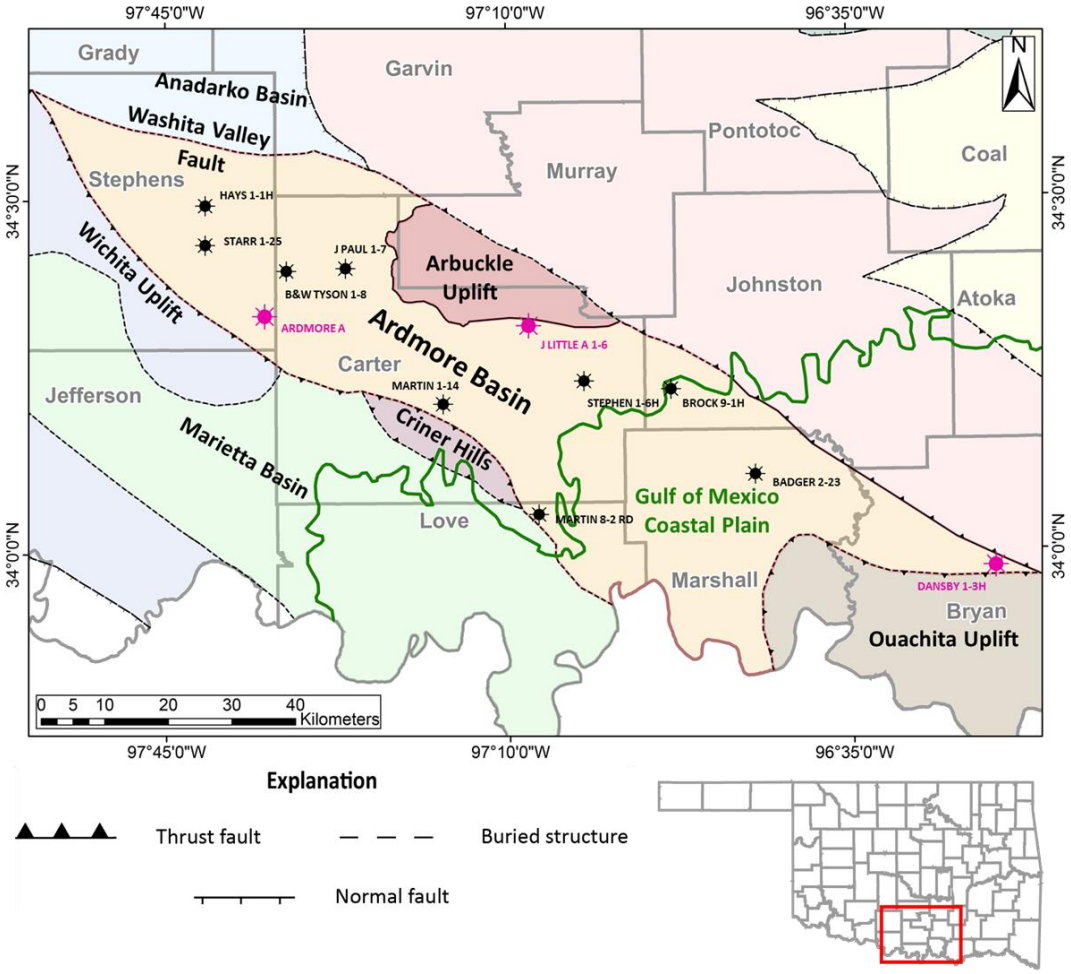

Figure 2.1. Map displaying present-day location of the Ardmore Basin and prominent surrounding structures (after Northcutt and Campbell, 1998). The northern boundary of the Gulf of Mexico Coastal Plain is denoted by the green line. Locations of wells used to construct 1D burial history model wells are shown. Burial history models included in this paper are highlighted in magenta; the other models are in Cox (2021).

A well-based cross-section was constructed that shows the structural style of the western Ardmore Basin in the area of the Ardmore A and Ardmore B wells, which were drilled as part of this project. Reflection seismic profiles, which were shot during the 1950s and 1960s were reprocessed using modern technology and depth converted on the basis of sonic velocity in selected wells in the basin. Reprocessing the profiles resulted in exceptional clarity that rivals data being shot with the latest technology. These profiles reveal further details of structural geometry that are relevant to Caney Shale exploration.

Thermal maturity data are available in the form of vitrinite reflectance data (e.g., Cardott, 2012) from the Woodford Shale, and modern temperature information is available in the form of bottom-hole temperatures and crustal heat flow analyses (e.g., Lee and Deming, 1999). These data were synthesized to map thermal maturity throughout the basin, to determine regional maturity-depth relationships, and to calibrate 1D burial and thermal history models. Analysis of burial history was based on nine wells distributed throughout the Ardmore Basin (Cox, 2021; Cox and Pashin, 2024) (Figure 2.1). Stratigraphic picks and geochronologic ages were compiled for the wells and loaded into PetroMod software. Information used included the location and magnitude of disconformities to estimate missing section. Models were run for each well, and the models were calibrated to match the stratigraphic and thermal maturity data. Models include burial history models, thermal models, and hydrocarbon maturation models based on thermal maturity and kerogen transformation ratio. The result is a detailed synthesis of the depositional, structural, and petroleum generation history of the Ardmore basin that clarifies the mechanisms and timing of hydrocarbon generation and defines areas that are candidates for future hydrocarbon exploration.

2.1.2. Results and Discussion

Stratigraphic Framework

Sedimentary rock in the Ardmore Basin nonconformably overlies Precambrian–Cambrian igneous basement that consists of plutonic and volcanic rocks (Hanson et al., 2013). The overlying sedimentary section primarily ranges in age from Cambrian–Cretaceous (Figure 2.2) and locally reaches thickness greater than 30,000 ft (Huffman et al., 1978; Suneson, 2020). The Tishomingo and Troy Granites (~1.4 Ga) form the basement of the Ardmore Basin and comprise the erosional substrate upon which all volcanic and sedimentary units were deposited (Bickford and Lewis, 1979). After a long hiatus, emplacement of one of the largest bimodal volcanic provinces in North America was initiated with Neoproterozoic mafic plutonism (552 ± 7 Ma) (Bowring and Hoppe, 1982) followed by extrusion of the Carlton Rhyolite Group and the Colbert Porphyry around the Neoproterozoic–Cambrian boundary (539 ± 5 Ma) (Hanson et al., 2013).

Sedimentation began with flooding associated with the Sauk transgression traversed southern Oklahoma from southeast to northwest, depositing sandstone, conglomerate, limestone, and dolomite of the Late Cambrian Timbered Hills Group (Ham, 1969; Johnson, 1989). Flooding continued into the Ordovician, which was a time of major cratonic carbonate deposition (Johnson, 1989). Limestone and dolomite of the Cambrian–Ordovician Arbuckle Group were deposited on a broad carbonate ramp, which has been referred to as the "Great American Carbonate Bank" (Fritz et al., 2012). Carbonate deposition was episodically interrupted by siliciclastic influx during deposition of the

Middle Ordovician Simpson Group, which disconformably overlies the Arbuckle carbonates.

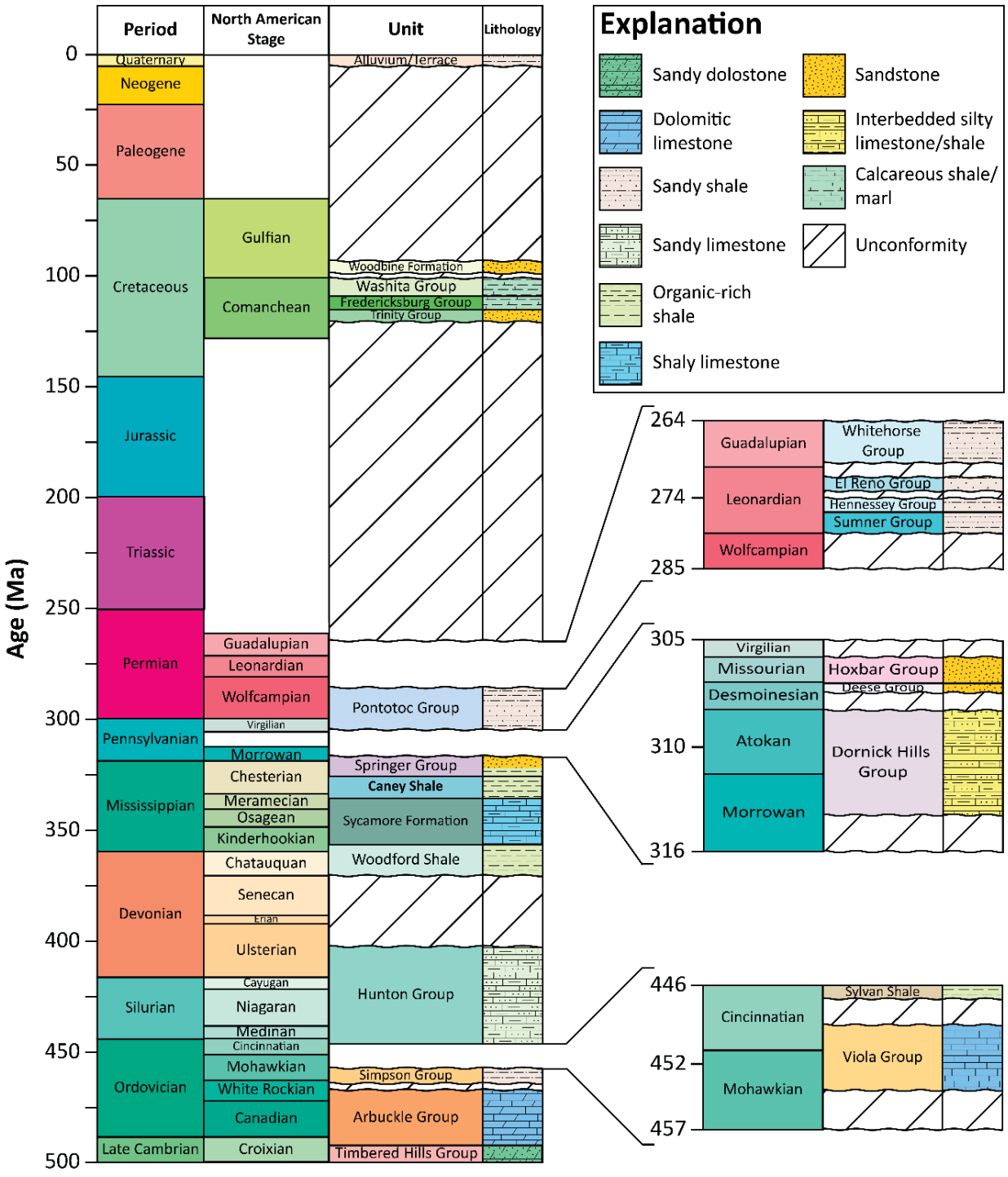

Figure 2.2. Generalized surface and subsurface stratigraphic column for the present-day Ardmore Basin. Solid horizontal lines represent conformable contacts. Wavy horizontal lines indicate an unconformity and bracket time periods of nondeposition and/or erosion (after Cox, 2021).

The Simpson Group comprises alternating layers of quartzarenite, shale, and limestone (Ham, 1969) that were deposited in eolian and shallow-marine environments (Johnson, 1989). Carbonate

deposition continued during the Tippecanoe onlap with deposition of Middle–Upper Ordovician Viola Limestone (Johnson, 1989), which disconformably overlies the Simpson Group. The Viola was deposited on a shallow-water carbonate ramp (Amati and Westrop, 2006). Subsequent deposition of the Late Ordovician Sylvan Shale and Ordovician–Devonian Hunton Group was punctuated by multiple unconformities in southern Oklahoma.

Following a ~15–20 m.y. period of erosion, Kaskaskia cratonic onlap led to deposition of Devonian–Early Pennsylvanian carbonaceous and calcareous shale and limestone (Fritz et al., 2012). These units are the Woodford Shale, Sycamore Limestone, Caney Shale, Goddard Shale, and the Springer Group (Latham, 1968; Wavrek, 1992; Johnson and Cardott, 1992; Johnson, 1989; Brown, 2002).

Pennsylvanian units consist of interbedded sandstone, carbonate, and shale (Suneson, 2020). Units comprise the Dornick Hills, Deese, Hoxbar, and Pontotoc Groups (Ham, 1969). During the Pennsylvanian, broad areas were uplifted and eroded, thus creating multiple unconformities (Latham, 1968; Ham, 1969). Sediment was mostly deposited in a broad, shallow sea that covered south-central Oklahoma during the Pennsylvanian, but also was deposited in marginal marine and terrestrial settings (Johnson, 1989).

The northwestern Ardmore Basin is blanketed by a veneer of Permian strata, mainly red sandstone, shale, and evaporites (Northcutt and Campbell, 1995; Heran et al., 2003). Permian sediment was eroded off low-lying mountains and deposited in alluvial and deltaic environments proximal to a shallow sea that rose and fell cyclically (Johnson, 2008).

Lower Cretaceous strata disconformably overlie Paleozoic strata in the southeastern part of the basin (Huffman et al., 1978, 1987). Here, the Pennsylvanian stratigraphic section is incomplete and Permian units are absent. Cretaceous Sandstone, shale, and limestone were deposited in shallow marine and marginal marine environments as well as in meandering rivers and lakes in coastal plain environments (Huffman et al., 1978; Johnson, 1989). Sediment was sourced from surrounding highlands including the Arbuckle and Ouachita uplifts (Huffman et al., 1978). Subsidence from accumulation of Cretaceous sediment was expressed as a regional south-southeastward tilt (Johnson, 2008). Quaternary strata are preserved locally in alluvial valleys that disconformably overlie Permian strata in the northwestern part of the basin and Cretaceous strata in the southeastern part.

Structural and Tectonic Framework

The Ardmore Basin is located in south-central Oklahoma and is separated from the Anadarko Basin to the northwest by the Washita Valley Fault and is a structurally low area between the Arbuckle Uplift in the northeast and the Criner Hills Uplift in the southwest; the eastern part of the basin has been overthrust by the Ouachita Uplift (e.g., Northcutt and Campbell, 1998; Turko and Tapp, 2021) (Fig. 2.2.1). The Arbuckle and Criner Hills uplifts can be characterized as large, northeast-verging, basement-cored frontal ramp anticlines of Pennsylvanian age (Granath, 1989; Allen, 2000; Walker, 2006) that are cut by numerous oblique faults with rhomboid map patterns in the forelimb, suggestive of oblique-slip fault-propagation folds with anticlinal breakthrough (e.g., Suppe and Medwedeff, 1990). A frontal thrust splay in the Pennsylvanian-Permian Ouachita Uplift was translated northwest and forms a prominent structural salient between the Arbuckle Uplift and the Criner Hills Uplift that defines the southeastern terminus of the Ardmore Basin (Northcutt and Campbell, 1998; Granath,

1989).

Thus, the structure of the Ardmore Basin is extremely complex, including a broad array of folds and faults that range in age from Cambrian to Permian (e.g., Granath, 1989). These structures reflect a diverse tectonic history ranging from Iapetan (Neoproterozoic-Early Cambrian) intracratonic transform tectonics through Carboniferous-Permian transpressive tectonics. Indeed, the tectonic history of southern Oklahoma, including the Ardmore Basin is characterized by five distinct tectonic events: (1) Iapetan intracontinental transform tectonics and associated plutonism and volcanism (2) thermal subsidence of a passive shelf during the Early Paleozoic; (3) Pennsylvanian orogeny and associated deformation, (4) tectonic quiescence from the Triassic–Early Cretaceous, and (5) subsidence of the Gulf of Mexico coastal plain in the eastern part of the basin during the Cretaceous-Paleogene. These events profoundly influenced sedimentation, structure, deformation, and the generation and entrapment of petroleum in the Ardmore Basin (Cox and Pashin, 2024).

Iapetan deformation was coincident with a major rifting event that formed the foundation for the Laurentian continental platform and resulted in major grabens, including the Rome Trough, Mississippi Valley Graben, and the Birmingham Graben in the eastern U.S. (e.g., Thomas, 1991). In southern Oklahoma, this deformation has been widely attributed to rifting (e.g., Shatski, 1941; Burke and Dewey, 1973; Hoffman et al., 1974), although more recent workers have recognized a lack of extensional faults and associated Early Cambrian graben fill that is characteristic of Iapetan rifts (e.g., Harding et al., 1983; Thomas, 2014). Abundant strike- and oblique-slip faults in southern Oklahoma (Harding et al., 1983; Harding, 1985; Allen, 2000) are more consistent with Iapetan continental transform tectonics. Indeed, Thomas (2014) proposed that the southern Oklahoma structures can best be characterized as part of an oblique-slip mobile zone that is associated with the Alabama-Oklahoma Continental Transform, which is a major Iapetan strike-slip zone separating the southeastern Laurentian craton from the oceanic Ouachita Embayment.

From the Late Cambrian into the Mississippian, the Ardmore Basin was part of the Oklahoma Basin (Johnson, 1989), which was dominated by cratonic carbonate, sandstone, and shale deposition (Arbuckle, Simpson, Viola, and Hunton groups) (Ham, 1969; Feinstein, 1981; Fritz et al., 2012). Decelerating thermal subsidence culminated in relative tectonic stability throughout the region until the Mississippian (Feinstein, 1981; Brown, 2002; Johnson, 2008). The Devonian through Late Mississipian was the main time of petroleum source-rock accumulation that includes the Woodford Shale and the Caney Shale (Comer, 1992; Wavrek, 1992; Brown, 2002; Wang et al., 2021; Spears and Pashin, 2022).

The Late Mississippian–Pennsylvanian was a time of widespread tectonic activity that occurred in concert with Appalachian-Ouachita-Ancestral Rocky Mountain orogenesis and tectonic closure of the Rheic Ocean, including the Ouachita Embayment (e.g., Thomas, 1977; Granath, 1989; Perry, 1989; Suneson and Stanley, 2017; Turko and Mitra, 2021). The late Paleozoic Wichita and Arbuckle orogenies elevated the northwest-trending Wichita, Arbuckle, and Criner Hills uplifts and caused major pulses of subsidence driven by intracratonic flexural loading in the Anadarko and Ardmore basins (Ham, 1969; Perry, 1989; Ye et al., 1996). This activity has been subdivided into three separate orogenies: the First Wichitan Orogeny (early Serpukhovian-late Bashkirian), the Second Wichitan Orogeny (late Bashkirian–early Moscovian), and the Arbuckle Orogeny (early Moscovian–late Gzhelian) (Van der Gracht, 1931; Granath, 1989; Suneson and Stanley, 2017).

Each major Pennsylvanian orogenic pulse resulted in an unconformity and deposition of syntectonic conglomerate associated with uplift of anticlines in the Ardmore Basin region (Van der Gracht, 1931; Granath, 1989; Suneson, 2020). As early as the Serpukhovian, the Ardmore Basin was established as an area of subsidence between large-scale reverse faults and the associated folds (Granath, 1989). Deformation and subsidence facilitated deposition of a thick succession of shale, limestone, and sandstone in the Springer Group (Serpukhovian–Bashkirian), the Dornick Hills Group (Bashkirian–Moscovian), the Deese Group (Moscovian) and the Hoxbar Group (Kasimovian–Gzhelian) (Ham, 1969; Suneson, 2020). The imbricate Ouachita salient overrode the southeastern end of the Ardmore Basin during the Pennsylvanian and Permian and offsets strata of the Hoxbar Group (Thomas 1977, Huffman et al., 1978, Granath, 1989). Major tectonic activity ceased near the end of the Pennsylvanian, and the Ardmore Basin continued to subside with deposition of red sandstone, shale, and evaporites in the Late Pennsylvanian–Early Permian Pontotoc Group (Gzhelian-Cisuralian) (Heran et al., 2003; Johnson, 2008; Suneson and Stanley, 2017).

The later Permian was marked by reduced rates and magnitudes of subsidence and deposition of shale, sandstone, and carbonate assigned to the Sumner, Hennessey, El Reno, and Whitehorse groups (Cisuralian-Guadalupian) (Miser, 1954; Heran et al., 2003; Stanley and Chang, 2012). Southern Oklahoma has essentially been tectonically dormant since the Permian. Deposition of a Cretaceous sedimentary wedge that overlies older strata with angular unconformity in the southeastern part of the basin records subsidence of the Gulf of Mexico Coastal Plain which was associated with gentle, south-southeastward regional tilting in this area (Johnson, 2008).

Structure Maps and Balanced Structural Cross Section

A structural contour map of the top of the Woodford Shale shows the general structural configuration of the Ardmore Basin (Figure 2.3). Prominent structures include two doubly plunging synclines with limbs dipping about 20–40°: (1) the Harrisburg Trough and (2) the Berwyn Syncline. Total stratigraphic thickness in these synclines is greater than 30,000 ft, and the Ardmore A and Ardmore B wells were drilled in the interior of the Harrisburg Trough. The Ardmore Basin fill also thickens to approximately 28,000 ft in the northwest, adjacent to the Anadarko Basin. Structural highs are associated with the Wichita Uplift, Arbuckle Uplift, Ouachita Uplift, Caddo Anticline, Alma Anticline, Criner Hills, and Arbuckle Uplift.

A balanced structural cross section, which is also constrained by reflection seismic data, illustrates the structural style in the Ardmore Basin as well as structural kinematics and its relationship to the timing of thermal maturation (Figure 2.4). The cross section extends through Stephens, Carter, and Garvin Counties from the southwest margin of the basin to the backlimb of the Arbuckle Anticline. The cross section intersects some major intrabasin structures including the Harrisburg Trough, Alma Anticline, and the Eola-Arbuckle Anticlinal Complex.

Deformation in Paleozoic strata is interpreted to be rooted at a mid-crustal detachment. The Alma Anticline is displayed as a thick-skinned, north-verging breakthrough fault-propagation fold with a positive flower structure in the forelimb that is thought to have formed from left-lateral transpression related to synorogenic stress during the Pennsylvanian (Figure 2.1.4). The main faults are characterized as high angle (>70°) reverse faults with up to 6,560 ft of vertical displacement. Fault

splays defining the positive flower structure branch off the main faults in Mississippian–Pennsylvanian strata. It appears that major deformation began during deposition of the Springer Group (Chesterian–Morrowan). Major syndepositional structural growth during deposition of the Deese (Desmoinesian) and Hoxbar (Missourian) groups indicates that deformation culminated during the Arbuckle Orogeny (Desmoinesian–Virgilian). Permian units overlap the Alma Anticline and pinch out in toward the Eola-Arbuckle anticlinal complex.

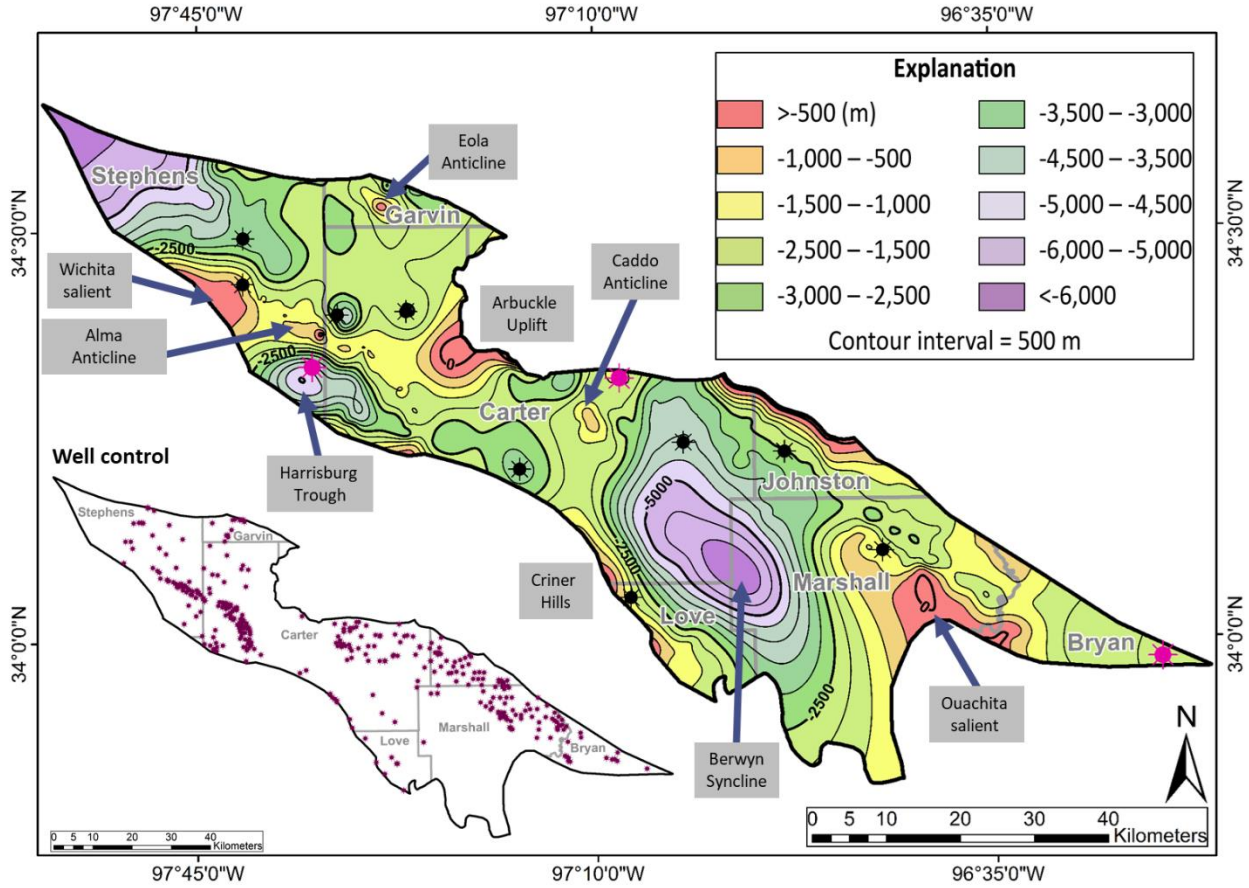

Figure 2.3. Structural contour map of the top of the Woodford Shale. Prominent structures are labeled. Refer to Figure 2.2.1 for the names of the wells used for modeling. The well control map displays wells in which the Woodford Shale is logged and used to make the map.

The Harrisburg Trough was a major depocenter that accommodated voluminous Pennsylvanian–Permian sedimentation during rapid, elevator-like subsidence of the Ardmore Basin. Towards the northwest, strata dip steeply in the backlimb of the Eola-Arbuckle Anticlinal Complex. The disconformity at the base of the Permian is nearly flat across the basin, suggesting that fault propagation and fold growth was effectively complete by the Permian, although thickening in the Harrisburg Trough demonstrates that the trough continued subsiding during Permian time. Reflection seismic data have now all been reprocessed, and depth converted and is currently in the interpretation phase. This data are providing new information on the geometry of the Harrisburg Trough, Berwyn Syncline and other major structures in the Ardmore Basin. A line through the Harrisburg Trough is being used as a basis for 2D thermal maturity modeling in PetroMod, and this work is approaching completion. The seismic data set is being incorporated into a new contribution that provides new

insight into the structural geometry and tectonic history of the Ardmore Basin.

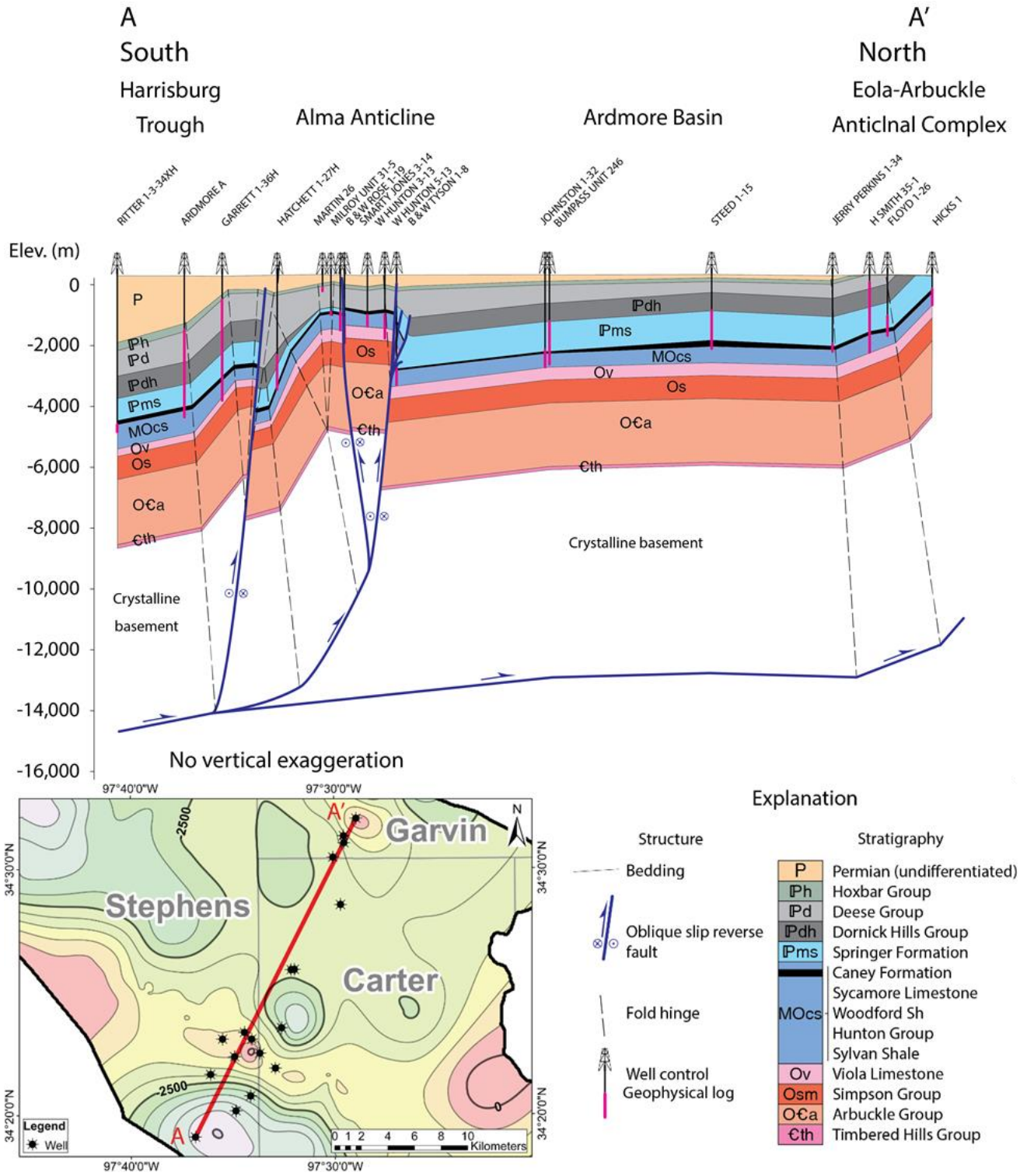

Figure 2.4. Balanced structural cross section in the Ardmore Basin displaying a north-verging breakthrough fault-propagation fold associated with high-angle basement faults. The map displays the structure of the top of the Woodford Shale and the locations of 18 wells from which stratigraphic contacts were projected orthogonally to the line of cross section. Ardmore A well in the cross section is the Ardmore A well.

Thermal Maturity

A vitrinite reflectance-elevation plot shows scattered vitrinite reflectance data at low levels of thermal maturity and a strong log-linear relationship above 0.8% R_o, which corresponds with the peak oil window as well as the onset of major thermogenic gas generation (Figure 2.5). Scatter at low thermal maturity is a result of variable organic composition and is common in many sedimentary basins. Overall, a strong, log-linear correlation exists between vitrinite reflectance and depth in the Ardmore Basin, reflecting a significant correlation with elevation. Indeed, isoreflectance contours are nearly horizontal and cut across structure in the Ardmore Basin (Figure 2.4). Analysis of kerogen by Rock-Eval pyrolysis in the Ardmore A well indicates that TOC ranges from 1-8% and that the data plot along the boundary between Type II sapropelic kerogen and Type III humic kerogen (Figure 2.6). The original kerogen was probably of Type II and has been thermally upgraded to the Type II-III boundary in the Harrisburg Trough, which presently sits in the condensate-wet gas window, which is optimal for oil, natural gas liquids, and natural gas from shale (e.g., Cardott and Comer, 2021).

The logarithmic least squares regression equation (Figure 2.5) can be used to predict vitrinite reflectance between control points (Figure 2.7). Minimum vitrinite reflectance of the Woodford Shale is estimated to be only about 0.35% R_o and thus submature with respect to petroleum generation at the surface along the Arbuckle Uplift (Lo and Cardott, 1995; Cardott and Comer, 2021). Maximum vitrinite reflectance of the Woodford Shale is estimated to be about 4.0% in the Berwyn Syncline. Vitrinite reflectance patterns closely follow structural contours in the basin, which is consistent with the strong vitrinite reflectance-depth relationship (Figures 2.3 and 2.7). Areas with vitrinite reflectance between 1.0 and 2.0 are interpreted to define the principal shale exploration fairways in the Ardmore Basin, which are in the Harrisburg Trough and the flanks of the Berwyn syncline and the structural low in the northwest corner of the basin (Figure 2.7).

The vitrinite reflectance data and modern geothermal gradients were important variables required to calibrate the burial and thermal history models. Plotting corrected bottom-hole temperature data versus depth yields a linear least squares regression line in which temperature increases with depth (Figure 2.8). Scatter in the data reflects variation of stratal thermal conductivity and basal heat flow, as well as error in the corrected temperature measurements. The bottom-hole temperature data were used to assess and map variation of the geothermal gradient in the Ardmore Basin (Figure 2.9). Results indicate that synclinal structures with thick sedimentary cover have geothermal gradient <30°C/km, whereas basement-cored uplifts have much higher geothermal gradient locally >50°C/km.

The vitrinite reflectance and corrected bottom-hole temperatures were used to estimate basal heat flow in the Ardmore Basin, which is essential for thermal history and petroleum systems modeling in Petromod software. Basal heat flow was estimated to be as high as 85 mW/m^2 during the Neoproterozoic–Cambrian Iapetan plutonic event. This event was followed by exponential thermal decay, which has prevailed from the Cambrian to the present. Modern basal heat flow is relatively uniform in the region, averaging 45 mW/m^2 and ranging from 39–55 mW/m^2.

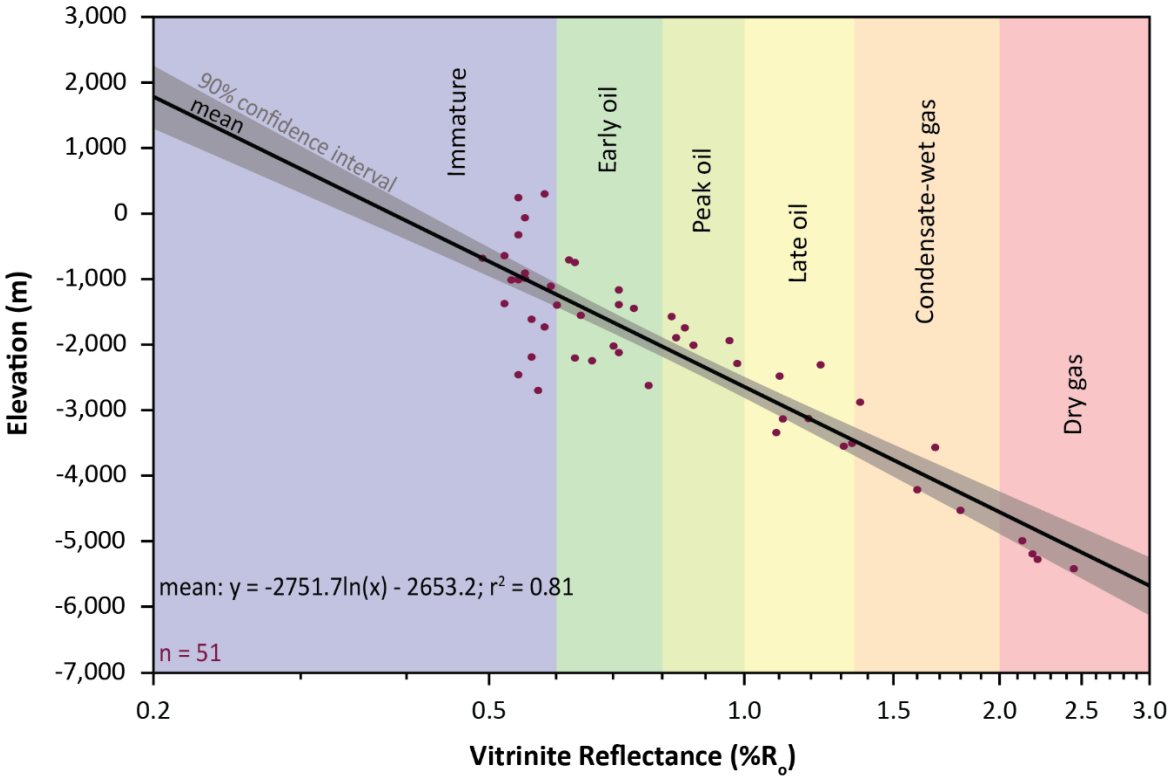

Figure 2.5. Vitrinite reflectance-elevation plot for the Woodford Shale showing log-linear thermal maturity-elevation trends in the Ardmore Basin.

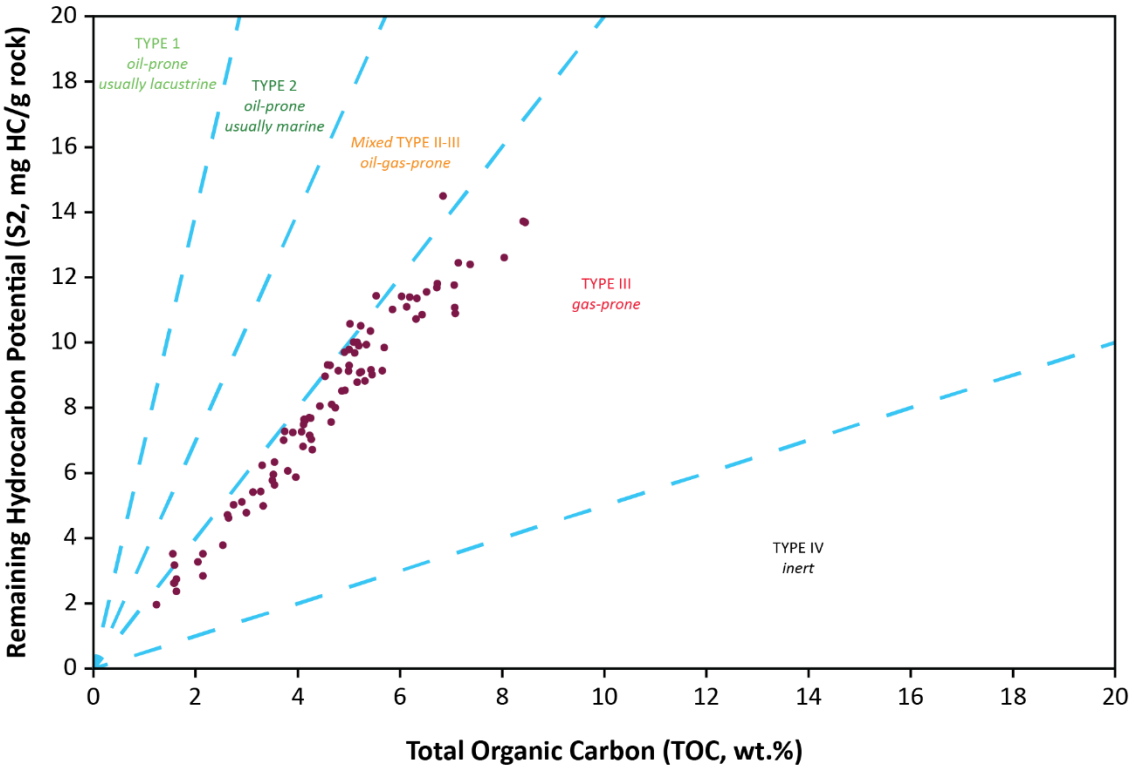

Figure 2.6. Kerogen quality diagram showing bulk kerogen type in Caney Shale in the Ardmore A well.

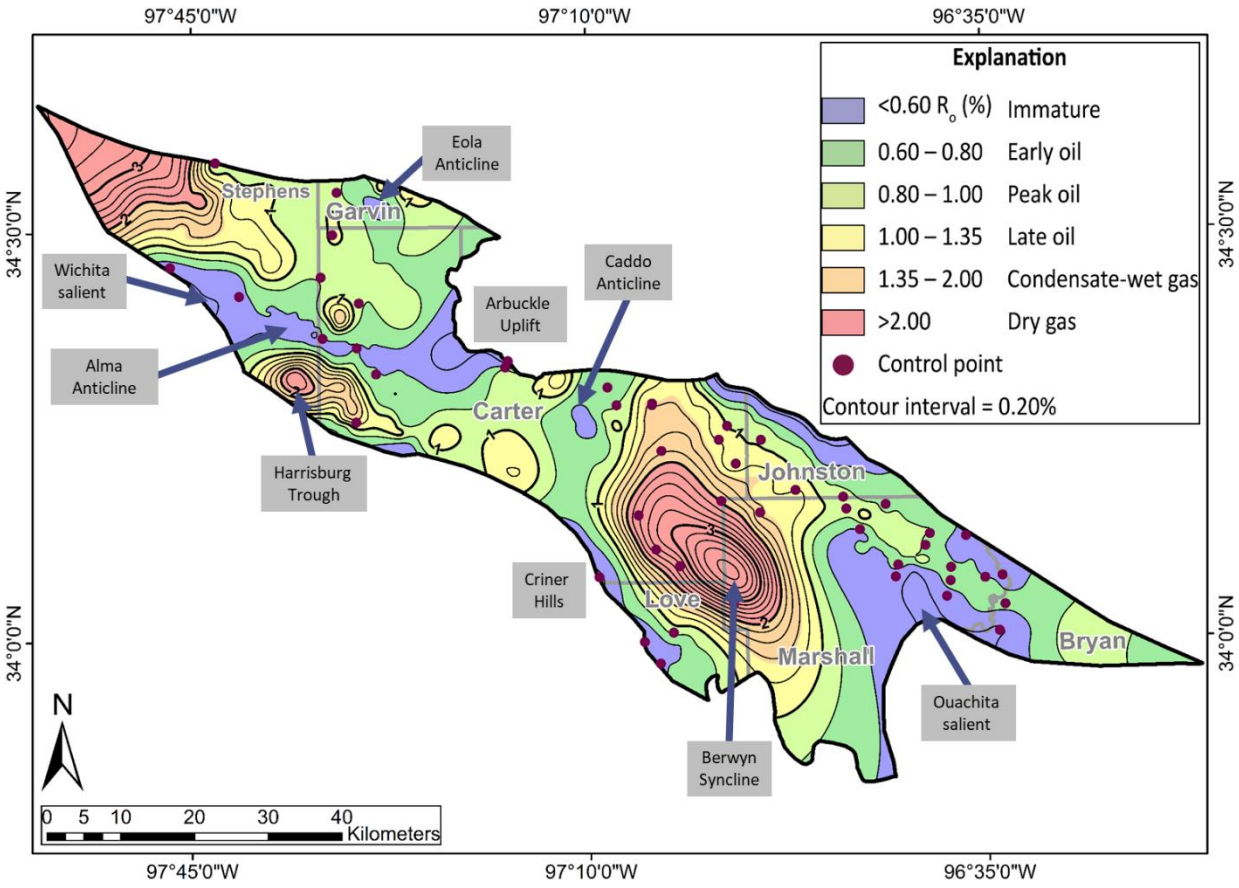

Figure 2.7. Calculated vitrinite reflectance contour map of the Woodford Shale. Control points show the locations of the 52 Woodford Shale vitrinite reflectance measurements in the Ardmore Basin (provided by Cardott, 2020, written communication).

Burial and Thermal History Models

The burial history plots (Figures 2.10-2.12) reveal the major tectonic events in the Ardmore Basin. Selected plots are presented here and were published in Cox and Pashin (2024), and all of the burial history plots are available in Cox (2021). Decelerating subsidence from Cambrian to Devonian time reflects Iapetan tectonics and post-Iapetan thermal decay during major carbonate bank development. Accelerating subsidence during the Carboniferous-Permian was driven by the Wichitan and Arbuckle Orogenies, and precipitous subsidence events during this time reflect major episodes of transgressional tectonic movement during which the Ardmore acted like an elevator basin, which is typical of sedimentary basins in oblique-slip tectonic settings. The Late Permian into the Early Cretaceous was a time of relative tectonic quiescence characterized by modest post-orogenic erosion. Cretaceous reburial associated with development of the Gulf of Mexico Basin and subsequent uplift and erosion is reflected in all the burial history models.

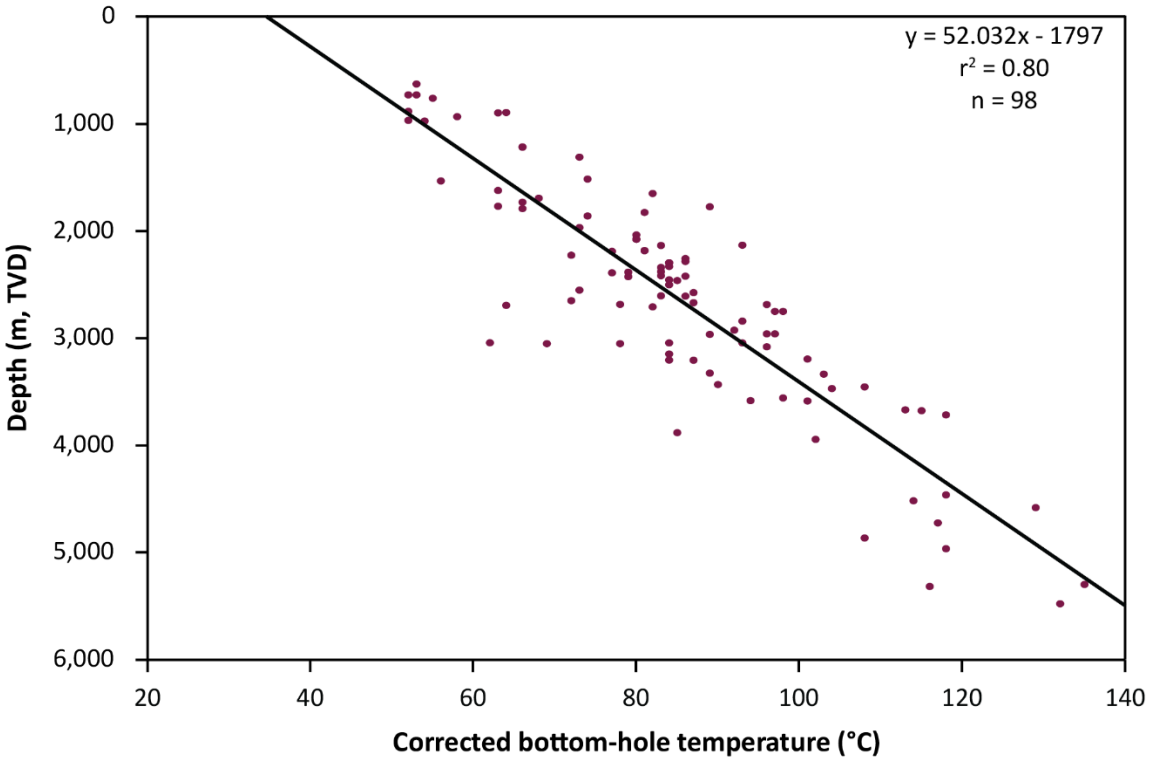

Figure 2.8. Graph of corrected bottom-hole temperatures versus depth from wells in the Ardmore Basin.

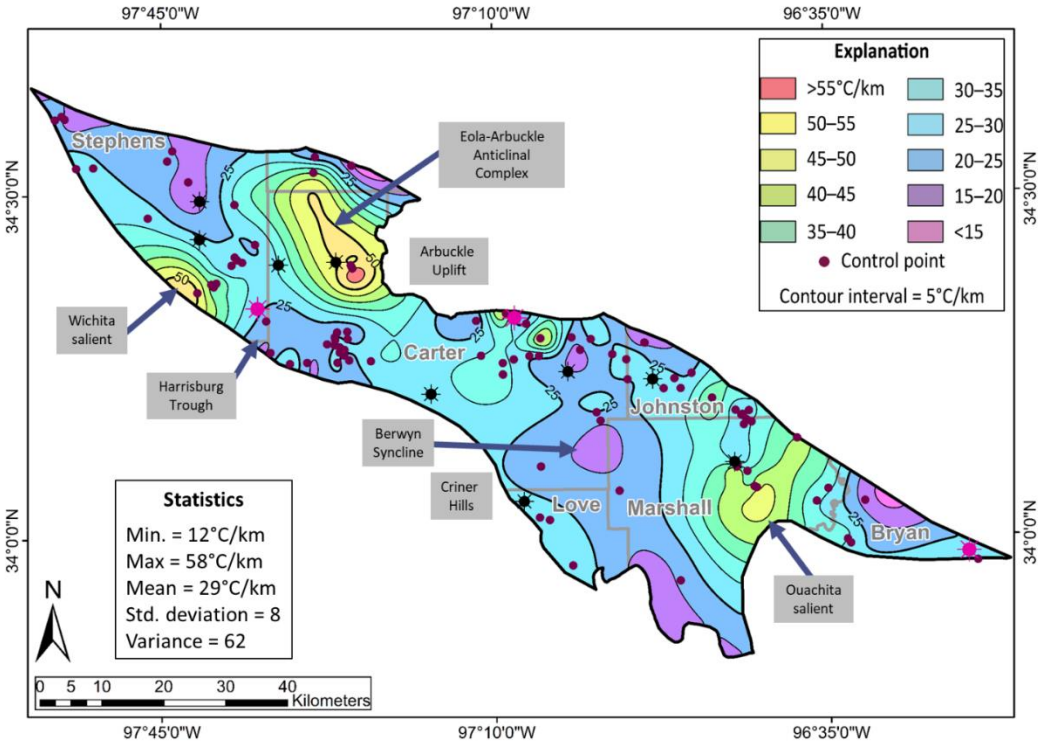

Figure 2.9. Contour map of geothermal gradient in the Ardmore Basin estimated using mean annual surface temperature and corrected bottom hole temperature.

Prior to Pennsylvanian time, only the Timbered Hills Group, Arbuckle Group, and part of the Simpson Group had entered hydrocarbon maturity windows (Figures 2.10-2.12). Throughout most of the Ardmore Basin, Woodford and Caney shale attained present-day thermal maturity after the Permian following accelerated Pennsylvanian (Desmoinesian–Missourian) subsidence and deep burial (>20,000 ft in synclines). Models representing structural highs, such as the J Little A model (Figure 2.11), show the Devonian–Mississippian shale section as being less thermally mature than in models representing synclines, such as the T model (Figure 2.10). Cretaceous deposition had a negligible effect on thermal maturation throughout much of the Ardmore Basin. In the Dansby model, which includes thick Cretaceous cover (Figure 2.12), however, the thermal maturity of Woodford and Caney shale increased only slightly and remained in the early oil window.

The temperature of the Devonian–Mississippian shale section began to increase substantially during the Middle Pennsylvanian, coinciding with major subsidence and burial. By end of the Permian, models representing synclinal areas (Figures 2.10, 2.13, and 2.14) show the Devonian–Mississippian shale was subjected to higher temperatures (~165°C; 329°F in the T model) than in models representing structural highs (~95°C; 203°F in the J Little A model) (Figures 2.11, 2.13 and 2.14). Temperatures began to plateau during the Permian–Triassic (Figures 2.13 and 2.14). A minor increase in temperature occurred during Cretaceous burial. Temperature began to decline in the Late Cretaceous and Paleogene, reflecting regional uplift and unroofing.

Kerogen Transformation and Petroleum Generation

For models that indicate oil generation in Woodford and Caney shale, initiation of primary kerogen cracking primarily occurred during the Late Pennsylvanian and Permian (Figures. 2.15, 2.16, and 2.17). Cracking of kerogen within the Caney Shale began during the later Mesozoic, however, in the J Little A model (Figure. 2.16), which is along the northern flank of the basin. Hydrocarbon source rocks typically began to generate oil once buried to a depth greater than 2 km and subjected to temperatures greater than 80°C (176°F).

Transformation percentages of 100% for Woodford and Caney shale were attained during the Permian in the Ardmore A well and Stephen models, which is the earliest of any models (Figures. 2.18 and 2.19). The Ardmore A and Stephen models contain the thickest Pennsylvanian–Permian sections (>18,000 ft). In these models, the Woodford and Caney shale were exposed to a temperature around 160°C (320°F) at the completion of oil generation. Transformation percentages of 100% for both Woodford and Caney shale in the T, Martin 1-14 and Hays models were attained during the Triassic–Paleogene. In these models, Devonian–Mississippian hydrocarbon source rocks underwent major Pennsylvanian–Permian burial (>16,000 ft) and were subjected to temperatures greater than 160°C (320°F) buy completion of oil generation. Complete transformation of Woodford Shale kerogen occurred during the Cretaceous in the Martin 1-14 and Badger models, which is the latest time for completion of oil generation in the Woodford Shale.

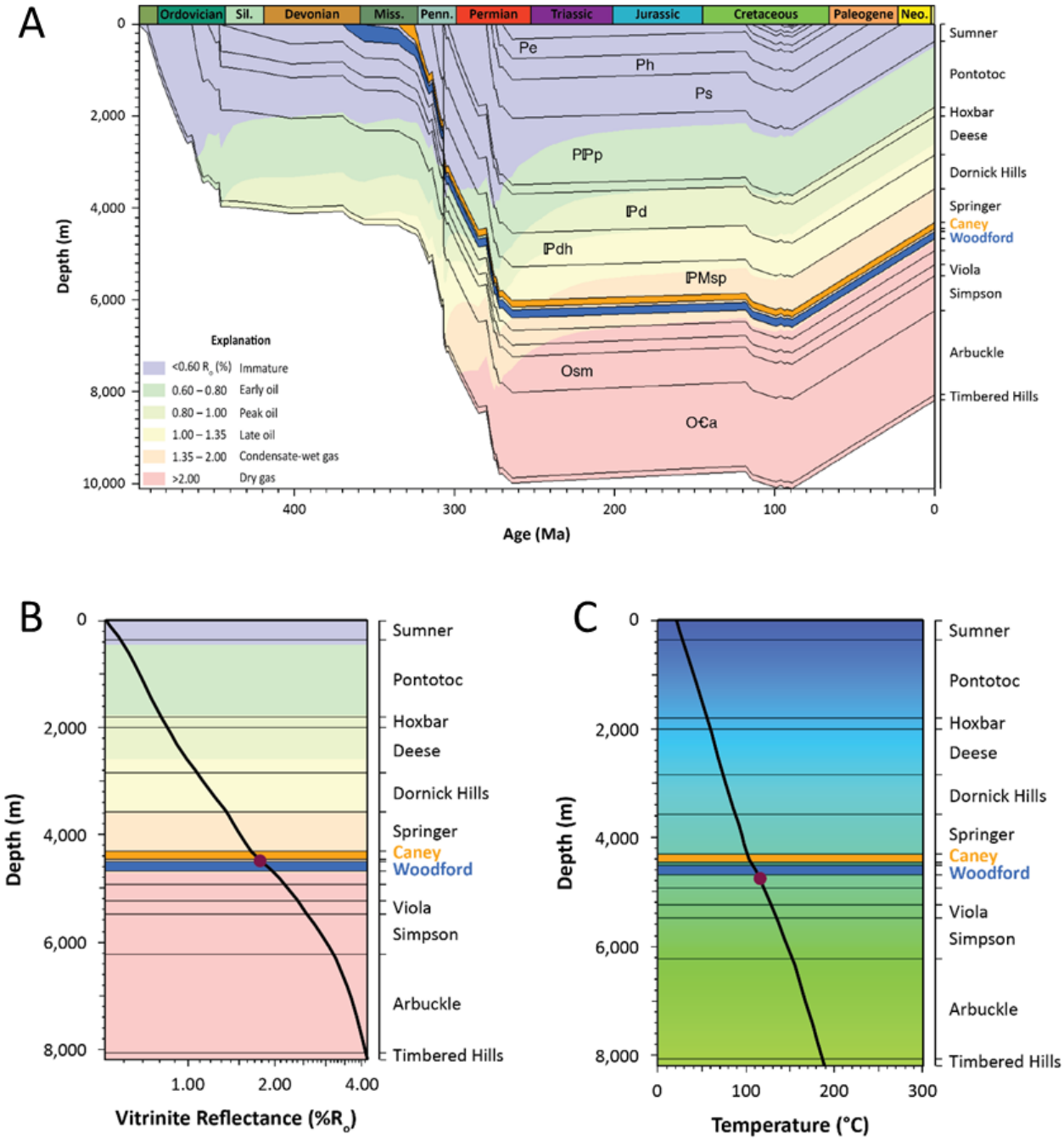

Figure 2.10. Burial and thermal history models of the Ardmore A well in the Harrisburg Trough of the Ardmore Basin. A) Burial history model showing evolution of thermal maturity windows. B) Modeled vitrinite reflectance-depth plot. C) Modeled temperature-depth plot.

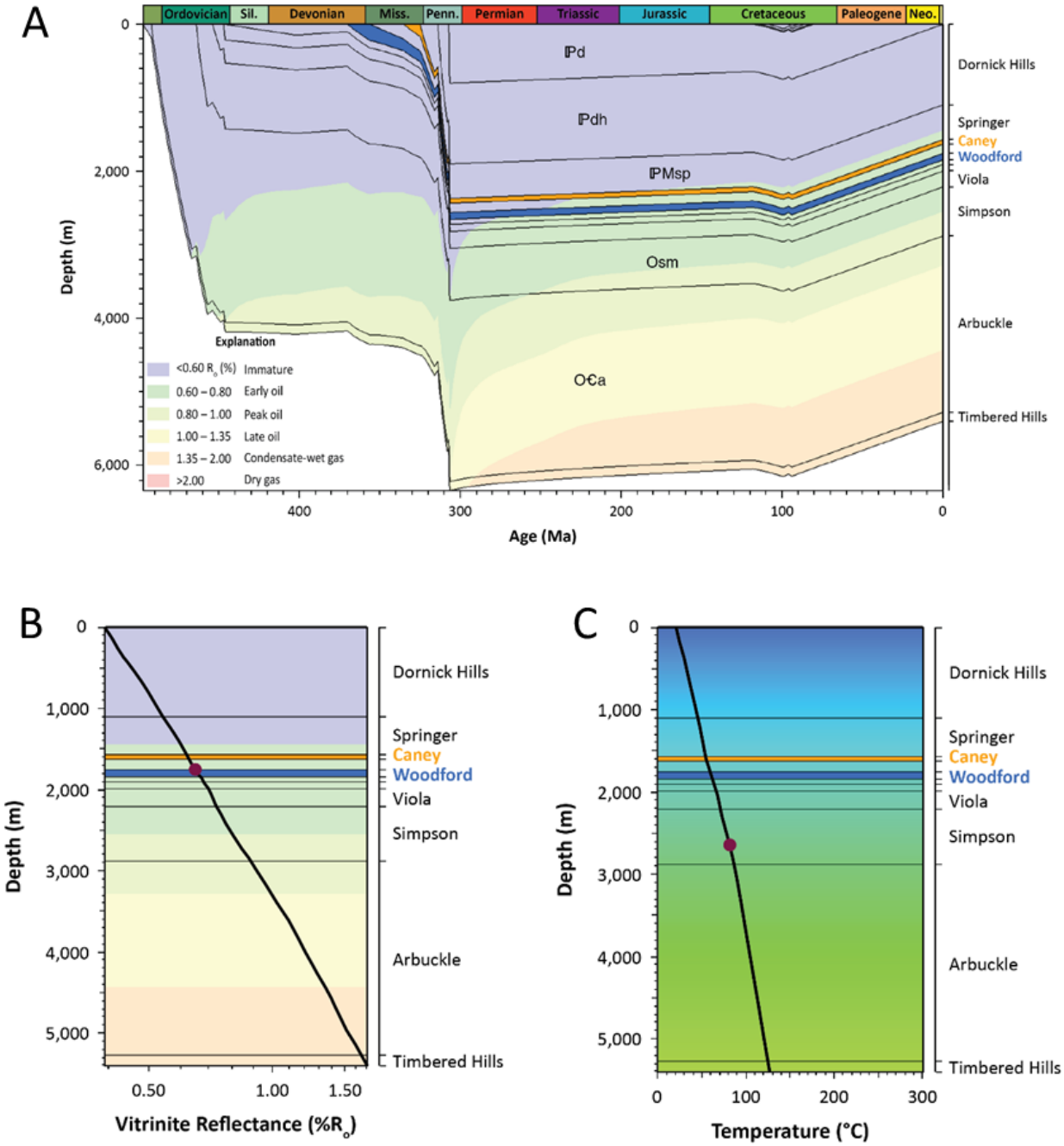

Figure 2.11. Burial and thermal history models of the J Little A 1-6 well in the northeastern flank of the Ardmore Basin. A) Burial history model showing evolution of thermal maturity windows. B) Modeled vitrinite reflectance-depth plot. C) Modeled-temperature depth plot.

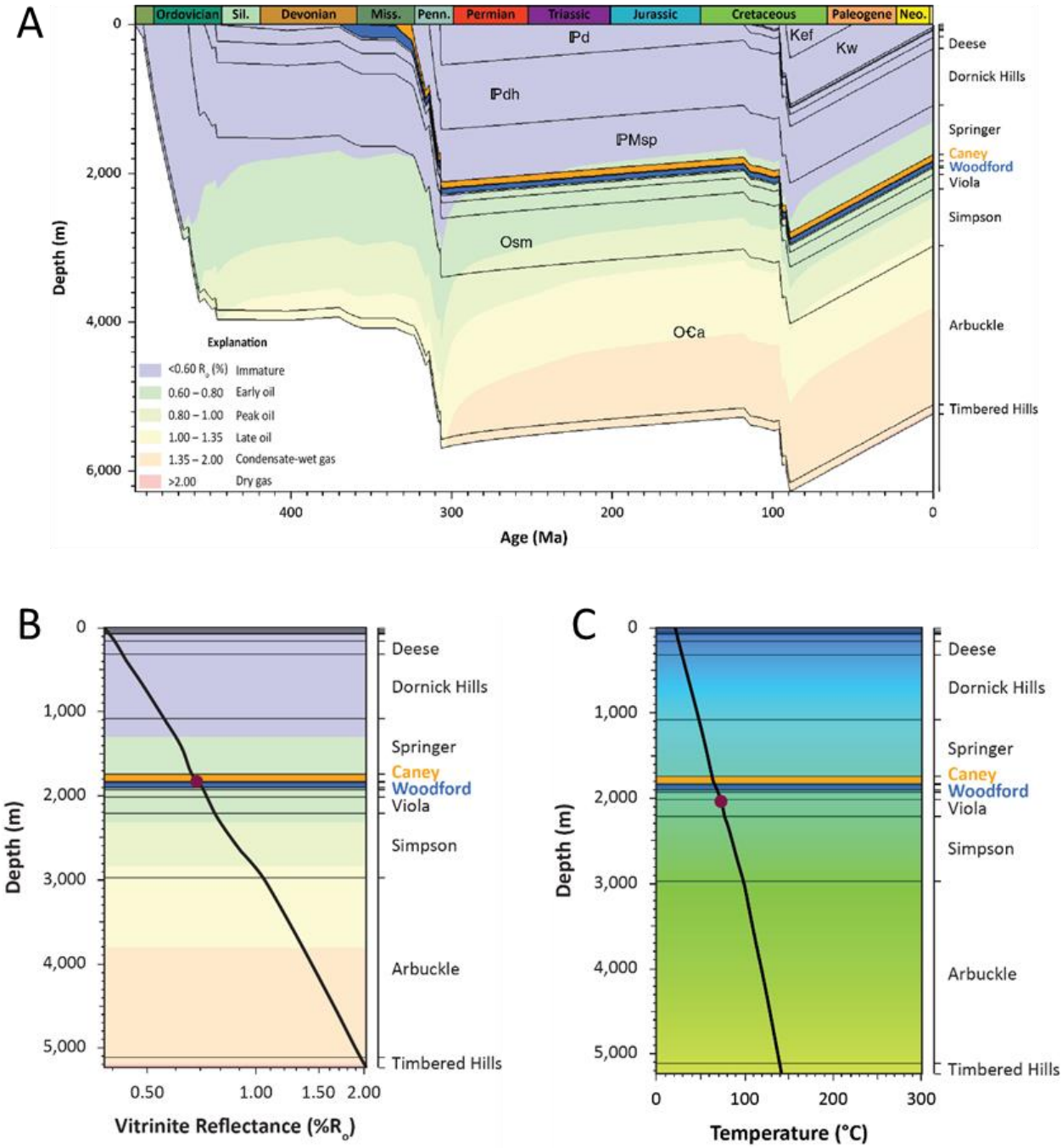

Figure 2.12. Burial and thermal history models of the Dansby 1-3H well in the southeastern Ardmore Basin. A) Burial history model showing evolution of thermal maturity windows. B) Modeled vitrinite reflectance-depth plot. C) Modeled temperature-depth plot.

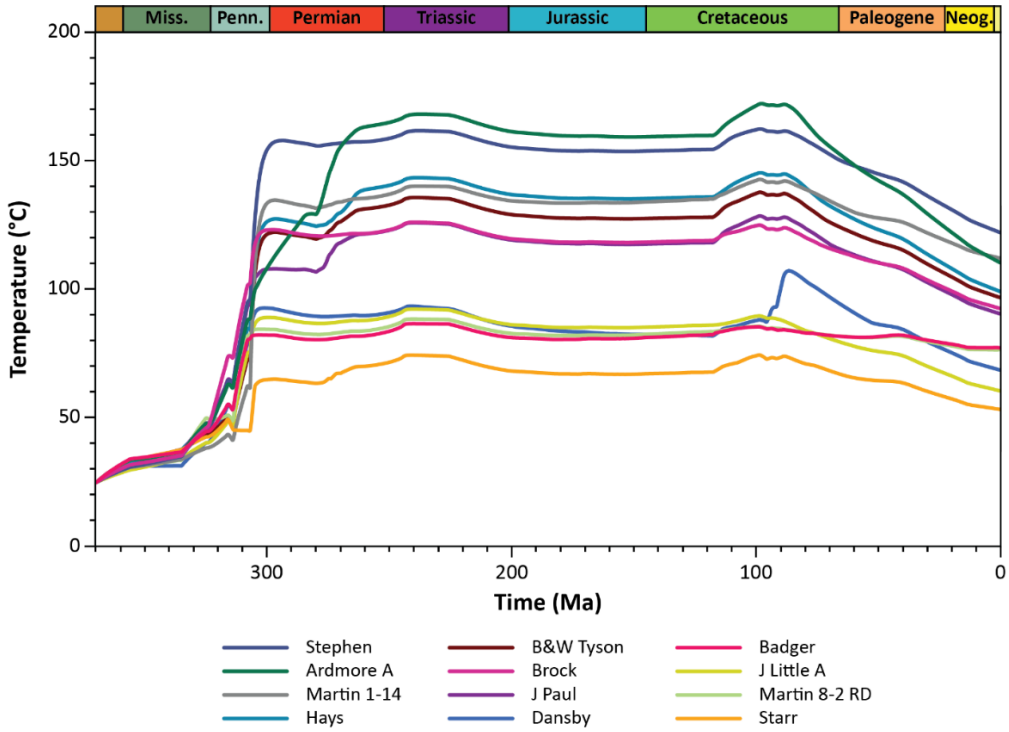

Figure 2.13. Time vs. temperature plot showing how temperature of the Woodford Shale changed in all burial history models.

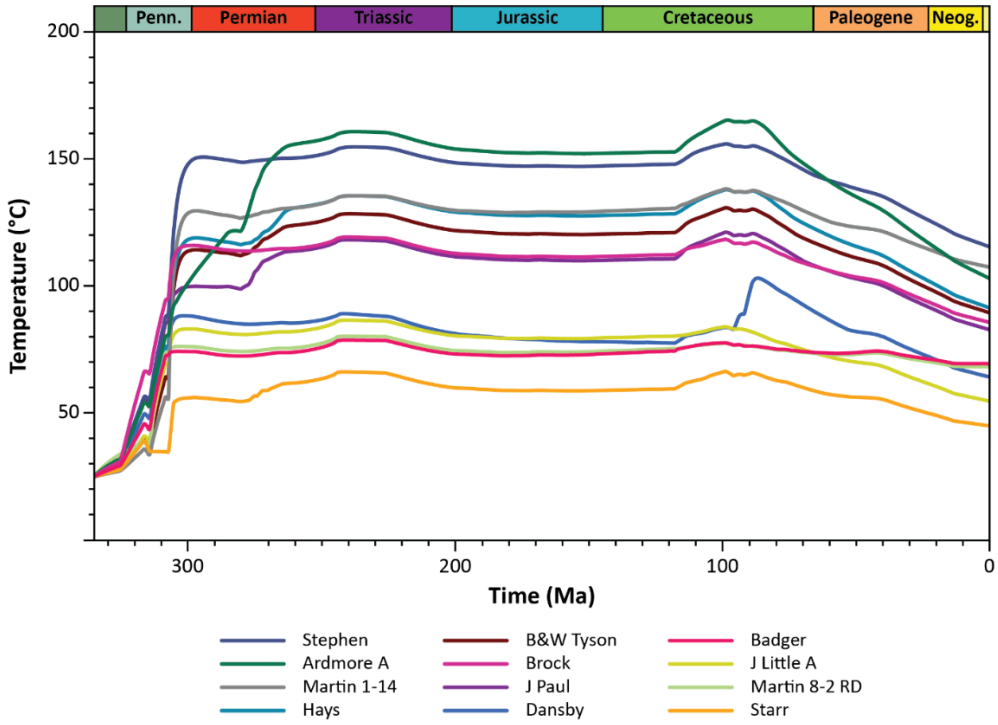

Figure 2.14. Time vs. temperature plot showing how the temperature of the Caney Shale changed in all burial history models.

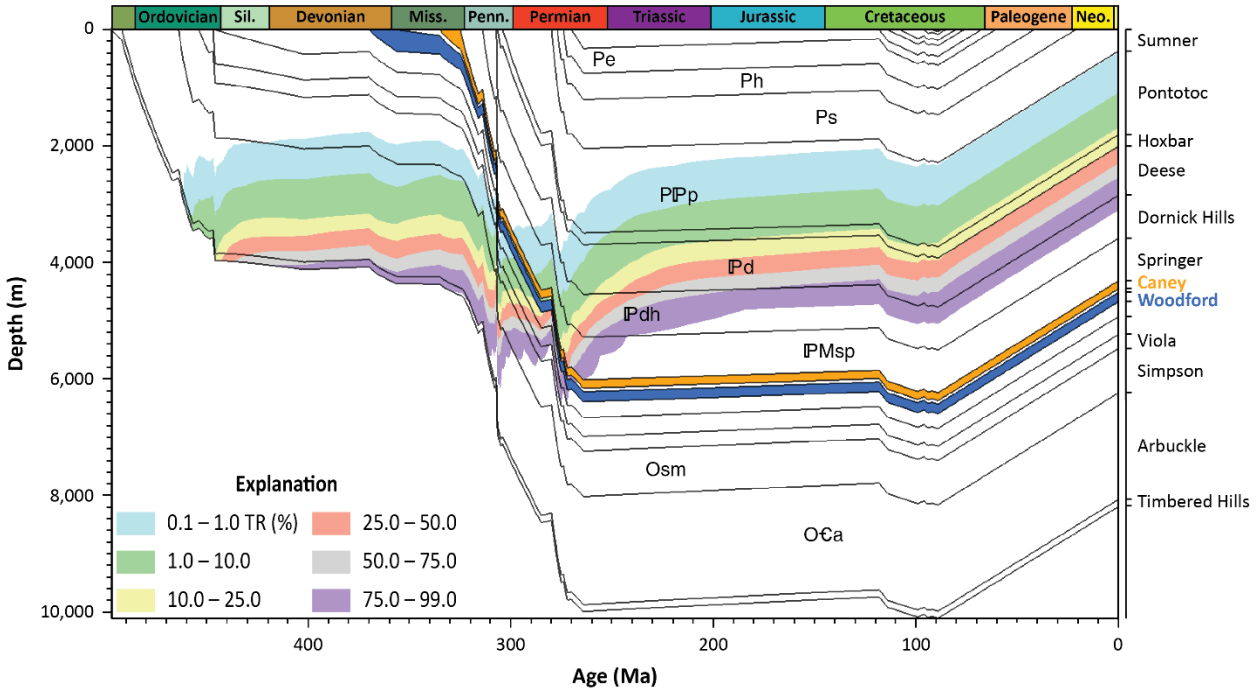

Figure 2.15. T burial history model showing how transformation ratio (TR) for Type II kerogen evolved through geologic time in the Harrisburg Trough.

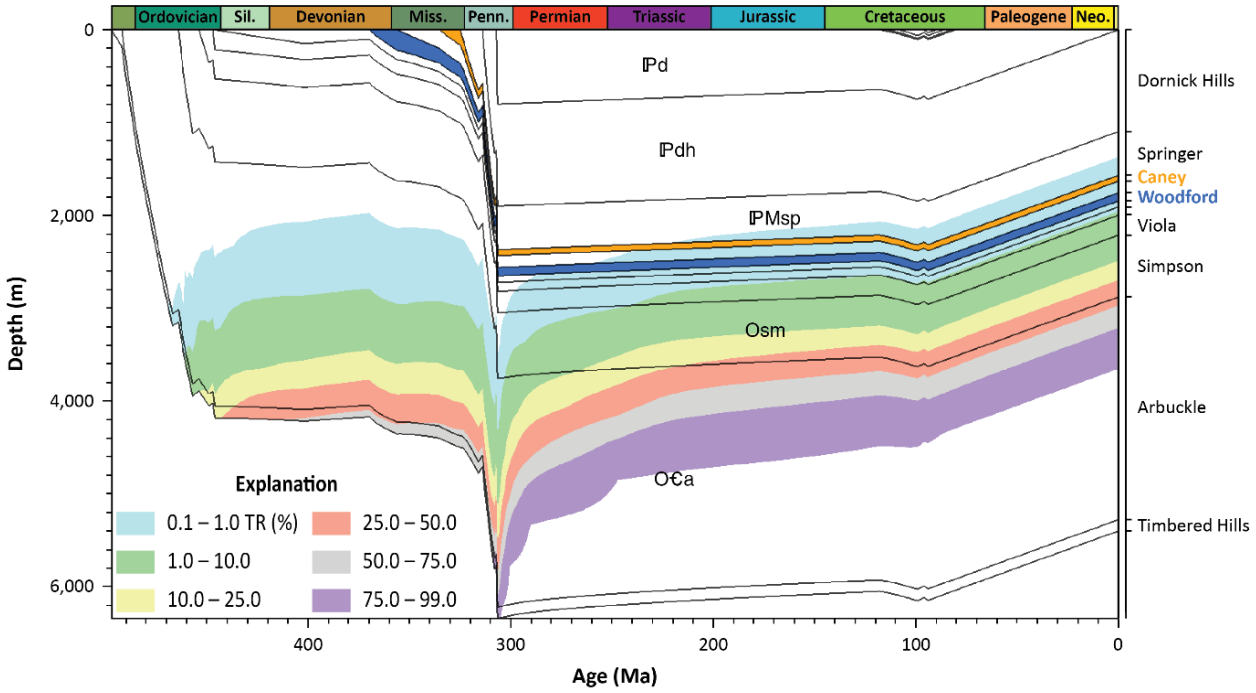

Figure 2.16. J Little A burial history model showing how transformation ratio (TR) for Type II kerogen evolved through geologic time in the northwestern flank of the Ardmore Basin.

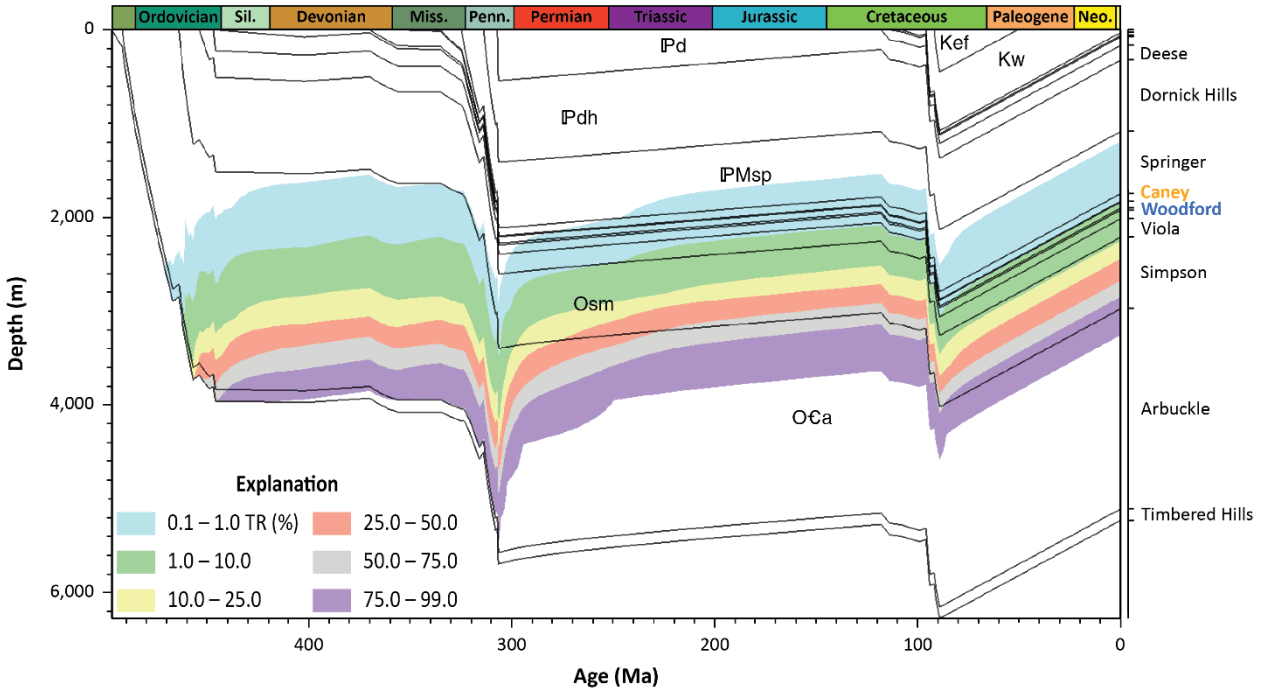

Figure 2.17. Dansby burial history model showing how transformation ratio (TR) for Type II kerogen evolved through geologic time in the southeastern Ardmore Basin.

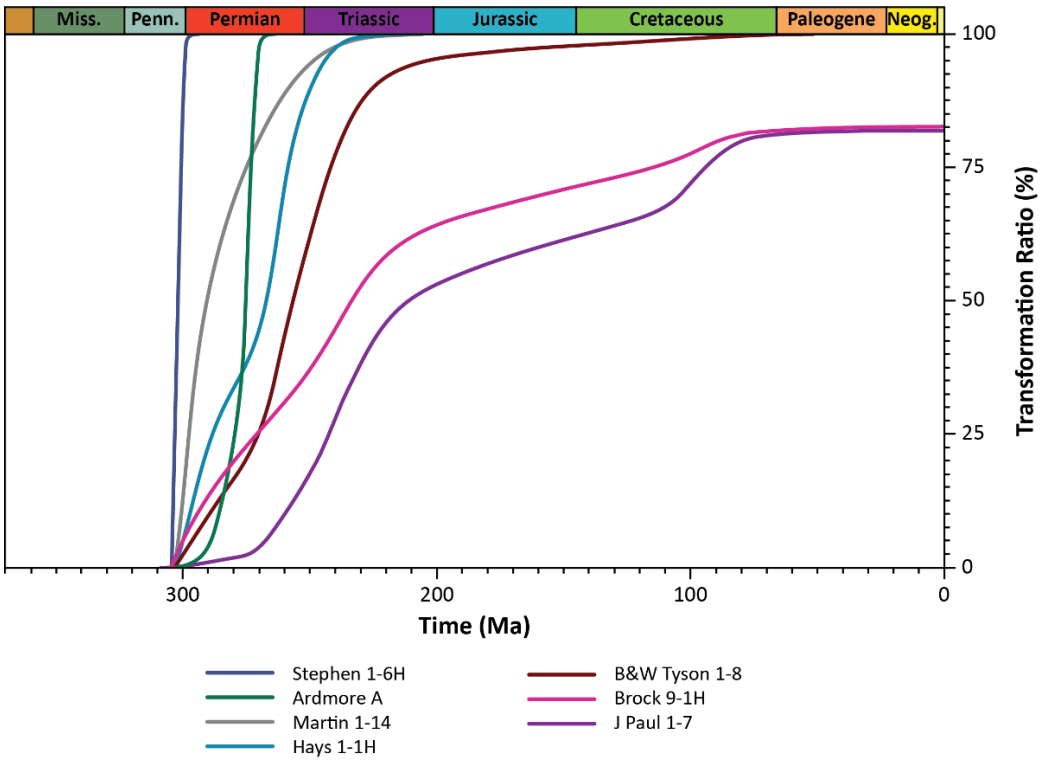

Figure 2.18. Time vs. transformation ratio plot showing how oil was generated from the Woodford Shale through geologic time in 7 wells in the Ardmore Basin.

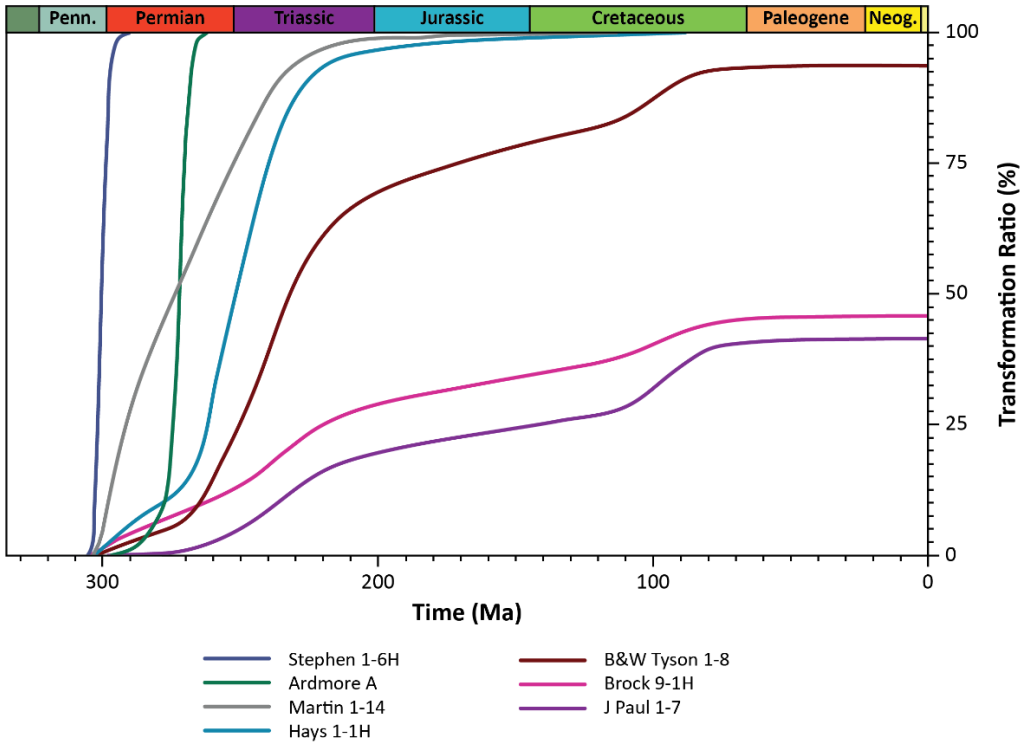

Figure 2.19. Time vs. transformation ratio plot showing how oil was generated from the Caney Shale through geologic time in 7 wells in the Ardmore Basin.

These models have low present-day basal heat flow averaging about 51 mW/m^2 (Figure. 2.20), as well as thick Pennsylvanian and Permian sections with original thickness averaging 8,600 ft. The latest time for Caney Shale kerogen to reach complete transformation was during the Cretaceous at a relatively shallow depth of 13,000 ft and a temperature of 130°C (266°F) in the Martin 1-14 model. No significant hydrocarbons have been generated in the Dansby, J Little A, Badger, Martin 8-2 RD, and Starr models where present-day transformation is less than 10% in Woodford and Caney shale (Figure. 2.20). The low transformation ratios are due to these models having thin and incomplete Pennsylvanian and Permian sections in structural highs.

Results demonstrate that the timing and degree of kerogen transformation and petroleum generation vary significantly in the Ardmore Basin on the basis of structural position (Figures. 2.3 and 2.20). High basal heat flow in structural highs was not sufficient to offset limited burial depth, making these areas unprospective for unconventional reservoir development in Woodford and Caney shale. The main hydrocarbon kitchens were in synclinal structures, which charged the Caney Shale, Woodford Shale, and conventional reservoirs throughout the basin. The major exploration fairways for unconventional development are along the flanks of the major synclinal structures, including the Harrisburg Trough, the Berwyn Syncline, and the synclinal structure in the northwestern corner of the basin. The deepest parts of the Berwyn Syncline and the nortwestern syncline are at the upper limit of the gas generation window, and in these areas there may be gas prospects, but prospects for oil and condensate preservation appear limited. An important outcome of this research is that the Ardmore A and Ardmore B wells were drilled in the Harrisburg Trough where conditions are optimal for preservation and recovery of oil and natural gas liquids, and similar conditions exist in the flanks of the Berwyn Syncline and the synclinal structure in the northwest corner of the basin, which provide

significant potential for expansion of the Caney Shale play.

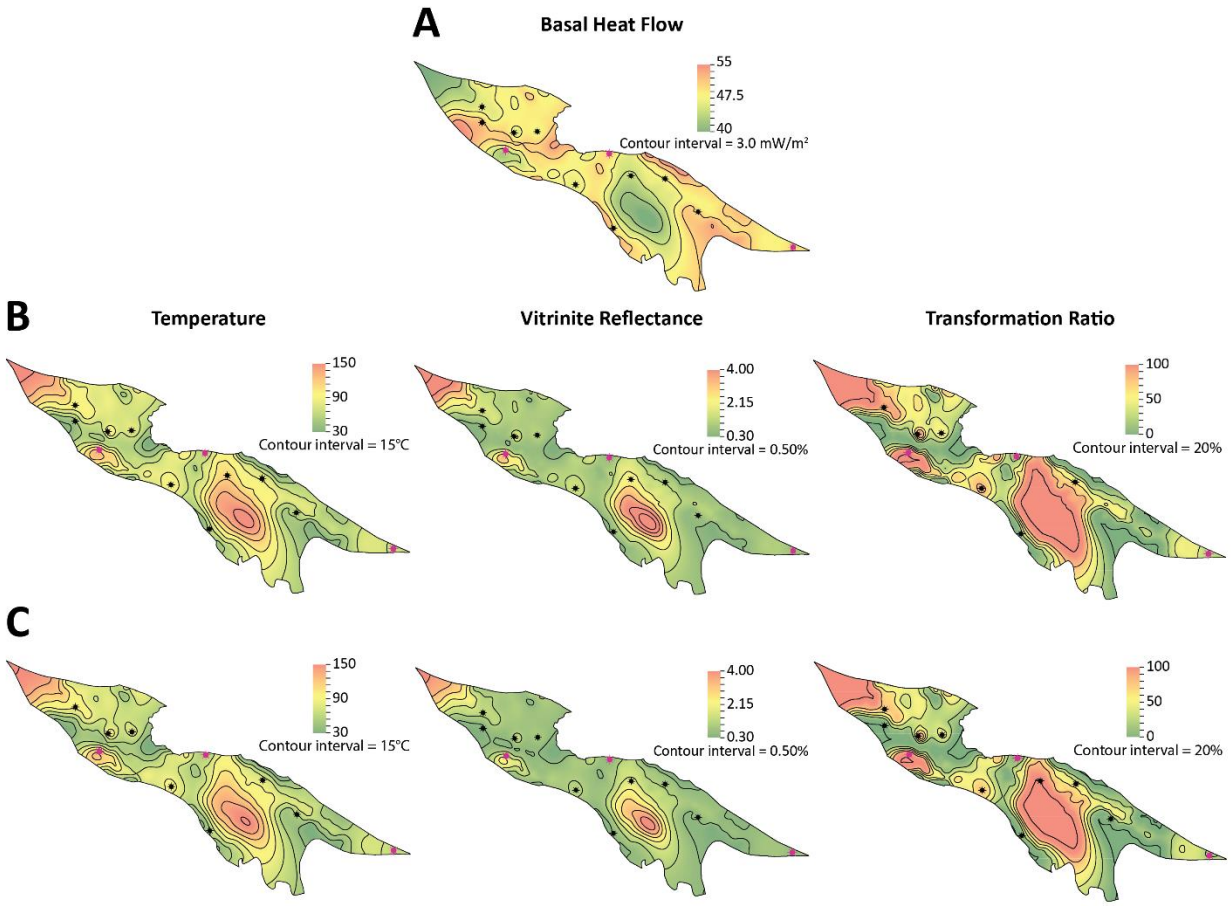

Figure 2.20. Summary maps displaying present-day basal heat flow, temperature, thermal maturity (vitrinite reflectance), and transformation ratio in the Ardmore Basin. A) Basal heat flow. Row B) Woodford Shale temperature, vitrinite reflectance, and transformation ratio. Row C) Caney Shale temperature, vitrinite reflectance, and transformation ratio.

2.1.3. Summary

Regional analysis of the Caney Shale and associated strata focused on the stratigraphic framework, structural framework, burial history, thermal history, and petroleum generation and preservation. The basin is developed on Mesoproterozoic, Neoproterozoic, and Iapetan basement and contains a succession of Cambrian-Permian sedimentary rocks that locally exceeds 30,000 ft in thickness. Basement is overlain by a Cambrian-Devonian carbonate section that formed during post-Iapetan thermal subsidence. This section is overlain by Devonian-Mississippian strata that include the petroleum source rocks and unconventional reservoirs of the Woodford Shale and the Caney Shale. The Caney shale is overlain by synorogenic strata Mississippian-Permian strata that were deposited in response to the transpressive Wichitan and Arbuckle orogenies. The southeastern part of the basin has been onlapped disconformable by strata of the Gulf of Mexico Basin, and in this area, much of the Pennsylvanian-Permian overburden has been eroded. The structure of the basin is highly complex, containing an array of deep synclines separated by basement-cored anticlines that can be

classified as oblique-slip fault-propagation folds with anticlinal breakthrough that includes flower structures. Structural growth of the anticlines and synclines occurred during the Late Mississippian and Pennsylvanian and locally continued into the Permian. Thermal maturity of the petroleum source rocks is near the top of the hydrocarbon generation window and undermature in the major uplifts. Isoreflectance lines are nearly horizontal, cutting across structure, indicating a net post-kinematic maturation pattern. Basin modeling indicates that Woodford and Caney shale attained their generative potential during and after synorogenic burial. Thermal maturation of the petroleum source rocks was largely complete by the end of the Mesozoic; the generative potential has been exhausted in the synclinal structures, whereas nearly all generative potential remains in the largest uplifts. The Woodford and Caney can be classified as self-sourced, continuous-type unconventional reservoirs, and hydrocarbons generated from these reservoirs also charged the conventional reservoirs that have long been productive in the anticlinal structures. Results of this study indicate that the most viable exploration fairways for unconventional shale oil and gas resources are in the synclinal structures, including the Harrisburg Trough, which contains the Ardmore A well and Ardmore B wells, and in the flanks of the Berwyn Syncline and an unnamed synclinal structure in the northwest corner of the basin. Accordingly, considerable room remains for the growth of the Caney Shale play.

2.2.Detailed Rock Analysis

2.2.1. Approach

Detailed rock analysis of the Caney Shale was undertaken to establish the micro- and macroscopic character of depositional facies and determine which facies are potential reservoirs and identify those facies that are seals or non-reservoirs. Macro- and microscopic analysis focused on lithofacies, composition and rock fabric (Wang et al., 2021) and included stratigraphy, facies patterns, structural style, bedding, physical sedimentary and biogenic sedimentary structures, natural fractures, and geomechanical properties. Microscopic components included framework rock composition and fabric, diagenetic alteration of the fabric, organic content, and pore structure (Loucks et al., 2012; Vanden Berg & Grammer, 2016). As the Caney Shale is highly susceptible to chemical modification by atmospheric moisture and oxygen, access to freshly cut core, which was sampled before it was altered by exposure to the atmosphere, was critical to this study. Once reservoir and non-reservoir facies were established, they were tied to open-hole wireline log signatures to calibrate petrophysical logging curves to rock data. Petrophysical facies were extended to wireline logs for wells without core, thereby facilitating the mapping of the spatial distribution of reservoirs, an essential step in developing oil and gas resources in the Caney Shale.

2.2.2. Results and Discussion

Lithofacies and Facies Groups

Detailed core description (650 ft/200 m) and petrographic analysis (N=100) were conducted to identify facies and interpret depositional processes. The lithology of mudstones are distinguished between mudstone-siltstone and carbonate mudstone by using a visual cut-off of 50% in carbonate or siliciclastic composition in thin section. The carbonate facies are divided into dolomitic and limestone facies based on the dominant mineralogy type, with the limestone facies being further

defined using the classification method of Dunham (1962) and Embry and Klovan (1971). At a whole core scale, a total of ten mixed carbonate-siliciclastic facies types are identified (Figure 2.21). These facies types include individual and often overlapping endmembers of mudstone, siltstone, and carbonate facies. To further facilitate the analysis of reservoir properties (e.g., porosity, permeability, fracture distribution, rebound hardness), all facies were grouped into facies groups based on the overall composition and fabric of the rock framework (Figure 2.21).

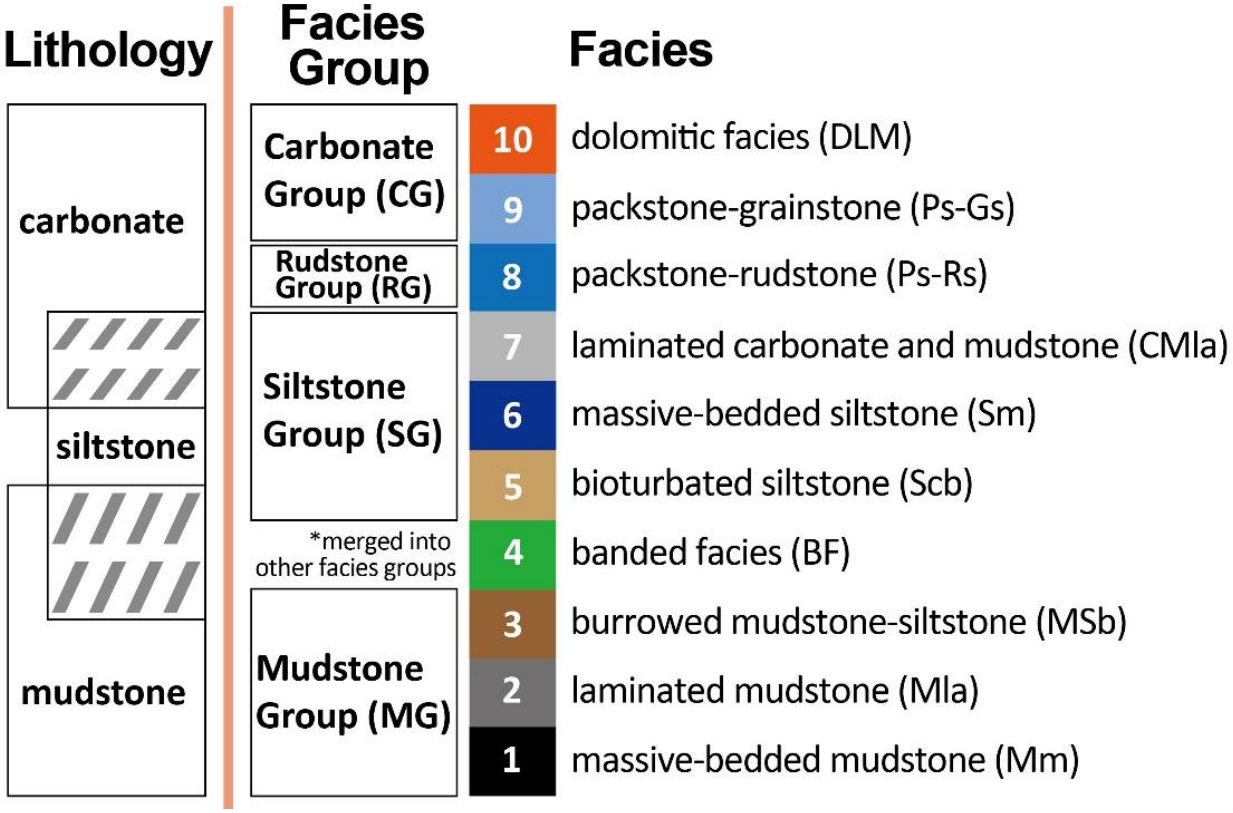

Figure 2.21. A total of 10 mixed carbonate-siliciclastic facies types are identified in this study using core and thin sections and mostly include mudstone (Mm, Mla, MSb), siltstone (Scb, Sm, CMla), and carbonate facies (Ps-Gs, DLM), which are grouped into four facies groups for facilitating petrophysical and rock mechanical analysis.

Based on the observations in individual facies as discussed above, several types of depositional processes are interpreted, and at a whole core scale, can be summarized as a seemingly dominant lower-energy background sedimentation with intermittent higher-energy event deposition (Figure 2.22). Mudstones characterize the lower energy deposits, with massive-bedded mudstone likely reflecting low-energy, restricted bottom water with occasional reworking by bottom currents (e.g., Loucks et al., 2011). For the laminated mudstones, its mud-dominated laminations and scattered grain-rich components suggest a somewhat similar origin (e.g., Liang et al., 2016), with the scattered wavy and cross laminations pointing to intermittent higher-energy conditions (e.g., Loucks et al., 2011). In the burrowed and bioturbated mudstone-siltstone, the common presence of millimeter-sized burrows in these two facies point to overall low-energy conditions with relatively poor to slightly oxygenated bottom water conditions, which can be episodic as indicated by the interlayered burrowed and bioturbated intervals. In contrast, three types of higher-energy depositional events are interpreted,

including turbidite, debris flow deposits, and storm deposits (or possibly contourites), all of which are present locally within the "background" mud-rich facies, likely indicating intermittent deposition into the low energy realm. For turbidites, representative examples are interpreted from vertically stacked facies that show systematic variations in sedimentary structures and grain size as observed in Figure 2.23.

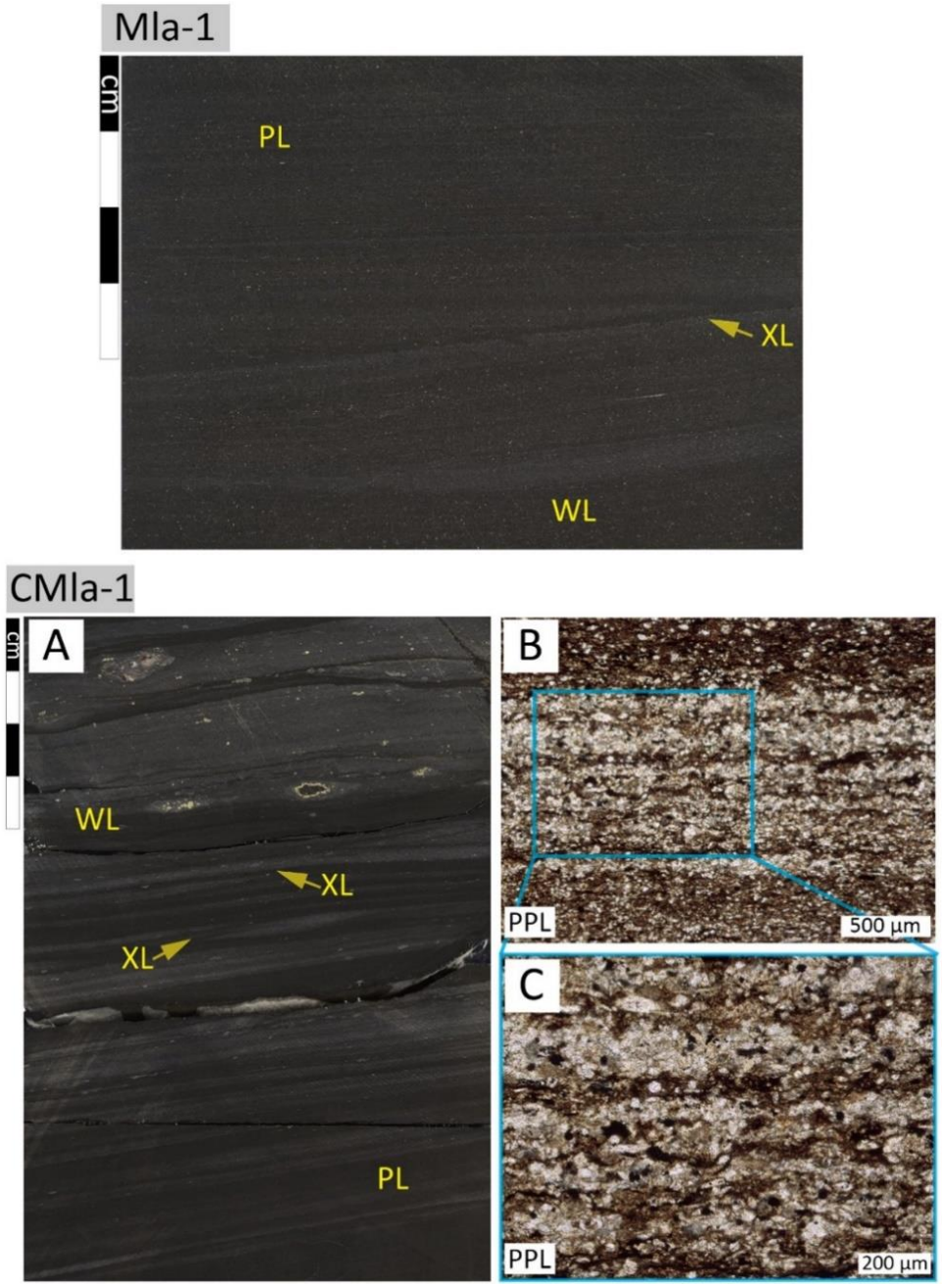

Figure 2.22. Core photo of laminated mudstone (Mla) and core photo (A) and thin section photomicrographs of laminated carbonate-mudstone (CMla; B, C). Both facies are characterized by abundant millimeter-thick laminations, which are dominated by mud in laminated mudstone (Mla-1) and by calcite-cemented silt-sized quartz and skeletal fragments in laminated carbonate-mudstone (CMla-1). Both facies can contain planar (PL) to wavy laminations (WL) and cross-laminations (XL). C is zoomed-in from B. Mla-1 and CMla-1 represents the most observed sub-type of laminated mudstone (Mla) and laminated carbonate-mudstone (CMla), respectively.

Similar vertical stacking of facies is commonly interpreted using the classic Bouma Sequence which contains five internal divisions of Ta to Te produced by waning turbidity current (Bouma, 1962; Shanmugam, 2000; Mulder and Alexander, 2001; Mulder et al., 2001; Gani, 2004; Mutti et al., 2009; Bourget et al., 2010; Loucks et al., 2011; Hurd et al., 2018; Kvale et al., 2020; Siwek et al., 2023), indicating that the observed patterns observed in Figure 2.3 likely represent distal portions of turbidite deposits. The massive bedded carbonate packstone-grainstone likely indicates rapid, high-energy deposition of grain-dominated sediments in a similar process with the basal unit Ta in a turbidite sequence (e.g., Kneller and McCaffrey, 2003) or deposited from sustained turbidity currents (Kneller and Branney, 1995; Stow and Johansson, 2000) or sandy debris flows (Stow and Johansson, 2000). Sample bias due to core size (width) and lack of lateral rock data from other cores, as well as the potential of amalgamated turbidites and debris flows, however, must be taken into consideration when making these depositional interpretations (Van Daele et al., 2017; Cunningham and Arnott, 2021).

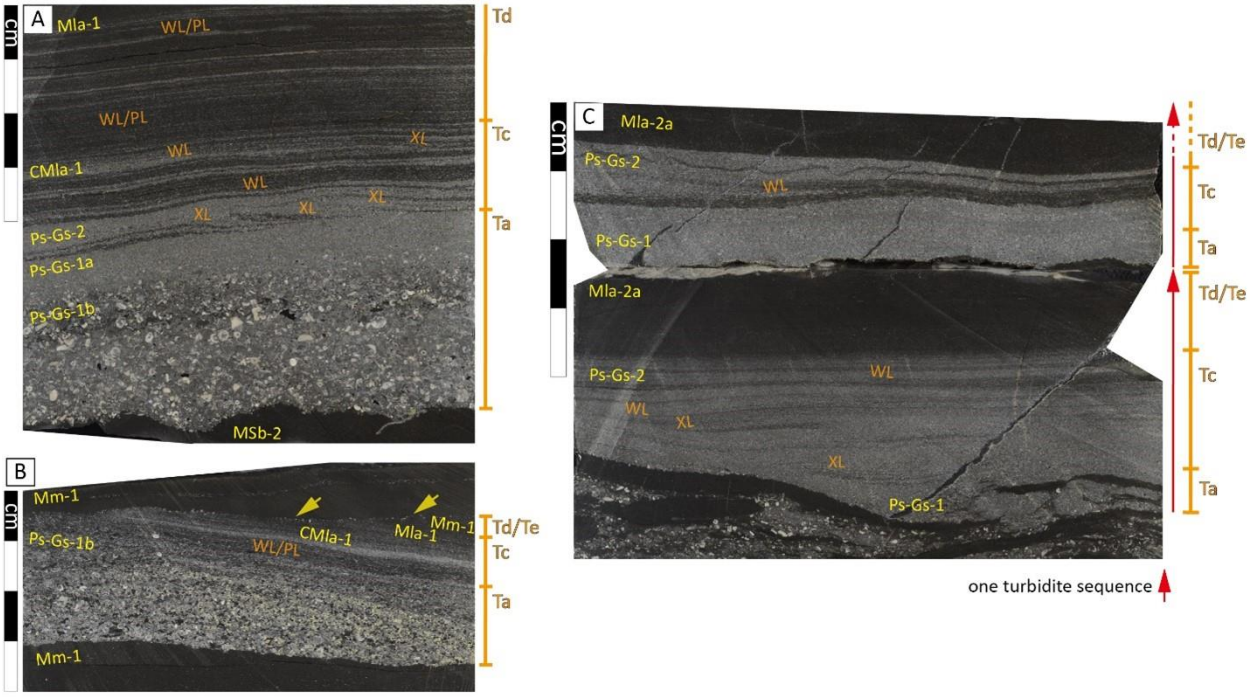

Figure 2.23. Core photos showing the interpreted turbidite intervals with individual (A, B) and stacked (C) turbidite sequences.

Debris flow deposits are represented by the packstone-rudstone facies (Figure 2.24), where the abundant poorly sorted and chaotically arranged, shallower marine grains (e.g., bryozoans, microbially coated grains, packstone-grainstone pebbles) point to an origin of debris flows (e.g., Lowe and Guy, 2000; Mulder and Alexander, 2001; Gani, 2004; Talling et al., 2004; Mutti et al., 2009; Campos et al., 2011; Ingram et al., 2011; Siwek et al., 2023) sourced from shallower marine carbonate platform at updip locations due to the failure of slope or platform margin, potentially triggered by sea-level variations and tectonic activities (Grammer and Ginsburg, 1992; Schlager et al., 1994; Bouma, 2000; Payros and Pujalte, 2008; Jablonska et al., 2018). In particular, pebbles of

various composition (e.g., mudstone, carbonate) and the presence of mudstone clasts within carbonate pebbles likely suggest multiple episodes of erosion-cementation events across various locations along the slope trajectory as the flow advances/reactivates and potentially merges with other flows, which have been documented in modern slope systems (e.g., Bahamas; Grammer and Ginsburg, 1992).

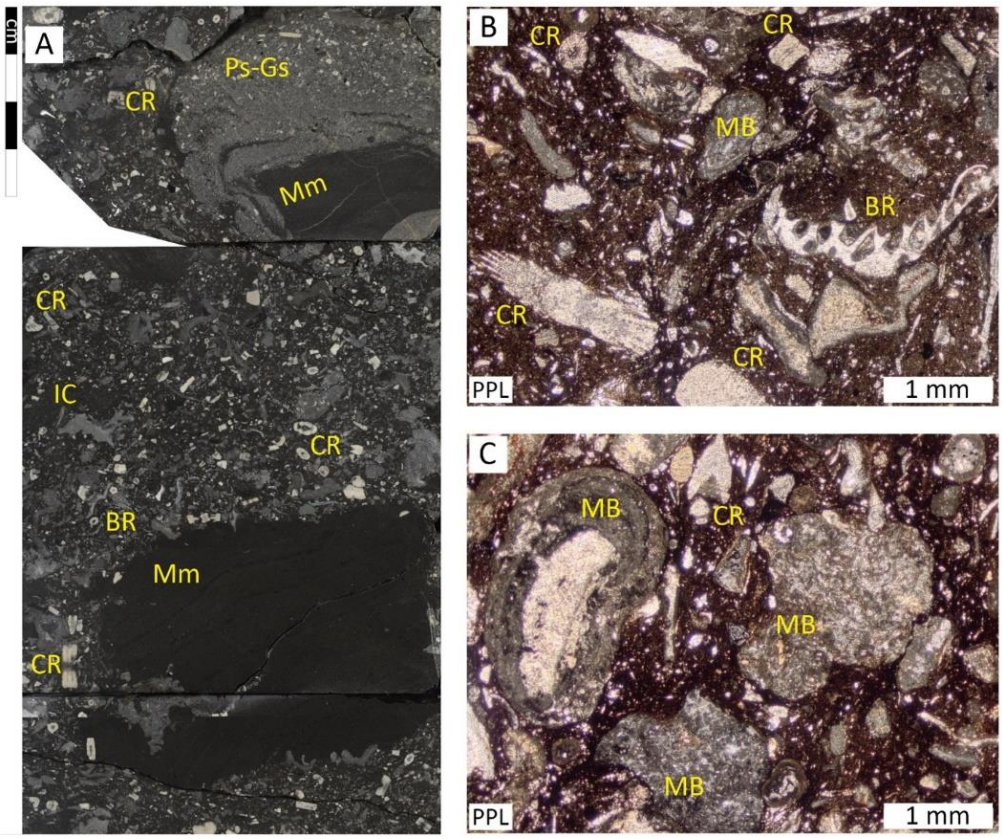

Figure 2.24. Core photos (A) and thin section photomicrographs (B, C) of packstone-rudstone (Ps-Rs) debris flows. These facies contain abundant poorly sorted, silt- to sand-sized grains and clasts. Common types include skeletal fragments (e.g., bryozoans or BR, crinoid or CR, and bioclasts with undiscernible types), microbially coated grains (MB), intraclasts (IC), and pebbles in various rock types (e.g., Ps-Gs and Mm in A). Ps-Gs: silty packstone-grainstone. Mm: massive-bedded mudstone.

Rebound Hardness

To analyze the distribution of relative rock strength, rebound hardness tests were conducted on core surfaces that were complete and free of roughness, unevenness, or cracks. Rebound hardness data were collected using an Equotip Piccolo 2 Unit-D hardness tester. When conducting the test, rebound hardness is automatically calculated by the testing device using the ratio of impact and rebound velocities, which is then converted into rebound hardness by multiplying this ratio by 1,000. Therefore, RHN is a proxy for relative rock strength by providing "a measure of the resistance of a surface to impact penetration of a plunger tip" (Aydin and Basu, 2005), rather than a physically defined hardness parameter. Because of its unitless nature, RHN can be conveniently compared with other types of rock data (e.g., mineralogy, porosity, sonic velocity, rock mechanical properties; Wang et al., 2021). Each data point is averaged from five to ten measurements, which are confined within

circular areas being less than 1 cm^2 in size without overlapping individual testing locations. Rebound hardness testing procedures and workflow has been addressed in detail by Wang et al. (2021) for characterizing the rebound hardness of the STACK play and the Vaca Muerta Formation.

At a facies group scale, the increasing average and range of RHN in the order of mudstone group, siltstone group, and carbonate group (Figure 2.25) suggest the vertical stacking of facies can create rock mechanical heterogeneity.

Facies Groups Defined from Core	**Mudstone Group**			**Siltstone Group**			**Carbonate Group**		**Rudstone Group**
RHN of Facies	**Mm**	**Mla**	**MSb**	**Scb**	**Sm**	**CMla**	**Ps-Gs**	**DLM**	**Ps-Rs**
Average	565	571	558	617	631	636	725	694	597
Maximum	765	701	745	789	770	775	870	793	725
Minimum	327	377	318	509	519	436	566	553	427
Std Deviation	54.5	76.0	66.8	60.8	45.1	78.9	47.6	66.3	96.0
Data Count	543	25	390	232	135	54	176	22	26

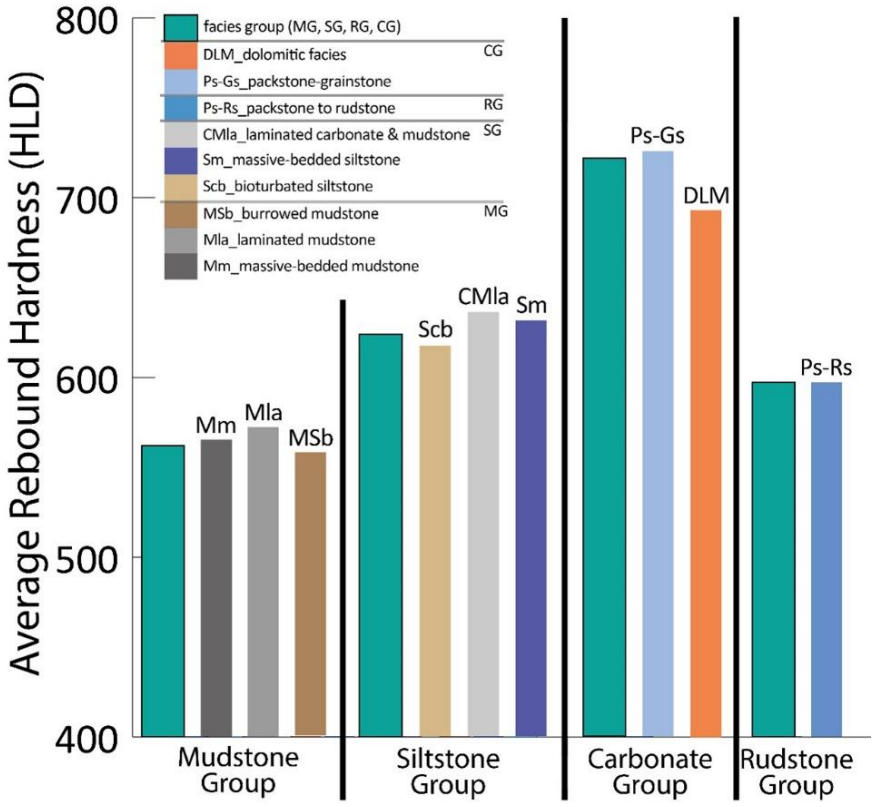

Figure 2.25. Upper: table showing the summary statistics of the rebound hardness values of all individual facies and facies groups. Lower: bar chart showing the average rebound hardness of facies groups and individual facies. In the legend of the lower bar chart, facies groups are noted with acronyms, including CG (carbonate group), RG (rudstone group), SG (siltstone group), and MG (mudstone group). Overall, carbonate group and mudstone group shows the highest and lowest average rebound hardness value, respectively.

Such a direct tie between rebound hardness and facies points to the correlation of rock framework with RHN in several aspects, such as lithology (muddy siltstone vs. calcareous siltstone), sedimentary structures (e.g., massive-bedded vs. laminated, burrowed vs. bioturbated), and cementation patterns (e.g., mud-dominated vs. carbonate grain-dominated vs. carbonate cement-dominated). Therefore, the vertical stacking of facies, which is heterogeneous across multiple scales in core (within and among segments) can potentially help predict the vertical heterogeneity in rock mechanical properties on a first-order pass (e.g., average RHN). However, overlaps in the ranges of RHN values among facies (Figure 2.25, table) indicate a lack of well-defined separations in RHN among different facies, implying the challenges by using RHN data alone to define facies groups. Such overlapped RHN ranges among facies can be related to the highly variable mineralogy of individual facies that corresponds well to the common presence of "transitional" facies types observed in core (e.g., silty mudstone vs. muddy siltstone, calcareous siltstone vs. silty carbonate). Another potential factor contributing to the overlapping RHN among facies is that RHN is likely affected by a combination of petrophysical parameters in a complex, multivariate manner, such as mineralogy, porosity, and sonic velocity, which has been documented in the partially time-equivalent "Miss Lime"/STACK play in North-Central Oklahoma and the Vaca Muerta Formation in Argentina, both of which contain similar facies types (Wang et al., 2021). Such a multivariate impact of petrophysical properties on rebound hardness may also explain the variable rebound hardness-porosity relationship in different zones within the stratigraphic framework. Nevertheless, the well-defined negative trend within the carbonate group of the whole core data and in Segment 1 and 4, as well as the positive trend in Segment 3 (Figure 2.26) indicates the potential value of utilizing rebound hardness to estimate porosity from the perspectives of facies and stratigraphic framework.

Fracture Analysis

Natural fractures, either open or cemented, can be important from the perspective of affecting fluid flow (e.g., reservoir performance and compartmentalization) and production/completion design (e.g., propagation of induced fractures) (Gale et al., 2007, 2014). To characterize the natural fracture system, the slabbed core surface was examined to describe individual natural fractures. In this study, fractures that are partially to fully mineralized are interpreted to be natural in origin, utilizing the same criteria used for the "Mississippian Limestone"/STACK play in north-central Oklahoma (Wang et al., 2019).

For each interpreted natural fracture, several attributes are documented and measured, such as height, kinematic aperture, orientation, termination style, spacing, type of host facies, and intensity (absolute and normalized count). Kinematic aperture is defined as the total distance between the two fracture walls in one fracture, including opening space and cementation ("accumulative opening of fracture"; Marrett et al., 1999). If the fracture extends into another facies, the dominant facies is used for characterization purposes. To quantify the distribution of fractures at different scales, fracture intensity and average fracture intensity are calculated. Fracture intensity represents the number of fractures per meter of core (i.e., absolute count). For the purpose of eliminating the biasing effect of core footage on fracture abundance (i.e., thicker interval in core can contain more fractures), average fracture intensity is derived by dividing the fracture intensity by the corresponding core footage of a selected interval (i.e., normalized fracture count per meter of core), such as facies and stratigraphic

framework. These fracture data are then tied to facies types and stratigraphic framework to evaluate statistical patterns. The methodology utilized for fracture description and the definition of fracture attributes, as well as distinguishing natural fractures from induced fractures, are based on Nelson (2001), Lorenz et al. (2002), and Gale et al. (2007, 2014).

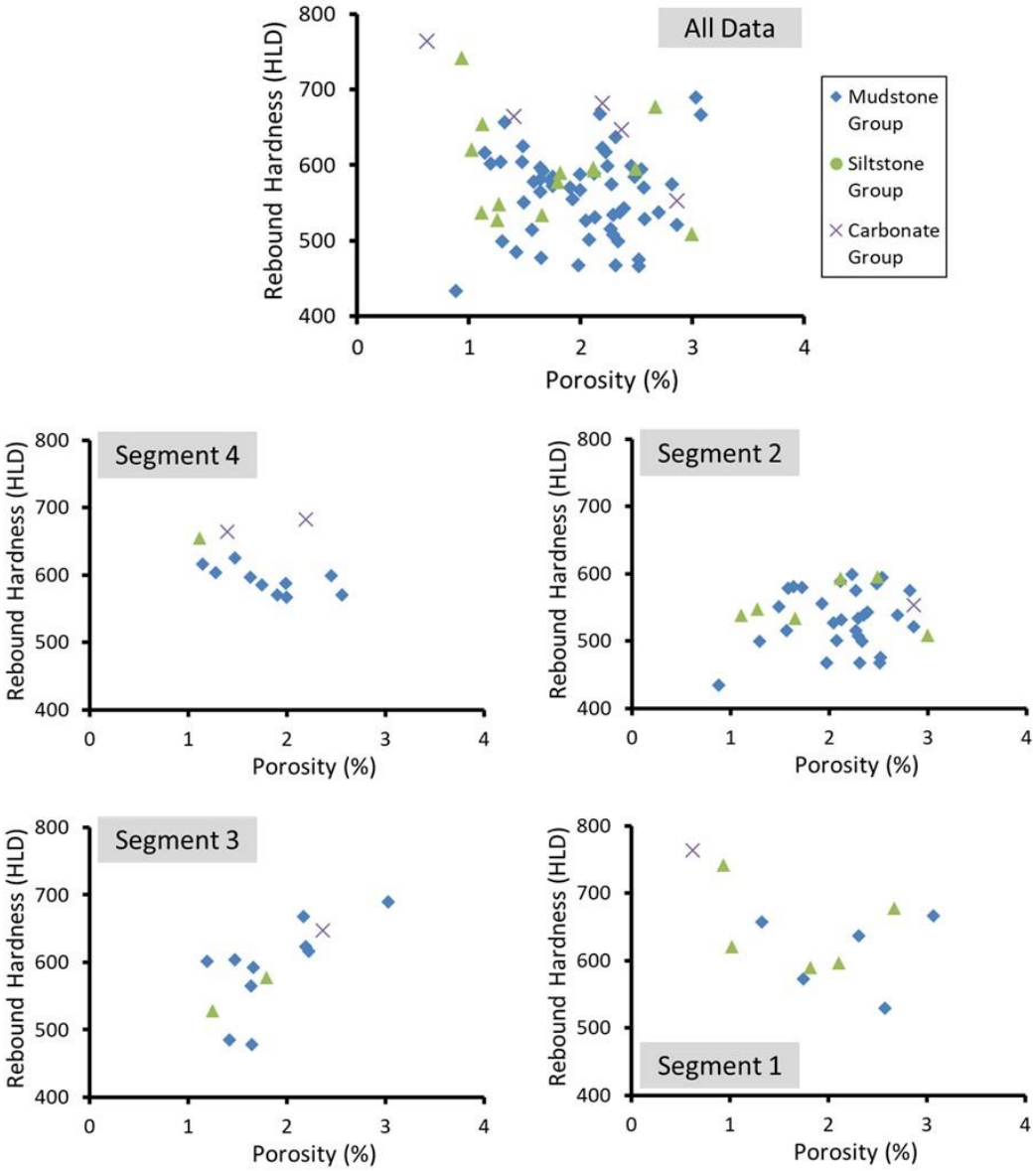

Figure 2.26. Cross-plots showing the porosity-rebound hardness relationship in this study arranged by whole core data (top cross-plot, "All Data") and by the four segments defined in core (lower four cross-plots, "Segment 1" to "Segment 4").

As observed in this study, the distribution of naturally mineralized fractures is heterogeneous across multiple scales, which are similar to the observations in the partially time-equivalent Miss Lime/STACK play in North-Central Oklahoma (Wang et al., 2019). At a whole core scale, the highest average fracture intensity occurs the in carbonate group. At a finer scale, mineralogy is a key factor in fracture abundance and intensity. Fracture termination at the boundaries of varying lithology is

not uncommon, resulting in a bed-bound fracture distribution pattern (Figure 2.27). Collectively, these observations indicate that layers with contrasting fabric and mineralogy of the rock framework, as well as the relevant petrophysical/rock mechanical heterogeneities, may be critical factors in determining fracture geometry and distribution, similar to the observations in the "Miss Lime"/STACK play in North-Central Oklahoma as documented by Wang et al. (2019).

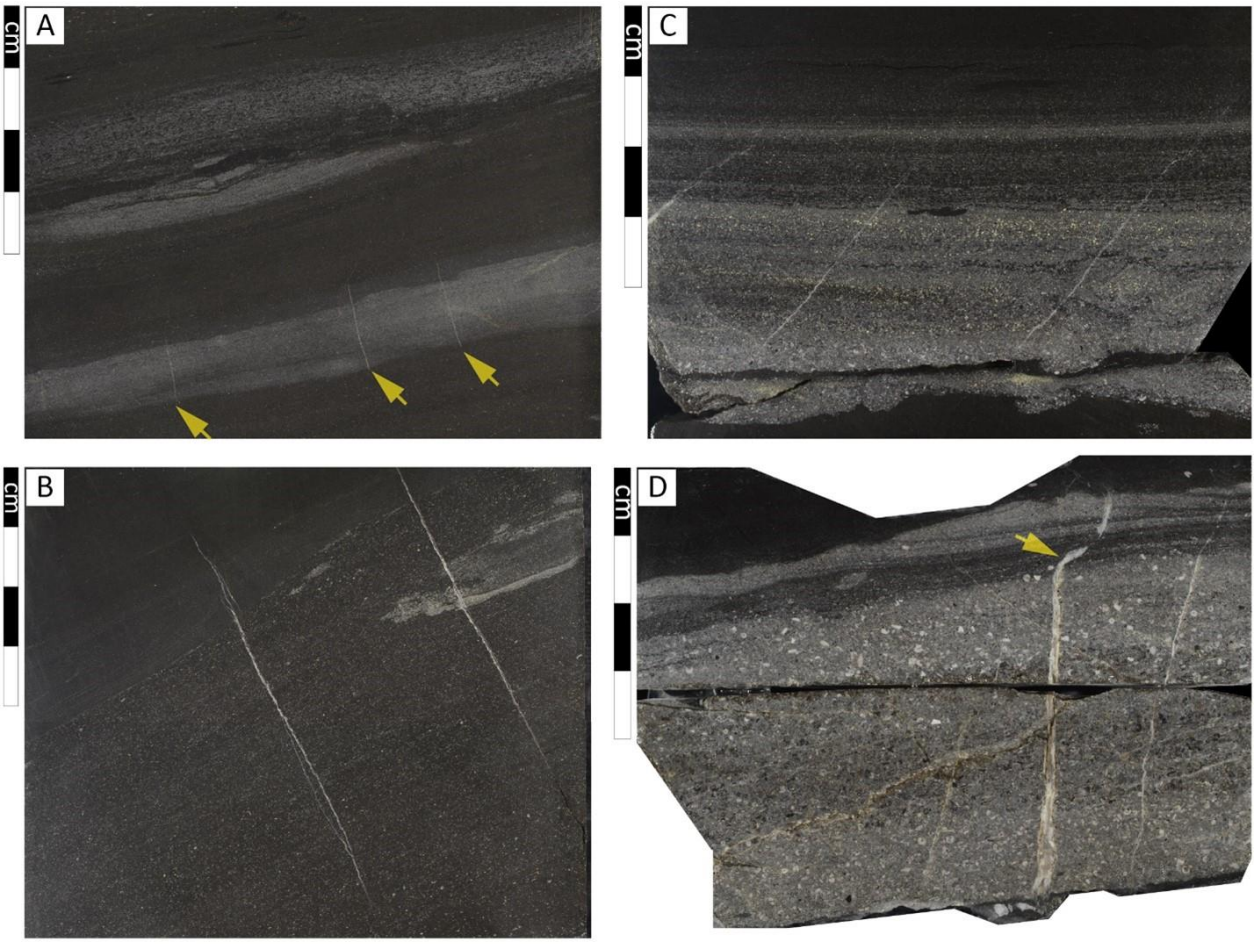

Figure 2.27. Core photos showing the bed-bound fractures observed in this study, which can be nearly perpendicular (A, marked by arrows; B, D) or oblique (C) relative to the host layers. In rare examples, fractures can show enhanced deformation when intersecting mud-rich layers (D).

In contrast, instances can also be common where fractures cut through multiple relatively rigid layers (e.g., carbonate) and extend far beyond the layering boundaries (e.g., Figure 2.28), or terminate within the hosting layer in places without distinctive mineralogy variations. These examples illustrate the complexity in the distribution pattern of fractures at a finer scale and can raise challenges in unequivocally assigning a particular facies to individual fracture. In addition, for adjacent rigid layers with similar rock framework composition, fractures can be present even in one but absent in the other. These observations point to complex mechanisms that affect the propagation and confinement of fractures, even in layers with relatively homogenous mineralogical composition.

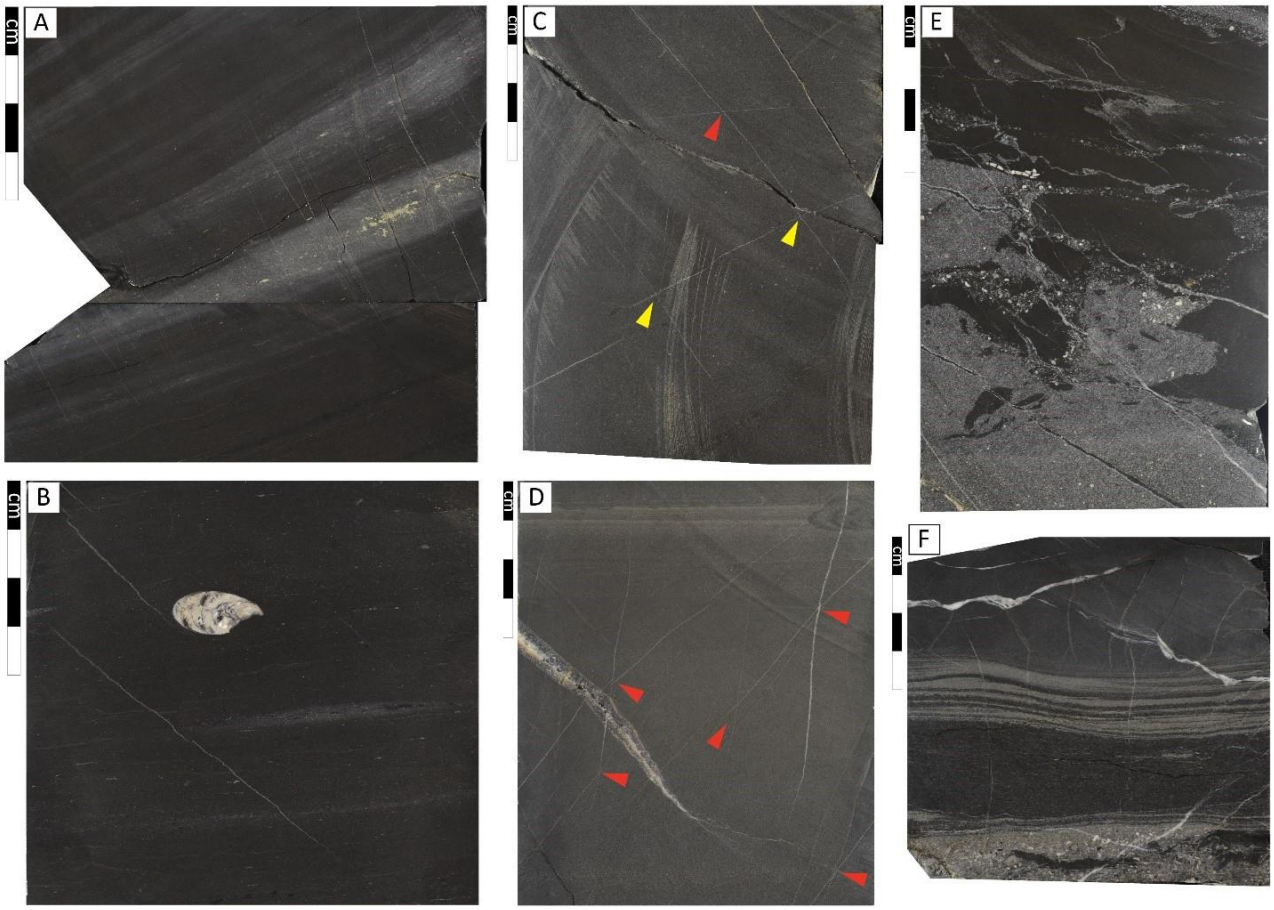

Figure 2.28. Core photos showing the various forms of presence of the naturally mineralized fractures observed in this study. When intersecting carbonate layers, these fractures can be perpendicular (A) or oblique (B) relative to the layers. The fractures can also form cross-cutting sets by nearly 90 degrees (C) or 60/30 degrees (D). Rarely, fracture swarms with chaotically distributed (E) and drastically changing kinematic aperture (F) are observed.

2.3.Pore System Architecture

2.3.1. Approach

Eight samples were selected to cover key facies types within the main facies groups, including mudstone (N=4), siltstone (N=2), and carbonate (N=2) facies groups Figure 2.21). To ensure successful imaging of the pores at a micron to nanometer scale, it is necessary to polish the sample surface using an ion mill (this study: JEOL IB-19500CP Cross Section Polisher). Via the argon-powered gun, an ion mill creates a finely polished surface which is essentially free of the surface roughness created on manually polished surfaces, and therefore, is crucial for imaging the pore systems under SEM (e.g., Loucks et al., 2009; Vanden Berg and Grammer, 2016). Each sample is milled for 12 hours then sputter-coated with gold to mitigate the charging effect that would be created during the SEM imaging. For each sample, 70 to 120 photos were taken using a FEI Quanta 600F field emission SEM to capture representative pore types. An approach of incrementally decreasing scale is utilized, meaning that a larger area was chosen (at the scale of 10 to 40 microns) and photos were then taken at incrementally finer scale in key areas (down to around 5 microns, 2 microns, 1

micron, and 500 nm in scale). Next, selective samples are imaged via the ThermoFisher MAPS software for auto-stitched maps built using hundreds of individual SEM images, which allow for high-resolution viewing at multiple scales without issues such as resolution degradation and view distortion that are challenging to achieve via manual SEM imaging and stitching.

Following the collection of SEM images, the subsequent pore architecture characterization workflow consists of three main steps, including identifying pore types using the classification method of Loucks et al. (2012), characterizing the geometrical parameters of pores by applying digital image analysis (DIA) on SEM images, and tying these parameters with petrophysical data. By color-segmenting different features on a SEM image based on gray-scale, digital image analysis is achieved via Leica's LAS Application Suite software. In this process, a series of measurements of individual pores is automatically captured, such as length, aspect ratio, area, and perimeter, which can be utilized for calculating additional parameters (e.g., perimeter-over-area). In particular, the color-segmentation step, which is automatically achieved by the software, is vulnerable to the potential misidentification of darker-colored pixel spots (i.e., noise in the image) as pores and the inaccurate delineation of pore boundaries, leading to over-counting of pores and erroneous measuring results (e.g., area, perimeter). To enhance the accuracy of the measurements, all pores are individually checked and manually refined for count and shapes (e.g., to remove noise and re-draw pore boundaries when necessary), which can help achieve an enhanced characterization of the pore architecture.

Following the digital image analysis (DIA), several additional pore geometrical parameters are calculated using the measurements collected during the DIA process, including pore size, perimeter-over-area (PoA), and gamma (γ), all of which are adopted from Anselmetti et al. (1998) and Weger et al. (2009) who analyzed various rock types to determine the most applicable geometrical parameters for porosity-permeability relationships. Specifically, pore size is calculated as the square root of the pore area (A) "as a linear value for an average pore length" (Anselmetti et al., 1998). A critical advantage calculating pore size in such a way, instead of using either length or width, is accommodating the vast range of pore geometries. Based on the resultant pore size values, median and 75th percentile pore size values are calculated to evaluate the statistical distribution of pore size of a given sample or facies. It should be noted that these pore size parameters are different from the "dominant pore size (DomSize)" used by Weger et al. (2009) and Verwer et al. (2011). As for perimeter-over-area (PoA), it is a ratio derived by dividing the perimeter by the area of a pore and is a measure of the complexity of the shape of a pore: the higher the PoA values, the more complex the pore geometry (Weger et al., 2009) which correlates to increasing pore connectivity. For a group of pores, PoAavg is calculated by dividing the total pore perimeter by the total pore area. Gamma (γ) is derived by normalizing PoA relative to a circle of a pore, meaning that for a perfectly rounded pore, $\gamma=1$, which is the lowest γ value possible for any pore, whereas an elongated pore shows distinctively higher γ value (e.g., 5; Anselmetti et al., 1998) which again is related to increasing pore connectivity. For a group of pores, γavg is calculated by weighing the individual γ by the area of all pores (Anselmetti et al., 1998). To classify the pores in terms of size, the classification method in Loucks et al. (2012) is adopted, which uses pore width to classify pores into picopores (less than 1nm), nanopores (1nm to less than 1μm), micropores (1 μm to less than 62.5 μm), mesopores (62.5 μm to less than 4 mm) and macropores (4 mm to less than 256 mm). For maintaining consistency with the

methodology of this study, pore size, instead of width as shown in Loucks et al. (2012), is utilized as the criterion for the pore size classification. Following the calculation of these pore geometrical parameters, statistical analyses are further performed to evaluate if the pore geometrical parameters (as discussed above) show different patterns in different facies (groups). In addition, the pore parameters are cross-plotted against petrophysical data tested from core samples (e.g., porosity, permeability) for different facies (groups) to evaluate statistical relationships.

2.3.2. Results and Discussion

Four general pore types are the most common in the Caney core, which include interparticle and intercrystallite (Figure 2.29, BP and IX), intraparticle, and pores related to organic matter and clay minerals (Figure 2.30, OM and WP/IX_Clay). Interparticle (BP) and intercrystallite (IX) pores are present within the mud-rich matrix in-between grains (e.g., quartz, skeletal fragments) and in-between the carbonate grains or crystals within carbonate cement (Figure 2.29).

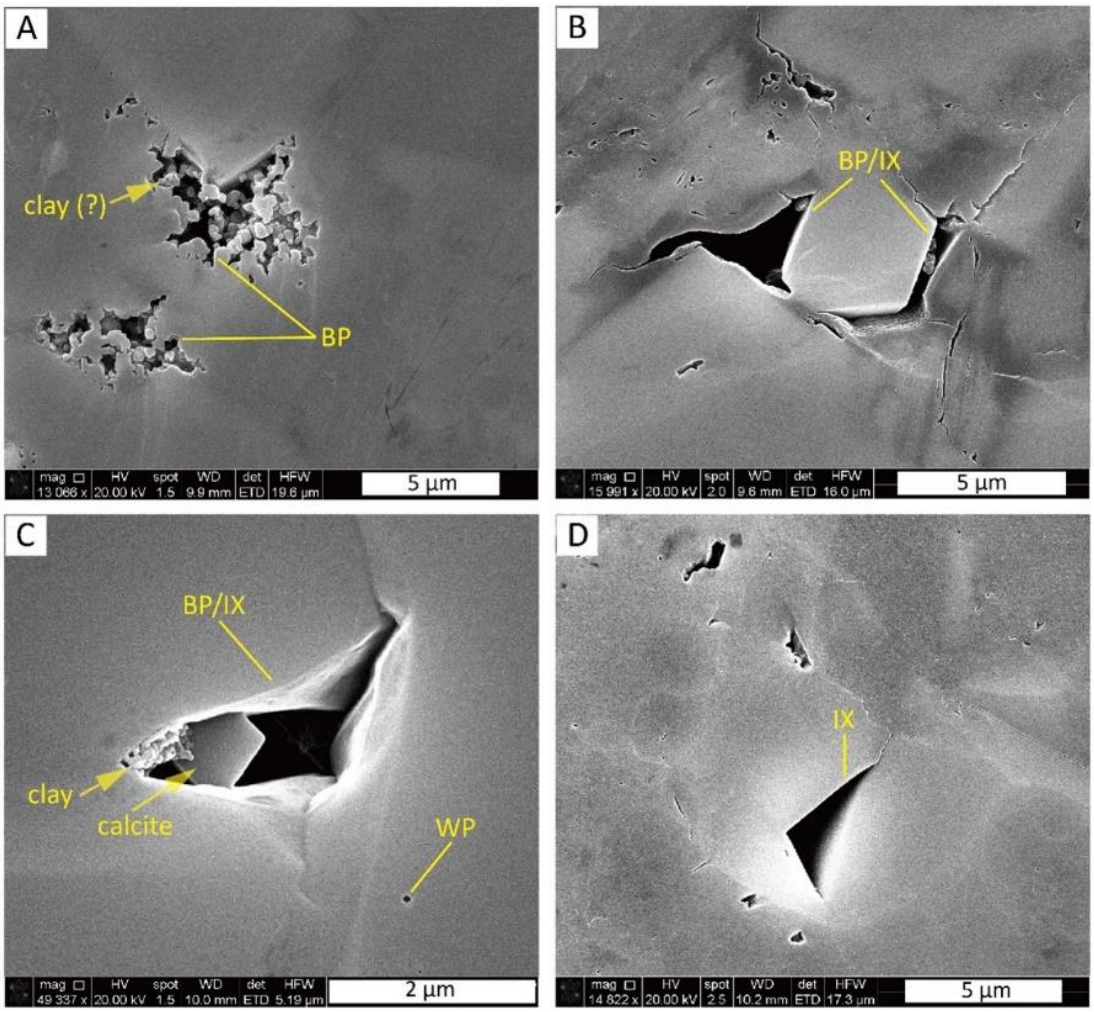

Figure 2.29. SEM photomicrographs showing the examples of interparticle (BP) and intercrystalline pores (IX). In C, the pore contains clay lining and a calcite crystal that bridges the pore. Also note the presence of intraparticle porosity (WP) in C (lower right). A and C are from the same sample from bioturbated siltstone (siltstone group). B is from dolomitic facies (carbonate group). D is from a silty packstone-grainstone (carbonate group).

Intercrystallite pores occur between carbonate crystals and can be challenging to be differentiate from interparticle pores. These pores may (Figure 2.29A, C) or may not (Figure 2.29B, D) contain clay lining. For intraparticle pores (WP), they can be within carbonate and quartz grains, and rarely within crystals. These pores may or may not contain clay infills. Organic Matter pores (OM) are present within the dark-colored mud-dominated matrix in-between the grains or crystals (Figure 2.30 A to E). These pores are characterized by a bubbly appearance and may or may not show preferred orientation. Pores related to the clay minerals (WP/IX_Clay) show a characteristic elongated appearance and often show preferred orientation (Figure 2.30C, E).

Rare examples of these clay pores are present in-between the kaolinite booklets (Figure 2.30D), although it can be challenging to identify the clay types in SEM, even with energy dispersive x-ray analysis (e.g., Figure 2.30C). In some cases, organic matter and clay pores can coexist and may be difficult to distinguish (Figure 2.30E). Considering the difficulty of defining the pores hosted by clay minerals as intraparticle or intercrystallite pores, and conjecture in the literature on this topic, this study adopts an inclusive approach by including both defining methods (i.e., "WP/IX_Clay"). In rare cases, some pores show perfect crystalline shape which can indicate the prior presence of calcite and/or dolomite. Apart from these aforementioned pore types, it is often difficult to unambiguously assign pore types for many pores.

Pore Size Distribution

A total of over 26,000 pores were measured in this study. For all pores, pore size (μm) ranges from 0.002 to 5.3, with mean being 0.06, median being 0.03, 25th percentile being 0.02, and 75th percentile being 0.06 (Figure 2.31). Based on the pore size classification method of Loucks et al. (2012), virtually all pores observed in this study (99.6%) fall into the category of nanopores with a minor portion being micropores (0.4%) (Figure 2.31). In addition, because petrophysical response (e.g., porosity) is produced by a combination of all pores in a sample, all pores are included in the analyses without treating micropores (i.e., largest pores measured) as outliers, despite the minor proportion of micropores as observed in this study. To visualize the pore size distribution in more detail, pore size data are binned using the log scale (μm) of 0.001, 0.01, 0.1, 1, and 10, due to the wide range across 1,000 units. Under such scaling, 81.8% of all pores fall in the range of 0.01 to 0.1, followed by 13.9% in the range of 0.1 to 1, 4.0% in the range of 0.001 to 0.01, and 0.4% in the range of 1 to 10 (Figure 2.31, lower right).

At a facies group scale, these four pore size ranges show variable percentages among the mudstone (MG), siltstone (SG), and carbonate (CG) facies groups (Figure 2.32). Among all facies groups, the "0.01 to 0.1" range (Figure 2.32, green bars) is dominant with the highest percentage observed. For the "0.1 to 1" range, the carbonate group shows the highest percentage, followed by the siltstone group and mudstone group with distinctively lower values. For perimeter-over-area (PoA), values range from 1.1 to 1156.0 and averages 16.5 among all pores. In the order of mudstone, siltstone, and carbonate groups, the average PoA is 46.5, 19.6, and 11.7, respectively (Figure 2.33, left). Gamma (γ) ranges from 1.1 to 7.0 and averages 2.0 in all pores.

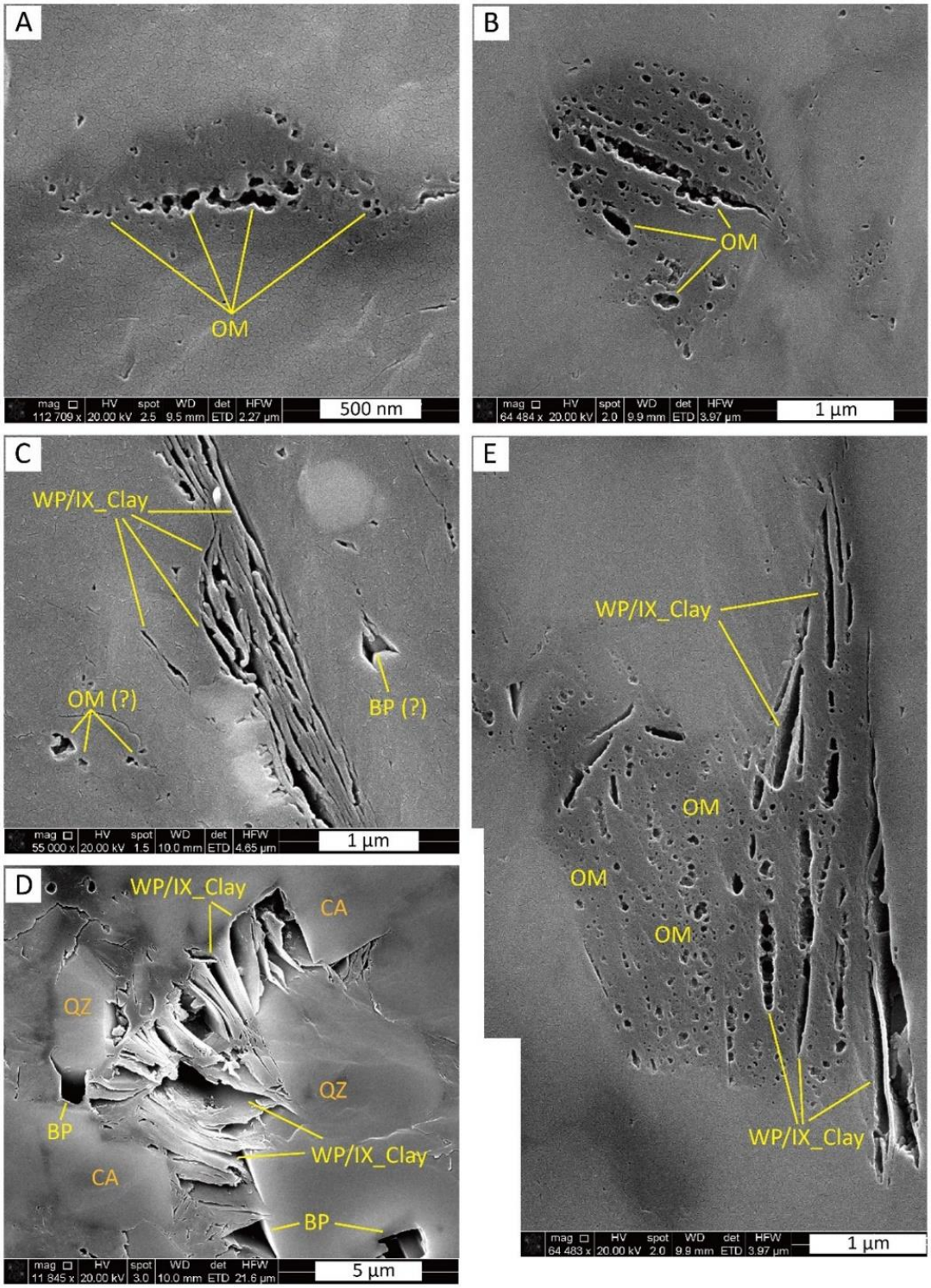

Figure 2.30. SEM photomicrographs showing examples of pores related to organic matter (OM) and clay minerals (WP/IX_Clay). The organic matter pores may (A) or may not (B) show preferred orientation. In D, also note the presence of interparticle pores (BP) and pores hosted by the kaolinite sheets between quartz (QZ) and calcite (CA) grains or crystals. In E, organic matter (OM) and clay (WP/IX_Clay) pores coexist. A is from burrowed mudstone-siltstone (mudstone group). B and E are from massive-bedded mudstone (mudstone group). C is from bioturbated siltstone (siltstone group). D is from dolomitic facies (carbonate group).

Pore Size (μm)	Max	Min	Mean	Median	25th Percentile	75th Percentile
	5.3	0.002	0.06	0.03	0.02	0.06

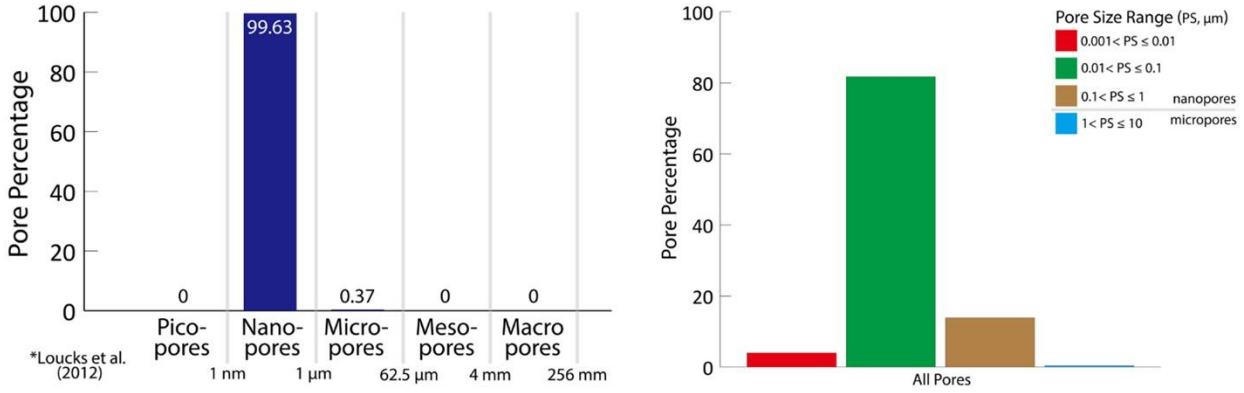

Figure 2.31. For all pores examined in this study, they range from 0.002 to 5.3 microns and average a few microns in size (top table) and are classified as nanopores (left bar chart) based on the classification method of Loucks et al. (2012). Among the four pore size ranges, 10 nanometers to 100 nanometers (green bar in the right bar chart) account for the majority of all pores.

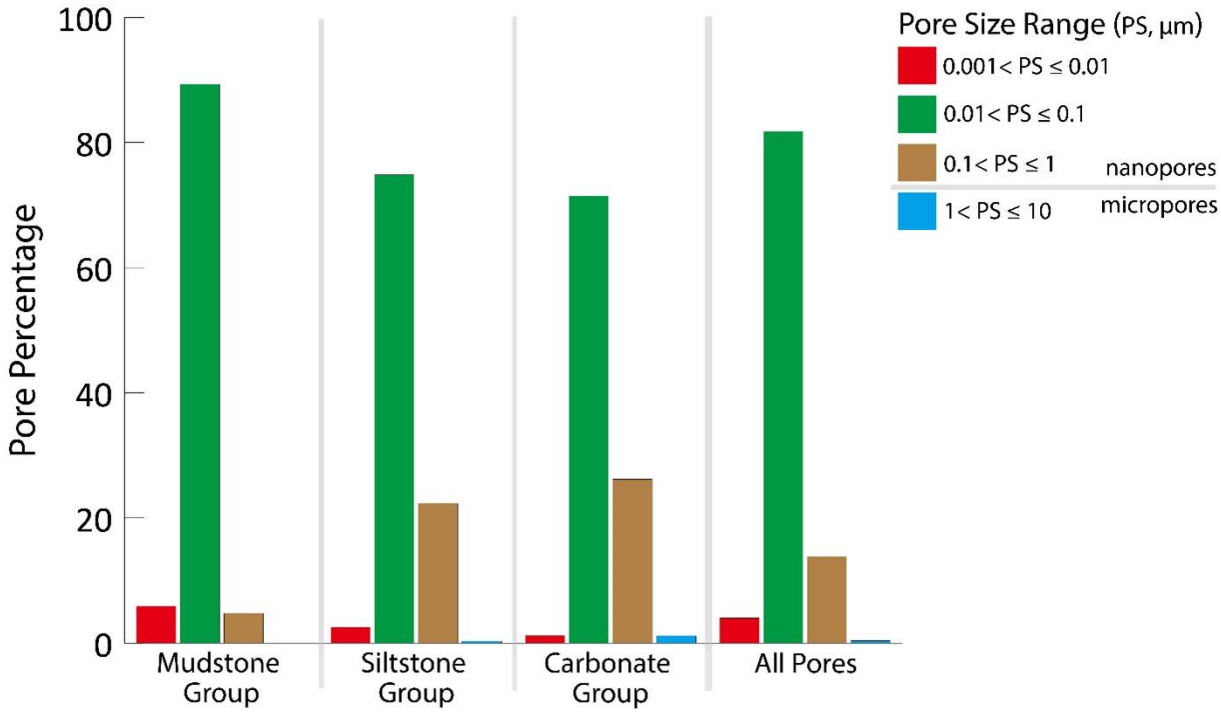

Figure 2.32. Bar chart shows the relative abundance of four pore size ranges for all pores and all facies groups. The size ranges of 10 nanometers to 100 nanometers (green bars), which account for the majority of all pores, also accounts for the majority of pores for each facies groups and shows a decreasing trend from mudstone to siltstone, and to carbonate group.

Pore Size and Geometrical Parameters tied to Facies and Petrophysical Parameters

When examining the pore size range in the order of mudstone, siltstone, and carbonate groups, the decreasing percentages of the pore size ranges of "0.001 to 0.01" and "0.01 to 0.1" and the increasing percentages of the ranges of "0.1 to 1" and "1 to 10" (Figure 2.32, lower right) suggest well-defined trends in the pore size ranges at a facies group scale. In addition, the increasing trends in median pore size and 75th percentile pore size from the mudstone group to the siltstone group, and to the carbonate group indicate an overall tendency of decreasing percentages in smaller pores and increasing percentage in larger pores. Furthermore, the decreasing trend in perimeter-over-area (PoA) indicates decreasing complexity of pore geometry from the mudstone group to the siltstone and then carbonate groups (Figure 2.33), which show similar overall proximity of the pores to a circle (i.e., Gamma; Figure 2.33).

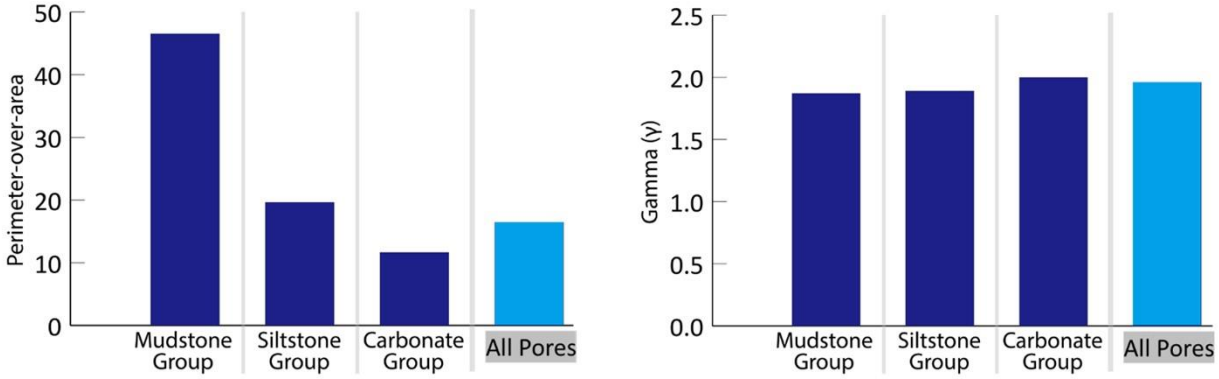

Figure 2.33. Bar charts showing the average values of perimeter-over-area (PoA, left) and Gamma (right) of all pores and of the pores in different facies groups. From mudstone group to siltstone group, and to carbonate group, PoA shows a decreasing trend whereas Gamma shows a consistent trend.

As further indicated by the negative trend between perimeter-over-area and pore size (median, 75th percentile; Figure 2.34), these observations point to an overall tie of facies with the relative percentages of different pore sizes and pore geometrical complexity at a facies group scale. Such an overall tendency of smaller pores with more complex pore geometry is also documented in carbonate rocks (Weger et al., 2009) and in the Vaca Muerta Formation in Argentina (Norbisrath et al., 2017), the latter of which is an "unconventional" mudrock reservoir with similar rock types to the Caney. The overall negative trends of porosity with pore size (median, 75th percentile; Figure 2.35) suggest an overall tie between higher porosity and smaller pores. In addition, the overall positive trend between perimeter-over-area and permeability (Figure 2.36) suggests an overall tie between more complex pores and higher measured permeability. Also, the mudstone group with overall smaller and more complex pores tend to show higher porosity and permeability (Figure 2.37), which is similar to the observations in Verwer et al. (2011). As such, pore geometrical data may help characterize the porosity-permeability relationships at the facies group scale. As indicated by the clustering of data (i.e., different statistical relationships) among facies groups in both porosity (Figure 2.35) and permeability (Figure 2.36), as well as in the porosity-permeability cross-plot (Figure 2.37), pore geometrical parameters can potentially be utilized to predict porosity, permeability, and their

statistical relationships at facies group scale. In particular, clustering of data among facies groups is observed in all scenarios as discussed above. These observations indicate that facies can create variable statistical patterns among pore geometrical parameters and between these parameters with porosity and permeability. Therefore, integrating pore architecture data with facies characterized based on core samples at multiple scales (e.g., individual facies vs. facies groups) may be valuable for analyzing the statistical relationships among pore geometrical parameters and petrophysical properties in these mixed carbonate-siliciclastic mudrock systems (Figure 2.38).

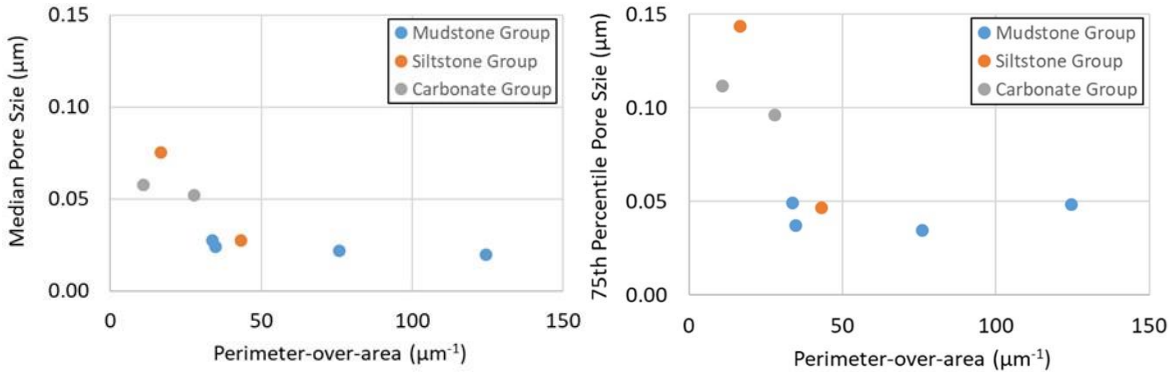

Figure 2.34. Cross-plots showing the relationship of perimeter-over-area (PoA) with median pore size (left) and 75th percentile pore size (right) categorized by facies groups. For both pore size, the data show an overall negative trend in all pores with clustering among facies groups. Mudstone group shows wider PoA range with narrower pore size range, whereas siltstone group and carbonate group show narrower PoA range with wider pore size range. These observations indicate an overall tie between smaller pores and more complex pore geometry. Each data point represents the average values of the pores analyzed in one sample.

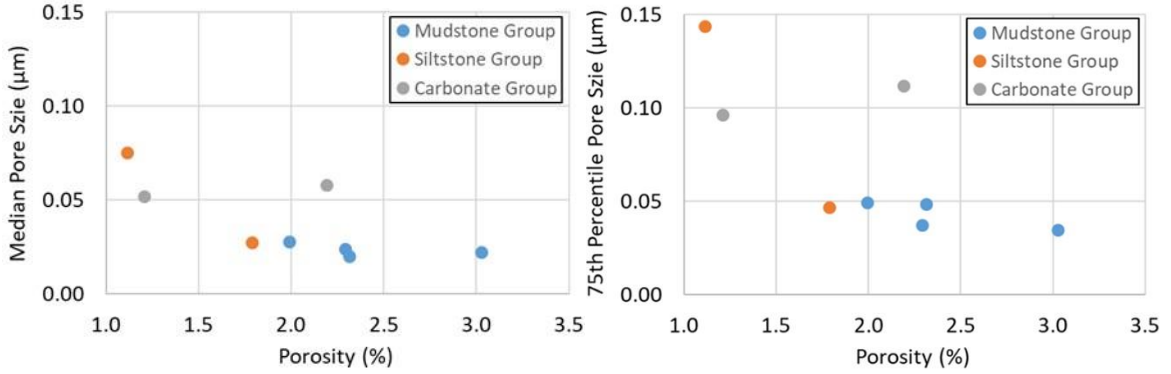

Figure 2.35. Cross-plot showing the relationship of porosity with median pore size (left) and 75th percentile pore size (right) categorized by facies groups. For both pore size metrics, the data show an overall negative trend with clustering among facies groups, pointing to an overall tie between smaller pores and higher measured porosity. Each data point represents the average values of the pores analyzed in one sample.

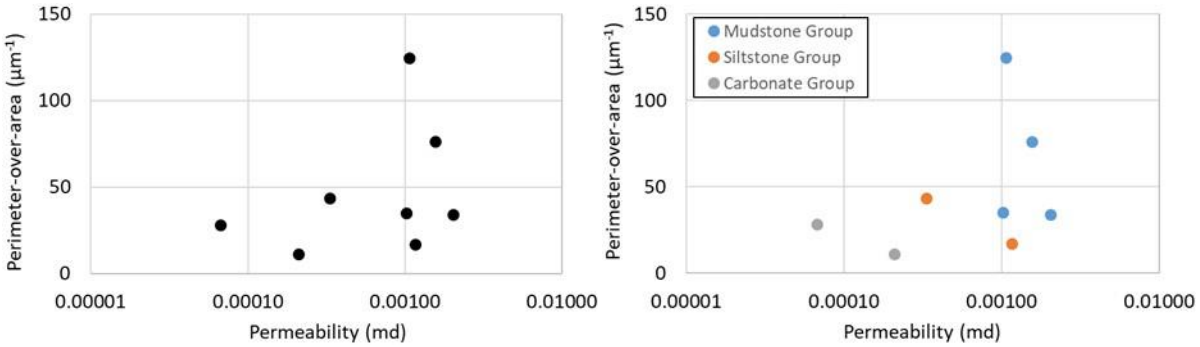

Figure 2.36. Cross-plots showing the relationship of permeability with perimeter-over-area without being categorized (left) and categorized by facies groups (right). For perimeter-over-area, it shows an overall positive trend with clustering among facies groups, indicating an overall tie between more complex pores and higher measured permeability. Each data point represents the average values of the pores analyzed in one sample.

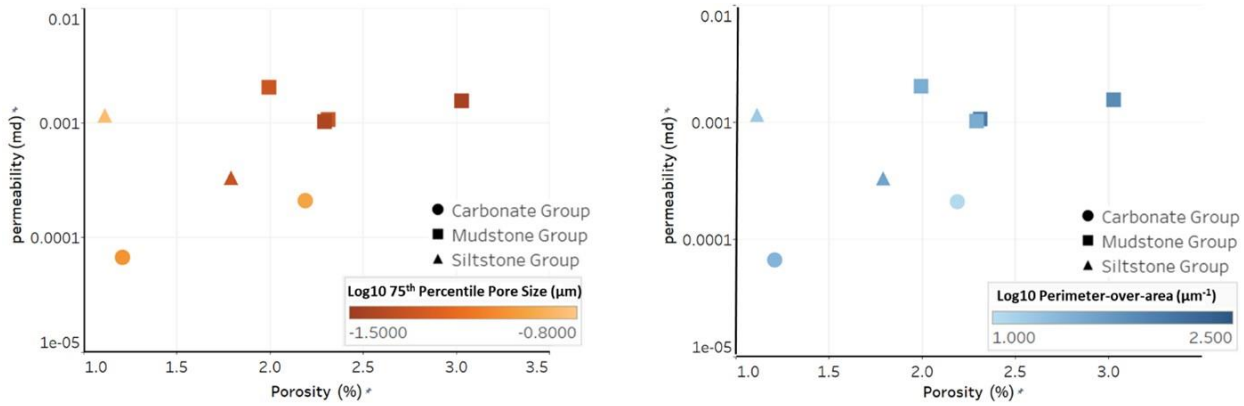

Figure 2.37. Cross-plots showing the relationship between porosity and permeability, with the data being overlain by the log values of 75th percentile pore size (left) and perimeter-over-area (right). The data are also categorized by facies groups. Specifically, the mudstone group tends to show smaller (left) and more complex (right) pores with higher porosity and permeability values. Therefore, pore geometrical data can help characterize the porosity-permeability relationships at facies group scale. Each data point represents the average values of the pores analyzed in one sample.

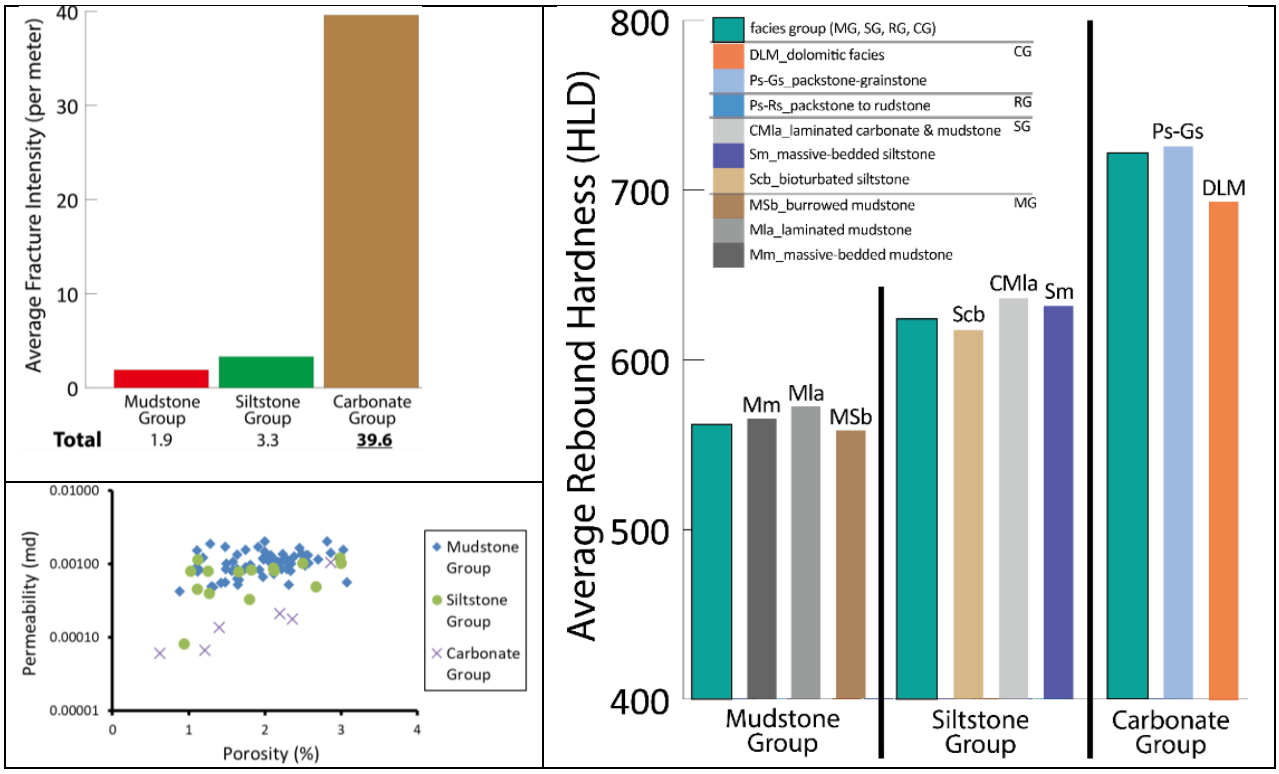

Figure 2.38. Bar charts showing the average fracture abundance (i.e., average fracture intensity) by facies groups (upper left) and the average rebound hardness values of facies groups and individual facies (right). In the right bar chart, individual facies are noted with acronyms explained in the legend at top left of the bar chart, where MG, SG, and CG represent mudstone group, siltstone group, and carbonate group, respectively. At a facies group scale, carbonate group shows the highest average fracture intensity and highest average rebound harness among all facies groups. In addition, porosity and permeability data are cross-plotted and arranged by facies groups (lower left), in which carbonate groups show clustering and different statistical patterns as compared to mudstone and siltstone groups.

2.4.Petrophysical Facies Analysis

2.4.1. Approach

Petrophysical facies analysis to determine the properties of reservoir and non-reservoir intervals of the Caney Shale was accomplished by correlating and calibrating core-derived porosity and permeability, composition, and mechanical properties of the Caney Shale to the response of wireline log curves. This calibration included comparing porosity and permeability as measured using tight rock analysis (TRA) with wireline log compensated density values and correcting the wireline log derived porosity for rock matrix density, drilling fluid composition and organic matter content. The relationship between standard wireline-log curves, mechanical properties and elemental composition as derived from x-ray fluorescence was used to establish petrophysical properties of ductile seals and distinguish seals from more brittle reservoir intervals. The response of other petrophysical curves across reservoir and non-reservoir intervals was analyzed to determine the wireline log curves more useful for identifying reservoirs in vintage wireline log data sets, the most commonly available data source in petroleum exploration.

2.4.2. Results and Discussion

Four (4) generalized petrophysical facies as defined by wireline-log responses are recognized in the Caney Shale: (1) more brittle reservoir zones with less clay-mineral content that are higher resistivity, lower neutron porosity and higher density porosity, (2) ductile seal zones with higher clay-mineral content that exhibit lower resistivity, higher neutron porosity and lower density porosity, (3) carbonate intervals with high resistivity, low neutron and density porosity, and low total gamma-ray values, and (4) detrital silt- and clay-rich intervals with wireline-log properties between those of facies 1 and 2 .

The total American Petroleum Institute (API) gamma-ray curve is not always diagnostic in separating ductile intervals from reservoirs and detrital silt and clay zones, but spectral gamma-ray logs provide insight into changes in elemental composition when the values for specific elements such as uranium are below those readily measured by x-ray fluorescence. Divergence between K concentration and U concentration as measured by spectral gamma ray, occurs in most reservoir intervals in the detrital feldspar-lean Caney Shale. Furthermore, in ductile intervals there is apparent convergence of the K and U curves. The divergence of K and U concentrations consists of a relative decrease in K concentrations (proxy for K-illite clay) that coincides with an increase in U concentrations in reservoirs. In ductile intervals, illite and K concentration increases in conjunction with a decrease in U concentration.

This relationship is important because a comparison of spectral gamma-ray derived U concentration to total gamma-ray values from core and total gamma-ray measurements from open-hole wireline logs indicates that U is the major contributor to the total API gamma-ray reading, whereas the contributions from K and Th are less important. That the U concentration is more important at the low concentrations in Caney Shale, suggests that the total gamma-ray is a useful tool for predicting reservoir and non-reservoir facies. The effectiveness of using the gamma-ray curve as a reservoir or non-reservoir indicator is enhanced when it is used in conjunction with resistivity and porosity curves from open-hole logs, spectral gamma-ray curves for K, U and Th, if available, and/or elemental data from x-ray fluorescence. In the absence of additional spectral gamma-ray or x-ray fluorescence data, the combination of the neutron porosity, resistivity and total API gamma-ray curves appears to provide the petrophysical data necessary to identify and delineate reservoir and non-reservoir facies. Elemental concentrations derived from x-ray fluorescence are a reliable indicator of reservoir and seal intervals in the Caney Shale. X-ray fluorescence (XRF) derived relative concentrations of detrital indicator elements titanium (Ti), zirconium (Zr), aluminum (Al), potassium (K) if in feldspar-lean rocks, and silicon (Si) are useful in distinguishing clay-mineral-rich ductile seal intervals from less-clay-mineral rich reservoir intervals. As in the Woodford Shale, the relative concentrations of detrital elements in the Caney Shale can be used to identify intervals where authigenic quartz and/or calcite cement contributes to the rigidity of the rock fabric (Figure 2.39) and increases brittleness of reservoirs that is essential for natural or induced fracturing.

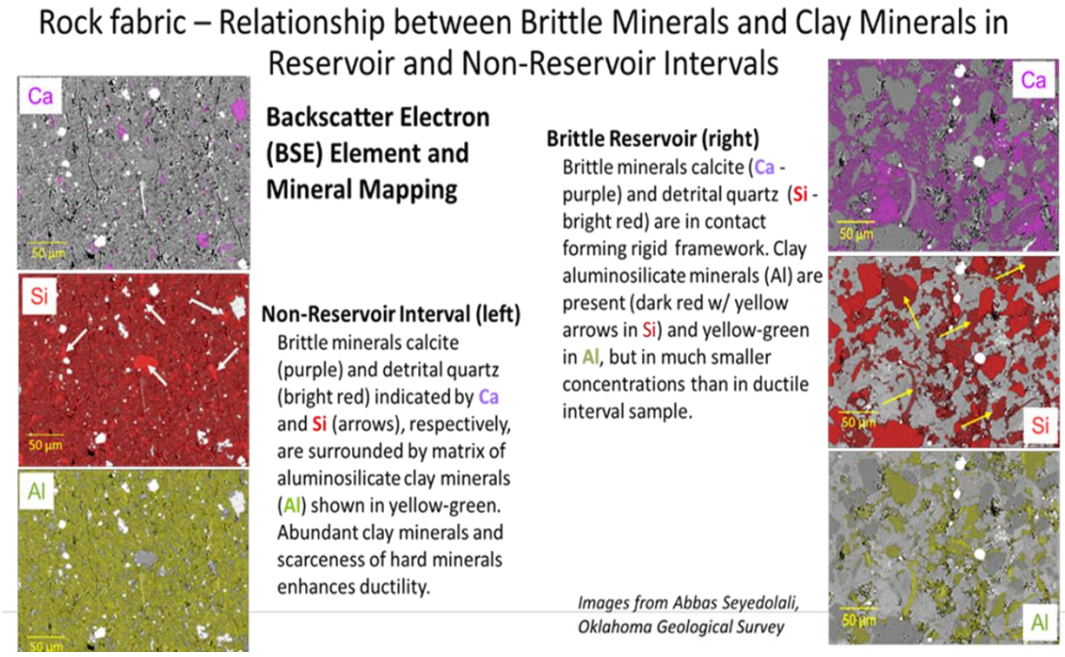

Figure 2.39. Backscatter electron (BSE) element mapping showing the aluminosilicate clay-mineral-rich fabric of ductile non-reservoir Caney Shale (left) and increased quartz and calcite and decreased aluminosilicate clay concentration in fabric of brittle reservoir (right).

The integration of XRF data and wireline-log response allows the identification of petrophysical facies. In addition to the three (3) more common petrophysical facies: (1) brittle reservoir, (2) ductile seal, and (3) carbonate, petrophysical facies 4, called detrital clay- and quartz-rich, is recognized by the simultaneous enrichment of all detrital elements. Wireline-log responses of the gamma-ray, resistivity, neutron and uncorrected density porosity and concentrations of selected detrital elements were graphed to establish petrographic facies (Figure 2.40). Petrophysical facies 1 is a brittle reservoir that is characterized by a relative decrease in the concentrations of Ti, Zr and Al, and an increase in the concentration of Si compared to clay-rich ductile intervals. As a result of decreased clay-mineral content and associated bound water, and increased hydrocarbon saturation, the resistivity of reservoir intervals is high and often exceeds 200 ohm-meters. As a result of the decreased clay-mineral and bound water content, reservoirs have lower neutron porosity, which causes the neutron curve to approach and sometimes cross over the uncorrected density porosity curve. Petrophysical facies 2 is ductile seal rock that is characterized by an increase in Al, Ti, and Zr concentrations and a decrease in Si concentration compared to brittle intervals. This elemental relationship reflects a decrease in silica cement and increase in clay-minerals and detrital quartz silt. The increase in clay-mineral content and associated bound water causes a decrease in resistivity to approximately 30 ohm-meters and increased neutron porosity, which greater than 10% higher than uncorrected density porosity. Petrophysical facies 3 is carbonate with low siliciclastic content and resulting low concentrations of Ti, Zr, Al, and Si, low neutron and density porosity of less than 6%, and high resistivity exceeding 100 ohm-meters. Facies 3 has high calcium (Ca) content due to its calcite and dolomite mineralogy. Petrophysical facies 4 relies more heavily on XRF provided elemental concentrations for identification. Facies 4 is rich in detrital quartz silt and clay minerals, and lacks authigenic cement. As a result, Ti, Zr, Al and Si all increase concurrently. Resistivity is

between 50 and 100 ohm-meters, and neutron porosity is around 10% higher than uncorrected density porosity with the two curves subparallel (Figure 2.41).

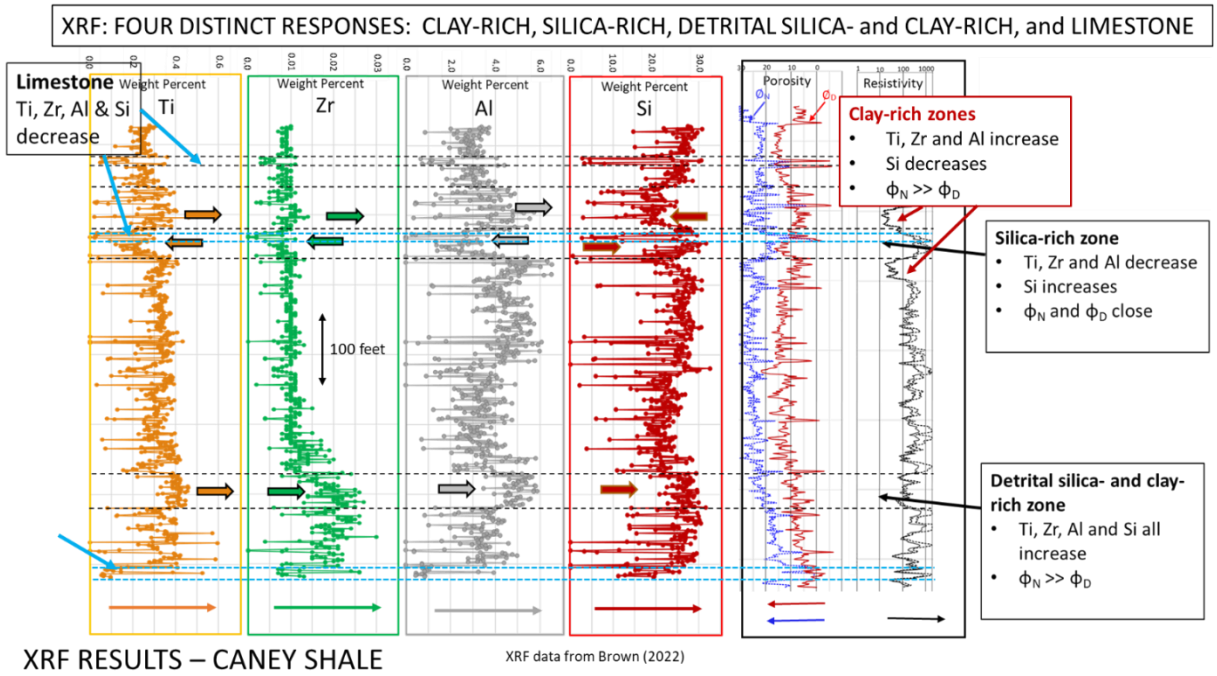

Figure 2.40. Concentrations of detrital elements Ti, Zr, Al and Si measured by XRF compared to neutron (ϕ_N) and uncorrected density porosity (ϕ_D) and deep resistivity (Rt) from wireline logs for the Caney Shale. Petrophysical facies 1 (silica-rich zone) has decreasing concentrations of Ti, Zr and Al, and increasing Si concentration, high Rt (>250 ohm-m) and ϕ_N and ϕ_D curves that converge. Petrophysical facies 2 (clay-rich zone) has increasing Ti, Zr, and Al with decreasing Si, low Rt (≈30 ohm-m) and diverging ϕ_N and ϕ_D curves. Petrophysical facies 3 (limestone) has low concentrations of all elements, high resistivity (>100 ohm-m), and low ϕ_N and ϕ_D (<6%). Petrophysical facies 4 (detrital silica- and clay-rich zone) has increasing Ti, Zr, Al and Si, intermediate Rt (≈50 ohm-m) and ϕ_N that is approximately 10% higher than ϕ_D.

Our comparison of elemental concentrations in cuttings and core demonstrated that XRF analysis of cuttings provided similar changes in concentrations of selected elements as core. The similarity between the two sets of data is better for thicker intervals such as those in Reservoir 1 and Reservoir 2, and subtle or undetectable in the thinner intervals encountered in the section containing Reservoir 3. Surprisingly, the thin carbonate in Reservoir 1 was detected and is expressed in the plots as decline in the concentrations of Ti, Zr, Al, and Si (Figure 2.y). The studied dataset supports the contention that if bit cuttings are collected diligently from wells with well managed drilling fluid systems, cuttings can provide critical information on relative clay content and help identify reservoir and seal intervals in unconventional plays. The petrophysical log signatures of the Caney Shale, Fayetteville Shale and Barnett Shale were compared to determine similarities of these partially stratigraphic equivalent unconventional plays (Figure 2.42). Log curves are scaled the same and include gamma-ray (GR), deep resistivity (RES), bulk density (RHOB) and neutron porosity (NPHI). The most obvious indicator of reservoir in these organic-rich mudrocks is the convergence of neutron porosity and bulk density. For the Fayetteville and Barnett shales, neutron porosity (red) and bulk density (blue) merge to point of touching. Neutron porosity and bulk density curves for the Caney Shale converge less, but the change is noticeable when compared to the diverging neutron porosity and

bulk density curves in adjacent clay-rich ductile zones. Resistivity increases across reservoir intervals compared to clay-rich sections for all three shales, with the most noticeable change occurring in the Caney Shale.

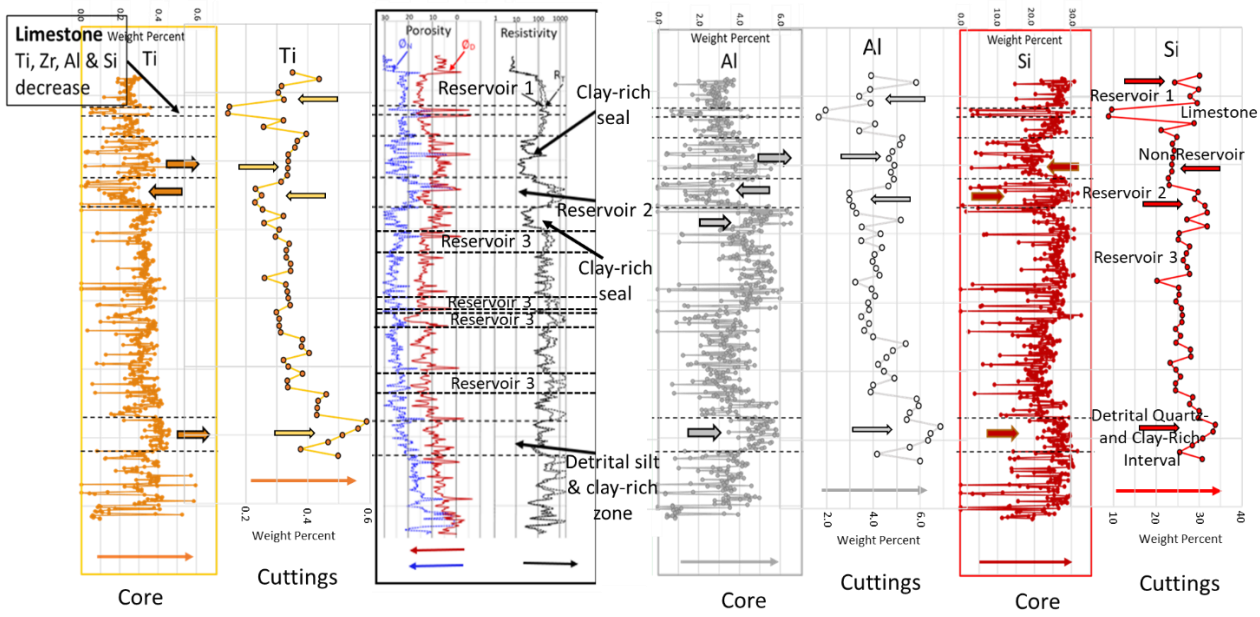

Figure 2.41. Comparison of concentration of Ti, Al, and Si from both core samples and cuttings showing the similarity of concentrations in thicker intervals. Annotated log shows selected petrophysical log responses of reservoirs and clay-rich seals. Downward shift in curves for cuttings is the result of travel time for cuttings to reach the surface.

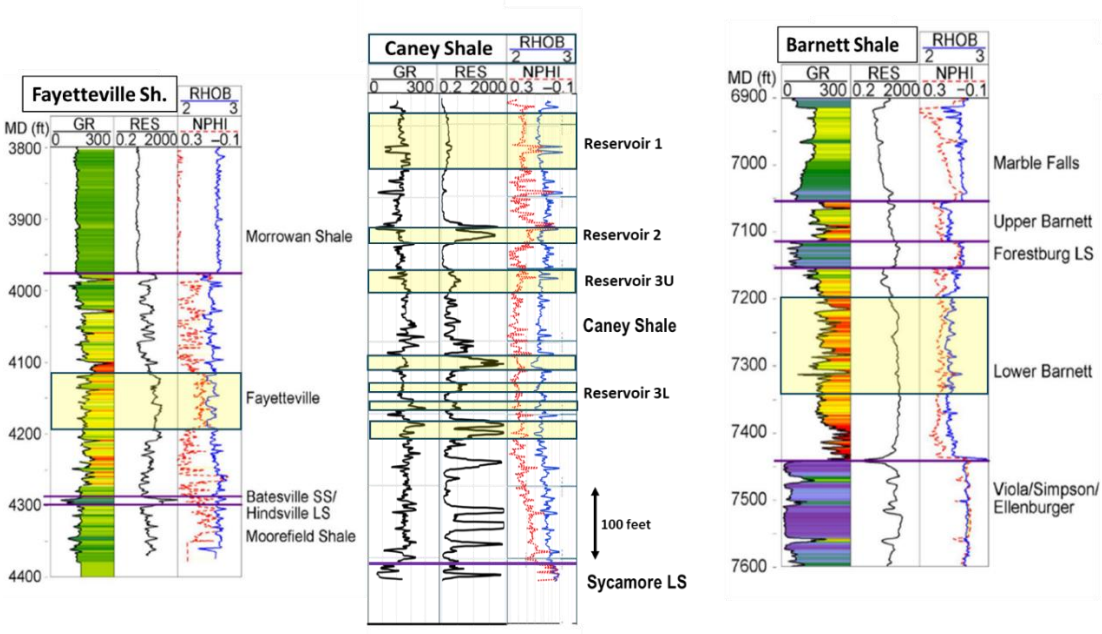

Figure 2.42. Petrophysical log responses across the Fayetteville Shale, Caney Shale and Barnett Shale with reservoir intervals shaded yellow. Gamma-ray (GR), deep resistivity (RES), bulk density (RHOB) and neutron porosity (NPHI) are scaled the same. Neutron porosity (red) and bulk density (blue) merge across reservoir intervals in the Fayetteville and Barnett shales. The response of neutron porosity and bulk density is subtler for Caney reservoirs but noticeable when compared to adjacent more clay-rich beds. Resistivity increases across reservoirs sections in all three plays. Fayetteville and Barnett examples are from Smye et al. (2019).

2.4.3. Summary

Petrophysical facies in the Caney Shale are directly related to rock composition. Reservoirs (Petrophysical facies 1) have high resistivity and lower neutron porosity that converges with the uncorrected density porosity. Ductile non-reservoir intervals (Petrophysical facies 2) have low resistivity and higher neutron porosity that diverges from uncorrected density porosity. Carbonates (Petrophysical facies 3) are thin non-reservoirs with low porosity, high resistivity and clean gamma-ray. Petrophysical facies 4 are detrital quartz- and clay-rich intervals with resistivity between that of reservoirs and ductile zones and neutron porosity that plots subparallel to the uncorrected density porosity curve. Facies 4 is best confirmed by its geochemical signature of all detrital elements increasing concurrently, which differs from the other petrophysical facies.

3. Rock-Fluid Characterization

3.1.Geochemistry Approach

The experimental approach for the rock-fluid interaction studies in the Caney Shale was meticulously designed to simulate subsurface conditions and capture both short-term and long-term geochemical interactions between the shale formations and various fracturing fluids. The objective was to investigate how these interactions influence mineral stability, particularly clay stabilization, and how they affect the petrophysical and mechanical properties of the rocks over time.

The methodology was divided into multiple phases, with each experiment focusing on different aspects of rock-fluid reactions. Initial experiments utilized powdered shale samples to maximize the surface area for fluid interaction, which mimicked conditions during hydraulic fracturing when fluids penetrate fractured rocks. This was followed by subsequent experiments with intact core samples to assess how rock-fluid interactions affect the overall structure and integrity of the rock matrix, including porosity, permeability, and fracture stability.

All experiments were conducted under controlled conditions using static batch reactors. These reactors were maintained at a constant temperature of approximately 95°C to simulate reservoir thermal conditions. The choice of temperature was critical, as it reflects typical subsurface temperatures in the Caney Shale formation and is known to significantly influence geochemical reaction rates, particularly in relation to mineral dissolution and precipitation. The reactors were designed to hold rock samples submerged in either synthetic or field-collected fracturing fluids and produced brines, ensuring that a range of fluid chemistries were evaluated.

Sampling was carried out at specific time intervals to capture the progression of chemical reactions. Fluid samples were collected on days 1, 3, 7, 14, 21, and 28, allowing for the analysis of time-dependent changes in elemental concentrations and mineral dissolution rates. These fluids were analyzed using high-precision analytical techniques such as inductively coupled plasma mass spectrometry (ICP-MS) to quantify elemental changes, while rock samples were examined using X-ray diffraction (XRD) and scanning electron microscopy (SEM) to identify mineral transformations and structural modifications.

In particular, this part of the study aimed to assess how various fracturing fluids, including potassium chloride and choline chloride solutions, as well as deionized water, affect clay stabilization. These fluids were selected due to their ability to modulate the ionic environment, which is crucial for preventing clay swelling and migration—phenomena that can severely impact well productivity by clogging pore spaces and reducing permeability.

The latter phases of the research employed intact rock cores with their original microstructures preserved, replicating more realistic subsurface conditions. These experiments provided insights into the mechanical and petrophysical effects of fluid-rock interactions, including fracture stability, changes in porosity, and the potential for mineral precipitation within fractures. The final stage involved dynamic core flooding experiments, which allowed the researchers to observe the behavior of fluid flow through fractured rocks under simulated pressure and temperature conditions. This phase was critical for understanding the cumulative effects of rock-fluid interactions over extended periods and provided the most accurate approximation of in-situ subsurface processes.

In summary, this comprehensive, multi-phase experimental approach integrated a variety of

analytical methods to offer a detailed understanding of how different fracturing fluids interact with Caney Shale rocks. The findings from this approach are intended to inform best practices in hydraulic fracturing, particularly in optimizing fluid formulations for long-term well integrity and maximizing hydrocarbon recovery.

3.2.Geochemical Characterization

The characterization of geochemical rock-fluid reactions in Caney shale was investigated in six main experiments. The first experiment was a baseline study to understand basic geochemical reactions as it relates to clay stabilization. In this experiment, single component fracturing fluids were used in static batch reactor experiments to investigate geochemical reactions and to study their capability in clay stabilization. The second and third experiments were used to investigate medium and long-term post-fracturing geochemical reactions in the subsurface. In these experiments, fracturing fluids and produced brines collected from the field were respectively reacted with powdered rock samples in static batch reactor experiments. The fourth and fifth experiments were premised on the results from the second and third experiments and explored static batch reactor experiments using fracturing and produced fluids to respectively investigate geochemical changes. However, the rock samples used in these experiments were solid with their microstructure completely intact. The aim of this experiment was to understand the impact of geochemical rock-fluid reactions on the microstructure, petrophysical and mechanical properties of rocks. The final experiment was a dynamic core flooding experiment that was built on all previous experiments and investigated the impact of geochemical rock-fluid reactions on microstructure, petrophysical and mechanical properties of rocks. This experiment replicated most accurately subsurface conditions as temperature, pressure and fluid flow were all replicated.
The methodology and results from these experiments are explained in the following.

3.2.1. Materials and Methodology

Baseline Studies

Materials

Samples used for experimental investigations include Caney Shale rocks selected from different depths from a well in the Ardmore basin of Southern Oklahoma. Analyses on the rocks with XRD show variance in mineralogical compositions. Though quartz is the predominant mineral in all the samples, the differences in relative amounts of quartz, carbonate, and clays are significant and samples are designated High Quartz (HQ), Moderate Quartz (MQ), and High Clay (HC), based on their relative mineralogical compositions.
Fluid samples used for experimental investigations are single component hydraulic fracturing fluids. These include 2% Potassium chloride and 0.5% Choline chloride both prepared in the laboratory using deionized water as base fluid and set to pH of 4 by adding hydrochloric acid. DI water is also used as a fluid in experiments to serve as a control. The relatively high clay mineralogical composition of the Caney Shale served as the main motivation for choosing temporal clay stabilizers as the main components of single component fracturing fluids.

Experimental Design

Batch reactor experiments are structured to mimic conditions in subsurface of the Caney Shale during shut-in periods. In standard hydraulic fracturing treatment of wells, there are a few days to several weeks of shut-in following completion of hydraulic fracturing treatments. During this period, the hydraulic fracturing fluids in the formation react with rock minerals causing dissolution and precipitation of new minerals. Following shut in, not all the fluid injected into the formation is recovered. Therefore, the reaction between formation and injected fluids continues.

Shale samples were crushed and ground to particle sizes below 100µm. This was to expose more surface area of the rock to react with the surrounding fluid. The initial liquid to solid ratio for the experiment was 200ml: 1g (i.e 0.7g of crushed rock reacted with 140ml of various simplified fracturing fluids). During this period, the reaction vessels are covered and placed in an oven pre-set to temperature of 95ºC. The period for the experiment was 28 days, representing a typical shut-in period. Sampling of effluent was undertaken at predetermined intervals: 1, 3, 7, 14, 21, and 28 days following the start of the experiment. During sampling, the reaction bottle was taken out of the oven and a syringe was used to collect about 10ml of reacted fluid from the sample. Sampled fluids were then sieved through a 0.22 µm filter and subsequently stored in a refrigerator pending analyses. Each sampling event lasts about a minute. Figure 3.1 shows the chart integrating all the experiments undertaken for geochemical rock-fluid reaction of Caney Shale.

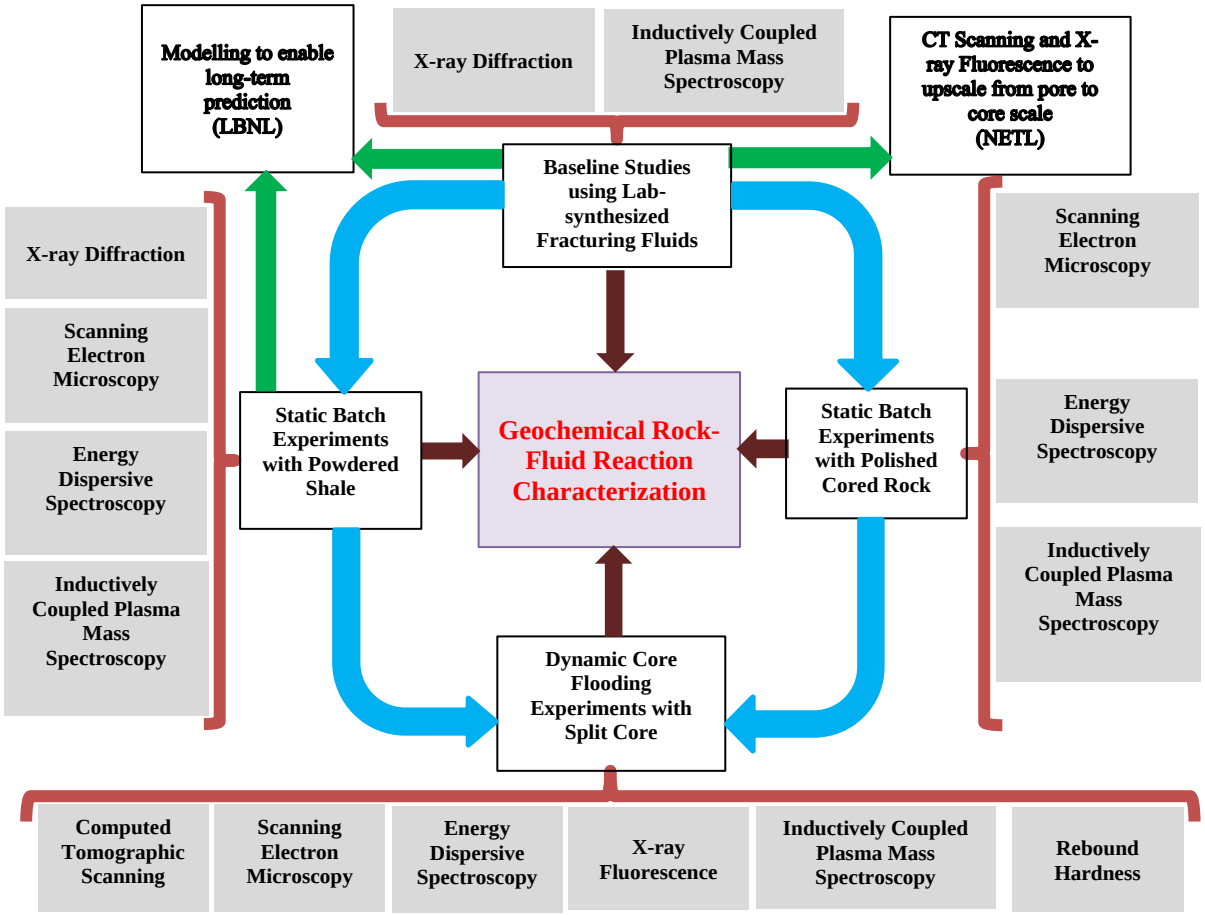

Figure 3.1. Experiments undertaken for geochemical rock-fluid reaction

Methods

The main analytical methods adopted in the experimental phase of this study included XRD for estimating the mineralogical composition of rock samples, ICP-MS for measuring the elemental concentrations in fluids. Results from these were coupled with results from medical CT scan and XRF of the entire length of drilled core to upscale results.

The following details of how each analysis was undertaken:

XRD analyses were performed on rock powder samples before the beginning of the experiments to assess their mineralogical compositions. This was achieved with a Bruker D8 advance X-Ray Diffractometer with Lynxeye detector. The scanning was run from 5 to 80 degrees 2-theta angle with a 0.01-degree step and dwell time of 0.5 seconds. Semi-quantitative analyses were also accomplished with BRUKER's Diffrac.suite eva.

To measure the elemental concentrations in fluids, the extracted fluids were first sampled through a 0.22 µm filter after extraction from the reaction vessel. The concentrations of elements in aqueous samples were evaluated at Lawrence Berkeley National Lab using an advanced Agilent 8900 triple quadrupole inductively coupled plasma mass spectrometry system (Agilent 8900 QQQ ICP-MS, Agilent Technologies). The instrument settings and analytical methods are similar to those reported by Belkouteb et al. (2023) and Agilent application notes (Agilent, 4th Edition). All the samples were prepared/diluted using 2% (v/v) ultrapure nitric acid in Milli-Q water (18.2 mΩ·cm) with analyses undertaken under a rigorous quality assurance (QA) and quality control (QC) protocol. The pH measurements were made with an Oakton pH 150 meter with the pH of each fluid measured three times and averaged.

The entire core run was sent to the National Energy Technology Laboratory (NETL) in Morgantown, WV for XRF and medical CT scans (Paronish et al., 2021).The Medical Toshiba® Aquilion TSX-101A/R medical scanner was used for the acquisition of medical CT scans at voxel resolutions of 0.43 x 0.43 mm in the XY plane and 0.5 mm in the core axis. For the purpose of this research, 3D volumes obtained from scans were re-sliced along the longitudinal axis and used as an image log. Images are observed to transition from dark to brighter scales. Totally dark regions in the scan represent areas of low density such as air, whereas brighter areas are associated with regions of high-density minerals such as pyrite. The portable handheld Innov-X® X-Ray Fluorescence Spectrometer was used for XRF analysis, aimed at measuring relative elemental abundances throughout the well. Also, the Mining-Plus suite was run at 6 cm resolution for 60 seconds of exposure time per beam through the entire 650 feet of core. The Mining-Plus suite utilizes a two-beam analysis to report the fractional elemental abundances relative to the total elemental composition (i.e. out of 100%), and resolve major (Mg, Al, Si, P, S, Cl, Fe, K, Ca, Ti), minor (V, Cu, Ni, Cr, Mn, Pb), trace elements, and an aggregated "light element" (H to Na). The data is filtered for errors exceeding 20% of the measured data (Paronish et al., 2018).

Static Geochemical Reactivity of Powdered Rock Samples

Materials

Rock samples used for this study were selected at designated depths from recovered cored-rock and rock-cuttings of the Caney Shale of Southern Oklahoma. These rocks were taken from two different

wells, one drilled vertically through designated zones of Caney Shale and the other drilled horizontally within the same part of formation. The vertical well was drilled across five (5) zones designated as reservoir and ductile formations within the Caney Shale (Radonjic et al. 2020; Wang et al. 2021) whilst the horizontal well runs approximately 8000ft within reservoir 3 (R3) of the Caney Shale. Samples were collected at every 1000ft in the horizontal well. Samples from the vertical well were originally retrieved as cored-rocks whilst samples from horizontal well were originally retrieved as rock-cuttings. For experiments with fracturing fluid, all the rock samples were collected from the same reservoir 3 zone (R3) within the Caney Shale. For the experiment with produced brines, the samples from the vertical well were collected from R1 (Reservoir 1), D1 (Ductile 1), R2 (Reservoir 2), D2 (Ductile 2) and R3 (Reservoir 3) whilst the horizontal well samples were all from R3.

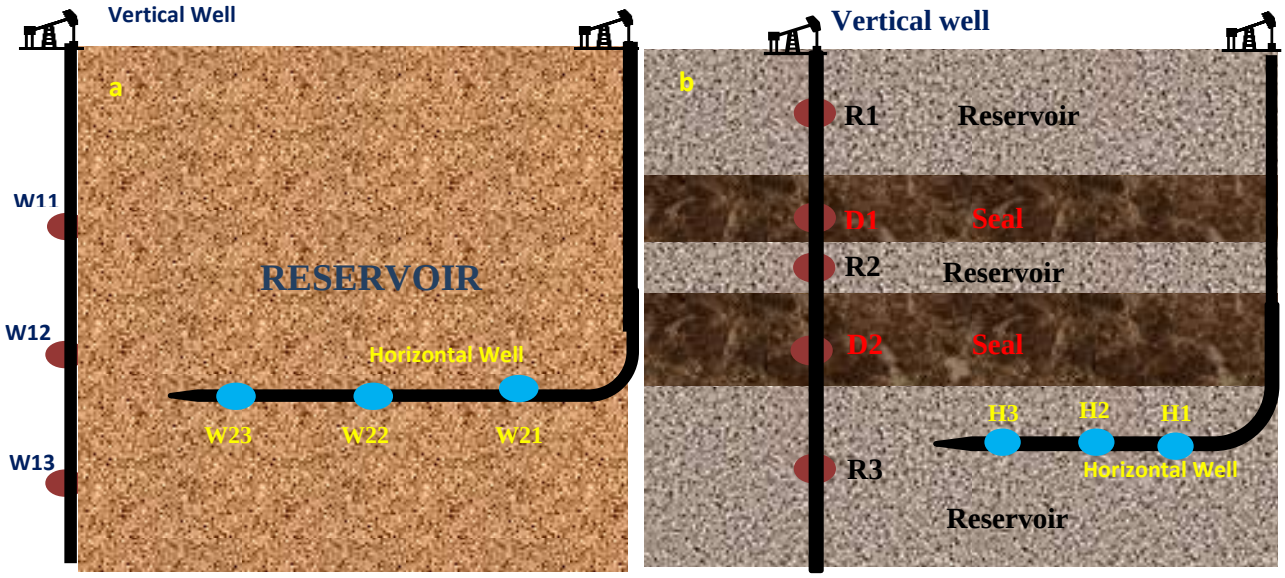

Figure 3.2. Schematics showing the sampling locations in vertical well and horizontal well for a. experiment 2 and b. experiment 3.

Fluid used for these set of experiments include fracturing fluids and produced brine both collected from the field. The produced brine was recovered after the reservoir had been hydraulically fractured and put into production. This fluid is therefore a hybrid of formation fluid and hydraulic fracturing fluid that has reacted with reservoir rocks. The fracturing fluid and produced brine were used in experiments as collected from the field, without any further treatments. At the onset of experiments, the pH of the fluids was 7.05 and 7.13 for fracturing fluid and produced brine respectively.

Sample Preparation

Given that the samples were obtained in different forms, sample preparation was conducted to get samples in powdered state for experiments. The procedure applied to prepare cored-rock was significantly different from rock-cuttings.

Cored-rock was recovered from well as 4-inches diameter cylindrical core. Samples were taken at selected depths as 1inch x 2inch core plugs from the original 4-inch core using core plugging mill that employed liquid nitrogen and bit coolant. The core plugs drilled out of the target depths were then crushed into smaller chippings with a hammer before they were ground to powder using a Spex

Ball Mill. On the other hand, rock cuttings from selected depths were collected in sampling buckets from the field. At the point of recovery, these samples were mixed with mud and produced fluids and therefore needed cleaning. To clean the samples, small quantities (quarter of a liter by volume) of the chippings mixed with crude and mud, were sampled into 2-liter beakers. Diesel was added to the cuttings swirled at high speed for 15 minutes before it was decanted. This process was repeated until the cuttings were clean of the crude and mud. Once the cuttings were sufficiently cleaned, they were washed with acetone by the same process as done for the diesel and left to dry for three days. Finally, the cleaned rock cuttings were selected by hand-picking them out from debris still left after the cleaning processes. These cuttings were ground to powder using a Spex Ball Mill. Final preparation of both sets of samples was achieved by micronizing with a McCrone Micronizer to reduce the particle size to particles passing 34-mesh size (100μm).

Experimental Design

The experimental method adopted for these studies was the static batch reactor experiments, where samples were prepared and put through experimental conditions in batches such that comparable samples were exposed to the same conditions at a given time. For this study, the experiments were run at temperature conditions of 95^{o}C. The reaction vessels used in these experiments were pyrex media storage bottles which have a volume of 250mL and tight seals with the ability to withstand dry temperatures up to 180^{o}C (356^{o}F). Samples were mixed in the bottles with an initial liquid to solid ratio of 150mL of liquid to 1g of rock powder. The bottles with samples were subsequently placed in heat resistant rectangular containers and put in an oven for the duration of the experiments. The temperature of the oven was monitored daily to ensure there were no fluctuations occurring.

Because the effect of temperature on geochemical reactions is expected to be significantly greater than that of pressure at reservoir conditions (~150 to 450 bar), it is envisaged that reactions during the experiments, approximate reactions between rocks and fluids in the reservoir. The experimental design did not cater for pressure and therefore the impact of pressure was not evaluated in this study. The reaction times for experiments were 7 days and 30 days.

During sampling, the fluids were separated from powders by decanting the fluid into empty Pyrex bottles and then filtering about 30mL through a 0.22μm filter into glass vials. The sampling of fluids from each reaction mixture lasted approximately three (3) minutes. The fluid samples were stored in sealed glass vials in a refrigerator waiting for further analysis.

The remaining rock powders in the bottles were dried through evaporation. This was achieved by putting the opened sample bottles in an oven set to vacuum and vent. The temperature of the oven was adjusted from approximately 30^{o}C to 60^{o}C (86^{o}F to 140^{o}F) over a period of 2 hours and left steady for the next 24 hours. During this period, the vent of the oven is opened to allow water vapor to escape. The rock powders left in the pyrex bottles were subsequently retrieved and stored in glass vials for further analysis.

Analytical Methods

Evaluation of changes that occurred in both original rock powder and fluid samples during the reaction involved several analytical methods and techniques. These include X-ray Diffraction (XRD), Scanning Electron Microscopy/Energy Dispersive Spectroscopy (SEM/EDS) and Inductively

Coupled Plasma Mass Spectroscopy (ICP-MS).

For rock samples, XRD analyses were used to determine the mineralogical contents of samples before and after reaction with produced brines. The Bruker D8 Advanced X-ray Diffractometer with a Lynxeye detector was employed to carry out the XRD measurements of samples. Scanning was run from 5 to 80 degrees 2-theta angles with a step of 0.01-degree and dwell time of 0.5 seconds. Once completed, XRD data were transferred to another computer where the BRUKER's Diffrac.suite eva software was used to undertake a semi-quantitative evaluation of samples. SEM was conducted on samples using the ThermoFisher FEI Scios2 Dual Beam Scanning Electron Microscope, in both secondary electron mode and in backscattered electron mode. EDS measurements were conducted with a Bruker EDS X-ray microanalysis system which is linked with the ThermoFisher FEI Scios2 Dual Beam Scanning Electron Microscope. The major EDS measurements included point analysis and spot analysis.

The concentrations of elements in aqueous samples were evaluated simultaneously using an advanced Agilent 8900 triple quadrupole inductively coupled plasma mass spectrometry system (Agilent 8900 QQQ ICP-MS, Agilent Technologies). The instrument settings and analytical methods are similar to those reported by Belkouteb et al. (2023) and Agilent application notes (Agilent, 4th Edition). All the samples were prepared/diluted using 2% (v/v) ultrapure nitric acid in Milli-Q water (18.2 mΩ·cm) with analyses undertaken under a rigorous quality assurance (QA) and quality control (QC) protocol. The pH measurements were made with an Oakton pH 150 meters with the pH of each fluid measured three times and averaged.

Static Geochemical Reactivity of Polished Rock Samples

Materials

Samples used for these static batch reactor experiments were mainly shale rocks and produced brines from the Caney Shale. The rock samples were polished rock-slab whilst the fluids used included field fracturing fluid (experiment 4) and produced brine (experiment 5). Rock-slab samples were extracted in two orientations: samples cored parallel to the bedding plane (horizontal samples) and samples cored perpendicular to the bedding plane (vertical samples). These samples were extracted at selected depths from the core retrieved from a vertical well in Caney Shale. These depths represent the seal/ductile and reservoir zones of the shale. The fluid used in the experiments was mainly produced brine from a well producing in the Caney Shale.

Sample Preparation

Sample preparation for rock-slabs was undertaken systematically and presented in the following:

- Core plugs are drilled from depths to be sampled at defined orientations. These are 2inch x 1inches (length and diameter respectively) in size.
- Rock-slab of half inch thickness is cut from the core plug with the fresh-cut face noted.
- The freshly cut face of the rock-slab is polished using alcohol-based polishing lubricants to ensure minimal reaction of shale minerals with polishing fluids.
- The polishing of each sample involves five levels of polishing surfaces – 400 grit paper, 600 grit paper, gold label polishing surface, white label polishing surface and black label polishing surface.

- The polishing fluids used include 6µm diamond polish, 1µm diamond polish, and silica gel, which are respectively used on the gold, white, and black polishing surfaces.
- The main lubricant employed for polishing is purple lube which is applied in all polishing stages except on the black label polishing surface where only silica gel is used.
- The amount of time during each stage of the polishing process averages 5 minutes.

Experimental Design

In this set of static batch experiments, the mass of each polished rock-slab sample was measured and recorded. The mass of produced brine, approximately fifteen (15) times the mass of the rock-slab is also measured, and the rock-slab placed in fluid giving a mass ratio of 1g of bulk rock to 15g of produced brine. The samples are placed in pyrex bottles and subsequently put in an oven preset to 95^{o}C (203^{o}F). The samples are allowed to react for four (4) weeks.

Sampling was undertaken at the end of experiment for both types of experiments. Description of the sampling process in both types of experiments is presented below. The samples were removed from the oven and the rock sample is removed from the produced brine. The rock-slab is rinsed with isopropanol for approximately 30 seconds before it is allowed to dry and placed in container. This is done to ensure the halting of further reaction on the sample. The brine was sampled with a syringe and filtered through 0.22µm filter. This reacted brine was stored in a refrigerator awaiting ICPMS elemental analysis.

Analytical Methods

Rock samples were analyzed before and after experiments to delineate the changes that occurred over the reaction period. The following is a summary of analytical techniques and conditions which were employed.

Scanning electron microscopy was used to study the microstructural configuration of the polished rock- slabs. This was achieved with Scios scanning electron microscope in backscatter electron mode with a working distance of approximately 7µm. No coating was applied for both unreacted and reacted samples. The voltage and current settings were 5kV and 3.2nA respectively and micrographs were acquired at various magnifications (x100, x200, x500, x1000 and x2000).

The different magnifications allowed perceiving of the microstructural configuration at different scales. The microstructural studies are complemented by elemental mapping using the Pathfinder EDS X-ray microanalysis software attached to the Scios scanning electron microscope. The EDS analysis was undertaken for both freshly polished rock-slabs and reacted rock-slabs.

The concentrations of elements in aqueous samples were evaluated simultaneously using an advanced Agilent 8900 triple quadrupole inductively coupled plasma mass spectrometry system (Agilent 8900 QQQ ICP-MS, Agilent Technologies). The instrument settings and analytical methods are similar to those reported by Belkouteb et al. (2023) and Agilent application notes (Agilent, 4th Edition). All the samples were prepared/diluted using 2% (v/v) ultrapure nitric acid in Milli-Q water (18.2 mΩ·cm) with analyses undertaken under a rigorous quality assurance (QA) and quality control (QC) protocol. The pH measurements were made with an Oakton pH 150 meters with the pH of each fluid measured three times and averaged.

Dynamic Geochemical Reactivity of Rock Core Samples in Flowthrough System

Materials

Rock samples used in these experiments were collected from specific depths representing Ductile 2 and Reservoir 3 zones within the Caney Shale. Rocks were initially recovered from a drilled well in the Caney shale as 4-inch diameter core over a depth of 650ft. The samples used in this experiment are extracted from the 4-inch diameter cores as 2-inch length by 1-inch diameter cores at the designated depths. For each depth, two samples were extracted, one sample oriented normal to the original 4-inch core (parallel to the bedding planes of formation) and the other sample was oriented parallel to the original 4-inch core (normal to the bedding planes of the formation). The samples were designated horizontal and vertical for samples parallel to the bedding plane and normal to the bedding plane respectively. In terms of the fluids, two types of fluids were used in this experiment. These include fracturing fluid used in field operations and producing brine recovered from producing well in the field.

Sample Preparation

To undertake experiments, rocks and fluid samples were first prepared with the aim of enhancing potential reactions and mitigating any mechanical damage to experimental units during the core flooding. The rock samples were split into two halves along the 2-inches diameter length to simulate a fracture space through which fluids will flow and interact with the fractured surfaces. To ensure rock samples were uniformly placed into the core flooding system as they were retrieved from the original core, the cores were reassembled, and a copper tape was used to wrap the external perimeter of the cores to hold them together. Copper tape was chosen because of the conducting properties of copper, to ensure minimal interference with the temperature distribution in the system. The main sample preparation used for fluids was filtration of produced brines to avoid solid particles in fluids to be used for core flooding experiments.

Experimental Design

The core flooding experiment was designed to replicate as closely as possible pressure, temperature, and flow conditions in the subsurface in hydraulically fractured Caney Shale reservoirs. To achieve this, rock samples were initially soaked in produced brine for 14-days at temperature of 70^{o}C to get them saturated with the produced brine, which was the closest fluid to formation fluid available for experiment. The core flooding was conducted by flowing fracturing fluid through core samples placed in a core holder at elevated temperature and pressure conditions. Conditions during the experiment were as follows; temperature of 95^{o}C, overburden pressure of approximately 4100 psi, and pore pressure of approximately 2100 psi. Temperature of fluid was maintained by setting oven containing accumulators with fracturing fluid to 95^{o}C and attaching a heater to the bottom of the core holder to maintain the temperature during flow. The temperature of the core holder during flow was measured by a thermocouple attached to the base of the core holder. Overburden pressure was reached by setting an initial overburden pressure of 1000 psi and gradually increasing the pressure by 500 psi every 2 hours till the desired pressure was achieved.

The flow was initiated by activating pumps on the core-flooding system. The maximum pore pressure

created by flow was set to 3800 psi with pressure consistently maintained between 2000 psi and 2200 psi. Effluents were collected as and when there was flow, their pH measured and then stored for further analysis. The experiments were completed in three weeks for each. At the end of experiments, the samples were removed from the core holder and CT scanning conducted. They were subsequently prepared for post-reaction analyses.

Analytical methods

Data was acquired before and after the experiment to enable comparison and make deductions based on changes observed from the data. To achieve this, computed tomographic (CT) scanning, x-ray fluorescence (XRF), rebound hardness (RBH), Raman spectroscopy, scanning electron microscopy (SEM) and energy dispersive spectroscopy (EDS) were employed. CT Scanning was used to study the internal microstructure of the samples to identify the relative positions of fractures and minerals within the core. XRF was employed to study the elemental compositions of samples at various points within the sample surfaces. RBH was used to study the mechanical properties of the samples to provide the extent of brittleness of the samples. Finally, Raman spectroscopy coupled with scanning electron microscopy and energy dispersive spectroscopy (SEM/EDS) helped to investigate the elemental and mineralogical compositions of the samples. These tools were used to measure sample properties before and after the experiment to identify the changes that occurred due to reactions during the experiment.

CT-scanning was conducted using a Yxlon FF20 CT Scanner at voltage and current of 175kV and 75µA in High Power mode. The frame rate during scanning was set at 2.5Hz and scanning was conducted at 360-degrees with 2160 projections. The sample was prepared for CT scan as follows. The two halves of each rock sample were bounded together with copper tape to re-create the shape in which the sample was cored. This sample is subsequently mounted on a foam and the foam placed on a turntable mount. The whole setup of the sample is fastened to the turntable mount for the scanning using a sellotape.

XRF was conducted using the handheld Niton TM XL3t GOLDD XRF analyzer. The radiation gun was hooked to the base of a holder and XRF data collected. For each half of the core-plug sample, fifteen (15) data points were identified, and XRF data collected from these points. Data points included three points across the 1-inch breath and five points along the 2-inch length of the sample. Therefore, for each sample, data was collected from thirty (30) points. Each measurement took 180 seconds.

Rebound hardness was conducted with an Equotip Piccolo 2/Bambino 2 rebound hardness tester. During measurement, the detector was calibrated after every ten (10) measurements. Measurements of rebound hardness were conducted on sample points on which XRF data was taken. To take these measurements, samples were placed on a clip which is mounted on sand. For each data point, five tests were conducted and then averaged.

Raman spectroscopy and profilometry were conducted on selected areas on the sample 'fracture' surfaces. These areas were selected based on the results of XRF data and Rebound hardness area. To conduct Raman Spectroscopy and profilometry, a stitch micrograph of 45 x45 was taken and an area of 2000µm x 2000 µm was selected for a large area scan in Raman mode with true surface activated. The 573nA laser was used for data acquisition. Areas were selected to incorporate dents created by

the rebound hardness tests.
SEM/EDS is undertaken using a Scios Scanning Electron Microscope, in both secondary electron and backscattered electron modes. SEM/EDS analyses are undertaken at 5kV and 3.2nA voltage and current respectively. SEM micrographs were captured for both backscatter and secondary electron detector modes at various magnifications ranging from 100x to 2000x. The elemental mapping and spot mode analyses were acquired using EDS and processed using the Pathfinder x-ray microanalysis software.

3.2.2. Results

Baseline Studies

Elemental concentration changes and inference of clay stabilization

Results from fluid analyses of the various reaction fluids with rocks show a complex trend of elemental concentrations over the reaction period. The first test to assess the main control of geochemical rock-fluid reaction revealed that the fluid composition determines the amount of reaction. This is true for our limited study where the rock compositions are not significantly different. In general, the trends and magnitude of elemental concentrations were similar when any of the single component synthetic fracturing fluids or deionized water was reacted with different rock samples. In contrast, when the same rock powder sample was reacted with the various single component synthetic fracturing fluids or deionized water, the magnitude of the elemental concentrations in reacted fluids varied significantly. The trends shown in Figure 3.3 are for Ca elemental concentrations after reactions described above.
The second purpose of the geochemical reaction was to identify the capacity of the fluids in stabilizing clay minerals. To achieve this, we applied a time-dependent measurement of the rates of concentration of elemental species to assess the relative stability of clay minerals.
The trends in elemental concentration changes with time observed in the experiments provide clues on the stabilization of clay, but do not explain the high concentration of other elements generally not associated with clay. In the time-dependent analyses of various elemental concentrations, we identified trends that revealed that the most critical activity helping to stabilize clay minerals is cation exchange.
For all the reactions (Figure 3.4), Potassium chloride solutions showed a higher rate of elemental concentration increase with time as well as larger changes in the rate, compared to Choline chloride solution and DI water. Cationic concentrations and trends in Choline chloride were marginally higher than in DI water. The shift in trends over the experimental period is attributed to cation exchanges between the clay components of rock and the fluids. The presence or absence of exchangeable cations in the fluid is the main condition that may cause released ions in solution to remain or be adsorbed by cation exchange processes. In Potassium chloride fluid, the presence of potassium cations, which easily exchange and get adsorbed on smectite surfaces as well as exchange in illite interlayers, leaves more released ions from the dissolution of calcite, dolomite, and silica polymorphs in solution. The most favorable cation in the interlayer of illite clays is the potassium cation. In the case of sodium and calcium cations released into Potassium chloride fluid, the potassium cations from Potassium chloride are more favored to act at the cation exchange sites of clays, leaving sodium and calcium in

solution. In the case of DI water and Choline chloride, excess released sodium and calcium ions in solution are adsorbed or exchanged at exchange sites of clay minerals.

It is also observed that, for anionic components like SO_4^{2-}, concentration trends with time in all fluids are similar. This is because the concentration of SO_4^{2-} in solution is not dependent on cationic exchange but likely due to dissolution and oxidation of sulfides such as pyrite. The consumption of ions by precipitation of new minerals is observed to be the main process by which anion concentrations in the sample are reduced. Therefore, SO_4^{2-} concentration follows this trend. In conclusion, potassium chloride fracturing fluid was more effective in stabilizing clay minerals through cation exchange relative to choline chloride fracturing fluid and deionized water.

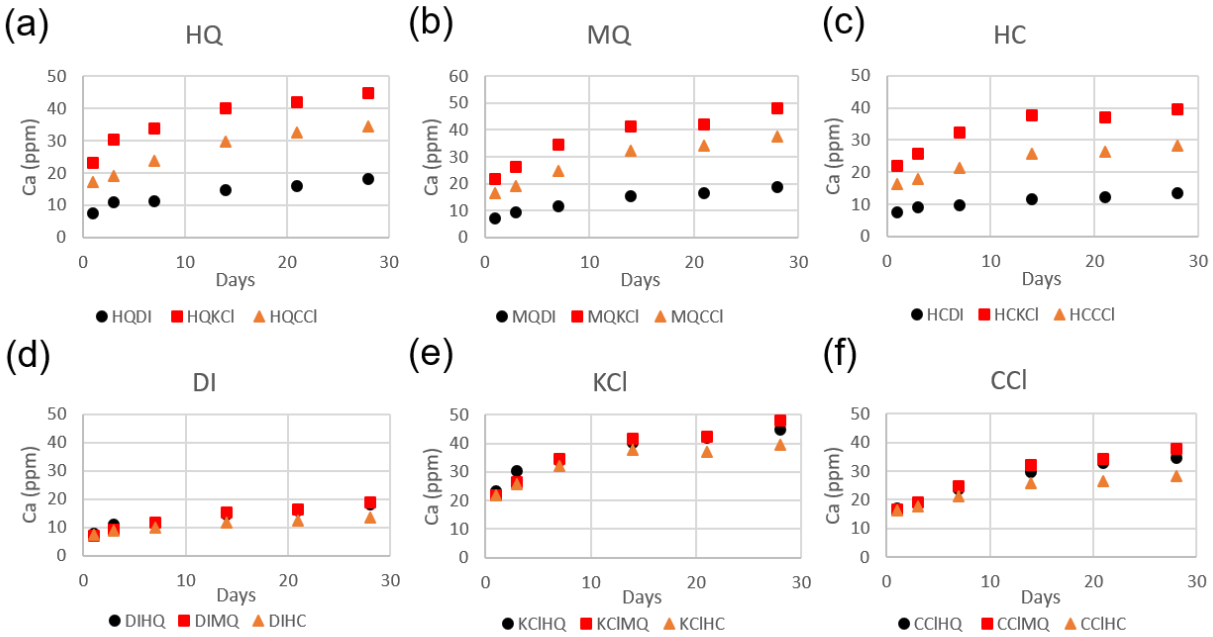

Figure 3.3. Trends of Ca concentration with time for different fluids and same rock sample **a.** High Quartz (HQ) **b.** Moderate Quartz Carbonate and Clay (MQ) **C.** High Clay (HC). Trends of Ca concentration with time for different rocks and the same reaction fluid **a.** DI water (DI) **b.** potassium chloride (KCl). **C.** choline chloride (CCl).

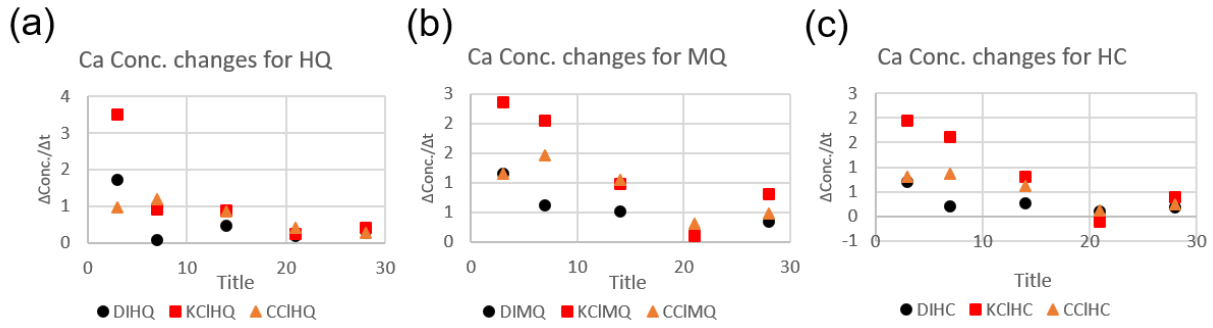

Figure 3.4. Rate of Ca concentration changes with time in fluids (DI, KCl, CCl) for different rock compositions: **a.** High Quartz (HQ) **b.** Moderate Quartz Carbonate and Clay (MQ) **C.** High Clay (HC).

Static Geochemical Reactivity of Powdered Rock Samples

Mineralogical Transformations

The initial mineralogy of powdered Caney shale samples used in experiments are consistent in the type of minerals present, but the percentage weight of individual minerals for each sample varies. The reservoir samples tended to have less clay minerals compared to the samples from the ductile (seal) zone. The main minerals identified in the samples included quartz, illite, albite, calcite, dolomite, and pyrite. Reaction with fracturing fluid and produced brines caused mineralogical changes in the shale samples. Pyrite and feldspar dissolution were common to all samples whilst carbonate dissolution was observed to be slow. This can be attributed to the circumneutral pH of initial fluids used as well as the high Ca concentrations in produced brines. The results from mineralogical changes in shales show geochemical reactions to proceed in the following format. Dissolution of pyrite and other sulfides is initiated by dissolved oxygen in the reacting fluid, which leads to the generation of transient and localized acidization by the oxidation of the sulfide to sulfuric acid. Feldspar, carbonates and clay minerals proximal to the sulfides therefore dissolve in response to the generated acidity. The dissolution of carbonates leads to buffering of the fluid pH to get it to equilibrium. The rate of dissolution of brittle minerals such as feldspar, pyrite and carbonates were observed to be higher than clay minerals. In most instances, the dissolution of feldspar with corresponding increase in illite weight percent suggests illitization. The following ternary diagrams (Figure 3.5a and Figure 3.5b) give an overview of the mineralogical transformations due to reaction of powdered rocks with fracturing fluids and produced brines respectively.

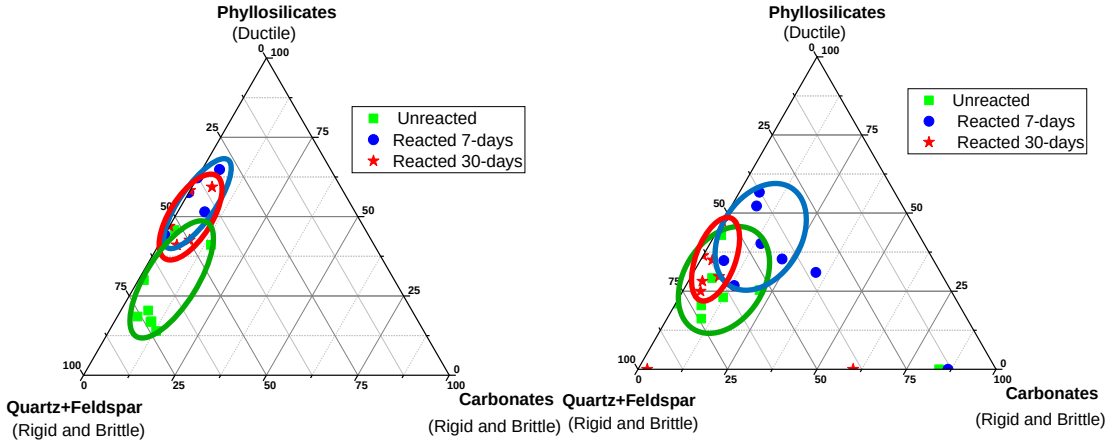

Figure 3.5. Comparison of unreacted samples to 7 days and 30 days of reaction 1a. Trends of reaction with Hydraulic Fracturing Fluid 1b. Trends of reaction with Produced Brine.

Effluent analysis

The concentrations of elements in reacted fluids corroborated the dissolution reactions observed in the mineralogical analyses. The trends in concentration of some key elements are summarized in the following.

Ca Concentration

Marginal changes in Ca concentrations were observed as seen in Figure 3.6a and Figure 3.6b. The

relative stability of Ca during reaction is due to the initial near-neutral pH of fracturing fluids and produced brines used for experiments. The initial drop in Ca concentration in experiments with produced brine is due to the extremely high Ca concentrations in the produced brine. The reaction trends observed in these experiments confirmed the role of mild acidization in carbonate dissolution in the subsurface. Carbonate dissolution is largely influenced by localized and transient acidization of surrounding fluids due to oxidation of sulfides. This causes the dissolution of proximal carbonate minerals leading to the marginal increase in Ca concentrations in reacted fluids. In the fracturing fluid, the influence of acidization is observed in increase of Ca concentrations after 7 days reaction, whilst for produced brines, this phenomenon is masked in the first week by the initially high Ca concentrations. Ca concentrations however increase in reactions with produced brine after 30 days.

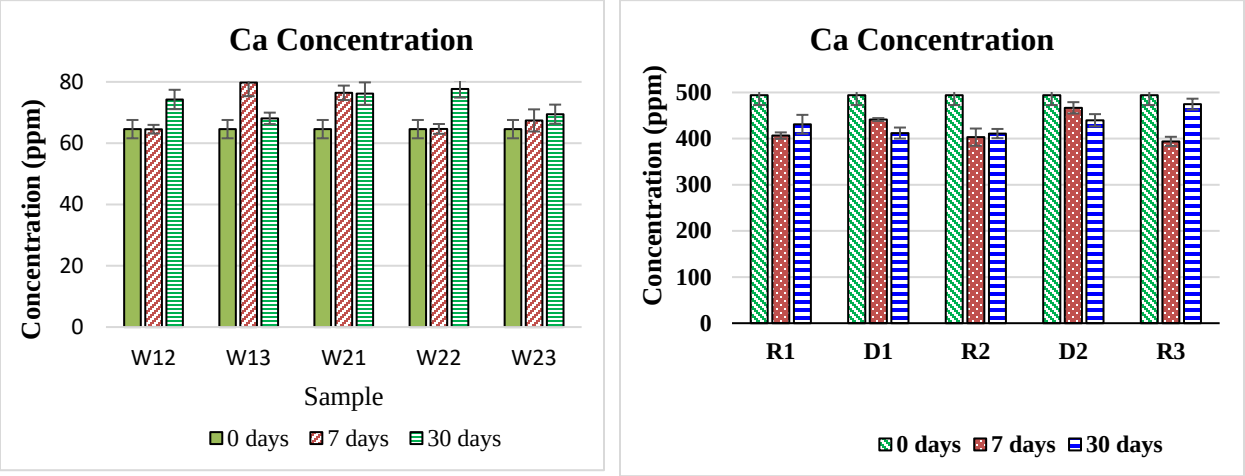

Figure 3.6. Ca concentration in fluid at 0, 7 and 30 days of reaction between rock samples a. fracturing fluid b. produced brine. Initial concentrations of Ca in produced brine are approximately nine times greater than concentrations in fracturing fluid.

K Concentration

K concentration in reacted fluids (Figure 3.7a and Figure 3.7b) is mainly from the dissolution of feldspars and contributions from desorption in clay exchange sites. Though potassium feldspars are not identified by XRD, they are present in trace quantities which are mostly below the detection limit of the XRD equipment. The initial increase in K concentration is due to breakdown of feldspar and unstable clay minerals present in rock. For most samples, the concentration of K in reacted fluid is relatively stable after a week of reaction. This is attributable to the total dissolution of traces of k-feldspar in rocks and stabilized ion exchange reaction at clay sites. Illite, the predominant clay mineral in the formation rock is mostly stabilized by absorbing K cations into its interlayer.

Si Concentration

Si concentrations in reacted fluids are generally from the dissolution of feldspar, clay minerals and microcrystalline quartz. Inorganic quartz is not expected to dissolve under the conditions of this experiment thus does not contribute to Si in solution. Si in reacted fluid is therefore expected to be from feldspar and clay minerals. Exchange of ions on clay surfaces and interlayers also contributes to Si in solution. Based on the trends observed on the graphs (Figure 3.8a and Figure 3.8b) and the

corresponding mineralogical trends, the initial Si entering solution is predominantly from feldspar and biogenic silica whilst the latter stage increase in Si is primarily from the breakdown of clay minerals.

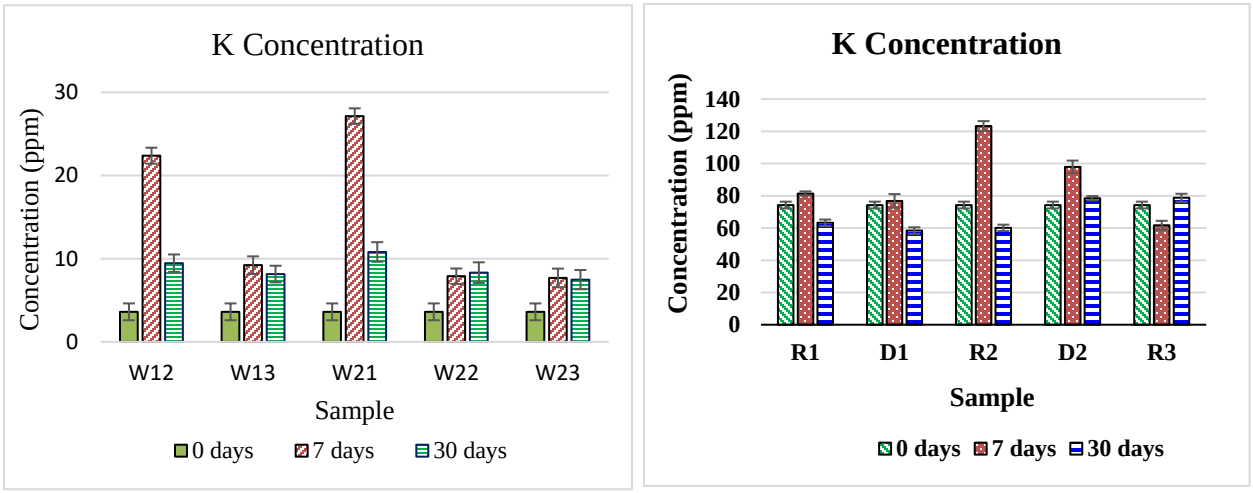

Figure 3.7. Ca concentration in fluid at 0, 7 and 30 days of reaction between rock samples a. fracturing fluid b. produced brine.

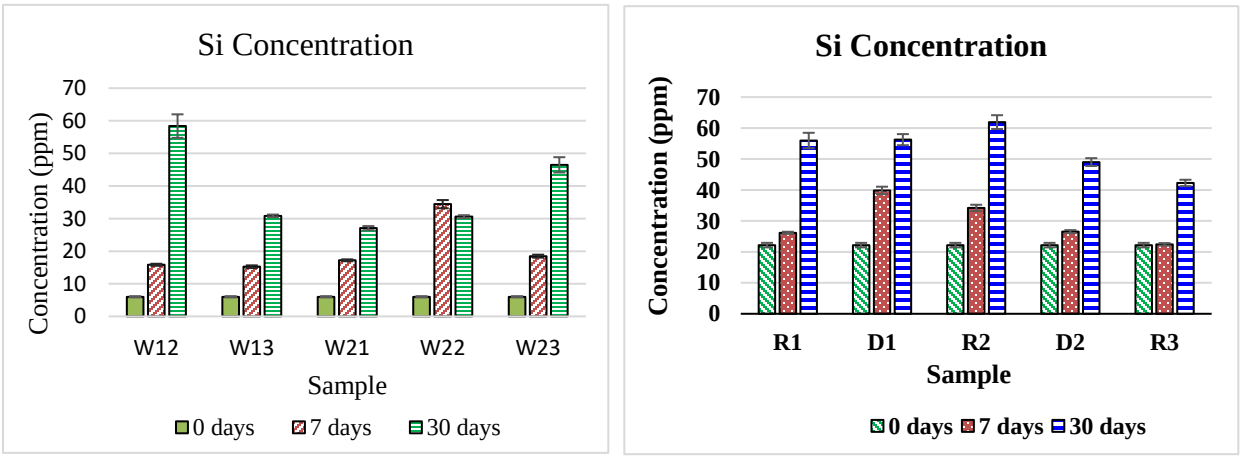

Figure 3.8. Si concentration in fluid at 0, 7 and 30 days of reaction between rock samples a. fracturing fluid b. produced brine.

Al Concentration

Aluminum in reacted fluid is mainly from the dissolution of feldspars and exchange in clay sites. The formation of clays, mostly through illitization is identified as one of the significant causes of Al depletion in reacted fluids. The precipitation of other Al-bearing minerals also leads to the depletion of Al from the reacted fluids. The trends in Al concentrations for experiments are presented in Figure 3.9a and Figure 3.9b.

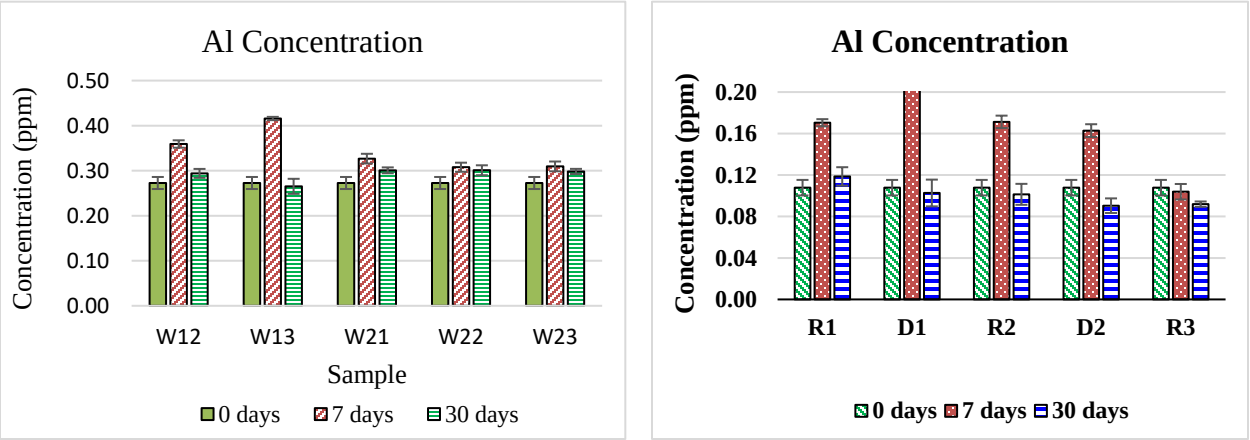

Figure 3.9. Al concentration in fluid at 0, 7 and 30 days of reaction between rock samples a. fracturing fluid b. produced brine.

Static Geochemical Reactivity of Polished Rock Samples

Microstructure of Samples

Ductile Horizontal Sample

The direction of coring of this sample is normal to the main core/wellbore axis (i.e., parallel to the bedding plane). The microstructural configuration of the sample before reaction shows grains of quartz, carbonates, framboidal pyrite and disseminated pyrite encapsulated in matrix of clay minerals. The grain sizes common in this sample range from 5µm to 30µm with an average grain size of less than 20µm. The common contact in the sample is grain-matrix contact. Preferred orientation of minerals is observed in this sample as shown in Figure 3.10a.

Ductile Vertical Sample

The direction of coring is along the main core/wellbore axis (i.e perpendicular to the bedding plane). The microstructural configuration of the pre-reaction sample shows grains of quartz, carbonates, framboidal pyrite and disseminated pyrite surrounded by clay minerals as shown in Figure 3.10b. The grain sizes most common in these samples range from 5µm to 30µm with an average grain size of less than 20µm. The common contact in the sample is grain-matrix contact, where the matrix is made of clay minerals. The sample also has significant pore and organic matter compositions as shown on Figure 3.10b. Preferred orientation of minerals is not observed in this sample.

Reservoir Horizontal Sample

The direction of coring is normal to the main core/wellbore axis (parallel to the bedding plane). The microstructural configuration of the sample before reaction shows grains of quartz, carbonates, feldspars, and pyrite (large grains, framboidal and disseminated) in matrix of clay minerals and carbonate cements. The sample shows significant pore volume along the grain contacts. The common contact in the sample is grain-grain contact relative to the grain to matrix contacts observed in the ductile samples. The grain sizes most common in these samples range from 15µm to 40µm with an average grain size of approximately 35µm shown in Figure 3.11a. Preferred orientation of minerals is generally absent in this sample though it was cored along the bedding plane of the sample.

Reservoir Vertical Sample

The direction of coring is parallel to the main core/wellbore axis (i.e perpendicular to the bedding plane). The microstructural configuration of the sample shows grains of quartz, carbonates, feldspars, and pyrite (large grains, framboidal and disseminated) in matrix of clay minerals and carbonate cements. The common contact in the sample is grain-to-grain contact with significant pore volume along these contacts as observed in Figure 3.11b. The grain sizes most common in these samples range from 10µm to 40µm with an average grain size of approximately 35µm. Preferred orientation of minerals is generally absent in this sample.

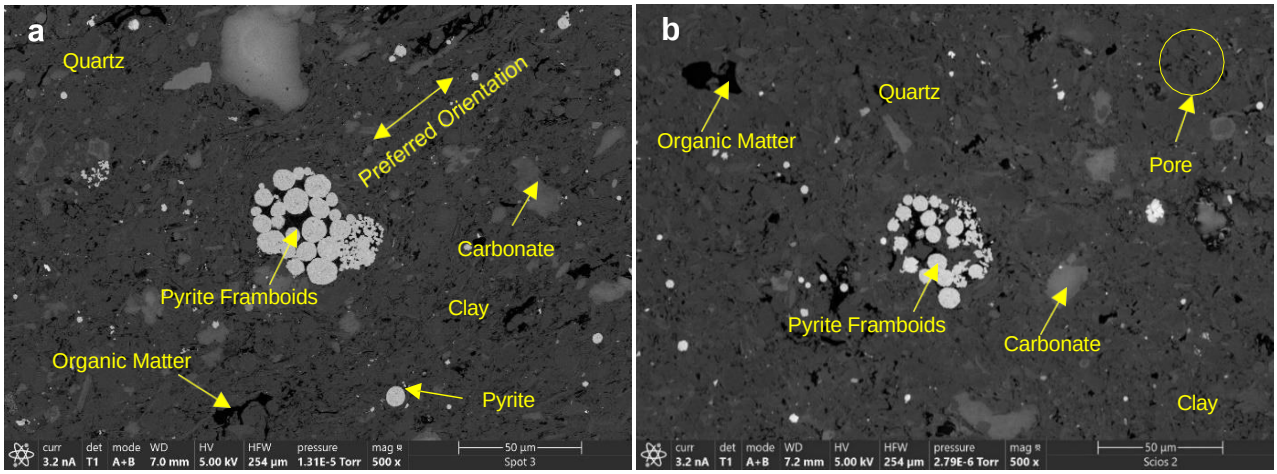

Figure 3.10. SEM micrographs showing the mineralogy and microstructural configuration of ductile samples cored a. horizontal to the bedding plane and b. vertical to the bedding plane. Clay minerals form a matrix with quartz, carbonate and feldspar grains completely embedded within the clay matrix. Preferred orientation is observed within the microstructure

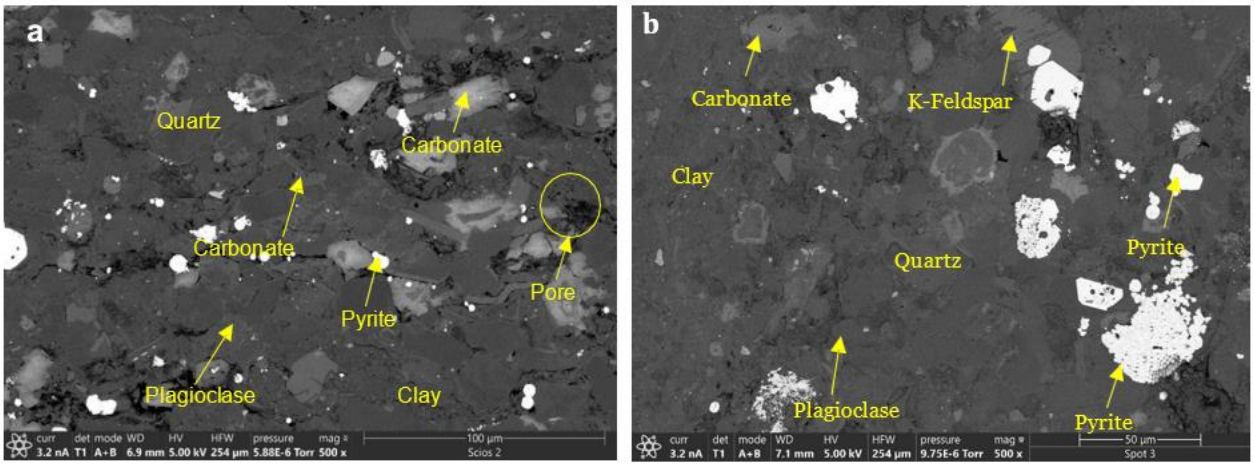

Figure 3.11. SEM micrographs showing the mineralogy and microstructural configuration of reservoir samples cored a. horizontal to the bedding plane and b. vertical to the bedding plane. The samples are characterized by bigger grains with significant grain-to-grain contacts.

Mineral Phase Changes

Results of static reactions between cored rocks and fluids (field fracturing fluids and field produced brines) showed less visible reactions and thus were not readily perceivable on SEM micrographs.

However, corrosion on pyrite surfaces and deposition of fines and amorphous phases on rock surfaces are observed from SEM micrographs. In terms of surface chemistry, there were significant changes observed on the surface chemistry and mineral phases identified on the rocks after reaction with both fracturing and produced fluids. In general, the deposition of Ca-rich amorphous phases in pores was predominant especially in rock samples cored in the horizontal position (parallel to the bedding plane). The transformation of dolomite to calcite and dissolution of plagioclase (feldspar) were also observed on mineral phase identification conducted on rock surface before and after reaction. The following SEM micrographs and spectral maps show the mineral phase transformation in cored rock samples after reaction with fracturing fluids and produced brines respectively.

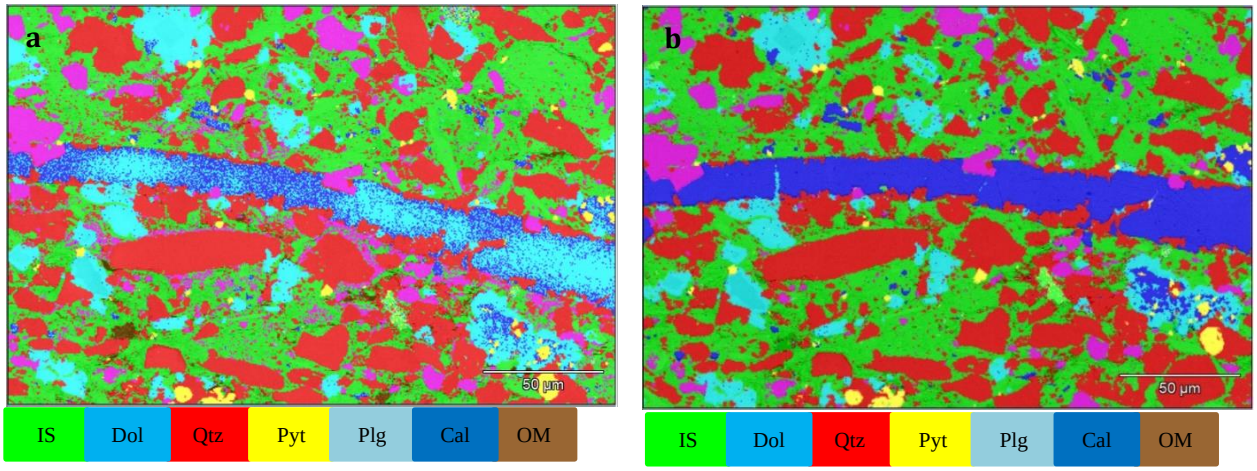

Figure 3.12. EDS microanalysis of surface chemistry of reservoir zone of cored rock **a**. before reaction and **b.** after reaction after reaction with fracturing fluid. The transformation of dolomite to calcite and dissolution of feldspar is observed. (Qtz - Quartz, Plg – Plagioclase, Pyt – Pyrite, Dol – Dolomite, IS – Illite-Smectite).

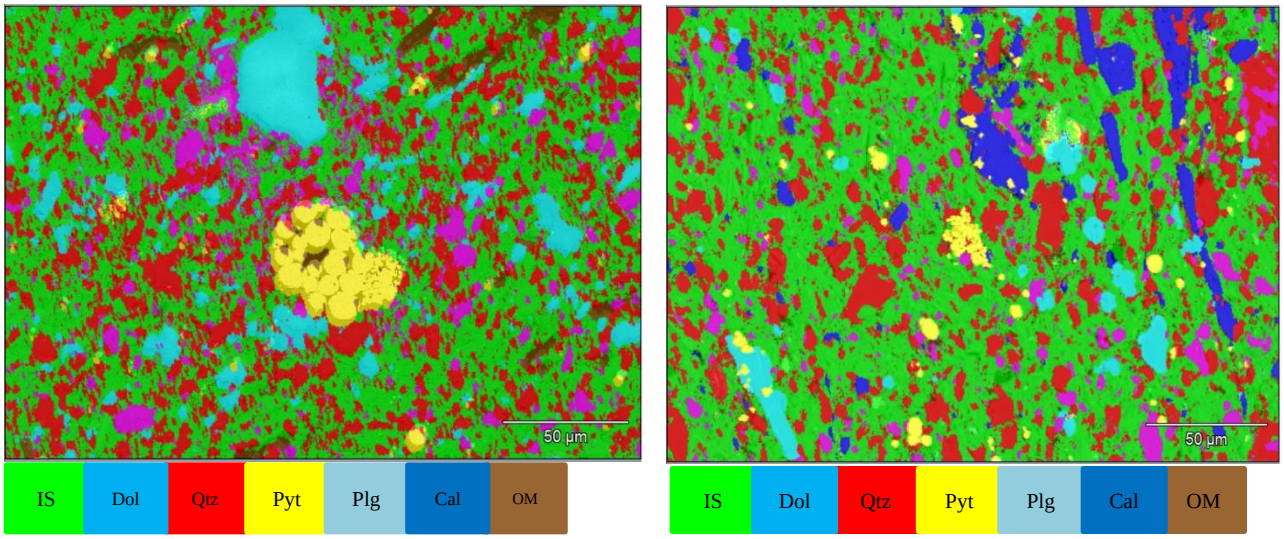

Figure 3.13. EDS microanalysis of surface chemistry of ductile zone of cored rock **a.** before reaction and **b.** after reaction with produced brines. The transformation of dolomite to calcite and dissolution of feldspar is observed. (Qtz - Quartz, Plg – Plagioclase, Pyt – Pyrite, Dol – Dolomite, IS – Illite-Smectite).

Dynamic Geochemical Reactivity of Rock Core Samples in Flowthrough System

Computed tomographic scanning

Pre-experimental CT scans show the presence of various mineral entities based on different shades of grey on the surface of reconstructed volume sliced along specific axes (Figure 3.13). Quartz and feldspars are dark grey compared to carbonates, which are lighter grey whilst pyrites and other heavy minerals appear as the brightest color in the scans. The CT scans of the samples revealed a general pattern where samples cored parallel to the bedding planes (horizontal samples) showed series of parallel microfractures. The fractures in the samples cored normal to the bedding planes (vertical samples) also tend to be parallel to the bedding. These fractures reveal zones of weakness which are fractured during coring and represent hydraulic fractures for the purpose of this study.
CT scans conducted after core flooding experiment show significant differences with the samples before core flooding (Figure 3.14).

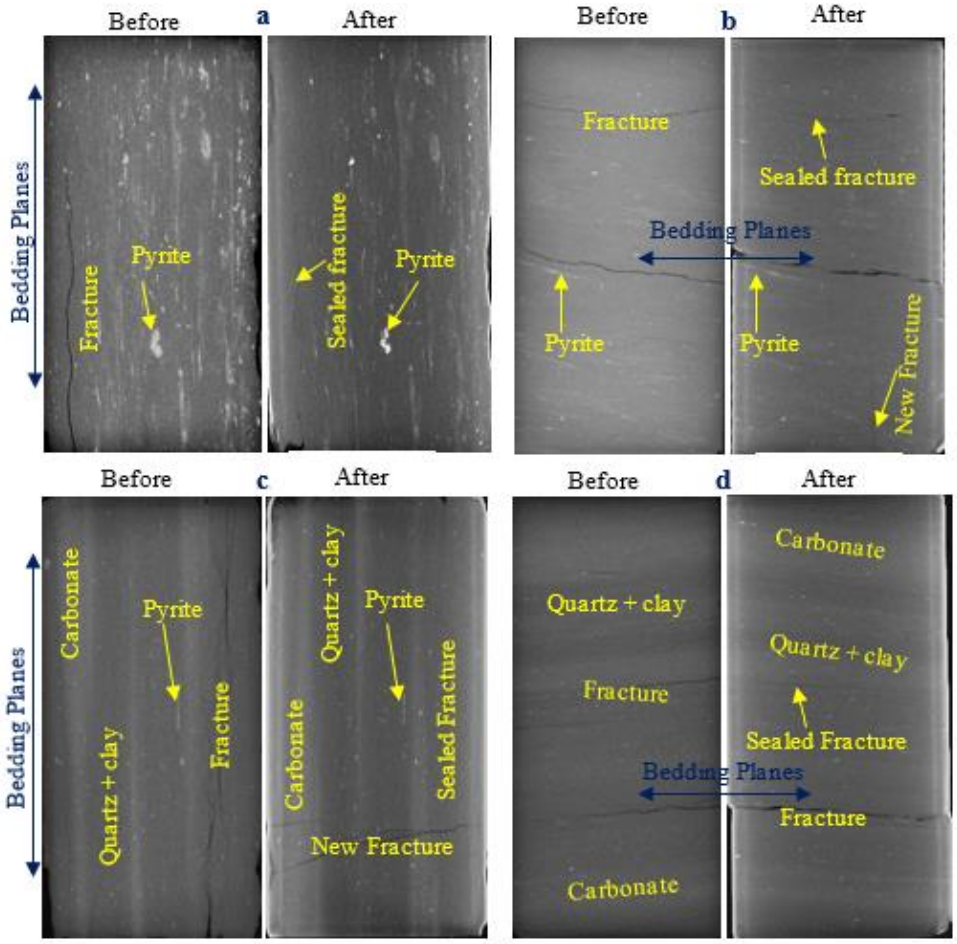

Figure 3.14. Computed tomographic scans of Caney Shale before and after core flooding experiments. In general, fractures present before experiments are sealed due to the impact of both confining pressure and geochemical reactions. New fractures are observed in some of the samples, with orientations generally perpendicular to the bedding planes. (a) Pre-experiment and post experiment CT-scan of a ductile sample cored along the bedding plane (D2H). (b) Pre-experiment and post-experiment CT-scans of a ductile sample cored perpendicular to the bedding plane (D2V). (c) Pre-experiment and post-experiment CT-scans of a

reservoir sample cored along to the bedding plane (D2V). (d) Pre-experiment and post-experiment CT-scan of reservoir sample cored perpendicular to bedding plane (D2V).

Most of the fractures observed on the pre-experimental samples have been sealed. This sealing may be the result of high confining stress applied on the sample during core flooding, however, sealing of fractures parallel to the direction of confining stresses indicates a geochemical cause of fracture closure. The geochemical cause of fracture closure may be due to swelling of clays, and/or precipitation and deposition of minerals and amorphous phases most likely of silica and carbonate composition. Minerals and amorphous phases may have precipitated during the soaking in produced brines due to their high elemental concentrations in these fluids.

CT scans also revealed that indentation marks on samples created during the measurement of Leeb's hardness significantly recovered with most indents disappearing totally following core flooding experiment. Whilst these indents remain conspicuous after soaking samples in produced brines, they are less prominent after core flooding with fracturing fluid. In this regard, the fracturing fluid is proposed as causing clay swelling which may have occasioned the recovery of the indentation marks.

X-Ray Fluorescence

XRF analyses are undertaken before and after the experiment to ascertain the elemental changes that occurred during core flooding. These measurements were made on the sample surface at fifteen points which is illustrated on Figure 3.15. The samples analyzed included reservoir and ductile samples cored at horizontal and vertical orientations respectively. Though the original XRF results from both horizontal and vertical samples are expected to be similar for each zone of the Caney shale, the post-experiment XRF results are of major significance as they show the level of reaction that took place due to rock-fluid reaction during core flooding. Figure 3.16 and Figure 3.17 show XRF before and after respectively.

In general, the key distinguishing feature between reservoir and ductile samples based on XRF data before core flooding is the significantly higher Ca content in the reservoir samples. The average Ca percent recorded in reservoir samples are 6.45%, 5.64%, 11.19% and 10.61% for R3H1, R3H2, R3V1 and R3V2 respectively whilst the average Ca percent recorded for ductile samples includes 0.47%. 0.51%, 0.81% and 0.83% for D2H1, D2H2, D2V1 and D2V2 respectively. The percentage of other significant elements such as Si, Al, K and Fe are observed to be higher in ductile samples. The higher percentage of Ca in reservoir indicates the presence of carbonate minerals which tend to increase the brittleness of the reservoir zone. In contrast, higher amounts of Al and K in the ductile zones is an indication of relatively higher clay content which tends to make these zones ductile and unsuitable for hydraulic fracturing.

In terms of uniform distribution of elements, all samples showed consistency except the reservoir samples cored perpendicular to the bedding. This is expected because heterogeneity of formations is mostly higher across the bedding compared to along the bedding. The consistency observed in the ductile samples cored perpendicular to the bedding plane can be explained by the generally high clay content in this zone, that mask the heterogeneity based on other minerals.

Results obtained from XRF analyses after core flooding showed significant shifts in elemental concentrations on cored rock surfaces. The most significant observation is the reduction of Ca in reservoir samples especially in the sample cored horizontal to bedding whilst ductile samples showed

a reverse trend with pronounced changes in the sample cored vertical to the bedding. The percentage concentration of Ca decreased between 20% to 40% in reservoir samples cored horizontal to bedding whilst for samples cored vertical to the bedding, the decline was 0.3% to 3%. In the ductile samples, the percentage increase of Ca concentration in samples cored horizontal to bedding ranged from 8% to 30% whilst for vertical samples, the range was 54% to 74%. The percentage concentrations of Si, Al and K generally decline in all the samples whilst the trend of Fe remains inconsistent. The drop in Si, Al and K concentrations can be attributable to the dissolution of feldspar or clay minerals, the former most plausibly dissolving at a higher rate.

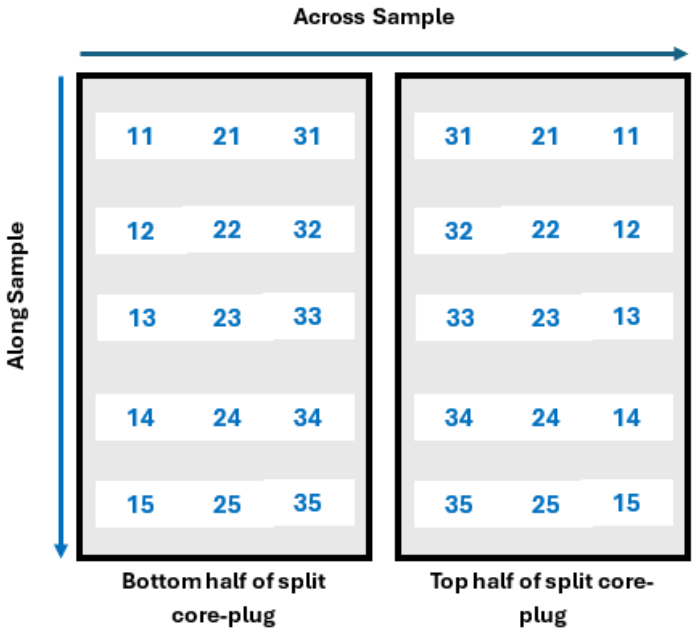

Figure 3.15. Illustration of locations of XRF measurements on samples. The locations on the top half of the split core are reversed because that component of the split-core lies upside down, directly on top of the bottom split core-plug. Therefore, when the top is closed on the bottom split-core-plug, the sampling locations form mirror-images of each other.

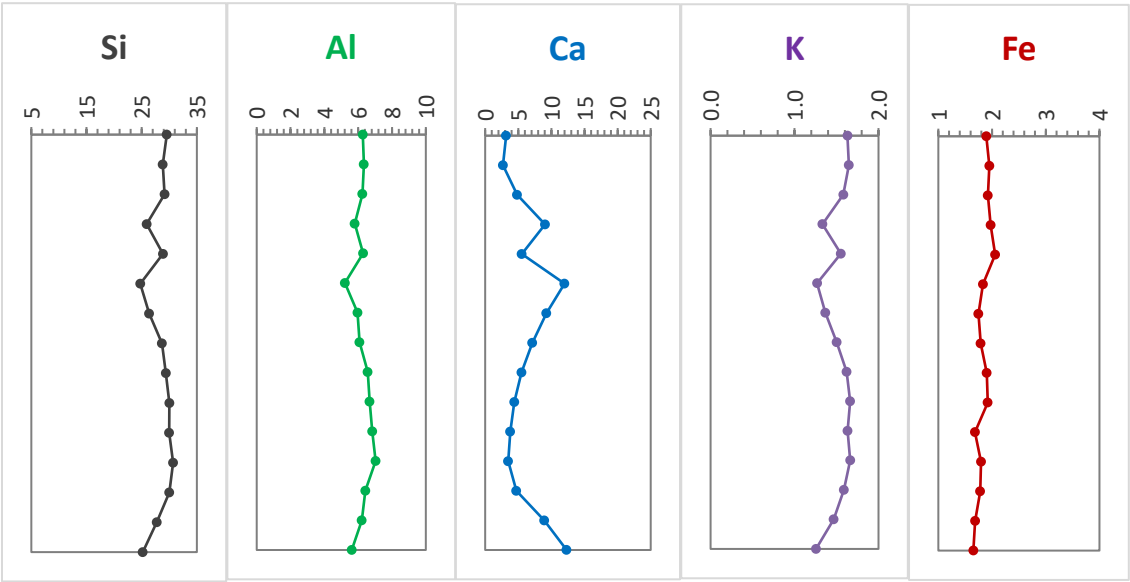

Figure 3.16. XRF measurements on rock surface of sample R3H before core flooding.

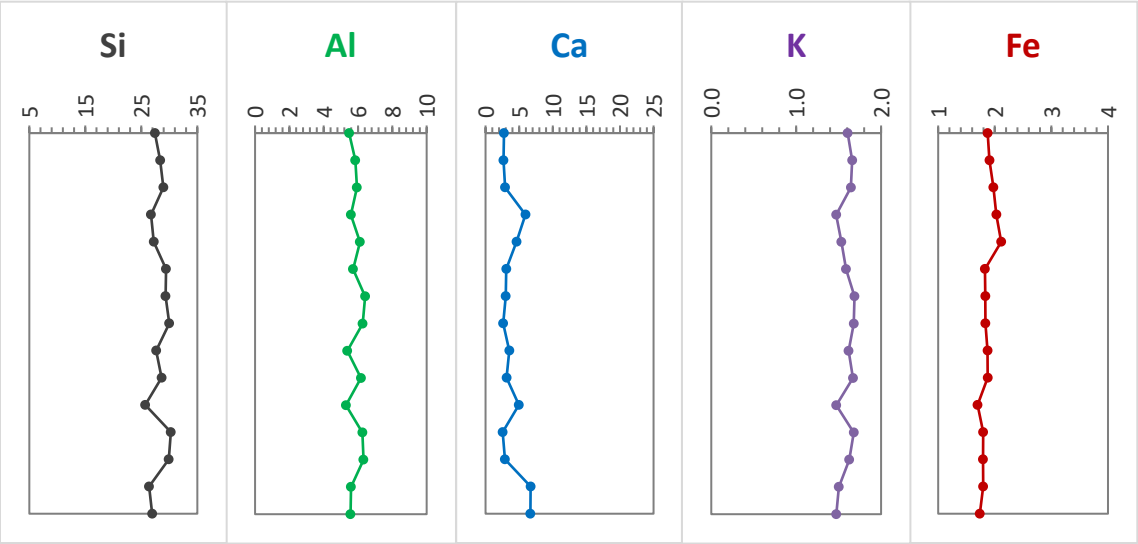

Figure 3.17. XRF measurements on rock surface of sample R3H after core flooding.

Leeb's rebound hardness

The rebound hardness of the rock samples is measured before and after the core flooding experiment to ascertain the impact of hydraulic fracturing on fracture face of shales. The rebound hardness is the ratio of the rebound velocity to the impact velocity of an impact body. This ratio is multiplied by 1000 to give the Leeb Hardness value of the sample. High Leeb hardness indicate a higher rebound, which implies that less energy is absorbed or dissipated by the specimen upon impact from the impact body. On the other hand, a low Leeb hardness implies a lower rebound, an implication of higher energy absorbed or dissipated by the specimen from the impact body. The Leeb hardness of rock samples therefore provides an understanding of the level of microstructural integrity as well as porosity of the sample.

According to Verwaal and Mulder, (1993), the Leeb hardness measured on a sample is dependent on thickness of the sample and tends to be lower for samples with thicknesses less than 50mm (~2in). Wilhelm et al., (2016) went further to examine two issues related to Leeb hardness and concluded that the suitable size of sample for Leeb hardness testing is dependent on the porosity and heterogeneity of the sample. In this study, the sample thickness is approximately 12.7mm (0.5in), thus the value obtained from Leeb hardness testing are assumed to be lower. However, the consistency of the testing protocol provides useful information on the porosity and structural integrity of the rock samples. Interpretation of Leeb hardness in this study is therefore to ascertain the changes in porosity (consequently fracture-face permeability) of the samples.

Rebound hardness levels of the rocks before the experiment are generally higher than the rebound hardness after the experiment in horizontal samples. However, the rebound hardness in vertical samples increases after core flooding. This can be attributed to the geochemical reactions and direction of fluid flow during core flooding. Whilst on the horizontal samples fluid flows parallel to the bedding and thus transport dissolved species (mostly carbonates) and fines the flow along the vertical samples is perpendicular to the fluid flow, therefore resulting in deposition of fines as well as relatively less transport of dissolved species. Ultimately, the porosity of the horizontal samples

increases whilst vertical samples reduce. These translate to the decline in rebound hardness of horizontal samples and increase of rebound hardness in vertical samples. Tables 3.1 to Table 3.4 show the Leeb's rebound hardness for reservoir and ductile samples cored in different orientations.

Table 3.1. Leeb's rebound hardness before and after core flooding for reservoir sample cored parallel to the bedding.

Leeb's Hardness of R3H				
Location ID	R3H-Top		R3H-Bottom	
	Before	After	Before	After
21	427.8	212.2	307.4	180.4
22	372.6	325.4	392.4	320.4
23	347.6	405	394.8	392.6
24	329.4	360.4	400.8	340.6
25	299.2	240.6	335.4	163.6
Average	**355.32**	**308.72**	**366.16**	**279.52**

Table 3.2. Leeb's rebound hardness before and after core flooding for reservoir sample cored perpendicular to the bedding.

Leeb's Hardness of R3V				
Location ID	R3V-Top		R3V-Bottom	
	Before	After	Before	After
21	295.8	229.8	351.6	277.6
22	315.4	394.6	282.8	374.6
23	236.8	365.4	211.2	344.4
24	255.2	339.8	241	264.4
25	228.6	204	334.8	268
Average	**266.36**	**306.72**	**284.28**	**305.8**

Table 3.4. Leeb's rebound hardness before and after core flooding for ductile sample cored parallel to the bedding.

Leeb's Hardness of D2H				
Location ID	D2H-Top		D2H-Bottom	
	Before	After	Before	After
21	305.2	224	313.8	170
22	374.4	190.2	384.2	270
23	379.4	272	385.8	352.6
24	369.4	267.4	321.8	295.2
25	317.4	362.8	299.6	192.4
Average	**349.16**	**263.28**	**341.04**	**256.04**

Table 3.3. Leeb's rebound hardness before and after core flooding for ductile sample cored perpendicular to the bedding.

Leeb's Hardness of D2V				
Location ID	D2V-Top		D2V-Bottom	
	Before	After	Before	After
21	335.8	341.8	409.4	351.6
22	353.8	363.4	333.2	422.2
23	281.2	423.6	245.8	408.4
24	291.4	408	306.6	397.6
25	339.8	301.8	372	371.2
Average	**320.4**	**367.72**	**333.4**	**390.2**

Ghorbani et al., (2023) showed in their study that Leeb rebound hardness has an inverse relationship with porosity, thus decreasing porosity leads to higher rebound hardness. Data from CT scanning shows that fracture sealing is predominant in the samples following core flooding. Though fracture closure along the axis perpendicular to confining stresses can be attributed to the confining stresses, the closure (sealing) of fractures parallel to confining stress cannot be attributable to confining stresses. Ultimately, the most plausible explanation for closure of fractures parallel to confining stress direction is due to clay swelling, precipitation of minerals or depositing of fines in these fractures

(these fractures are generally perpendicular to flow direction within the core flooding system). It is observed in the rebound hardness measurements that sampling points proximal to micro-fractures returned lower rebound hardness. The low rebound hardness values at sampling points near fractures may be attributed to the dissipation of the energy exerted by the impact body through these micro-fractures. Based on the discussion above, it can be averred that the increased rebound hardness of samples post-experiment is largely attributable to porosity impairment.

3.2.3. Investigating the potential environmental effects of hydraulic fracturing of shales: comparing Caney to Marcellus shale flow back waters at laboratory scale

We compared the geochemical processes of the Caney and Marcellus shales when treated with hydraulic fracturing fluids. The study focused on clay stabilization, mineral dissolution, and hazardous elements in flowback waters. Effluent analysis from horizontal sections of the Marcellus (S2 and S7) and Caney (R1 and R2) shales over a four-week period revealed distinct geochemical reactions. This comparison emphasizes the elemental alterations and environmental considerations linked to hydraulic fracturing in diverse shale formations, suggesting the necessity for shale-specific monitoring and regulatory strategies. Ca, Al, Fe, Si, As, B, Cd, Se, and Pb were the elements of interest for this paper.

For the Marcellus shale, core samples were crushed to a particle size of 120 µm to maximize surface area for reactions. Leaching tests were performed to evaluate the solubility of clay minerals. A hydraulic fracturing fluid, consisting of 99% water and 1% additives, was used. The pH of the fluid was measured before and after interaction with the shale, with samples analyzed weekly at 60°C. The pH was maintained at 7.8 throughout the experiments. For the Caney shale, core samples were exposed to two simulated fracturing fluids and deionized (DI) water at 95°C for four weeks. Three major rock types were identified: high quartz content (HQ), high clay content (HC), and moderate quartz, clay, and carbonate content (MQ). The fluids included DI water with a pH of ~7, DI water with 2% KCl, and DI water with 0.5% ChCl, both of which were adjusted to a pH of ~4.

In the Caney shale, pH increased due to carbonate dissolution, with a sharp rise after seven days, indicating pH-driven dissolution kinetics of carbonate minerals. Silica dissolution, higher than expected, stemmed from soluble silica polymorphs and clay mineral desorption. Interaction with hydraulic fracturing fluids led to calcite and pyrite dissolution, increasing silica and reducing aluminum and magnesium levels via secondary aluminosilicate formation. These reactions risk fines migration, emphasizing the need for appropriate fracturing fluids to prevent deflocculation.

In contrast, the Marcellus shale showed a preference for Ca^{2+} ions in cation exchanges with K^{+} and Na^{+}, common in montmorillonite and illite clays. Calcium-rich additives mitigate clay swelling by promoting cation exchange, preserving permeability through flocculation. However, excessive Ca^{2+} can lead to deflocculation. Pyrite oxidation in Marcellus, facilitated by dissolved oxygen, increased sulfate ions, leading to Fe^{2+} and SO_4^{2-} ions. The oxidation of Fe^{2+} to Fe^{3+} produced iron oxides, potentially clogging pores. Sulfate reactions with Ba^{2+} and Sr^{2+} further threaten reservoir productivity, independent of salinity. Boron, integrated into illite structures, plays a critical role in clay stabilization in both formations, influenced by historical salinity. KCl fluids stabilized Caney shale during pH increases from carbonate dissolution, while Ca^{2+} in the Marcellus shale reduced clay swelling and maintained permeability. Scale formation, driven by fluid pH and temperature,

highlights the need for carefully formulated fracturing fluids to maintain reservoir performance. Figure 3.18 illustrates the various reaction mechanisms observed in our experiments. These results emphasize the importance of geochemically compatible fracturing fluids to ensure formation stability and reservoir efficiency.

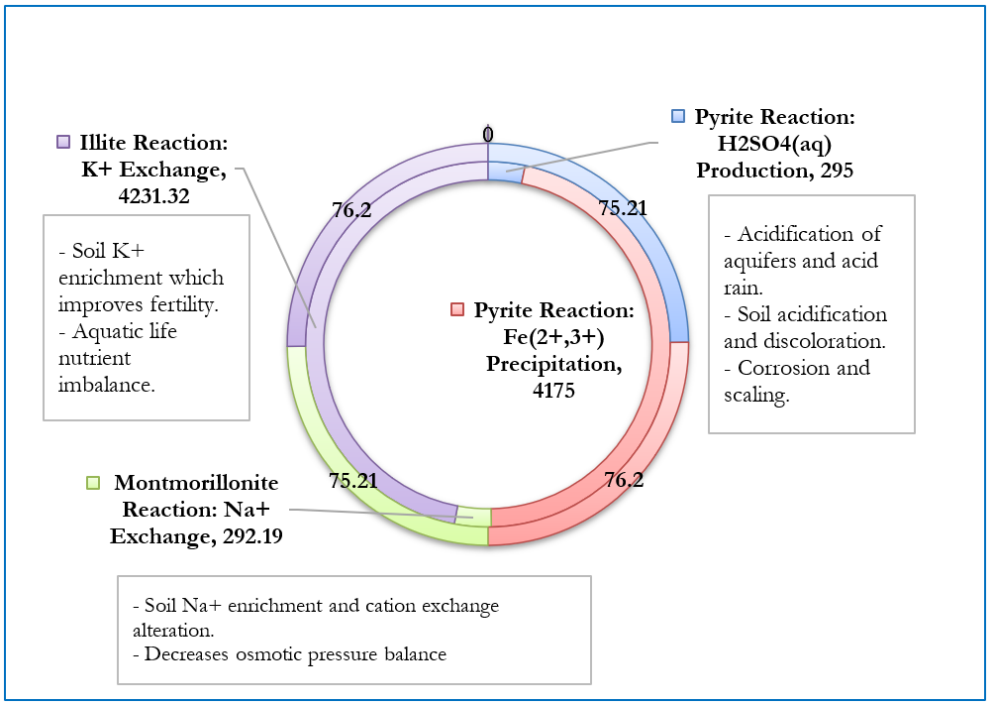

Figure 3.18. Geochemical processes in the Marcellus shale and overall influence on flowback waters

Our study found chromium (0.32 ppm) and arsenic (0.36 ppm) levels above safety thresholds, suggesting organic sediment presence and potential water infiltration. Arsenic exceeds drinking water limits (0.01 ppm), as shown in Figure 3.19. As poses health risks such as cancers and vascular diseases. Similarly, cadmium and chromium levels necessitate strict environmental monitoring and remediation due to their association with serious health issues. Arsenic's prevalence in organic-rich shales and cadmium's mobilization from organic matter underlines the need for diligent management in hydraulic fracturing operations to mitigate environmental and health risks. The Caney shale, with boron (B) levels at 128.35 ppm, far exceeds the Marcellus shale's 4.35 ppm, suggesting potential health risks if these levels enter water supplies. Similarly, selenium (Se) content is much higher in Caney (75.36 ppm) compared to Marcellus (0.77 ppm), with Caney's levels vastly surpassing EPA's safety thresholds (0.05 ppm), indicating a risk of selenosis and environmental concerns. Our results are shown in Figure 3.3. The Marcellus shale has a lead (Pb) concentration of 1.9 ppm, significantly higher than the Caney shale's 0.52 ppm, potentially due to specific minerals or historical anthropogenic influences. This elevated level, especially concerning Pb’s toxicity and its severe effects on cognitive and neurological health, far exceeds the EPA's safety threshold of 0.015 ppm for water. These disparities underscore the critical need for monitoring and addressing pollution sources in shale formations. Figures 3.20 and 3.21 display the comparisons for contamination potential for soil and ground water.

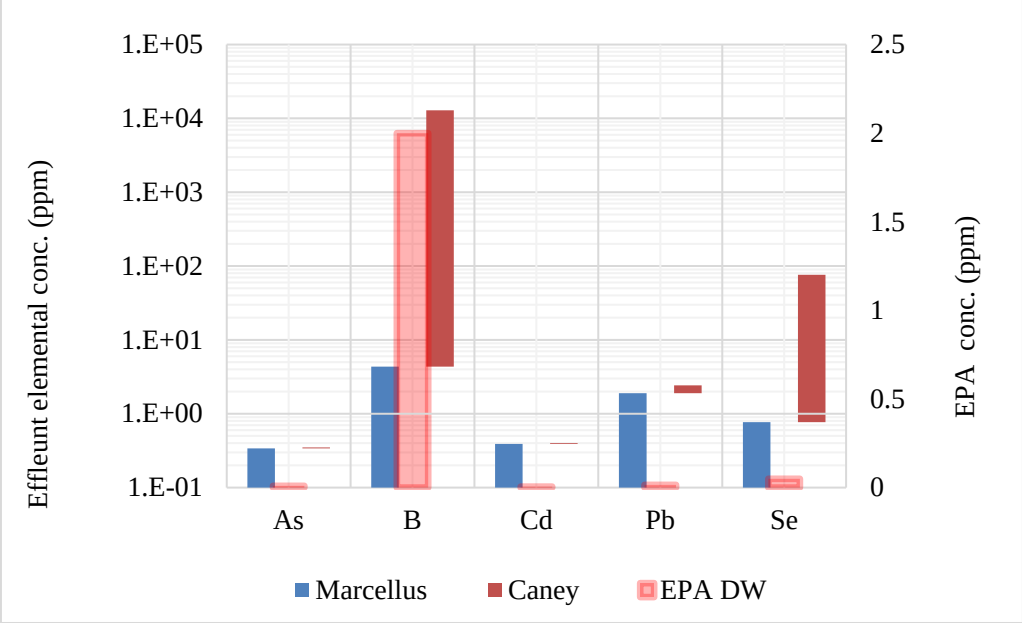

Figure 3.19. Bar chart showing a comparison of effluent concentration in hazardous elements with EPA standards for drinking water (DW)

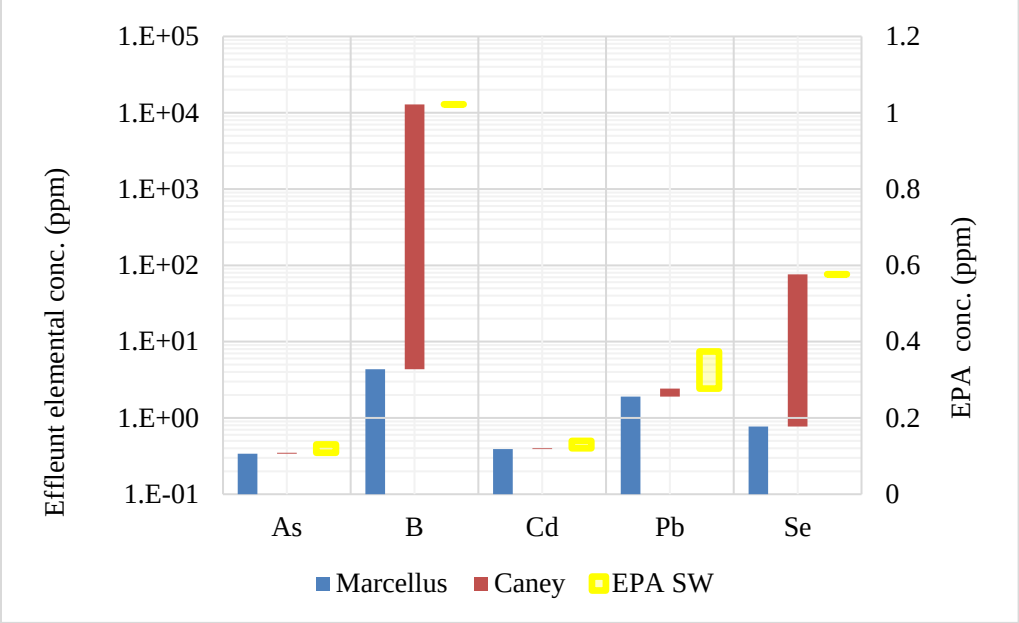

Figure 3.20. Bar chart showing a comparison of effluent concentration in hazardous elements with EPA standards for soil water (SW)

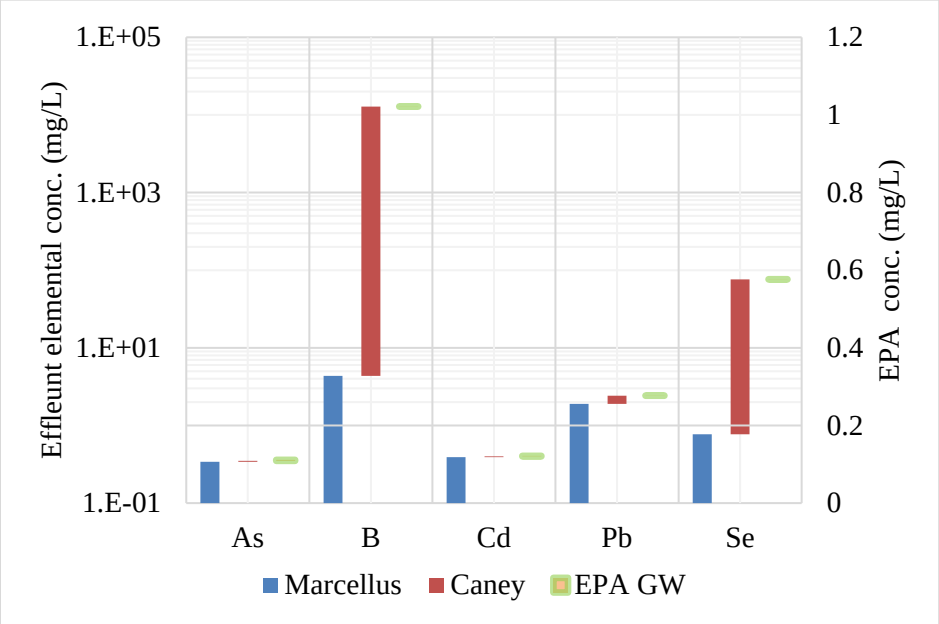

Figure 3.21. Bar chart showing a comparison of effluent concentration in hazardous elements with EPA standards for ground water (GW)

3.3. Interactions Between Rock and Fluids

3.3.1. Introduction

This study investigated the interactions between rock and fluids using geomaterial microfluidics, focusing on the effects of salinity and heat treatment on the stability of illite, and illite-smectite, and shale coatings on borosilicate glass surfaces. Illite and smectite are 2:1 clay mineral with low swelling potential and particularly relevant to unconventional shale formations like the Caney Shale in Oklahoma. The research aimed to understand how different salinity levels in brines influence the adsorption of clay particles onto glass surfaces and how subsequent heat treatment impacts the stability of these coatings. By replicating the pore-scale clay chemistry of shales, the study seeked to better comprehend the interactions between clay, water, and hydrocarbons in such formations. Additionally, it examined how water-based fluids affect clay minerals, including swelling, fines migration, and wettability alteration, which can significantly impact shale producibility by reducing pore space and permeability. Various factors, such as interfacial tension, ion exchange, pH changes, and mineral dissolution, were also explored for their influence on the wetting characteristics of surfaces.

3.3.2. Methodology

Material

Minerals

Illite, mixture of illite (70 wt.%)-smectite (30 wt.%), and shale were utilized to study the rock-fluid interactions. Illite and smectite clay minerals were sourced from the Cambrian Shales of Silver Hill in Jefferson Canyon, Montana, USA. Shale samples were extracted from Caney Formation of Southern Oklahoma. The samples were used to coat glass capillary tubes and resealable flow cells for characterization. Whereas the wettability of the minerals at different rock-fluid systems were

studied by coating thin bottom flow cells with the minerals.

Fluids

Sodium chloride (NaCl) brine solutions with different salinities: 0 ppm (DI Water), 5000 ppm, 10000 ppm, and 30000 ppm were used to prepare mineral slurry for coating. These NaCl brine solutions were prepared by dissolving required amounts of 99% NaCl, sourced from Sigma Aldrich, in DI water. Crude oil, n-decane, and produced water along with brines were used to study rock-fluid interactions. Produced water and crude oil were obtained from the industry partner. The viscosity and density of the fluids were measured and reported in Table 3.5. Viscosity was measured using a Rheosense microVISC, which assesses viscosity via pressure drop through a rectangular channel. Fluid densities were measured with a Mettler Toledo DA-100M density meter, which employs the oscillating body method. Interfacial tensions reported in Table 3.6, were determined using the pendant drop method, with image analysis performed using the ImageJ software's drop analysis plugin.

Table 3.5. Density and viscosity of fluids at 1 atm.

Fluids	**Viscosity at 20° C (cP)**	**Density at 18° C (g/cm^3)**
DI water	1.04	0.994
5,000 ppm brine	1.12	1.001
10,000 ppm brine	1.23	1.004
30,000 ppm brine	1.26	1.018
n-Decane	0.92	0.732
Crude oil	2.25	0.790
Produced water	1.15	1.020

Table 3.6. Interfacial tension of brine-n-Decane systems, and Produced Water-Crude oil system obtained from the industry partner at 1 atm and 20°C.

Non-aqueous Phase	**Aqueous Phase**	**IFT (mN/m)**
n-Decane	DI water	51.18
	5,000 ppm brine	47.51
	10,000 ppm brine	46.27
	30,000 ppm brine	43.81
Crude oil	Produced water	4.90

Solid substrates

Borosilicate glass capillary tubes from DWK Life Sciences were used to develop a coating technique for minerals. Resealable flow cells from Micronit Technologies were employed to study heat treatment's impact on the stability of clay coatings. These flow cells consist of two layers of glass, a top glass slide with an elastomer defining the flow path and a bottom glass slide. Additionally, thin

bottom flow cells from Micronit Technologies were used for wettability and fines migration experiments. The thin bottom flow cells are made of borosilicate glass and feature three distinct channels: A, B, and C with the widths of 0.5 mm, 1.5 mm, and 1 mm respectively. The depth of each channel is 50 µm.

Syringe pumps

A Standard Infuse/Withdraw PHD ULTRA™ Programmable Syringe Pump, acquired from Harvard Apparatus, was used to transport fluids to and from the micromodels and capillary tubes. This pump enables continuous fluid delivery at nanoscale flow rates with the help of glass syringes, also from Harvard Apparatus, and its programmable functionality allows for automated process control.

Tubing and valve

FEP (Fluorinated ethylene propylene) tubing, with an inner diameter of 0.25 mm and an outer diameter of 1.6 mm (1/16"), was used to connect the capillary tube to the pump. PEEK tubing, with an outer diameter of 3.175 mm and an inner diameter of 1.6 mm, connected the syringe pump to the microfluidic chip. Both types of tubing are chemically compatible with the aqueous and organic phase liquids used in the study. Swagelok three-way valves were also utilized in this setup for conducting wettability and fines migration experiments.

Microscope, camera, and light source

In the microfluidic setup, a 50MP 1080P 60FPS 4K camera with a 0.7X-4.5X magnification C-mount lens was used to capture high-resolution images and videos of the untreated and clay- and shale powder-coated glass surfaces during wettability experiments. Illumination was provided by an LED-ring light source, paired with an adjustable optical iris diaphragm (1.5-36 mm). The camera and lens were sourced from Eakins Repair Tools, the light source from Insein Li Fung Store, and the iris from Walley Optics Store on AliExpress.

Experimental procedure

Solution preparation

Mineral slurry prepared with 10 wt.% mineral powder in NaCl brine, was used to coat glass capillary tubes and resealable flow cells. The thin-bottom flow cell was coated with a mineral slurry containing 2 wt.% of mineral powder because of its low pore volume. The effect of brine salinity on mineral adsorption was studied using four different salinities: 0 ppm (DIW), 5000 ppm, 10000 ppm, and 30000 ppm.

Zeta potential measurement

Mineral solution with illite and mixture of illite-smectite showed a stable dispersion whereas shale particles significantly experienced rapid sedimentation in the brines. Hence, zeta potentials of the shale particles were measured dispersing the particles in 30,000 ppm NaCl brine at different pH levels to assess the tendency of sedimentation. The pH was controlled using NaOH and HCl, and the zeta potential measurements were recorded using an optical method, Dynamic Light Scattering (DLS).

Mineral coating

The coating procedure for glass surfaces involved two main methods: physical adsorption and layer-by-layer deposition. The study focused on physical adsorption, where a mineral slurry in NaCl brine solution was used to coat the substrates. To maintain a homogenous particle dispersion, slurries were vigorously stirred for 30 minutes and then ultrasonicated for 1 hour before injection into the micromodels. Figure 3.22 illustrates the experimental setup for coating a resealable flow cell.

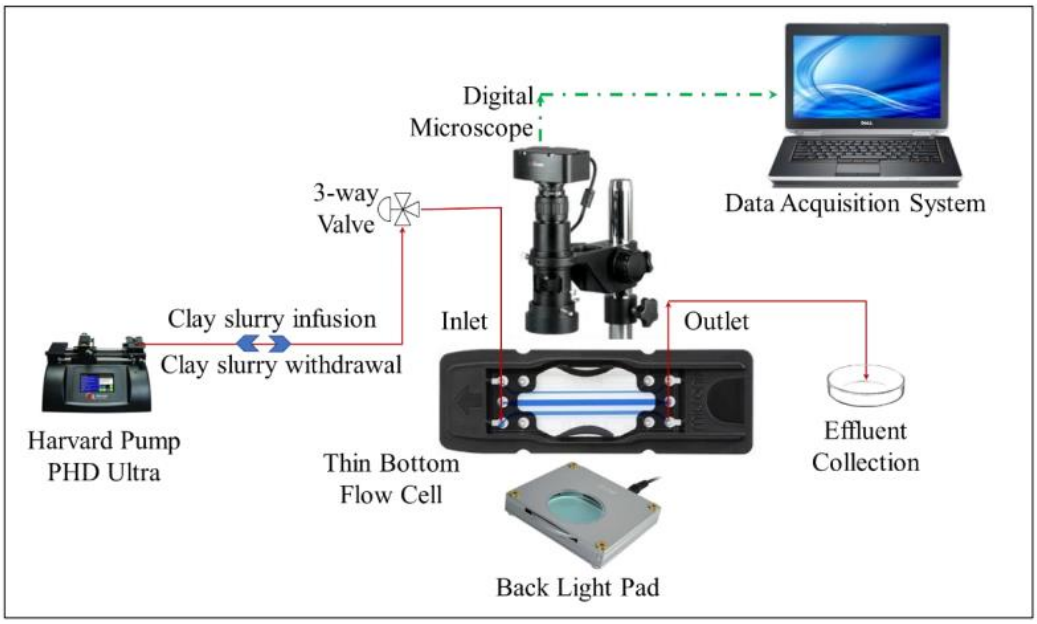

Figure 3.22. Process flow diagram for mineral coating on thin bottom flow cell.

The process included several cycles of slurry infusion-delay-withdrawal, with each cycle consisting of infusion at 26.5 m/h, a 2-minute delay, and withdrawal at 2.65 m/h, using a syringe pump. A vacuum was applied for slurry withdrawal to avoid air channeling. To coat the glass capillary tubes, 100 cycles of slurry infusion-delay-withdrawal were carried out and the mineral solution was ultrasonicated after every ten cycles to keep the particles dispersed. After coating, the tubes were air-dried at 25°C for 1 hour. A similar method was used to coat the resealable and thin-bottom flow cells, but only three cycles of infusion-delay-withdrawal were needed for each. This approach ensured uniform coating while allowing for visibility of flow through the coated surface.

Effect of salinity and heat treatment on coating

To assess how the salinity of the base fluid affects mineral adsorption on glass surfaces, glass capillary tubes and resealable flow cells were coated with the prepared mineral slurries and then air-dried at 25 °C for 1 hour. This study additionally investigated how heat treatment affects the coating's stability of a glass micromodel coated with a 10 wt.% Illite clay slurry in a 30,000 ppm NaCl solution. The micromodel was dried using two methods: air drying at room temperature (25 °C) for 1 hour, and gradual air drying up to 125 °C for 25 minutes. The release of clay particles from the surface could occur due to either coating instability or the clay's sensitivity to the fluid flowing over it. The former depended on how well the clay particles were attached, while the latter was influenced by the salinity and counterion content of the fluid. To distinguish between these causes, it was important to

test the coating's stability by evaluating whether the clay particles detach when exposed to brines with different salinities. A stable coating should resist significant particle release during this test. Fluids with lower salinity might increase particle release, but none should entirely remove the coating if it is stable.

To assess how the coated surface reacts to different fluids, the micromodels were flooded with base brine (30,000 ppm), reduced salinity brine (10,000 ppm), and deionized (DI) water for 6 hours. After each flooding, vacuum suction was used to remove loosely attached particles and brine. The fluid flow rates were kept low maintaining a capillary number of 1×10-6 to ensure that any particle release was due to clay-fluid interaction rather than viscous forces. After the tests, the surfaces were dried in an oven at 100°C for 30 minutes to remove any remaining water.

Characterization and Coating Stability

After oven-drying, the coated capillary tubes were carefully broken into small pieces for microscopic analysis. The coating morphology and elemental composition were examined using SEM and SEM-EDS. Whereas, the resealable flow cells were disassembled and the bottom glass slide, which had a higher coating density due to gravity, was analyzed using optical microscopy, SEM, and SEM-EDS. Additionally, the coating density was estimated using Fiji software, and confocal laser scanning microscopy (CLSM) was used to create 3D images of the mineral coatings after each stability test, revealing how effective the heat treatment was.

Wettability and fines migration experiments

An experimental setup illustrated in figure 3.23 was prepared to study the wetting characteristics of the coated surface in different fluid systems (water/brine-air, water/brine-oil, oil-air). The experiments were conducted on both the untreated and mineral coated channel C of thin bottom flow cells by infusing and withdrawing different fluids. Two scenarios were tested: one where the microfluidic chip was first exposed to water or brine and another where it was first exposed to oil. In both cases, fluids were injected and withdrawn at 50 nl/min maintaining capillary number between 10-7 and 10-5 to measure advancing and receding contact angles. Additionally, the advancing and receding contact angle measurements for each case were phased in two: one is before aging and the subsequent one is after aging with the fluid that was not exposed first. For example, the water was infused in an air-filled chip that denotes the case of chips exposed to water first and withdrawn to measure the water-advancing and receding contact angle respectively in a water-air system. Water or brine was re-infused to fill the channel with water. Following the re-infusion of water, oil was infused and withdrawn to measure the water-receding and advancing contact angles, respectively, in a water-oil system. This phase was considered as before aging wettability experiment. Subsequently, the chips were reinfused with oil having a water column still ahead of it. Ensuring the oil column completely covered the chip, it was aged for about 24 hours to observe the effect on wettability. Oil was withdrawn and reinfused at the same flowrate of 50 nl/min to measure the water-advancing and receding contact angles in a water-oil system after. Thus, the phase was considered as after aging wettability experiment. A similar procedure was followed to conduct the wettability experiments for the chips exposed to oil first. Fines migration was phenomena was visually studied while the fluids were infused and withdrawn.

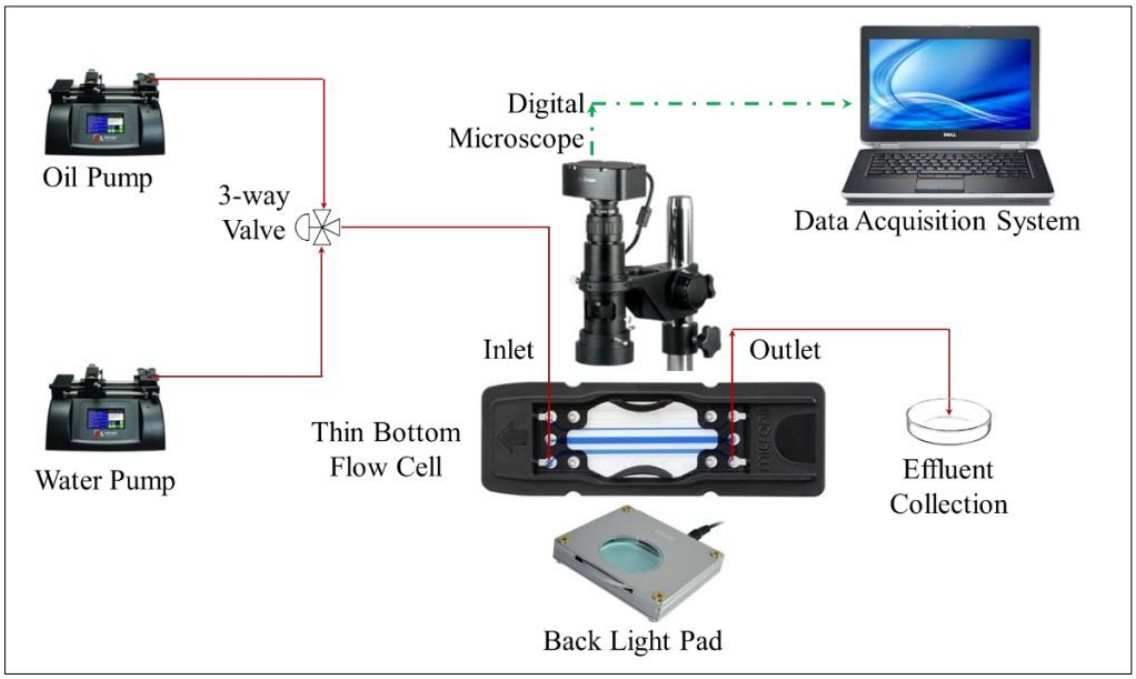

Figure 3.23. Schematic of the experimental facility used for wettability experiments.

Swelling experiments

The swelling potentials of illite and illite-smectite (70:30 by weight) clays were evaluated when exposed to various fluids: produced water, deionized water, 5,000 ppm NaCl, 10,000 ppm NaCl, 30,000 ppm NaCl, n-decane, and crude oil. The clay minerals were taken in borosilicate glass vials having a 15 mm diameter and 45 mm height. After marking the initial height of the clay minerals, different fluids were introduced in the vials and kept letting the clay minerals swell. The differences in height were measured after 27 hours and 44 hours for n-decane and brines respectively. Whereas the data were recorded after 24 hours for produced water and crude oil.

3.3.3. Results and Discussion

Stability of mineral solution

The zeta potential (ZP) of the shale particles either exceeding +30 mV or dropping below -30 mV indicates good colloid stability. The recorded zeta potential values were plotted in figure 3.24 that showed the solutions with pH 5.45 and 8.75 had the ZP values below -30 mV. Additionally, the lower polydispersity index (PDI) values of these two solutions had supported them as better mineral solution for ensuring the uniform size of the mineral particles. But the mineral particles dispersed in 30,000 ppm NaCl brine showed a pH of 5.45 whereas NaOH was added to adjust the pH level of the solution to 8.75. To avoid the addition of foreign chemicals, the solution of pH 5.45 was used as the stable coating solution among these two solutions.

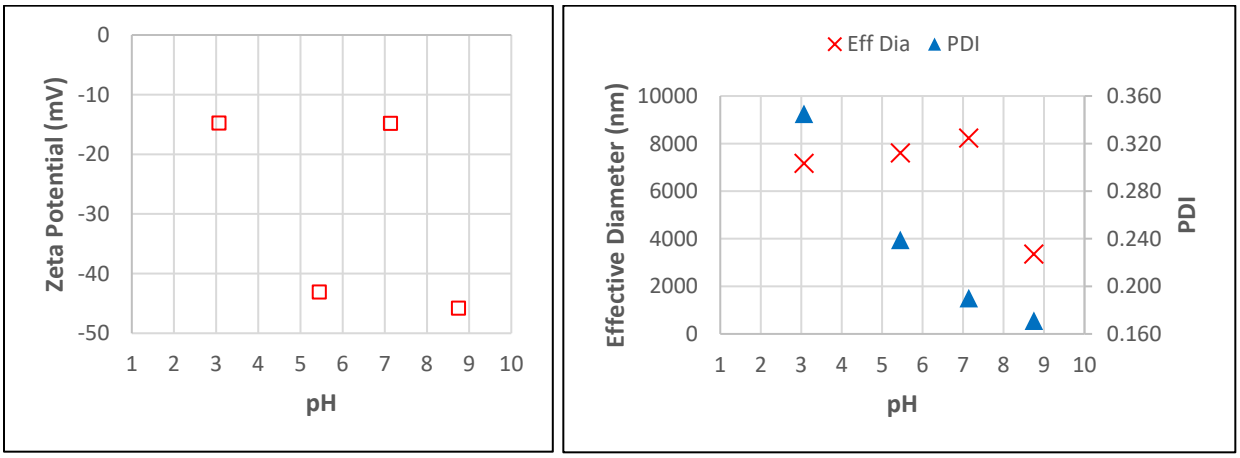

Figure 3.24. Zeta potential, effective diameter and polydispersity index of shale particles in 30,000 ppm brine at different pH levels.

Effect of salinity

Glass capillary tubes were coated with illite clay prepared in NaCl solutions of varying concentrations (0, 5000, 10,000, and 30,000 ppm). Figure 3.25 demonstrated that clay coverage on the glass capillary tube improved as salinity increased, with almost complete coverage at 30,000 ppm.

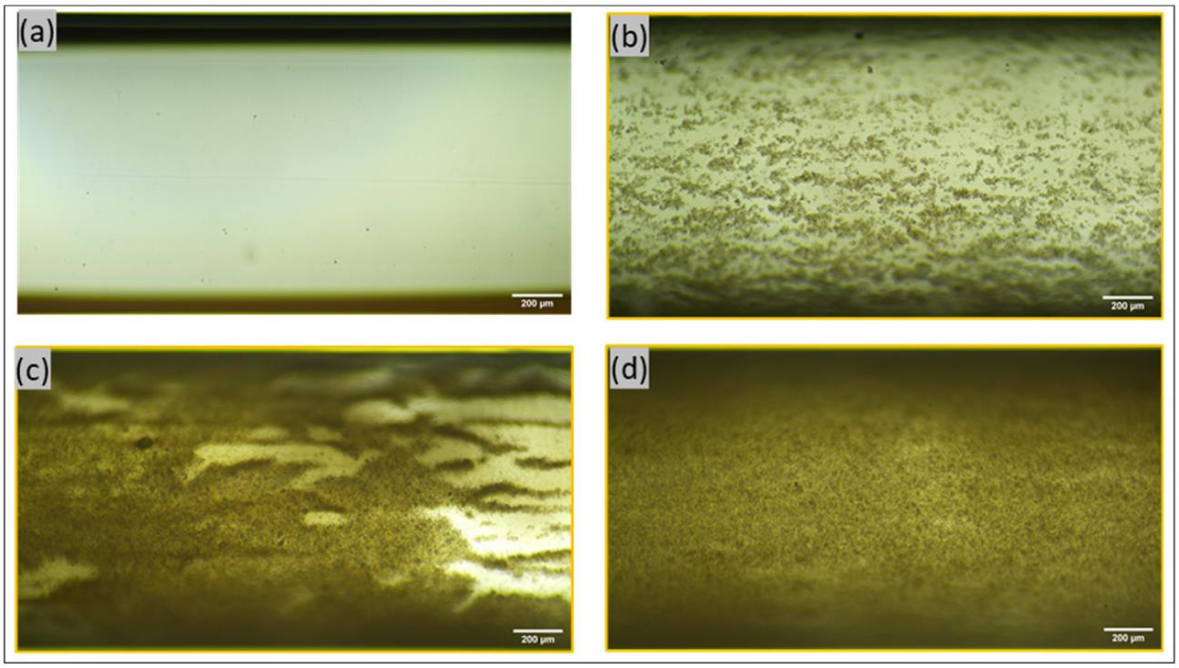

Figure 3.25. Glass capillary tubes coated with 10 wt.% Illite clay slurry prepared with: (a) DI water, (b) 5000 ppm NaCl, (c) 10,000 ppm NaCl, and (d) 30,000 ppm NaCl. Images are taken after drying the coated capillary tubes at 25 °C.

The DLVO theory explains this behavior: higher salinity reduces the electrostatic repulsion between the negatively charged clay particles and the glass surface, allowing van der Waals forces to dominate and enhance clay adsorption. Thus, higher salinity results in better clay coverage on the glass surface.

However, the shale coating on the resealable flow cell resulted in a thick and homogenous layer when the mineral solution was prepared with deionized water (Figure 3.28).

Preparing the mineral coated micromodel

Figure 3.26 showed the process of coating a resealable microfluidic chip with illite clay. The chip was fully saturated with clay slurry, and vacuum suction effectively displaced the slurry, leading to a uniform distribution of clay particles on the glass surface. High magnification images confirmed the even coating of the chip's surface with illite particles. Figure 3.27 shows a coated glass surface of thin bottom cell with illite and shale using a similar approach.

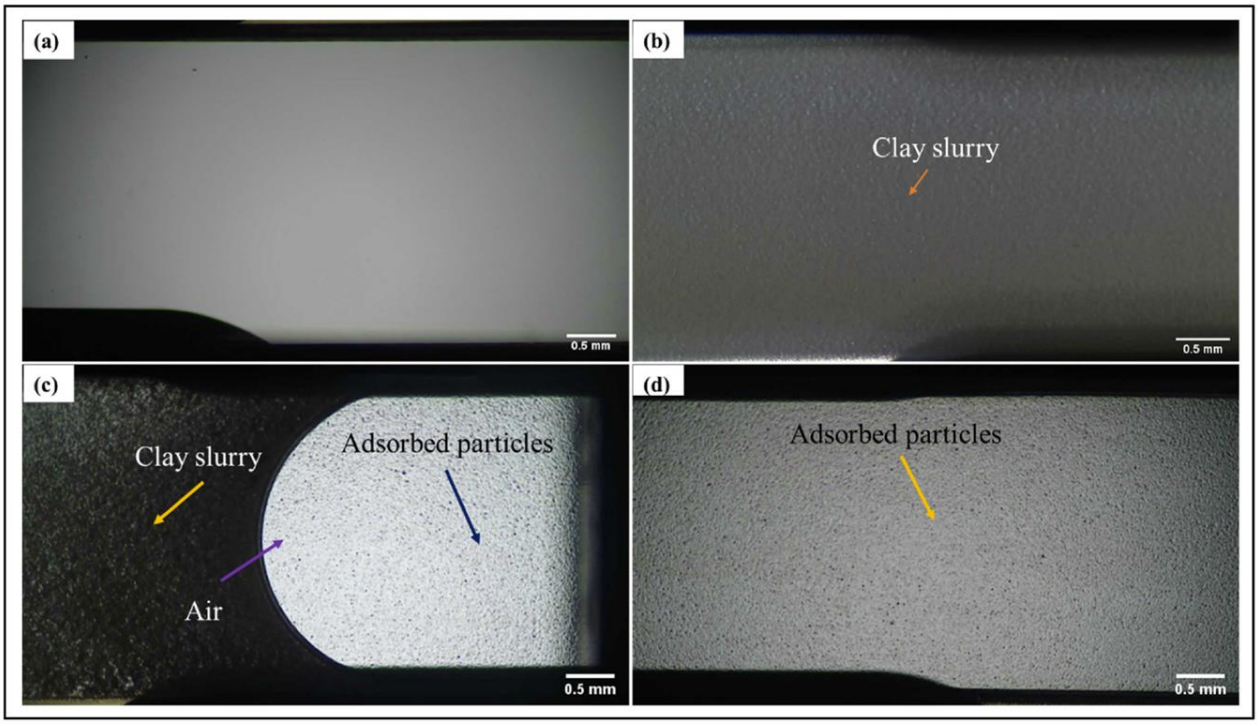

Figure 3.26. Surface of resealable flow cell at different states: (a) uncoated surface, (b) completely saturated with clay slurry after infusion, (c) vacuum suction leading to a uniform displacement of clay slurry, and (d) even distribution of adsorbed clay particles on the glass surface after completing withdrawn of the clay slurry.

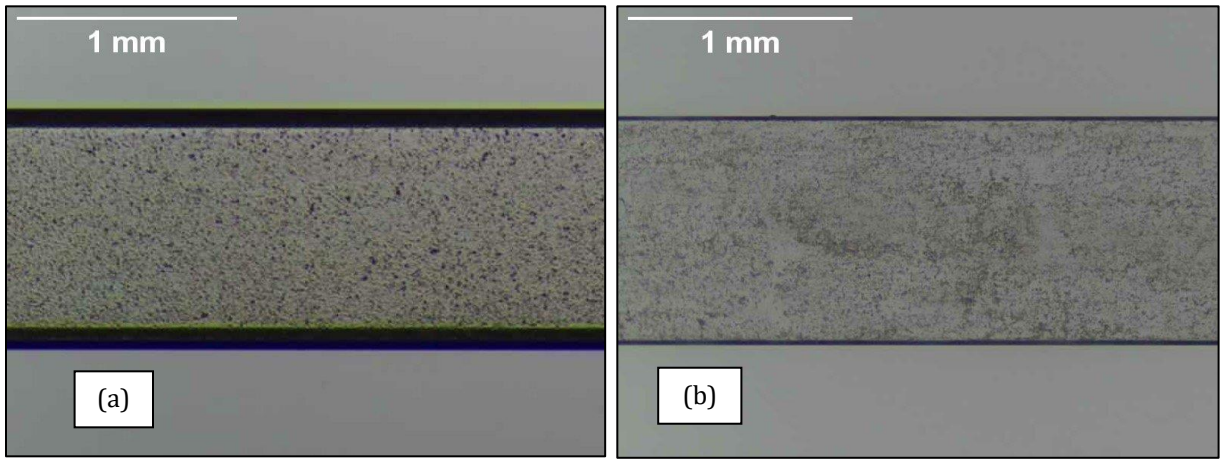

Figure 3.27. Channel-C of thin bottom flow cell coated with (a) illite and (b) shale particles.

Effect of heat treatment on coating stability

The study compared the stability of illite clay coatings on surfaces dried at different temperatures (25°C and 125°C) when exposed to brines of varying salinity and deionized water. Optical microscopy, SEM, and CLSM all reveal that surfaces dried at 125°C retain more clay particles and show greater coating stability than those dried at 25°C. Although both surfaces experience some particle detachment, particularly when exposed to lower salinity brines and deionized water, the 125°C treatment results in a more resilient coating that better withstands fluid flow. A similar test was conducted on shale coated surface of resealable flow cells. But the shale solution was prepared in deionized water and the coated surfaces were dried only at 125° C for 1 hour after completing coating procedure. Figure 3.28 showed SEM images of shale-coated glass surfaces before and after the flooding DI water, 5000 ppm NaCl, and 30000 ppm NaCl. It demonstrated that the coating was stable enough to withstand the capillary flows.

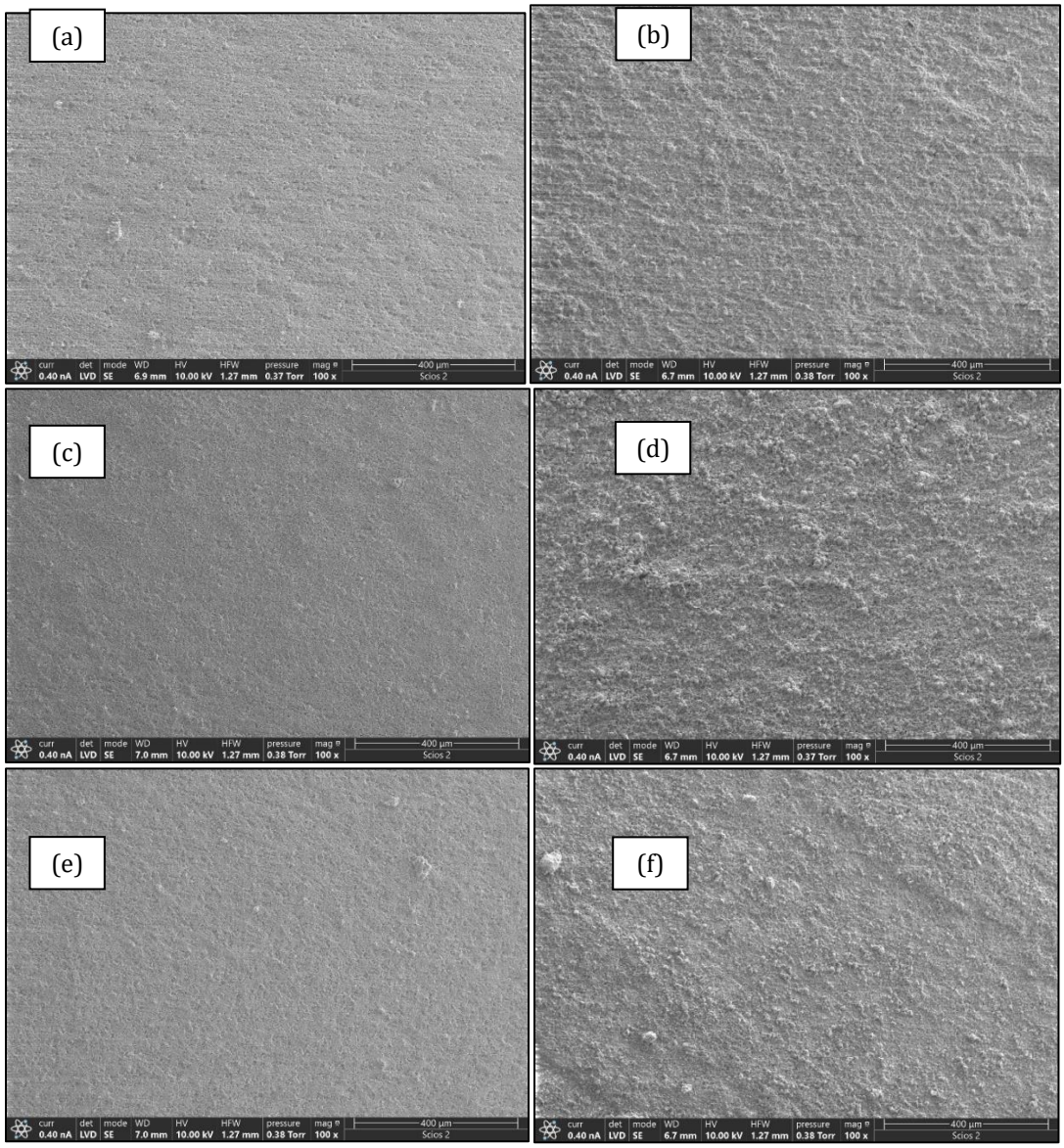

Figure 3.28. SEM images (100x magnification) of shale-coated (prepared in DI water) resealable flow cell (a,c,e) before and after flooding with (b) DI water, (d) 5000 ppm NaCl, and (f) 30000 ppm NaCl.

Measurement of swelling potential

Illite clay showed minimal swelling over a day, while illite-smectite clay swelled immediately upon contact with DI water and brine solutions but exhibited only slight swelling (0.06 mm) in n-Decane. The swelling behavior was more pronounced in aqueous environments compared to non-aqueous ones like n-Decane, highlighting that these clays' swelling is not only mineral composition-dependent but also highly fluid-dependent.

Wettability analysis

The wetting behavior of different fluid systems in the untreated, illite-coated, illite-smectite-coated microfluidic channels, respectively, are reported in tables 3.5, 3.6, and 3.7. The wettability of the microfluidic surfaces depends upon first contact fluid, brine salinity, and aging. In untreated channels, initial wettability with DI water-n-Decane system showed water-wet and oil-wet states, depending on the initial contact fluid, which shifted to intermediate-wet state after aging. Illite-coated channels generally remain strongly water-wet or strongly oil-wet when DI water or n-Decane first contacted the channel, respectively, before aging, but both shifted to oil wet after aging. A significant fines migration was noted when the channel was first contacted by DI water. Illite-smectite coated channels showed similar trends and exhibited fines migration and snap-off phenomena, particularly when brine or DI water are involved. Low salinity (5k ppm) brine injection results in wettability alteration in untreated, illite and illite-smectite coated surfaces. In high salinity environment (30k ppm), wettability of brine-first-contacted illite (Table 3.6) and illite-smectite (Table 3.7) -coated surfaces were different. Significant fines migration was observed in the case of illite-smectite coated surface when it was first contacted by DI water.

Table 3.7. Wettability results of untreated microfluidic channel.

Experiment	Fluid contacting the microfluidic chip first	Wettability			
		Advancing Contact Angle (°)		Receding Contact Angle (°)	
		Before Aging	After Aging	Before Aging	After Aging
DIW/ n-Decane	n-Decane	Oil Wet	Intermediate-Wet	Oil Wet	Water Wet
	DIW	Water Wet	Intermediate-Wet	Water Wet	Water Wet
5k ppm brine/ n-Decane	n-Decane	Oil Wet	Water Wet	Oil Wet	Water Wet
	5k ppm brine	Water Wet	Water Wet	Water Wet	Water Wet
10k ppm brine/ n-Decane	n-Decane	Oil Wet	Oil Wet	Oil Wet	Oil Wet
	10k ppm brine	Water Wet	Water Wet	Water Wet	Water Wet
30k ppm brine/ n-Decane	n-Decane	Oil Wet	Oil Wet	Oil Wet	Oil Wet
	30k ppm brine	Oil Wet	Oil Wet	Oil Wet	Oil Wet
Produced water/ Crude oil	Crude oil	Oil Wet	Oil Wet	Oil Wet	Oil Wet
	Produced water	Intermediat-Wet	Oil Wet	Water Wet	Water Wet

Table 3.8. Wettability results of Illite clay-coated microfluidic channel.

Experiment	Fluid contacting the microfluidic chip first	Wettability			
		Advancing Contact Angle (°)		Receding Contact Angle (°)	
		Before Aging	After Aging	Before Aging	After Aging
DIW/ n-Decane	n-Decane	Oil Wet	Oil Wet	Oil Wet	Oil Wet
	DIW	Water Wet	Oil Wet	Water Wet	Oil Wet
5k ppm brine/ n-Decane	n-Decane	Oil Wet	Water Wet	Oil Wet	Water Wet
	5k ppm brine	Water Wet	Water Wet	Water Wet	Water Wet
10k ppm brine/ n-Decane	n-Decane	Oil Wet	Oil Wet	Oil Wet	Oil Wet
	10k ppm brine	Water Wet	Water Wet	Water Wet	Water Wet
30k ppm brine/ n-Decane	n-Decane	Oil Wet	Oil Wet	Oil Wet	Oil Wet
	30k ppm brine	Oil Wet	Oil Wet	Oil Wet	Oil Wet
Produced water/ Crude oil	Crude oil	Oil Wet	Oil Wet	Oil Wet	Oil Wet
	Produced water	Water Wet	Water Wet	Water Wet	Water Wet

Table 3.9. Wettability results of Illite-smectite clay-coated microfluidic channel.

Experiment	Fluid contacting the microfluidic chip first	Wettability			
		Advancing Contact Angle (°)		Receding Contact Angle (°)	
		Before Aging	After Aging	Before Aging	After Aging
DIW/ n-Decane	n-Decane	Oil Wet	Oil Wet	Oil Wet	Oil Wet
	DIW	Water Wet	Oil Wet	Water Wet	Oil Wet
5k ppm brine/ n-Decane	n-Decane	Oil Wet	Water Wet	Oil Wet	Water Wet
	5k ppm brine	Water Wet	Water Wet	Water Wet	Water Wet
10k ppm brine/ n-Decan	n-Decane	Oil Wet	Oil Wet	Oil Wet	Oil Wet
	10k ppm brine	Water Wet	Water Wet	Water Wet	Water Wet
30k ppm brine/ n-Decane	n-Decane	Oil Wet	Oil Wet	Oil Wet	Oil Wet
	30k ppm brine	Water Wet	Water Wet	Water Wet	Water Wet
Produced water/ Crude oil	Crude oil	Oil Wet	Intermediate-Wet	Water Wet	Water Wet
	Produced water	Water Wet	Water Wet	Water Wet	Water Wet

3.3.4. Conclusion

This study successfully demonstrated that higher salinity levels in NaCl brines significantly enhance the adsorption of illite and illite-smectite clay particles onto borosilicate glass surfaces, resulting in more uniform and dense coatings. However, the shale particles got uniformly coated on the glass surface when the solution was prepared in deionized water. Heat treatment, particularly at 125°C, further improved the stability of these coatings, though lower salinity fluids still caused some particle detachment. The research provided valuable insights into the behavior of clay formations, including swelling potential, fines migration, and wettability alteration when exposed to model fluids like NaCl brine and n-Decane, as well as field fluids such as produced water and crude oil. Notably, low salinity brine injection altered wettability across untreated, illite, and illite-smectite coated surfaces, with significant fines migration observed in illite-smectite coatings. Wettability analysis of Caney Shale

core samples from reservoir zones indicated a predominantly water-wet to intermediate-wet state. These findings underscore the importance of controlling salinity and applying appropriate heat treatment to create stable clay-coated geomaterial surfaces that mimic natural shale conditions, aiding in the optimization of hydrocarbon recovery processes. Future research should focus on developing more complex microfluidic models with intricate flow networks and conducting experiments under high-pressure, high-temperature conditions to better replicate reservoir environments.

4. Coupled Processes Modeling of Caney Shale

This section presents the final report related to Task 7 and Task 13 of the project Field Evaluation of the Caney Shale as an Emerging Unconventional Play, Southern Oklahoma. Tasks 7 and 13 are related to coupled multiphase fluid flow and geomechanical modeling of the Caney shale. The objectives are aligned with the project as a whole to increase the understanding of current problems of low and declining production in shale plays with high clay-mineral content, and to investigate novel methods for improved and more sustainable production. In Task 13, during Phase II of the project, the coupled multiphase fluid flow and geomechanical model developed and demonstrated under Task 7 in Phase I of the project has been applied for more site-specific modeling of the Caney Shale Field Laboratory horizontal well. We have included data and information from the Phase I laboratory and site investigations. Further, improved constitutive model have been developed as a result of the detailed core-studies and flow through experiments performed at the University of Pittsburgh and Oklahoma State University.

4.1. Approach

The numerical modeling is performed considering advanced multiphase fluid flow equation-of-state (EOS) with plastic and visco-elastic (creep) constitutive models as required for ductile shales of high clay content. It is accomplished through TOUGH-FLAC (Rutqvist, 2011), which is a coupled processes modeling framework, based on linking LBNL's TOUGH-family codes (Pruess et al., 2012) to the FLAC3D geomechanics code (Itasca, 2011). For simulations of different aspect as presented in the report, TOUGH-FLAC have been applied for coupled multiphase fluid flow and geomechanical analysis or conducted as fluid flow only using TOUGH or as mechanics only using FLAC3D without considering the coupling between the two simulators. Tasks 7 and 13 were originally focused on multiphase fluid flow and geomechanics, whereas geochemistry modeling was added to the work scope. In that case the TOUGHREACT simulator (Xu et al., 2014a, 2014b) is used for the modeling of reactive chemistry. Task 7 and 13 involved modeling at different scales, including single proppant scale, drill core scale, and well or reservoir scale (Figure 4.1).

4.2. Modeling of OSU Phase II API experiments

Modeling of the API experiments on proppant-filled Caney fractures was conducted. This include modeling of both observed proppant embedment and stress dependent hydraulic conductivity of the proppant filled fractures. The modeling performed here was also presented in collaborative papers between OSU and LBNL was published at US Rock Mechanics Symposium held in Santa Fe in June 2022 (Katende et al., 2022) as well as in Journal publication (Katende et al., 2023a)

4.2.1. Proppant embedment modeling of the OSU API experiments

The surface profiles of shale platens in the API experiments were evaluated by OSU. A profile over some proppant embedment pits was extracted by the OSU team. LBNL performed model simulations of proppant embedment considering elasto-plastic properties for the unit denoted Ductile 2. Those properties were evaluated previously based on triaxial tests at University of Pittsburgh and also validated by modeling micro-indentation tests from OSU. Figure 4.2 shows simulation results of indentation profiles that matches indentation profiles for a 250 and 350μm proppant size. The

maximum stress applied in the API test was 12,000 Psi (83 MPa) and this would lead to proppant forces close to these numbers (20 and 32 N) for relatively packed proppants. The embedment depth is about 60 to 70 μm.

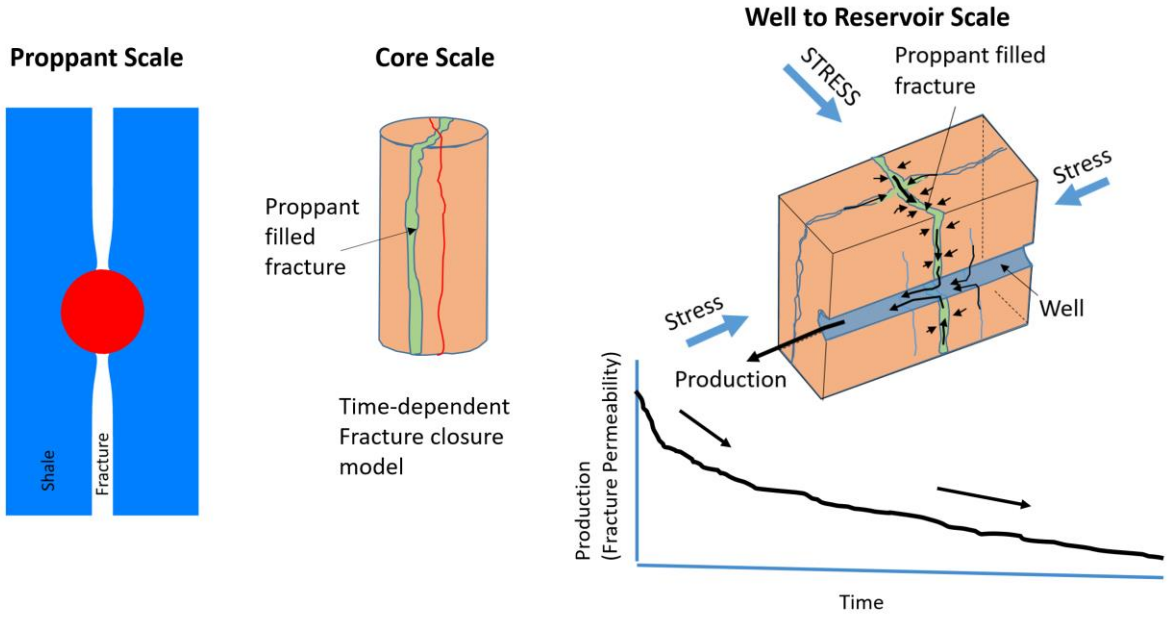

Figure 4.1. Different scales of coupled processes modeling.

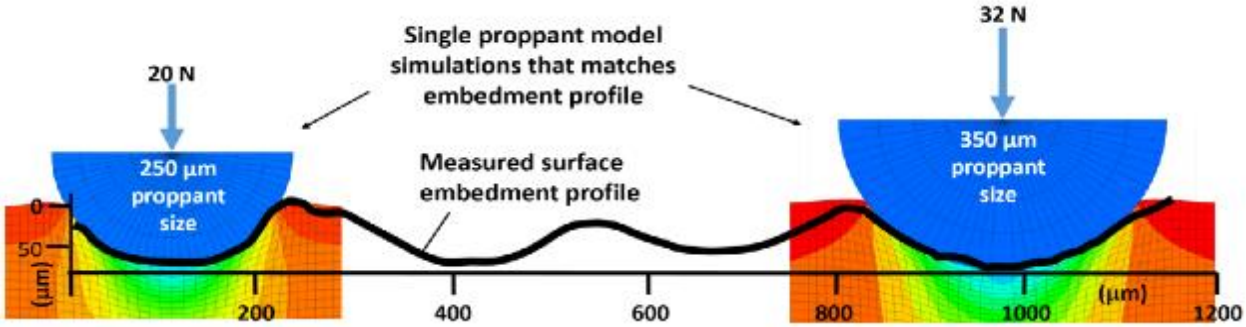

Figure 4.2. Model simulation results of proppant embedment that matches the measured surface profile of Ductile 2 sample after API test (Katende et al., 2023a). The color scale represents vertical displacement.

4.2.2. Fracture conductivity modeling of the OSU API experiments

The modeling of stress-dependent fracture conductivity of the API tests is done using a continuum model of the proppant-pack in-between the two shale platens of each experiment. Fracture conductivity is here defined as the permeability times the fracture width and the oil-field unit for such fracture conductivity is mD-ft (milliDarcy-foot). The experimental results of the API tests show that the increased stress up to the maximum of 12,000 psi (83 MPa) causes a mechanical compaction of the proppant pack (sand layer) and a significant fracture conductivity reduction. Both the proppant-pack compaction and permeability reduction are highly irreversible meaning that there is no significant rebound when stress is subsequently reduced.

For the modeling of the compaction of the proppant pack (unconsolidated sand layer) we applied the Cam-Clay constitutive model from soil mechanics; the model is applied in this case because it can

handle plastic pore-collapse as a result of high compaction stress.

Figure 4.3 shows experimental and modeling results of mechanical compaction and fracture width as a function of applied stress for a set of best fit model parameters. The four different experiments show similar behavior and similar amount of compaction followed by a small rebound. This irreversible compaction is supposedly a result of grain rearrangement and grain crushing that obviously has taken place based on the experimentally determined pre and post proppant size distributions. The permeability, k, of a proppant pack at the initial stabilized state under a compressive stress 1,000 to 2,000 psi may be estimated according to the Kozeny-Carman equation considering the median particle size, dm, and porosity, ϕ. This equation was then applied to evaluate the proppant pack permeability and resulting fracture conductivity. However, a correction had to be applied based on calculated plastic strain to consider the effect of grain rearrangements and particle crushing. In the experiments, the compaction accompanied by significant grain crushing that results in small sized debris that could seal bigger pores between the larger scale grains. The results in Figure 4-3b where agreement between model and experiment is encouraging, showing this as a plausible approach for modeling stress-dependent fracture conductivity of proppant-filled fractures. More research and dedicated experiments would be needed to further develop and validate such a model.

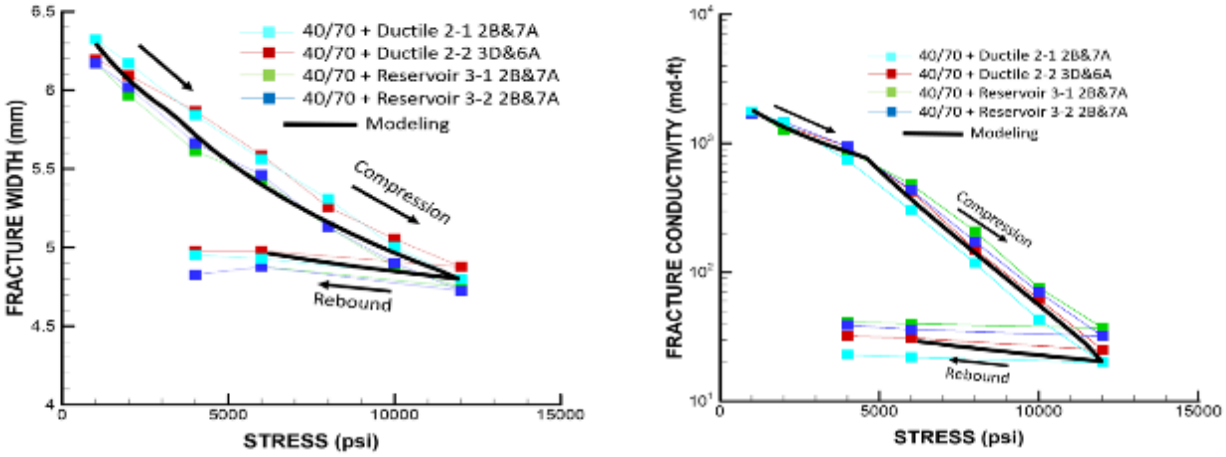

Figure 4.3. Experimental and modeling results of (a) width and (b) fracture conductivity of proppant-filled fracture as a function of applied stress (Katende et al., 2023a).

4.3. Modeling of OSU Phase II Propped Fracture Flow Experiments

The modeling of the flow-through experiments was conducted with the aim of a better understanding of the mechanisms of fracture conductivity reduction and the role of proppant embedment. Moreover, the modeling provides information on fracture conductivity changes with confining stress for the production modeling. Modeling was first performed at the proppant scale to analyze the embedment depth as observed from surface profilometry. Thereafter modeling of the fracture conductivity tests were conducted to analyze the stress-dependent conductivity of proppant-filled fractures.

Figure 4.4 shows a close up of the profiles across of two locations of with proppant embedment of respectively 80 and 30 µm. Shown also for modeling results that matches the embedment profiles at the two locations. In the case of 80 µm, the embedment profiles match the shape of a spherical

proppant 400 µm in diameter and the force required for such embedment is 45N. In the case of 30 µm, the profile matches a spherical proppant 300 µm in diameter and the force required is 14N. Based on the confining stress applied on the sample, i.e. 4000 Psi, corresponding to 27 MPa, the proppant force could be estimated based on an average proppant spacing. These larger diameter intact grains may be significant in keeping the fracture open for fluid flow to permeate through the fracture at the high load of 4000 Psi.

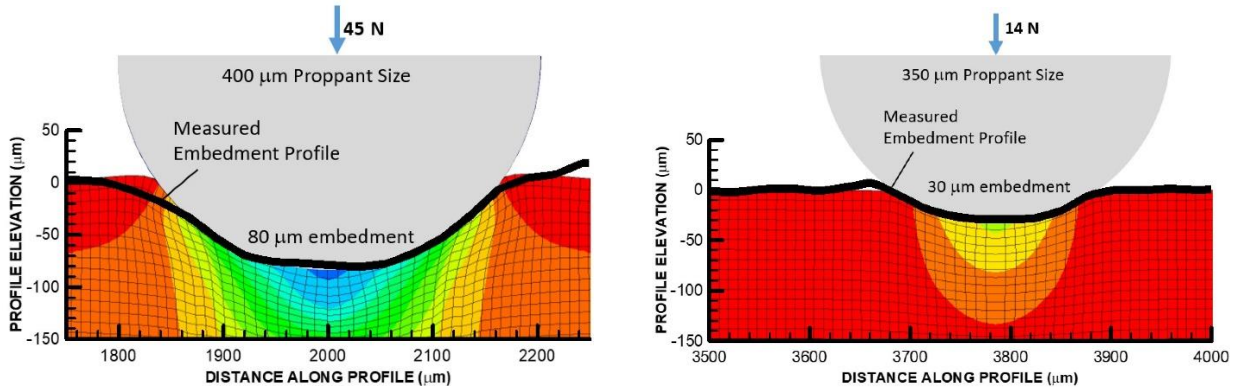

(a) **(b)**

Figure 4.4. Model simulation results of proppant embedment in a Ductile 2 sample that matches the measured surface profile. The y-axis shows the depth along the profile and the x-axis is the distance along the profiles. (a) 80 µm embedment modeled with 400 µm proppant size and 45 N load, and (b) 30 µm embedment modeled with 350 µm proppant size and 14 N load (Katende et al., 2023b).

The modeling of stress-dependent fracture conductivity of the flow-through experiment was done through the consideration of fluid flow through a rough fracture considering couplings between mechanical fracture closure and fluid flow through a hydraulic conducting aperture. Fluid flow along fractures is known to be very sensitive to changes in fracture aperture through a cubic relation between aperture and fluid flow rate. A hydraulic conducting aperture bh can be defined from fracture transmissivity T through the so-called cubic law (Witherspoon et al., 1980) as

$$b_h = \left(\frac{T12\mu_f}{\rho_f g}\right)^{\frac{1}{3}} \tag{4.1}$$

where µf and ρf are dynamic viscosity and density of the fluid, and g is the gravitational acceleration. The hydraulic aperture is coupled to the mechanical aperture according to:

$$b_h = f \cdot b_m \tag{4.2}$$

where bhr is the residual hydraulic aperture when the fracture is mechanically closed at a very high closure stress across the fracture and f is a factor that compensates for the deviation of flow in a natural rough fracture from the ideal case of parallel-plate-type fracture surfaces (Witherspoon et ., 1980). In this case, the factor f would be impacted by the proppants within the fracture that causes additional tortuosity of the flow paths through the proppant-filled fracture.

The fracture conductivity in the unit of mD-ft corresponds to a permeability thickness kh in the unit of m^3 with unit conversion according to 1 mD-ft = 3.048×10-16 m^3 = kh. Moreover, the permeability thickness can be related to fracture transmissivity as

$$T = \frac{kh\rho_f g}{\mu_f} \tag{4.3}$$

Inserting Equation (4.3) into Equation (4.1) leads to

$$b_h = (kh12)^{\frac{1}{3}} \quad (4.4)$$

Using this formula, we can estimate the hydraulic conducting aperture from fracture conductivity results. Figure 4-5 shows that matched fracture conductivity as a function of stress. At near zero confining stress, the fracture conductivity of 700 mD-ft corresponds to a permeability thickness kh = 700 x 3.048×10^{-16} m^3, which correspond to a hydraulic conducting aperture b_h = 137 µm. The exact mechanical aperture b_m is not known, but may be estimated considering the proppant size distribution. Considering the two fracture surfaces held up by such proppants we may estimate the initial mechanical aperture to $b_m \approx 350$ µm. This would in turn indicate that the parameter f ≈ 0.4. Considering the modeled proppant embedment for a 350µm diameter proppants spaced 1.4 mm, along with an initial fracture aperture of b_m = 350µm and f = 0.4, the modeled fracture conductivity versus stress follows experimental values reasonably well (Figure 4.5). Such a model on how fracture conductivity decreases with confining stress can be applied in models of hydrocarbon production to consider impact of fracture closure on production.

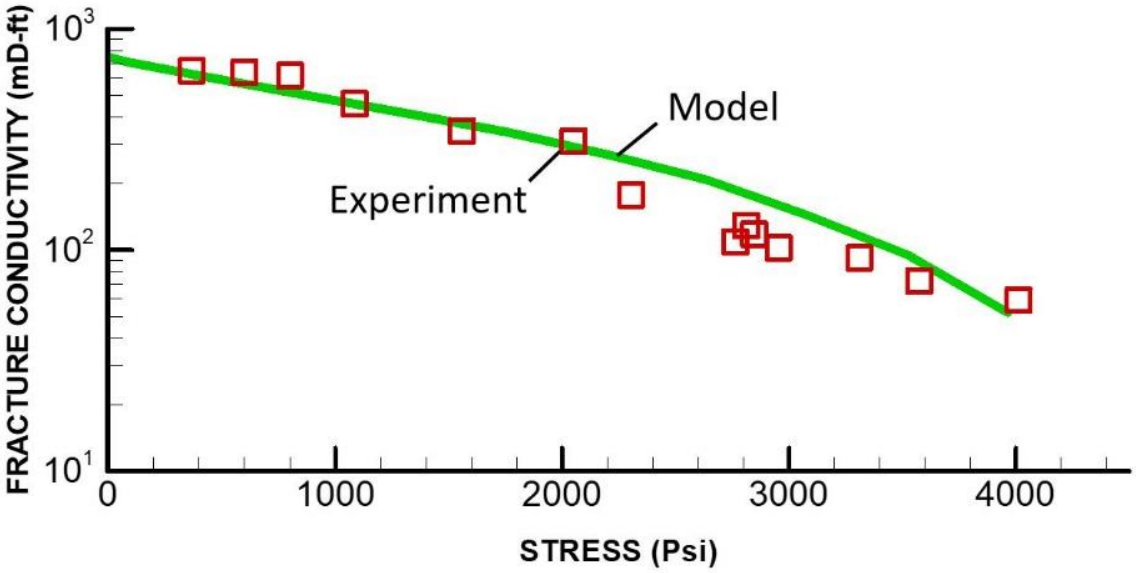

Figure 4.5. Modeled fracture conductivity versus stress with comparison to OSU flow through fracture experimental results (Katende et al., 2023b).

4.3.1. Proppant creep embedment modeling

Proppant creep embedment modeling is conducted using creep laboratory data from University of Pittsburgh. The proppant modeling was updated by considered proppant diameters of 0.15 mm (150 µm) and 0.3 mm (300 µm) to represent commonly used proppant mesh sizes for production from shale gas reservoirs. The 0.15 mm proppant diameter corresponds to a 100 mesh size proppants, whereas the 0.3 mm corresponds to an approximate average diameter for 40/70 mesh size proppants. The results shown in Figures 4.6 and 4.7 are shown for an idealized case of 0.15 mm (150 µm) diameter proppant located at a center-to-center distance of 0.3 mm in a monolayer of proppant. For the fracture closure stress of 10,000 psi (72 MPa), the average load on a proppant agent is estimated at 5.4 N for an extreme case of complete pressure depletion due to fluid production. Figure 4-6 shows

the evolution of proppant embedment, including the initial elasto-plastic embedment followed by time-dependent creep embedment during five years of constant proppant load. The model simulations show the amount of elastoplastic creep embedment is much larger for Ductile 1 properties. Moreover, creep embedment is very different for the nominally ductile and nominally brittle formation properties. Thus, we may conclude creep embedment is negligible in the case of the reservoir zone, whereas creep is significant in the case of the ductile zone. This confirms a correlation between the clay content of a formation and its susceptibility for creep fracture closure. For the particular case studied, assuming 0.15 mm diameter proppant spaced 0.3 mm apart, the fracture would still be held open after five years even for the high-clay-content formation. The aperture at the mid distance between neighboring proppants after five years of creep is calculated as 0.125 mm for Reservoir 2 properties (Figure 4.7a), and 0.05 mm for Ductile 1 properties (Figure 4.7b). If flow through the fracture is proportional to the cube of the aperture, then the reduction in conductivity of Ductile 1 would be around 16 times greater than Reservoir 2.

We have performed additional sensitivity studies considering different proppant distances and two different proppant diameters. The results of different proppant spacing shows that proppant embedment depends strongly on the proppant spacing because the load taken by each proppant will increase with proppant spacing (Figure 4.6). For example, if the proppant spacing increases just from 0.3 mm to 0.4 mm, the proppant load would almost double from 5.4 to 9.6N and the fracture would close completely after 2.4 years (Figure 4.6). If on the other hand, proppants are placed in perfect arrangement next to each other (i.e. distance 0.15 mm for 0.15 mm diameter proppants), the force taken by a proppant would be 1.4 N and the proppant embedment would be quite limited. However, then the cross sectional area open to flow through the propped fracture would be quite small resulting in a relatively low fracture permeability. In the case of larger diameter (0.3 mm) proppants, the fracture aperture would be larger and can stay open longer for a given proppant distance.

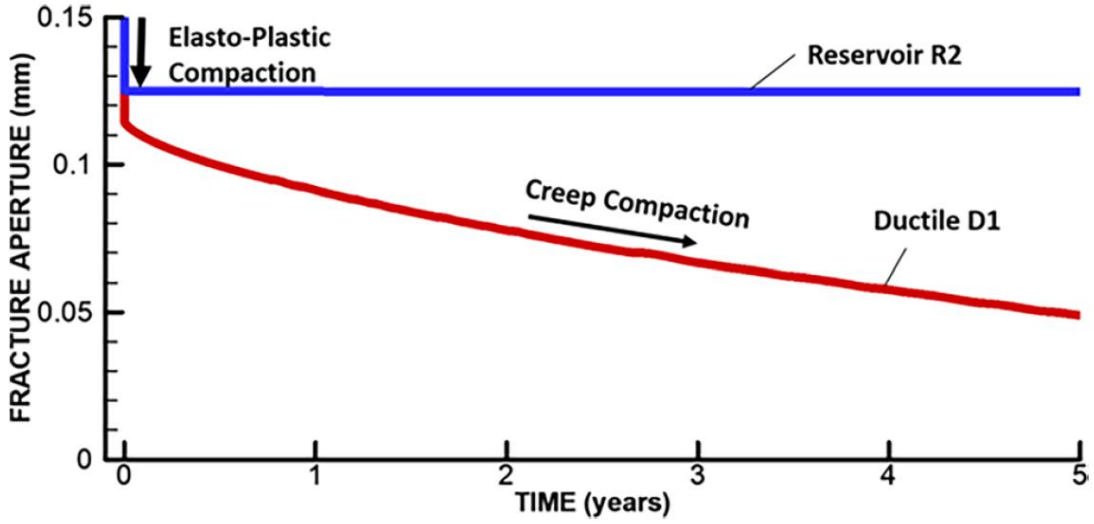

Figure 4.6. Simulation results of elasto-plastic and creep compaction with calculated fracture aperture evolution as a results of proppant embedment for Reservoir 2 and Ductile 1 properties (Benge et al., 2023).

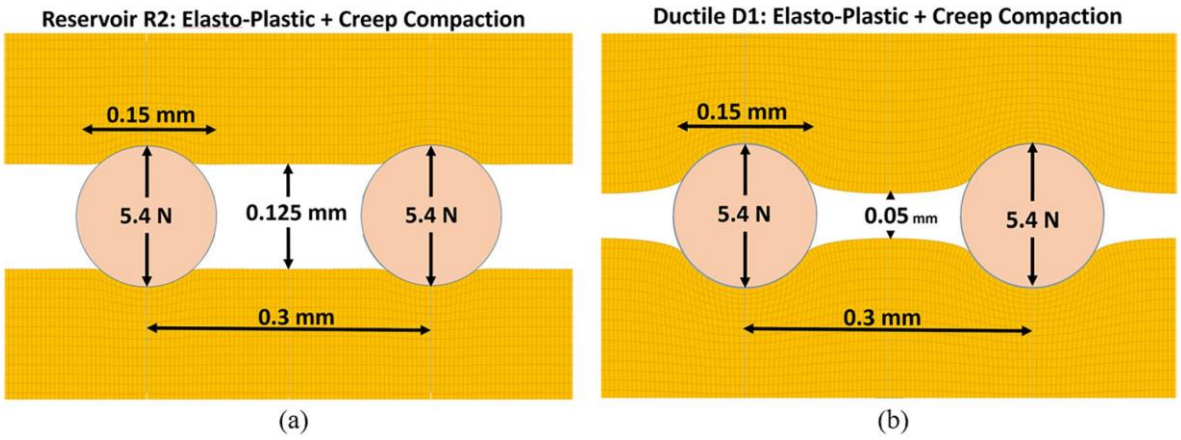

Figure 4.7. Simulation results of proppant embedment after elasto-plastic and five years of creep compaction for (a) Reservoir 2 properties and (b) Ductile 1 properties (Benge et al., 2023).

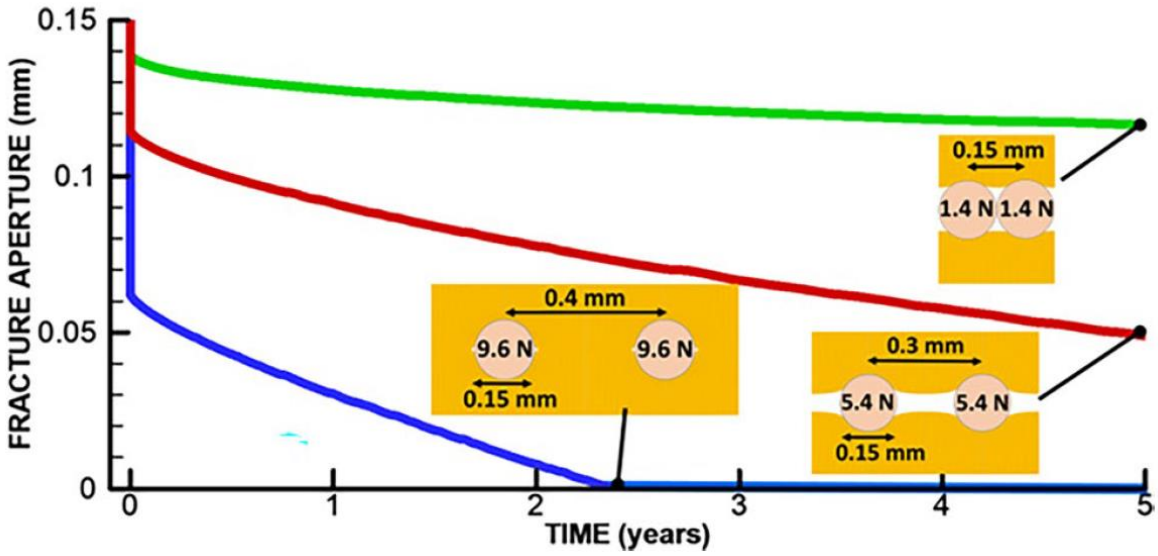

Figure 4.8. Fracture opening width for Ductile 1 formation and 0.15 mm diameter proppant, plotted as a function of time with diagrams of final fracture geometry after 5 years of simulated time (Benge et al., 2023).

4.4. Hydrocarbon Production Modeling

Production modeling of a generic site based on the Caney Shale includes two parts, (1) application of a semi-analytical solution to a simplified version of the problem, and (2) development and application of a numerical model, which enables more realism to be employed, including brittle and ductile layers in the reservoir, and fracture permeability reduction due to creep compaction. The basic conceptual model represents one hydrofracture stage: a horizontal well intercepting a single planar vertical fracture (the primary fracture), which is surrounded by a stimulated reservoir volume (SRV) consisting of a network of secondary fractures (Figure 4.9). Beyond the SRV, permeability is assumed to be negligible.

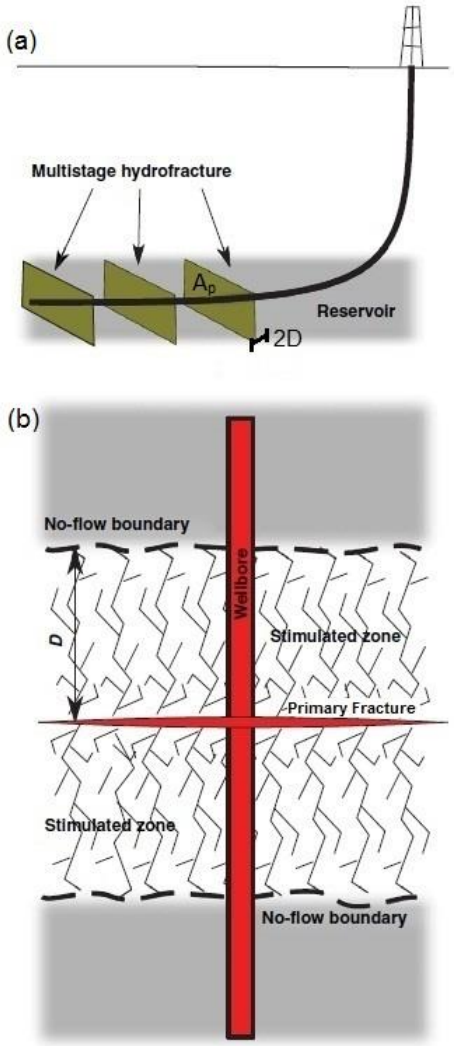

Figure 4.9. (a) Schematic of the generic production modeling problem. (b) One stage of the hydrofracture is modeled, shown as a plan view centered on the primary fracture.

4.4.1. Semi-analytical solution for production decline

In previous work, we developed a semi-analytical solution for a bimodal production decline curve for hydraulically fractured shale-gas reservoirs and implemented it in an Excel spreadsheet (Doughty and Moridis, 2018). The key feature is that the early-time portion of the production decline curve, which has slope -½ in the traditional analysis, has slope –n, where n is determined by curve fitting to field data. The parameter n can be related to the flow dimension of the fracture network within the Stimulated Reservoir Volume (SRV) created by hydraulic fracturing. Fracture network geometry can vary greatly, in particular between ductile and brittle layers, with corresponding large variation in flow dimension. The late-time portion of the production decline curve is exponential. An important parameter of the solution is the transition time between early-time and late-time behavior, denoted t*, which is when the extent of the SRV is felt.

In the present work we made several improvements to the semi-analytical solution. First, we simplified the solution by eliminating a flow-dimension dependence of the transition time t*.

Previously, comparison of the semi-analytical solution to numerical simulation results made it look like t* became later as flow dimension increased, but this is counter to basic physics and was determined to be an artifact of the smaller slope of the early-time decline curve as flow dimension increases, which makes it harder to identify the transition time. Keeping t* independent of flow dimension removes a fitting parameter, simplifying use of the semi-analytical solution. Second, using a numerical model, we investigated the transition from initial-time behavior (constant flow rate), which reflects flow through the primary fracture, and early-time behavior (linear flow rate decline on a log-log plot), which depends on flow through the SRV. We found that this transition time, denoted t1, is well described by the diffusion time for flow across the primary fracture. Prescribing t1 as a function of primary fracture width enables it to be eliminated as a fitting parameter, again simplifying use of the semi-analytical solution.

We also investigated applying the semi-analytical solution in two new ways. First, with a focus on adsorbed gas, which is expected to be important for the Caney Shale and Fayetteville Shales because Kerogen content is significant. Second, we applied the semi-analytical solution at the laboratory experiment scale as opposed to the field scale for which it was designed. Because laboratory experiments attempt to replicate field conditions as much as possible (e.g., pressure, temperature conditions, choice of fluids), it appears that simple changes in scale of thickness and area of the SRV and the thickness of primary fracture will enable the semi-analytical solution to be used to analyze laboratory experiments, as long as gas is the only flowing phase.

Applying the semi-analytical solution for production rate to Caney conditions is a useful first step for developing a numerical model. It requires that permeability is unchanging in time, and that the SRV has spatially uniform properties, two restrictions that will be removed for numerical modeling. Using the properties shown in Table 4.1, and assuming the primary fracture plane also has spatially uniform permeability and that the secondary fracture network is well connected, produces the production decline curve labeled 'base case' shown in Figure 4.10. This case represents one-dimensional flow through the SRV to the primary fracture. The linear portion of the curve shows the response before the far edge of the SRV is felt and has a characteristic slope of -1/2 on the log-log production rate plot. Once the pressure pulse reaches the far edge of the SRV, the production rate declines more rapidly. The bimodal solution enables two alternative scenarios to be examined. If the primary fracture plane has non-uniform permeability, with limited high-permeability channels surrounded by tighter zones, then flow from the SRV to the primary fracture would have a converging nature and produce a production curve like the one labeled 'non-uniform primary fracture' in Figure 4-10. The production rate starts out lower than the base case, since not all the primary fracture is being utilized, but the slope of the linear portion of the curve is shallower than the base case, showing a slower decline rate. Conversely, if the primary fracture plane has uniform, high permeability, but the secondary fracture network in the SRV is sparsely connected, then flow from the SRV to the primary fracture would have a diverging nature and produce a production curve like the one labeled 'sparsely fractured SRV', which has a more rapid linear decline than the base case.

The dashed lines shown in Figure 4.10 represent cases where adsorbed gas is present (Sk = 0.2), which show a significantly delayed production rate decline. Thus, at a given time, production rate is higher for a system with adsorbed gas. In particular, t*, the time at which the outer bound of the SRV is felt, and production rate decline transitions from linear to exponential, is later when adsorbed

gas is present.

Table 4.1. Properties for the semi-analytical bimodal solution for Caney-like.

Property	Value	Comments
P reservoir	440 bars	
P well	381 bars	$(P_w/P_r)^2$ =0.75
Temperature	363 K	
D half-thickness of SRV	115 m	
A area of SRV	24,000 m^2	
Porosity SRV	0.15	Represents brittle layers
Permeability SRV	1.0E-17 m^2	Represents brittle layers
S_k Relative volume Kerogen	0 or 0.2	Adsorbed gas

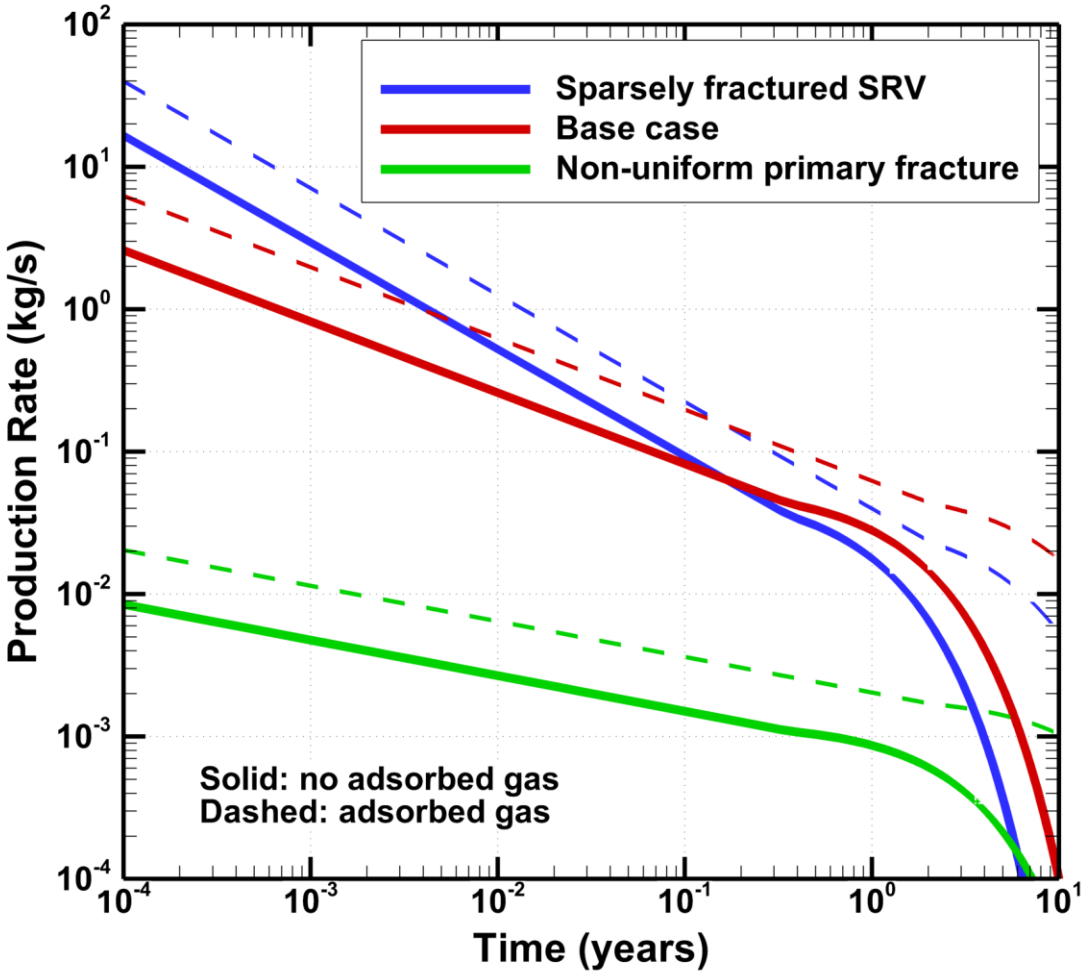

Figure 4.10. Production decline curves from the semi-analytical bimodal solution, for Caney-like conditions (rates from the semi-analytical solution should be divided by 8 when comparing to numerical model results).

Numerical modeling

In order for the production modeling of the Caney Shale to consider the structurally complex shale play according to the current understanding, including the organic-rich shale layers with subordinate

interbeds of siltstone, sandy siltstone, and limestone, a numerical model must be used. The non-shale reservoir interbeds will have significantly different properties, being more brittle and permeable than the ductile shale layers. Brittle and ductile layer thicknesses (20-25 m) are loosely based on the Ardmore A well logs. Both brittle and ductile layers are modeled as continua, but the secondary fracture network is considered to be much more highly connected within the brittle layers, producing a higher effective porosity and much higher effective permeability. Table 4.2 shows the properties for the numerical model.

Initial conditions are a reservoir pressure of 440 bars and temperature of 90oC, both chosen to represent a reservoir at a depth of 4400 m. Production is modeled by holding pressure in the grid block representing the location where the well intersects the primary fracture at a constant value of 381 bars. All other model boundaries are closed. The simulations are isothermal. The numerical code TOUGH3 (Jung et al., 2018; Pruess, 2004) is used for the simulations, with the equation of state package EOS7C (Oldenburg et al., 2004). In the next section, gas-phase methane is the only fluid present in the pore space. The following section examines a two-phase system consisting of gas - phase methane and brine. No adsorbed methane is considered in either case.

Table 4.2. Properties for the numerical model.

Property	Value	Comments
Primary Fracture		
porosity	0.90	
permeability (m^2)	1E-10	Cubic law for 500-micron fracture yields k =3.5E-7 m^2. Represented by a 5-cm thick grid block: k_{eff} = 3.5E-7*500.E-6/0.05 = 3.5E-9 m^2. By trial and error, find maximum value for numerical stability is 1E-10 m^2.
Brittle Reservoir Layer		
Porosity	0.15	
permeability (m^2)	1E-17	
Ductile Reservoir Layer		
Porosity	0.05	
permeability (m^2)	1E-20	

The grid is shown in Figure 4.11. Note that only 1/8th the problem needs to be modeled, by symmetry. The well grid block (where the well intersects the primary fracture) is held at constant pressure and all other boundaries are closed (no-flow), either because they are planes of symmetry (x = 0, y = 0, z = 0) or boundaries with intact shale, which has a vanishingly small permeability (x = 120, y = 114, z = -55). The grid is finer near the primary fracture and the well, to resolve large pressure gradients. Grid spacing ranges from 5 cm to 18 m. The grid consists of 4284 grid blocks.

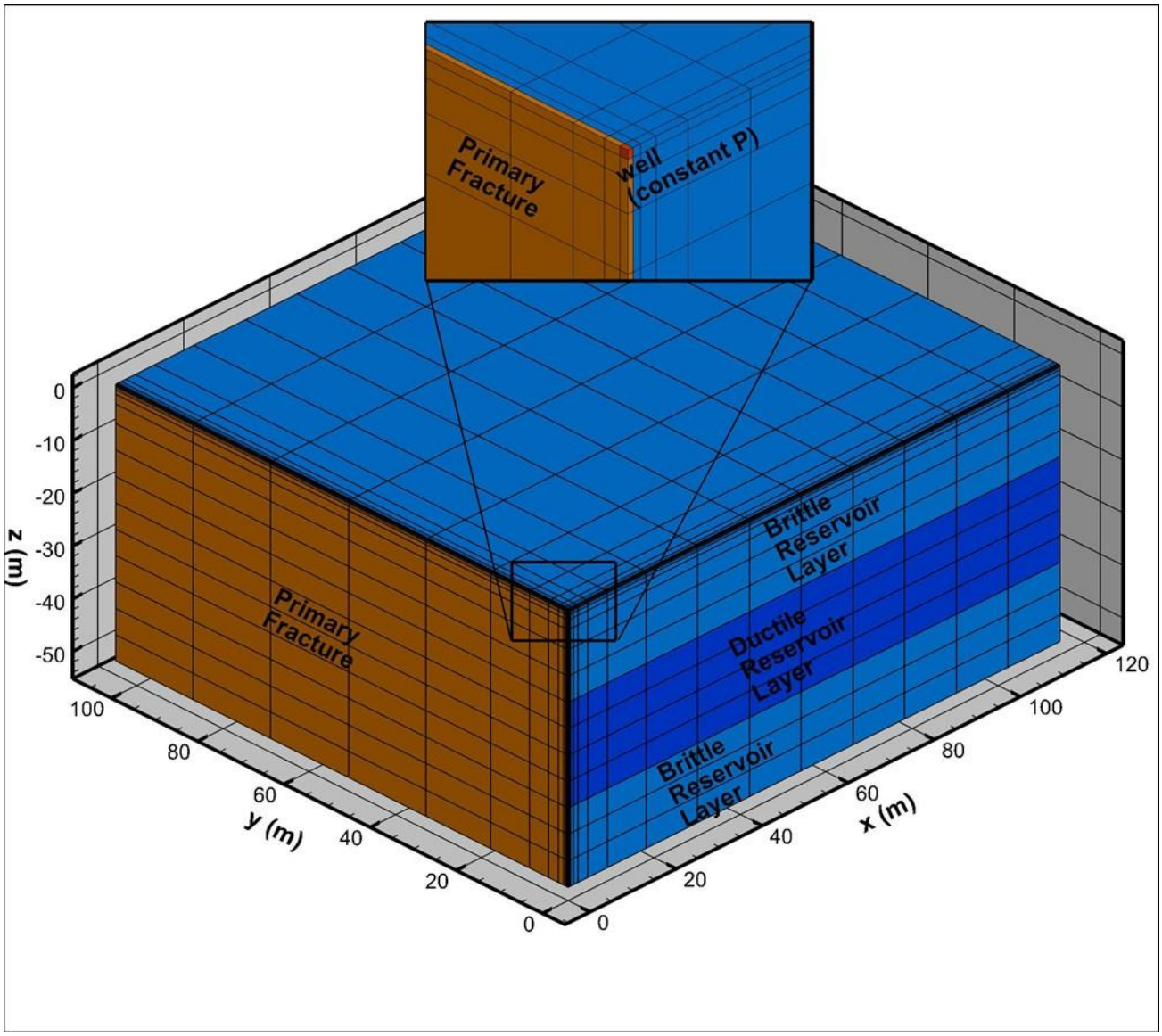

Figure 4.11. Grid used for the numerical model. The well extends all along the edge of the model at z = 0, y=0, but pressure is just held fixed at the intersection of the well and the primary fracture (x = 0, y = 0, z = 0).

Numerical modeling

Figure 4.12 shows production rate decline for a 10-year simulation when the reservoir contains 100% gas-phase CH4, on a log-log scale. At early times (< 1 year), before the outer boundary of the SRV is felt, the decline is linear, with a slope of -1/2. At times >1 year, the outer boundary of the SRV is felt in the brittle layers, resulting in a faster production rate decline. Despite the layering in the SRV, the numerical model results are quite similar to those of the bimodal solution (Figure 4.10).

To model permeability reduction due to fracture creep compaction, we assign a time-dependent permeability reduction factor, using the equation

$$k_{fact} = (b(t)/b_0)^3 \quad (4.5)$$

where b(t) is fracture aperture at time t and b0 is initial fracture aperture. The function for b(t) is derived by curve-fitting to a previous geomechanical simulation of creep compaction:

$$b(t) = b_0 - 0.22E\text{-}9*t^{0.716} \quad (4.6)$$

where time is in seconds and b0 = 0.37E-3 m. Table 4.3 shows kfact for some times of interest. Note that over the entire 10-year production period, the permeability decreases by a factor of about 50, which is far smaller than the differences in the permeabilities of the different components of the system: brittle SRV is 107 times less permeable than primary fracture, and ductile SRV is 103 times less permeable than brittle SRV.

Table 4.3. Values of K_{fact} for selected times

Time	k_{fact}
1 day	0.998
30 days	0.932
1 year	0.638
10 years	0.021

Figure 4.14 shows the production decline curve for constant primary fracture permeability, and for a primary fracture with permeability reduced by Kfact, plotted on a log-log scale. The two curves overlie one another exactly. In Figure 4.14 the very-early-time behavior (t < 10-4 years ~ 1 hour) reflects flow from the primary fracture, the linear section shows flow from the SRV before the outer extent of the SRV is felt, and the faster late-time decline (t > 1 year) shows flow from the SRV after the outer extent is felt. For the case in which primary fracture permeability is reduced, permeability is still pretty big during the very-early-time response (t < 1 hour), so there is no change to production rate then, and later, when primary fracture permeability has declined significantly, the SRV flow is dominating the response, so there is no change to production rate there either.

To model permeability reduction due to fracture creep compaction, we assign a time-dependent permeability reduction factor, using the equation

$$k_{fact} = (b(t)/b_0)^3 \quad (4.5)$$

where b(t) is fracture aperture at time t and b0 is initial fracture aperture. The function for b(t) is derived by curve-fitting to a previous geomechanical simulation of creep compaction:

$$b(t) = b_0 - 0.22E\text{-}9*t^{0.716} \quad (4.6)$$

where time is in seconds and b0 = 0.37E-3 m. Table 4.4 shows kfact for some times of interest. Note that over the entire 10-year production period, the permeability decreases by a factor of about 50, which is far smaller than the differences in the permeabilities of the different components of the system: brittle SRV is 107 times less permeable than primary fracture, and ductile SRV is 103 times less permeable than brittle SRV.

Table 4.4. Values of K_{fact} for selected times

Time	k_{fact}
1 day	0.998
30 days	0.932
1 year	0.638
10 years	0.021

Figure 4.14 shows the production decline curve for constant primary fracture permeability, and for a primary fracture with permeability reduced by Kfact, plotted on a log-log scale. The two curves

overlie one another exactly. In Figure 4.14 the very-early-time behavior (t < 10-4 years ~ 1 hour) reflects flow from the primary fracture, the linear section shows flow from the SRV before the outer extent of the SRV is felt, and the faster late-time decline (t > 1 year) shows flow from the SRV after the outer extent is felt. For the case in which primary fracture permeability is reduced, permeability is still pretty big during the very-early-time response (t < 1 hour), so there is no change to production rate then, and later, when primary fracture permeability has declined significantly, the SRV flow is dominating the response, so there is no change to production rate there either.

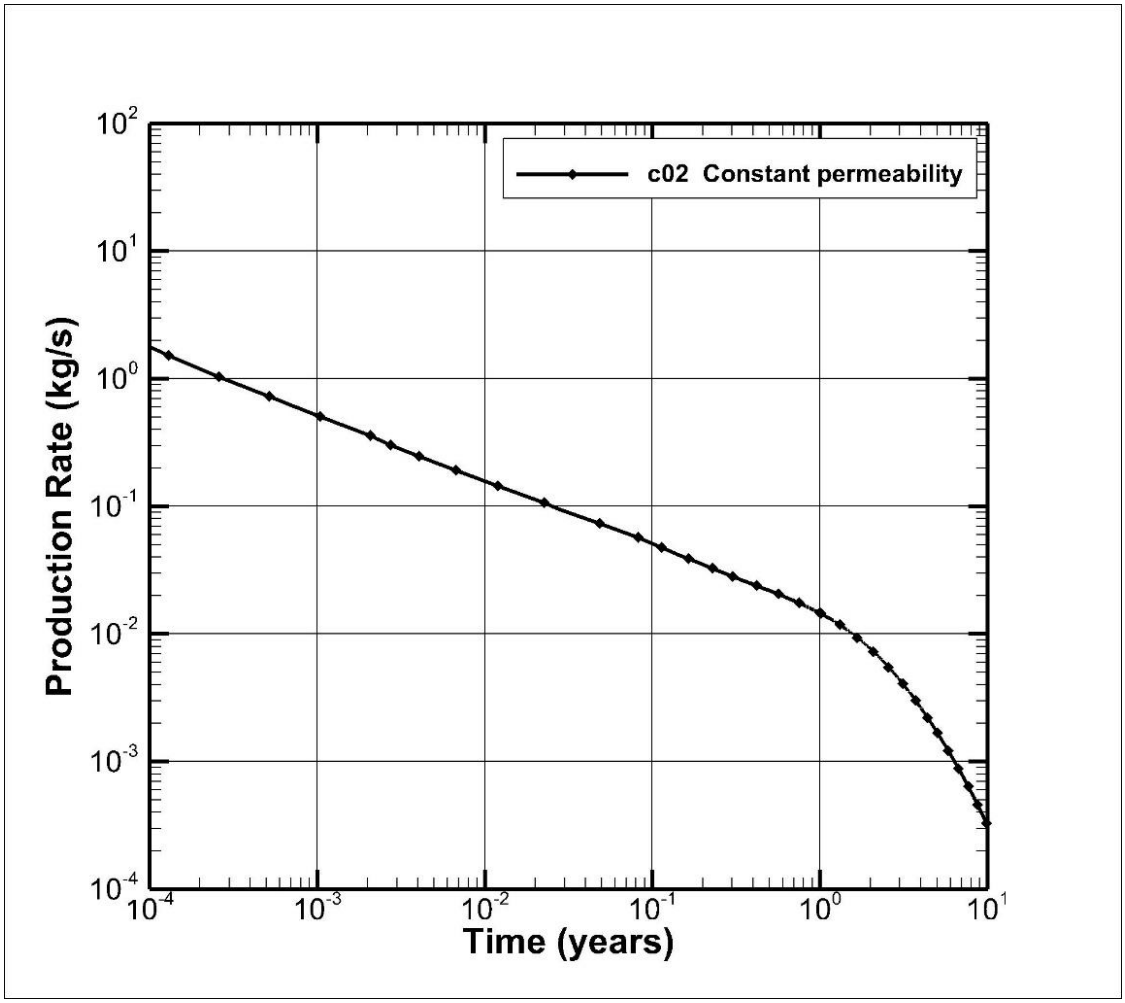

Figure 4.12. Production decline curve for the numerical model.

Figure 4.13 shows the pressure distribution in the model at a series of times. Note that the pressure is uniform over the primary fracture plane because its permeability is large enough to be effectively infinite. Pressure diffuses much faster into the brittle layers than into the ductile layers because the effective permeability is 1000 times larger, to represent a much better-connected fracture network. By 1 year the pressure pulse has reached the outer limit of the SRV in the brittle layers. By 10 years, it has reached the outer limit of the SRV everywhere.

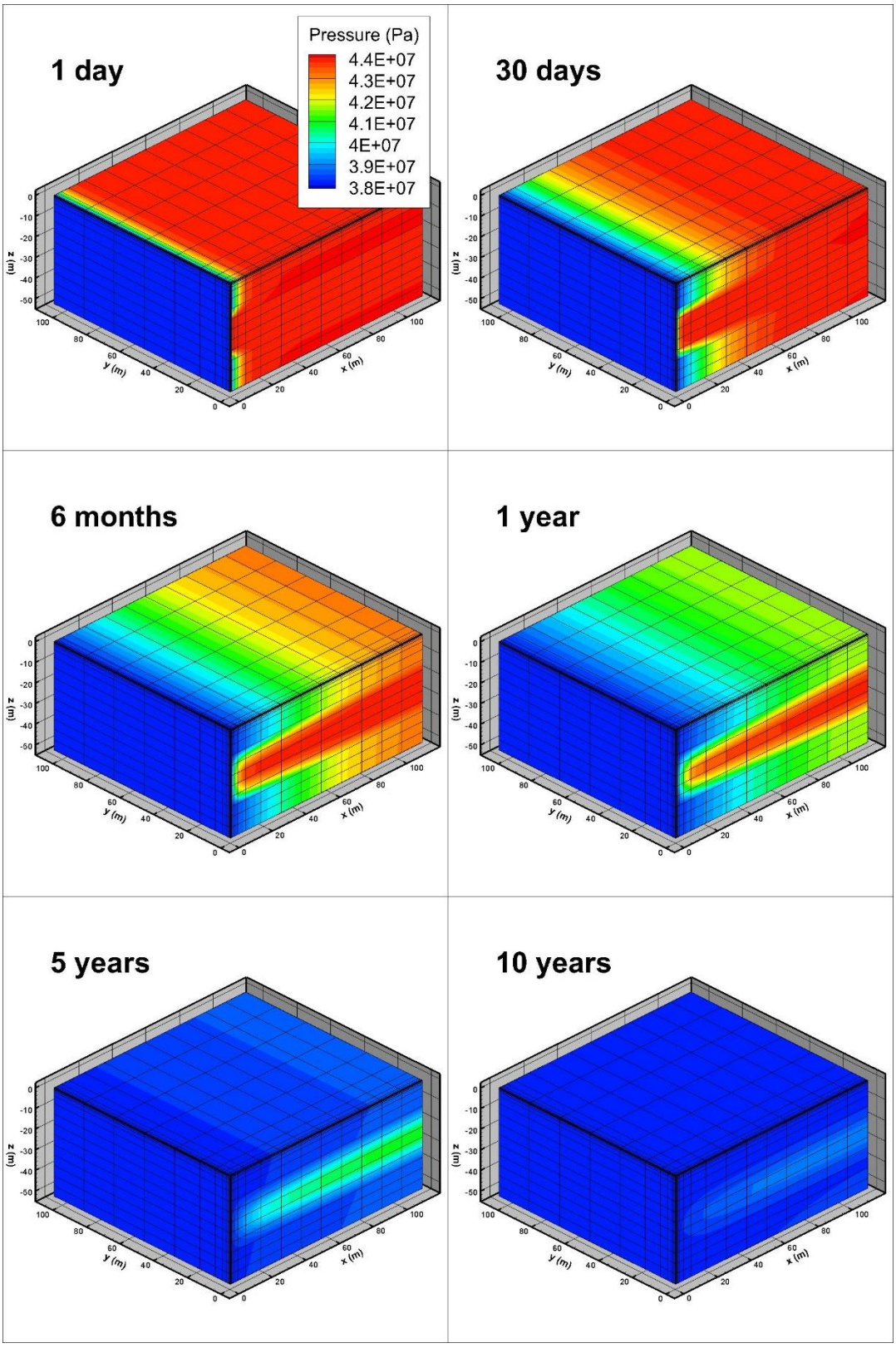

Figure 4.13. Snapshots of the numerical-model pressure distribution at various times, for the constant-permeability case.

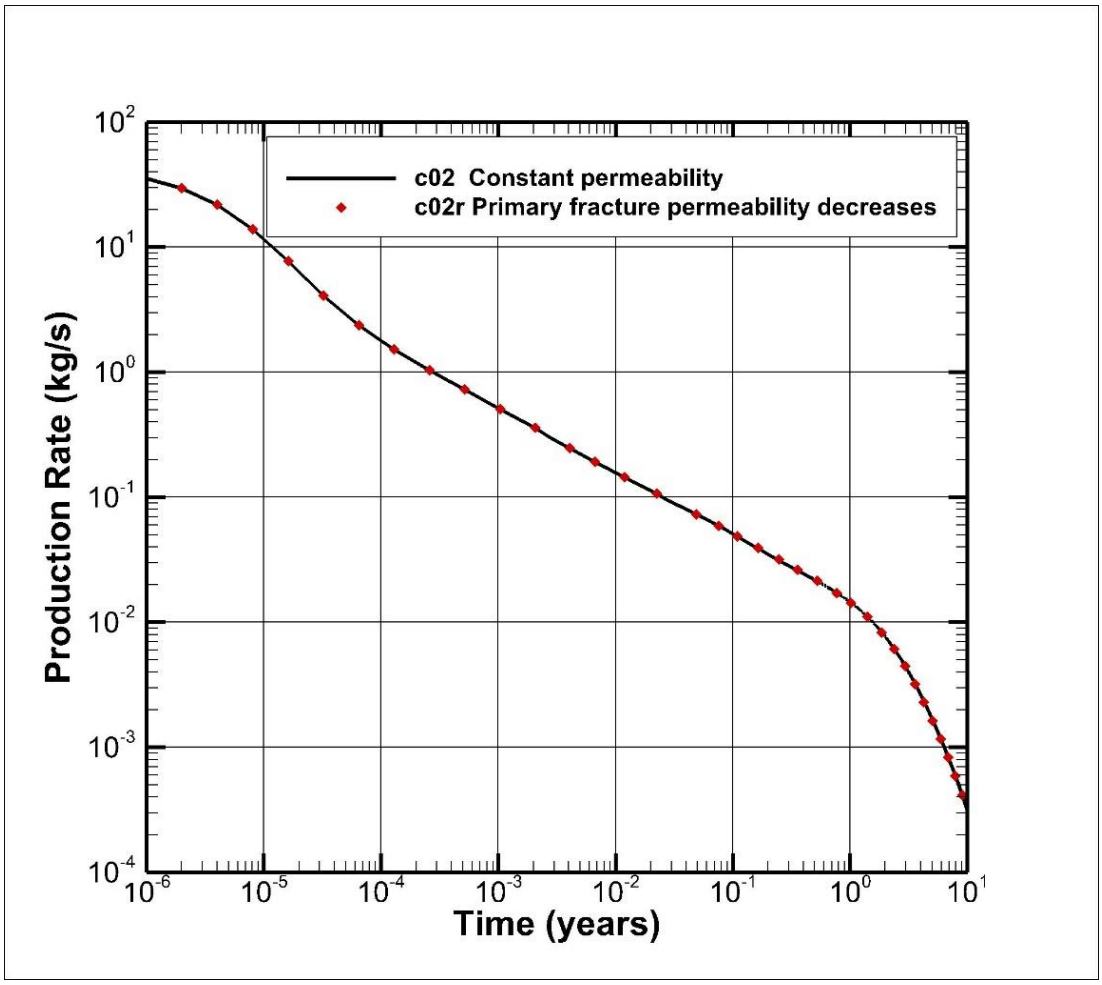

Figure 4.14. Production decline for constant permeability and permeability decreasing in the primary fracture. The curves overlie one another exactly.

Figure 4.15 shows the production decline curve when the permeability reduction factor is applied to various materials: the primary fracture, the ductile part of the SRV, the brittle part of the SRV, and the entire SRV. The plots show time on a linear scale, to enable more detail to be shown. When permeability of the ductile layer is reduced, the production rate does not change until about 2 years, because the low original permeability in the ductile part means it only supplies gas after other parts of the system are exhausted. When permeability of the brittle layers is reduced, the production rate change starts earlier, after only a few months, because after the quick exhaustion of the primary fracture, it is the main supplier of gas. When the permeability of both ductile and brittle layers is reduced, the production rate starts early and continues long times, reflecting both the individual effects. If we consider the 10-year production rate of the constant-permeability case as a lower limit for useful production rate, Figure 4.15 shows that it is reached much sooner, within 8 years, for the reduced permeability case.

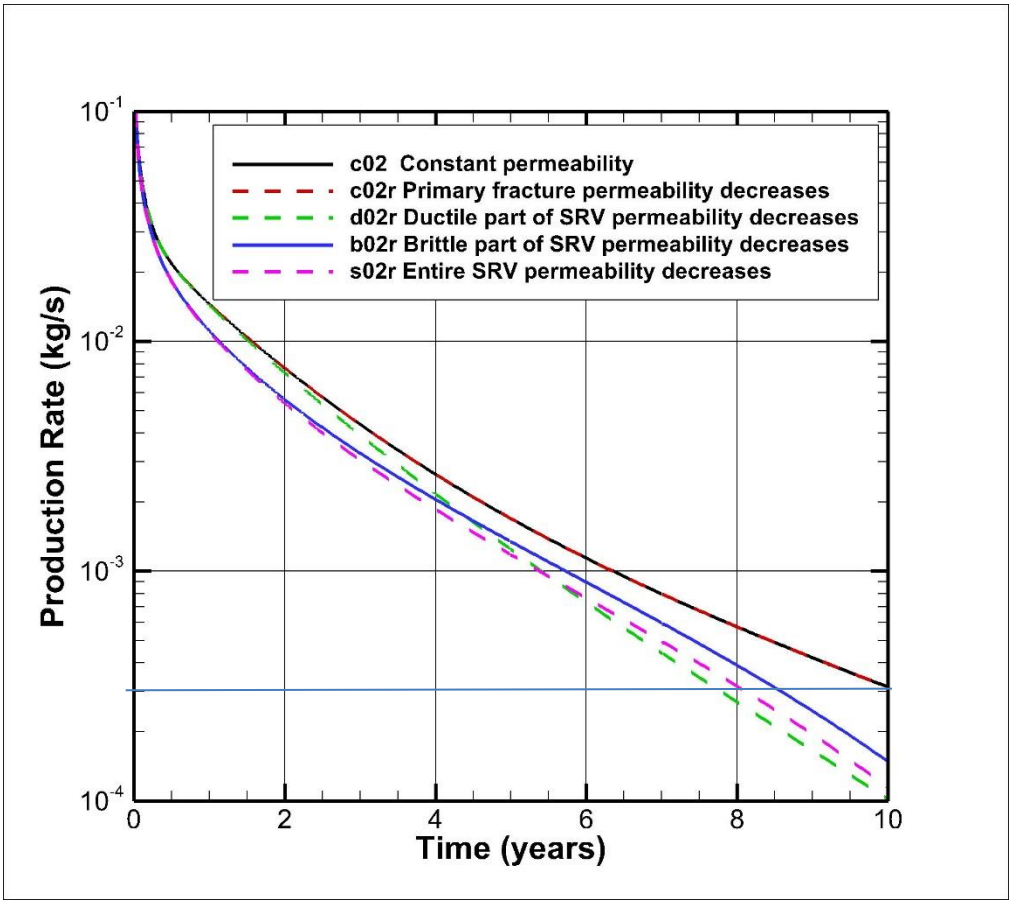

Figure 4.15. Production decline for permeability reduction in different materials of the model. The blue line shows the 10-year production rate for the constant permeability case – note how much earlier it is reached for the decreasing permeability cases.

Reservoir Fluid is Two-Phase Gas-Aqueous

In this section, we consider two-phase production of CH_4 and brine. Figure 4.16 shows results for preliminary studies with constant permeability, considering reservoir fluids composed of 100% CH_4, 90% CH_4 and 10% brine (brine is immobile), and 75% CH_4 and 25% brine (brine is mobile). Even when the brine is immobile, production rate is reduced by the presence of brine, and when the brine is mobile, production rate is reduced even more. Figure 4.17 shows production rate when permeability reduction occurs, in either the brittle or ductile portions of the SRV. Previously we found that decreasing permeability in the primary fracture does not affect production rate, because the primary fracture only acts as a source of produced fluid at very early times, before significant permeability decrease has occurred. Permeability reduction in the brittle zone starts to affect production rate earlier than permeability reduction in the ductile zone, and this holds true for both single-phase gas flow and two-phase gas/brine flow.

The two-phase flow cases shown here use generic relative permeability curves, but OSU laboratory results indicating that the Caney rocks are not strongly water wet to production fluids have been used to choose parameters of the liquid relative permeability curve. Specifically, the liquid phase is highly mobile for the cases shown in Figure 4.17, because for a mixed-wet system, water is not so strongly

partitioned into small pore spaces, resulting in larger liquid relative permeability

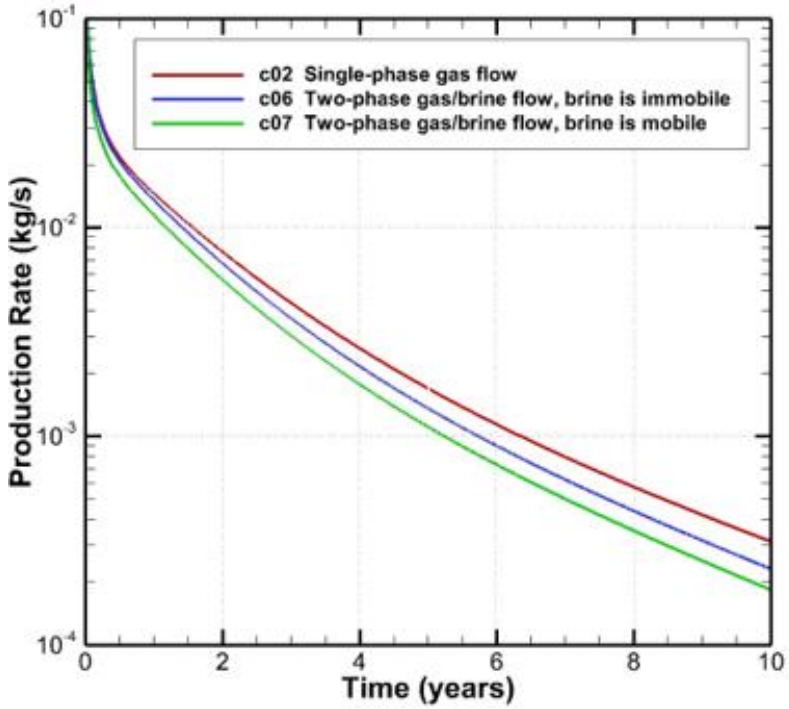

Figure 4.16. Preliminary studies with constant permeability, showing the effect of two-phase reservoir fluid on production rate.

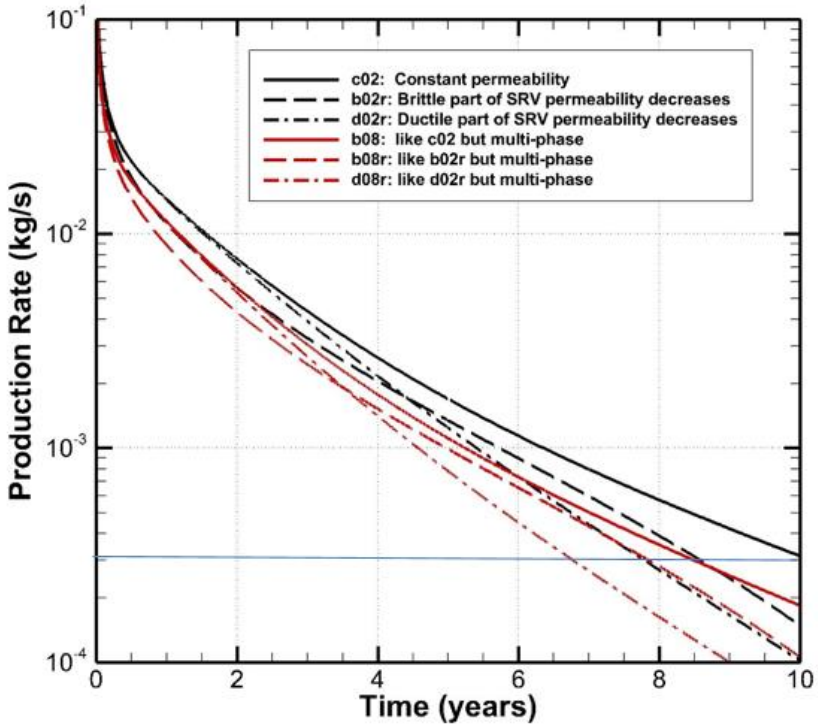

.

Figure 4.17. Production rate when permeability decreases, for both single-phase (black lines) and two-phase (red lines) flow. The blue line shows the 10-year production rate for the constant permeability case – note how much earlier it is reached for the two-phase decreasing permeability cases.

Reservoir is mixed-wet rather than water-wet

Because the 3D production-scale model used for previous studies has many grid blocks and a large range of response times for the fracture, brittle, and ductile zones, simulations are rather time consuming. This is not a problem when just a few simulations are required, but to study multi-phase flow when the relative permeability and capillary pressure functions are not known with certainty, doing many simulations with a range of parameters is helpful. Therefore, a laboratory-scale model, with a simple one-dimensional geometry, was created. It runs very quickly, enabling sensitivity studies with different relative permeability and capillary pressure curves, and will be useful to compare to laboratory data from flow-through experiments that becomes available. The 1D model can represent either a planar fracture, or a section of brittle or ductile shale, depending on the material properties assigned. We can also use a time-dependent permeability to represent fracture closing, but this option is not used for the present studies.

The model is 10 cm in length and is initialized with a two-phase mixture of gaseous CH_4 and liquid water at constant temperature and pressure, with the pressure held fixed at both ends. The pressure is then dropped at the x=0.1 m end, to initiate flow through the model. The transient response of pressure, aqueous-phase saturation, and gas and aqueous flow rate is then recorded, along with the steady-state values.

We continue to make use of OSU laboratory studies on wettability to improve realism of models. Previously, we used the finding that micromodels coated with clay were mixed-wet by employing the usual capillary pressure functions for water-wet systems but making the aqueous phase more mobile than usual. Here, we develop and apply capillary pressure functions that represent mixed-wet systems explicitly, by covering both positive and negative values of capillary pressure, as illustrated in Figure 4.18. Both these techniques are taken from Abdallah et al. (2007). For the mixed-wet case, when aqueous saturation $S_{aq} < 0.5$, the system is water-wet, and for $S_{aq} > 0.5$, the system is gas-wet. Figure 4.19 shows simulation results for the base case of a water-wet system, initially saturated with 25% CH_4 and 75% water. At t=0, the pressure is dropped at x=0.1 m, and thereafter pressure is held fix at both ends to sustain flow through the system in the positive x direction (from left to right in the plots). Steady-state conditions are reached within 1 hour. The increase of S_{aq} near the outlet is a hallmark of a water-wet system, as capillary forces try to hold onto the water flowing out of the system. There is an initial pulse of gas and aqueous flow from the down gradient end of the model at early times (red and orange curves), after which a steady flow rate is quickly established. Because S_{aq} is higher than S_g, aqueous relative permeability is higher than gas relative permeability, and thus aqueous flow is larger than gas flow.

Figure 4.20 shows simulation results for a mixed-wet system. For initial conditions of $S_{aq} = 0.75$, the system is gas-wet, as illustrated by the decrease in S_{aq} (and a corresponding increase in S_g) near the outlet of the model, as capillary forces now try to hold onto the gas flowing out of the system. Gas-phase flow is similar to the water-wet case shown in Figure 4.19, but the aqueous-phase flow has a much larger initial pulse from the downgradient end of the model at early times, because now water is not being strongly held in place by capillary forces.

Figure 4.21 shows simulation results for a water-wet system in which the saturation at the inlet is held fixed at $S_g = 0.75$, much higher than the initial saturation of $S_g = 0.25$. In the upgradient portion

of the model, S_{aq} steadily decreases as gas flows in, but in the downgradient portion of the model capillary forces maintain S_{aq} near its initial value. As more gas flows into the model, the gas flow rate increases, and the aqueous flow rate correspondingly decreases.

Figure 4.22 shows simulation results for a mixed-wet system in which the saturation at the inlet is held fixed at S_g =0.75. Now when S_{aq} decreases due to gas flowing into the model, the system transitions from gas-wet back to water-wet wherever $S_{aq} < 0.5$, and the curvature of the S_{aq} profile near the outlet reverses direction. The steady-state gas flow rate is larger than for the water-wet case Additional simulations were run with saturation at the inlet held fixed at $S_g = 0.10$, so the system has more water and less gas in place over time, but this did not change the fundamental character of the results, as the mixed-wet system began gas-wet, and stayed gas-wet. The lab-scale modeling results have demonstrated the types of flow behavior that occurs for mixed-wet systems, using a capillary pressure function with positive and negative portions, to explicitly represent water-wet and gas-wet domains. This is a new capability for the TOUGH simulator, which will be broadly applicable within and beyond Caney Shale modeling. The next step will be to apply this capability to the production model, to assess the impact of mixed wettability on production rate decline.

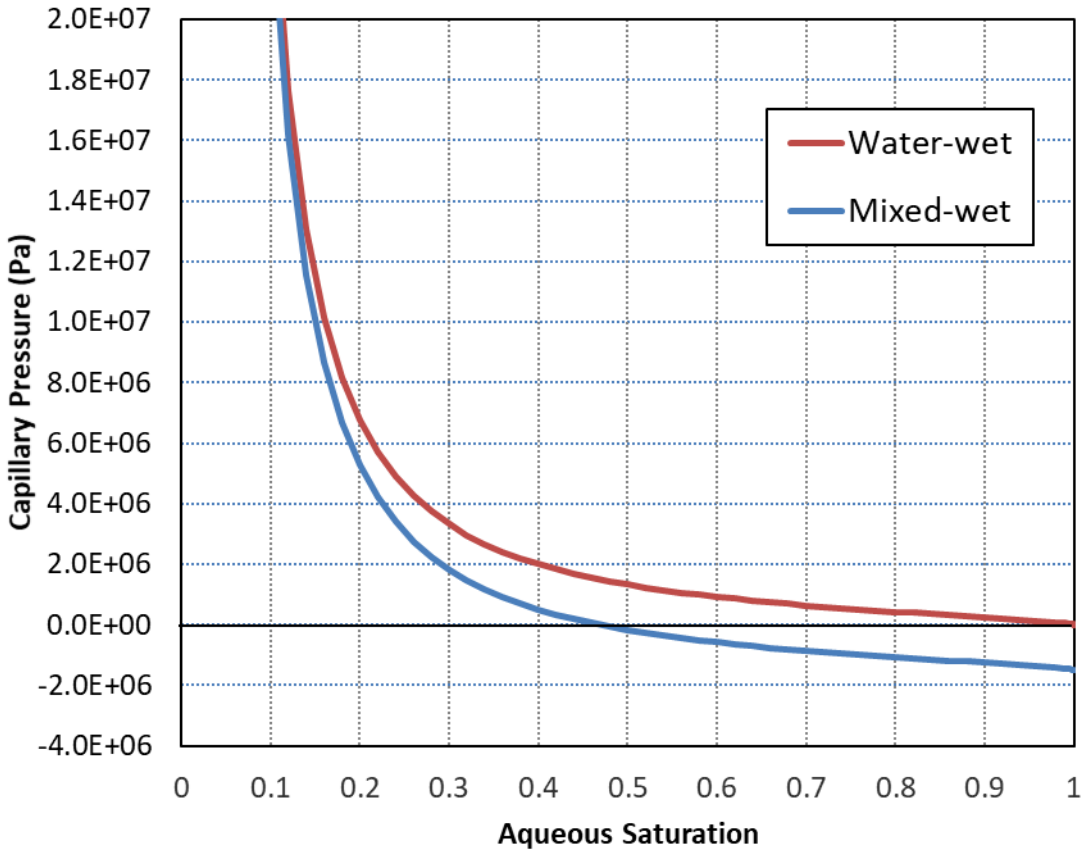

Figure 4.18. Capillary pressure functions for water-wet and mixed-wet reservoirs. For the mixed-wet case, the system is water-wet for $S_{aq} < 0.5$ and gas-wet for $S_{aq} > 0.5$.

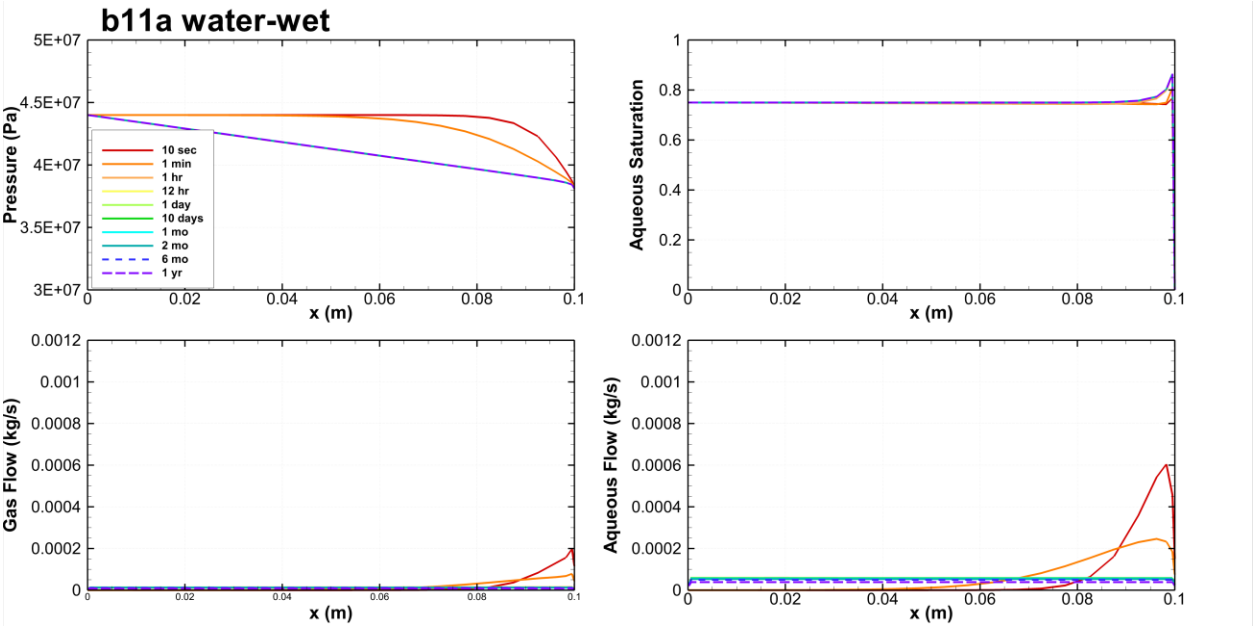

Figure 4.19. Simulation results for water-wet base case. Flow is from left to right.

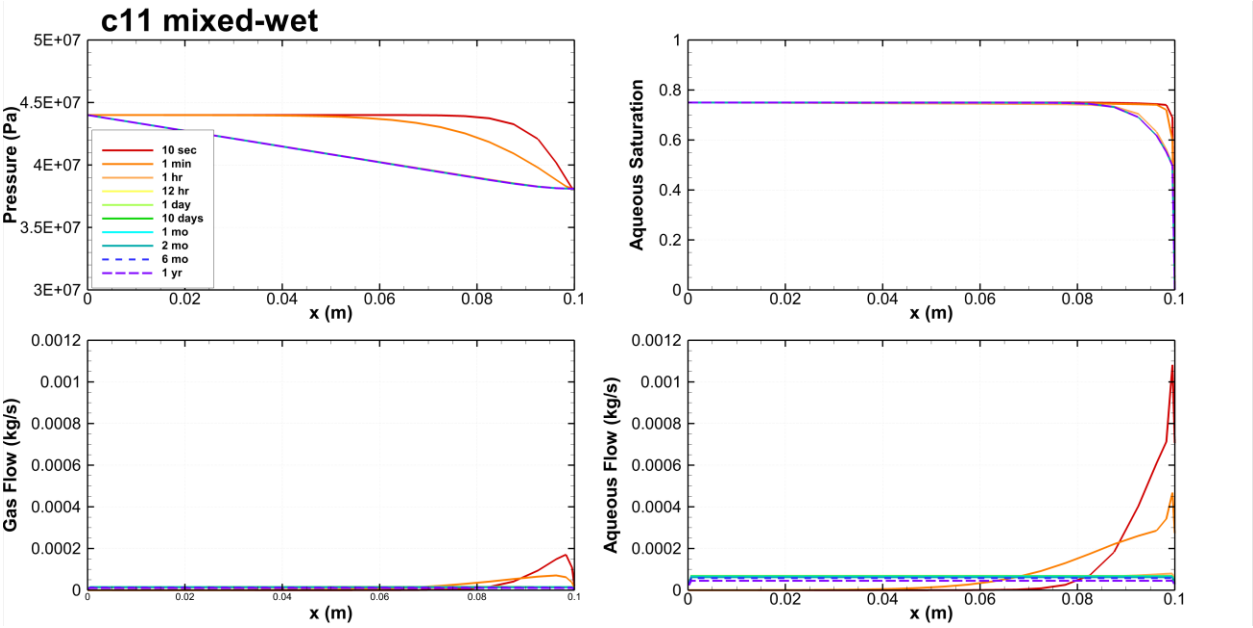

Figure 4.20. Simulation results for mixed-wet base case. Flow is from left to right.

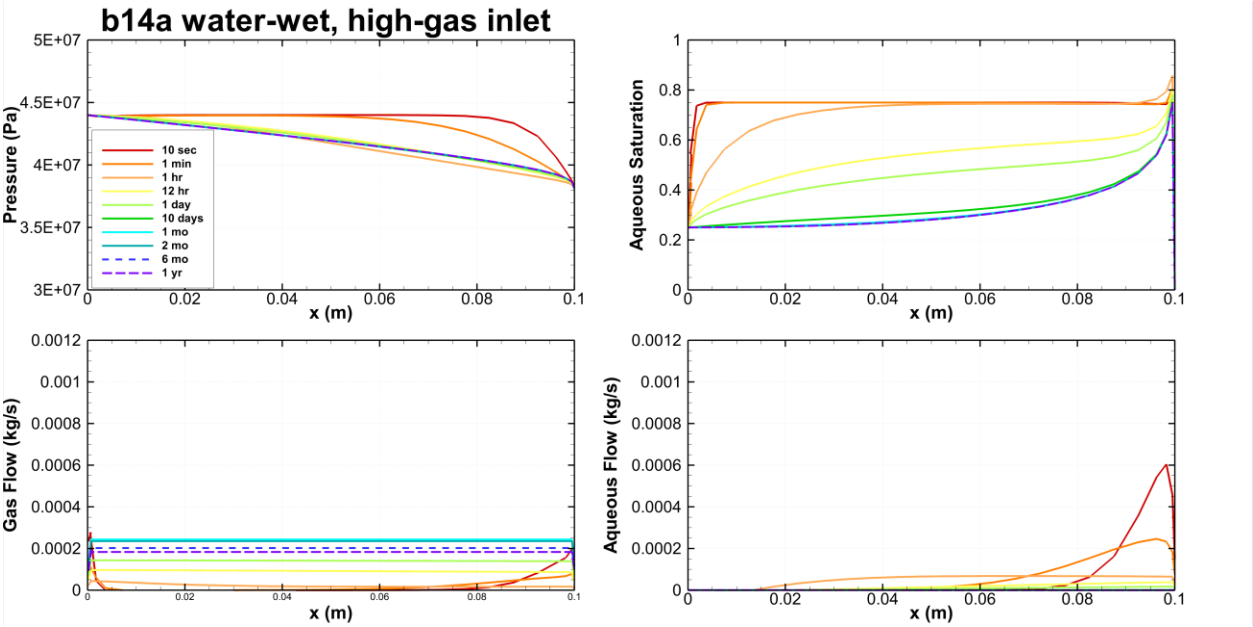

Figure 4.21. Simulation results for water-wet case with S_g= 0.75 at x = 0. Flow is from left to right.

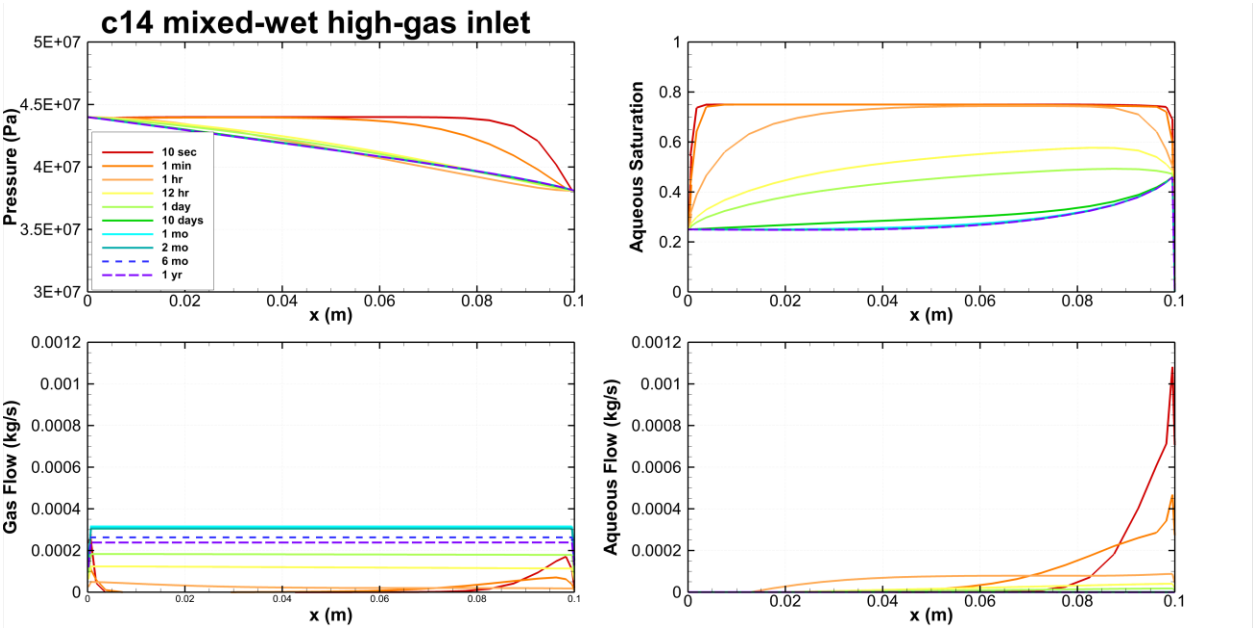

Figure 4.22. Simulation results for mixed-wet case with S_g= 0.75 at x = 0. Flow is from left to right.

Comparison with Ardmore B well Production data

Field data from the Ardmore B well is shown in Figure 4.23, using customary field units MSCF/month for gas production and BOPD for oil production. Converting these into common volumetric flow rate units indicates that oil only makes up 1/1000th of the total production. Hence, our models that do not include a separate oil phase may not be that bad a representation of reality. Figure 4.24 compares the Ardmore B well gas production data and the bimodal solution for the parameters shown in Table 4-4, assuming no adsorption (S_k = 0). For times between 2 and 10 months, the match is reasonable on average, but the late-time (exponential decline) begins too soon (that is,

t* is too early). This suggests that adsorption may need to be included in the bimodal solution.

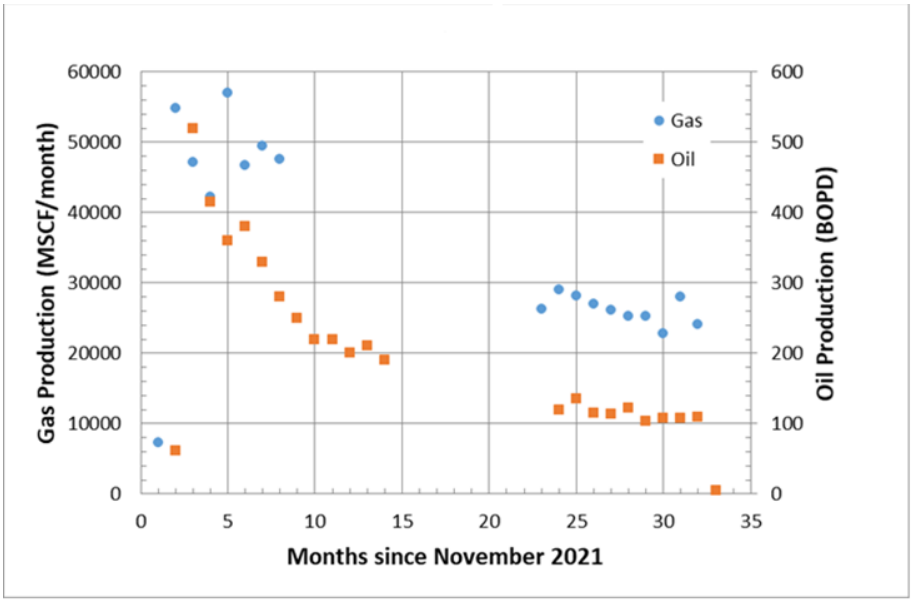

Figure 4.23. Publicly available production data for the Ardmore B well from Oklahoma Corporation Commission.

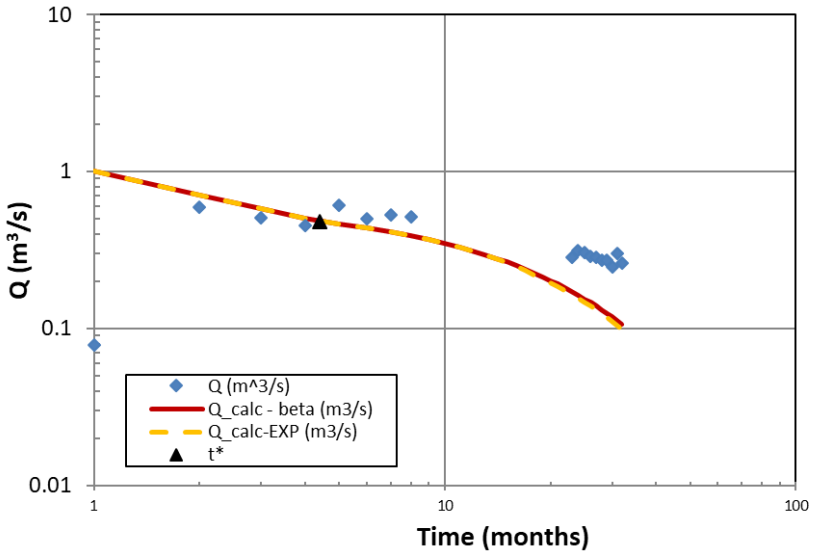

Figure 4.24. Ardmore B well gas production data (blue symbols) and bimodal solution using properties Table 4.4 and $S_k = 0$.

Increasing the relative volume of kerogen, S_k, from 0 to 0.05 yields a later t*, but the whole decline curve is now a little too high (Figure 4.25). This suggests that permeability of the SRV or primary fracture area A is a little too big. Decreasing A from 24,000 m^2 to 22,000 m^2 yields the decline curve shown in Figure 4.26, which matches the Ardmore B well data very well starting with month 5. It is not uncommon for the first few months of production data to not fit the idealized bimodal solution as early-time transient processes not included in the bimodal solution occur. Other combinations of parameters could also provide reasonable fits to the production data, as this is a rather short time series of production data. Nonetheless, the matching process can provide useful insights into the conditions in the reservoir.

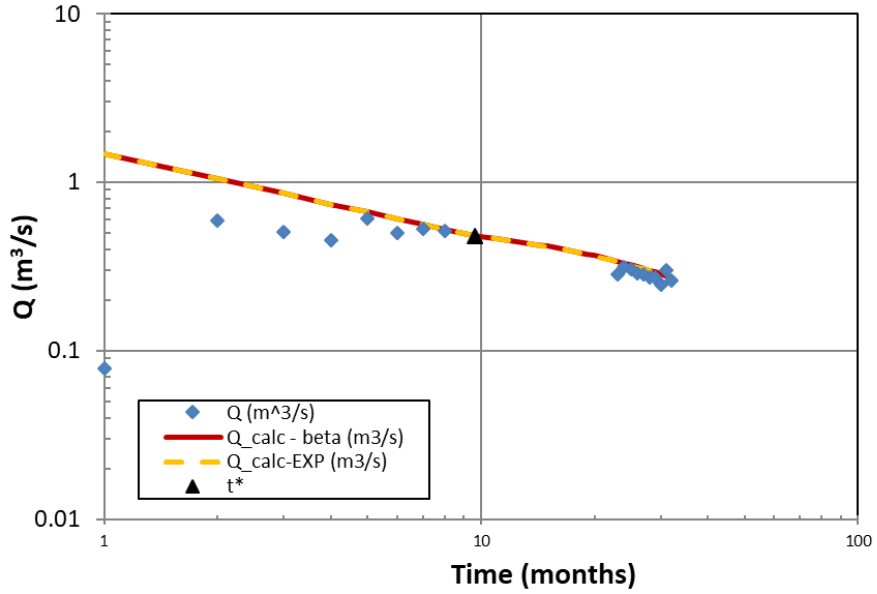

Figure 4.25. Ardmore B well gas production data (blue symbols) and bimodal solution using properties of Table 4.4 except S_k = 0.05.

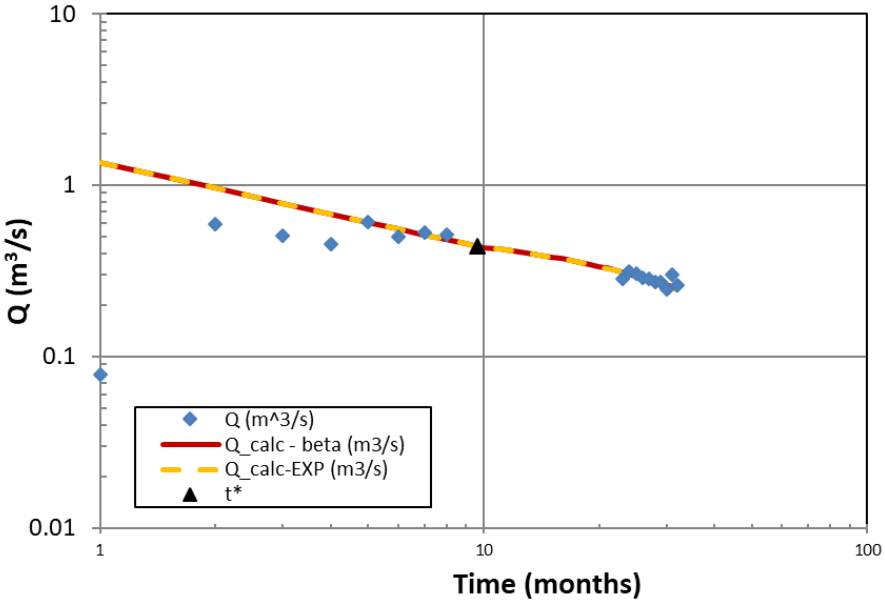

Figure 4.26. Ardmore B well gas production data (blue symbols) and bimodal solution using properties of Table 4-4 except S_k = 0.05 and A=22,000 m^2.

4.5. Modeling of reaction between Caney Shale and completion fluids

The LBNL code TOUGHREACT (Xu et al., 2014a, 2014b) was used to do geochemical modeling of batch reactor laboratory experiments being conducted by OSU to investigate mineral reactions between Caney Shale and completion fluid. Two major sets of simulations are run, including Caney Shale with fracturing fluids (FF) and then Caney Shale with deionized water (DI). For the TOUGHREACT model, a single grid block represents the reaction chamber, which is held at constant pressure and temperature. Sampling is represented as a mass sink lasting one minute at the specified

times (1, 3, 7, 14, 21, 28 days). The primary aqueous species included are H^+, H_2O, Na^+, K^+, Ca^{2+}, Mg^{2+}, Fe^{2+}, Al^{3+}, Cl^-, $SiO_2(aq)$, HCO_3^-, HS^-, and SO_4^{2-}. The initial minerals considered are quartz, albite, pyrite, calcite, dolomite, illite, montmorillonite-Ca, clinochlore-14A, kaolinite as primary (existing) minerals, and gibbsite, boehmite, siderite and goethite as potential secondary (forming) phases. Gases representing contact with air include O_2 and CO_2. Changes in aqueous and mineral composition were monitored. Figure 4.27 shows a comparing aqueous composition for model and lab results showing a general agreement. The results and detailed interpretation of the TOUGHREACT modeling can be found in the Awejori et al. (2024).

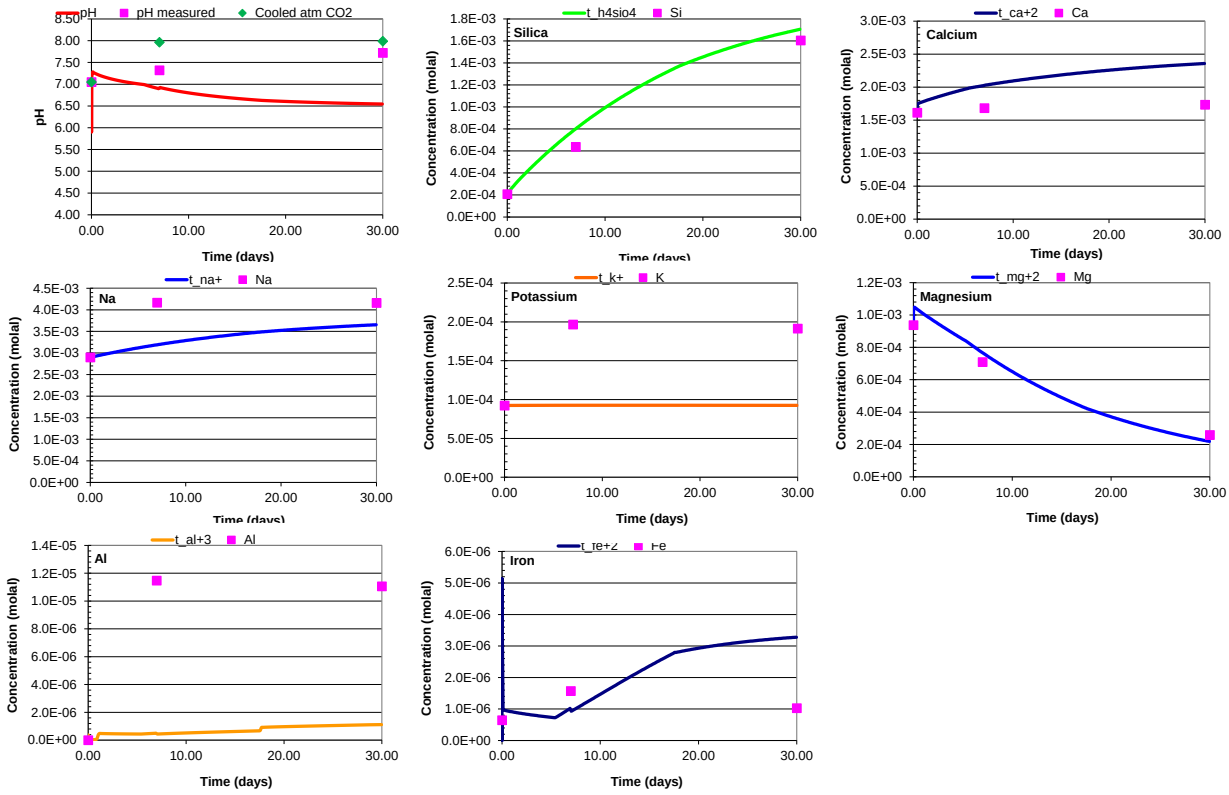

Figure 4.27. Comparison of fluid compositions and concentrations obtained from TOUGHREACT modelling (lines) and measured from experiment (squares).

4.6. Concluding remarks on Caney coupled processes modeling

The section of the report focused on the coupled processes modeling of the Caney shale. In Task 13 as described in this section, the model that was selected and demonstrated in Task 7 has been applied considering the new Phase II data provided from Caney shale, including numerous laboratory data from UPITT and OSU.

- The modeling of Caney mechanical core-scale and indentation experiments, along with hydro-mechanical flow through experiments on proppant filled fractures help us to define time-dependent fracture closure models for the hydro-carbon production simulations.
- The modeling of the laboratory testing demonstrated that nominally ductile shale with high clay content fail at lower stresses and are much more creep prone and therefore can have a significant impact on the long-term production decline.

- Permeability reduction in the brittle zone starts to affect production rate earlier than permeability reduction in the ductile zone, and this holds true for both single-phase gas flow and two-phase gas/brine flow.
- Modeling considering two-phase, shows that production rate is reduced by the presence of brine, and when the brine is mobile, production rate is reduced even more.
- Whether water-wet or mixed-wet two-phase flow system can have a significant impact on gas and water production.
- The gas production history of the Ardmore B well could be matched using a bi-modal semi-analytic model, considering different combinations of reservoir parameters, such as the surface area of the primary fracture and the presence of adsorbed methane.

The developed model approach can be applied for investigating ways to optimize hydrocarbon production from a system similar to the Caney shale. Further investigation of other mixed-wet capillary pressure functions is recommended. Moreover, future work could include a three-phase (gas/oil/water) system and consideration of adsorbed methane.

5. Drilling, Stimulation and Production Technical and Economic Analysis

5.1. Approach

Chapter 5 is focused on the collection and analysis of geomechanical data to characterize the properties of the Caney Shale formations. This process involved gathering and analyzing offset drilling and log data, as well as testing and evaluating core samples obtained from a well drilled through the Caney Shale as part of this project. The goal was to establish correlations between various geomechanical and petrophysical properties. Once the geomechanical logs were developed for the different reservoirs in the Caney Shale, drilling data was employed through inverted Rate of Penetration (ROP) models to create depth based geomechanical and petrophysical profiles along the wellpath. Unconfined compressive strength (UCS) values were calculated from the drilling data using the inverted ROP models and validated through mechanical testing of Caney Shale rock samples. The UCS profiles were then developed along the vertical and deviated wellbores using the D-Series software, which includes D-WOB and D-ROCK (Thameen et al., 2019). D-WOB was employed to determine the Down Hole Weight on Bit (DWOB) and D-ROCK was employed to calculate petrophysical properties using the derived correlation such as porosity and permeability, as well as geomechanical properties like Confined Compressive Strength (CCS), UCS, Young's Modulus, and Poisson's Ratio, providing a comprehensive geomechanical property log along the wellbore. The Pason Drilling Simulator (PDS), which also employs inverted ROP models and offset well data to estimate rock strength, was used to develop an optimized drilling plan for the upcoming planned Well D.

The petrophysical and geomechanical data were integrated into a comprehensive earth model for use in simulation of the hydraulic fracturing along lateral wells in the Caney Shale. This chapter assesses the effectiveness of using drilling data to construct this earth model, as opposed to relying solely on log data. The primary goal is to analyze the geomechanical and petrophysical properties of the Caney Shale and utilize these insights to develop the required geomechanical and petrophysical properties along the wellbore to simulate and optimize drilling and completion operations. Specifically, UCS data was employed to construct rock strength logs for Well A and Well B which were drilled in 2014 and 2015, targeting reservoirs 2 and 3 of the Caney Shale, respectively. A geomechanical stimulation log for Well B was also developed, incorporating simulations of the planned stimulation design for Well D using the GOHFER multistage fracturing simulation software. The accuracy of these simulations was validated by comparing them with actual production results. Additionally, the chapter references findings from a study of 97 horizontal wells in the Springer field and includes completion data from Well A and Well B.

5.1.1. Drilling Offset Data Collection and Simulation Inputs

Two software programs, D-WOB and the Pason Drilling Simulator (PDS), were utilized to simulate and optimize the planned Well D. First, D-WOB was employed to calculate the coefficient of friction and the downhole weight on bit (DWOB) on a foot-by-foot basis for the lateral section of Well B which was drilled through Reservoir 3 which was also the planned reservoir for Well D. The drilling data from Well B was first quality controlled to ensure accuracy and remove any redundant data.

There is a feature in D-WOB that allows the depth-based file to be quality controlled. This feature enables easier quality control job and smoother trends to be formed. Lower and upper bounds for WOB, RPM and ROP can be adjusted to ensure the removal of values outside limits of reasonable extremity that are usually caused by inaccurate rig measuring or non-drilling time. The following inputs were necessary to run the software:

- Survey data (measured depth (MD), True Vertical Depth (TVD), inclination, and azimuth)
- Drilling data (date & time, bit depth, MD, TVD, Weight on Bit (WOB), rotational speed (RPM), ROP, standpipe pressure, hook load, flow rate, motor differential pressure, mud plastic viscosity and weight)
- Drill-string configuration (drill-string section lengths and dimensions, including the Bottom Hole Assembly (BHA) components)

The time and depth file contains information that enables the Torque and Drag (T&D) models in D-WOB to be executed. The BHA files were provided where each BHA was described in detail. The survey file included the depth, azimuth, inclination, and dogleg angle. Additional data that was necessary to run the application included the drawworks information like hook weight, number of lines and sheave efficiency. These variables were found from provided drilling data where a 96% sheave efficiency and 10 lines were used. The hook weight of 40 klbf was found by plotting the hookload during connections. The data was then converted to text files and transferred into the D-WOB software. The D-WOB software then calculates the friction in the wellbore while drilling, which is then subtracted from the surface measured weight on bit (SWOB) to determine the Downhole Weight on Bit (DWOB). These DWOB values are subsequently used as inputs into the D-ROCK and PDS software's for the deviated section of the well.

The PDS software was then used with Well B's drilling, lithology and bit information files to generate the Apparent Rock Strength Log (ARSL). The drilling data was obtained from daily drilling reports, followed by a thorough quality control process using Microsoft Excel and the D-WOB software. After ensuring the data quality, the drilling data was categorized into three separate files: the drill file, which contains operational drilling parameters; the lith file, which includes lithology information; and the bit file, which contains the necessary bit information. These files were imported into the PDS software to simulate and optimize the drilling process of the planned Well D. A correlation between Well B's ARSL and Well D's ARSL was established by adjusting formation tops to match the provided Well D formation top depths. Detailed information was provided on formation top markers, bit details, and BHA specifications. The formation tops for both Well B and Well D are listed in Table 5.1. The adjustment was performed within the PDS and involved shrinking and stretching certain formations to align with the provided formation top prognosis to create an accurate depiction of Well D's ARSL.

The PDS uses inverted ROP models and operating parameters in conjunction with the bit design parameters and the field reported bit wear to calculate the ARSL. Because the calculated apparent drilling strength (ARS) is also a function of the bit wear at depth and the bit wear is a function of the ARS values for each bit run, it is an iterative process to get the final ARS values and match the field reported bit wear. Figure 5.1 presents the ARSL generated for Well B including the operational drilling parameters used, while Figure 5.2 displays the adjusted ARSL for Well D (developed from Well B), incorporating the updated Well D formation tops and a set of simulated drilling parameters.

Table 5.1. Formation Tops for Well B and Well D

Estimated Tops (ft)			
Well B		Well D	
Tops	TVD (pilot)	Est. Tops	Est. MD
HOXBAR	2148	HOXBAR	3222
DEESE	4298	DEESE	5505
UP. FUSULINID	4559	UP. FUSULINID	6334
FUSULINID	4960	FUSULINID	6471
TUSSY	5491	TUSSY	6935
ATOKA	6552	TUSSY BASE	7607
DORNICK HILLS	7300	ATOKA	9092
SPRINGER	8239	DORNICK HILLS	9928
HUMPHRIES	8353	DORNICK HILLS BASE	10400
SIMS	8742	SPRINGER	11105
GOODWIN	9263	HUMPHRIES	11275
FALSE CANEY	10618	SIMS	11595
CANEY	10870	GOODWIN	12471
		GOODWIN BASE	12581
		FALSE CANEY	13540
		CANEY	14095

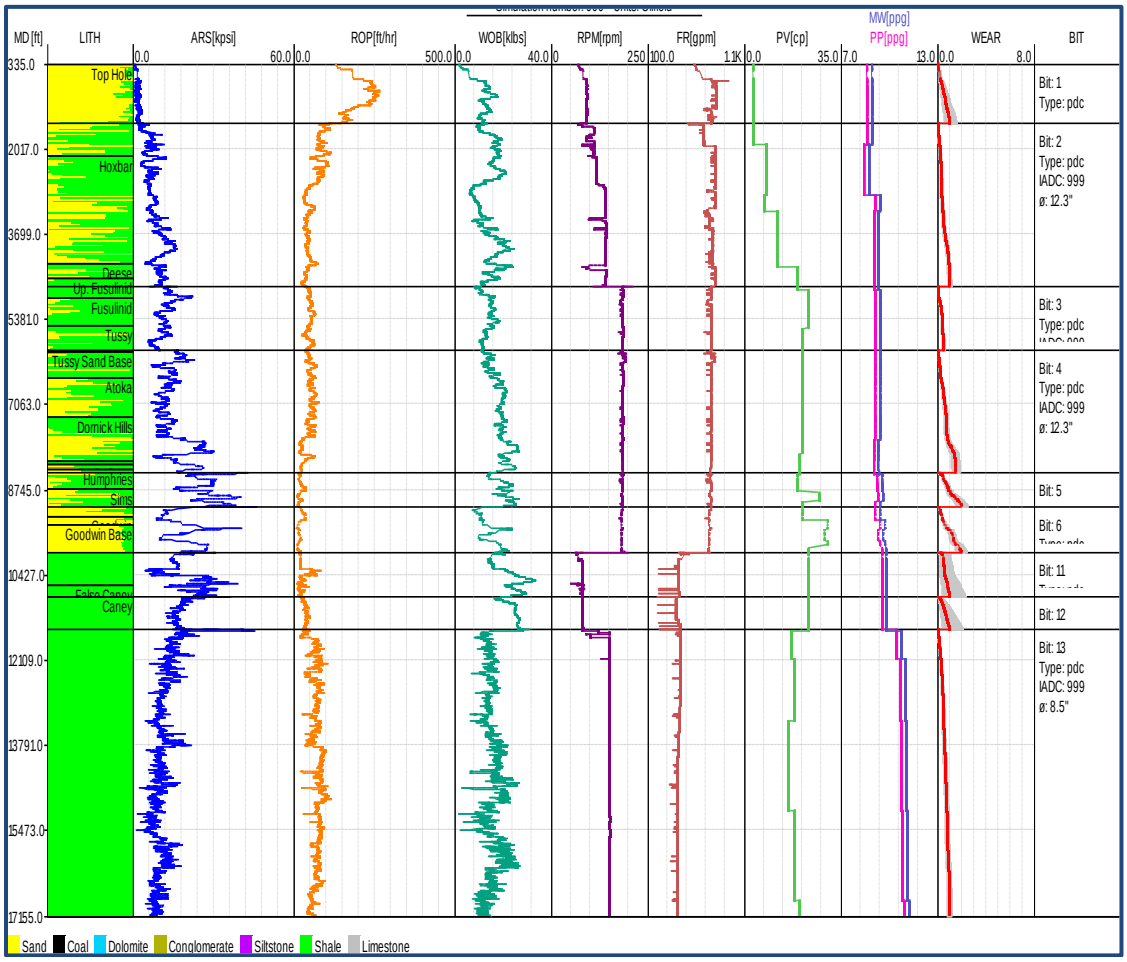

Figure 5.1. PDS Output of Well B ARSL

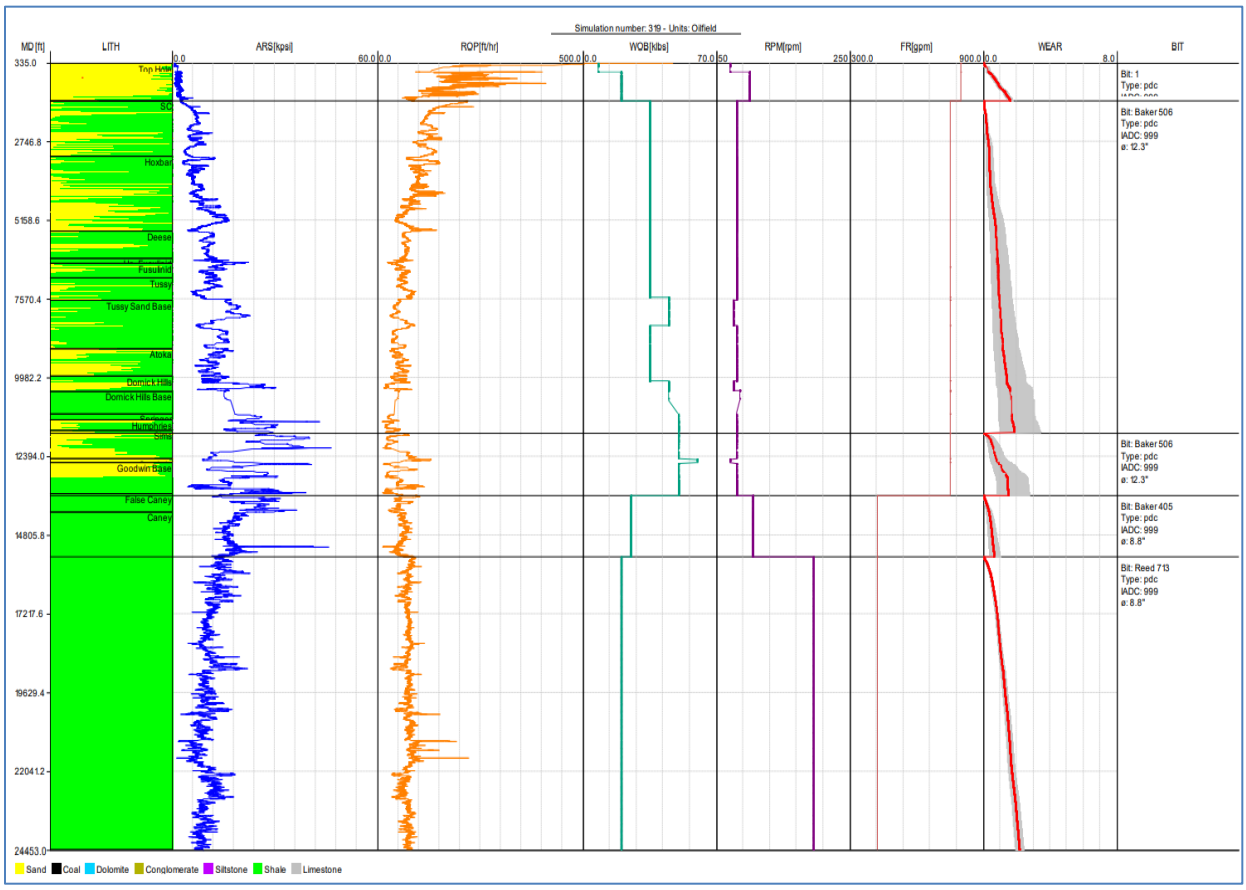

Figure 5.2. PDS Output of Well D Optimized Simulation

Using drilling data from Well B, an optimized drilling program was created through a series of simulations using the PDS. The detailed simulation and optimization approach implemented for Well D is summarized in Table 5.2 for each section. A more comprehensive simulation approach, from the PDS, is presented in Table 5.3 showing an optimized average well ROP of 61 ft/hr and an optimized total on-bottom drilling time of 394 hrs.

Table 5.2. Well D Simulation and Optimization Results

Section	Details
17.5″	• Optimization in the 17.5″ section resulted in an average ROP of 167 ft/hr. • Controlled drilling was advised for this section.
12.25″	• Two HC-bits with tier 1 cutters were used to drill the 12.25″ section. • This section was simulated using a weight-on-bit (WOB) of 60 klbs at an average ROP of 58 ft/hr and 37 ft/hr for bit 1 and bit 2, respectively. • A 0.08 revolutions per gallon (rpg) motor was also implemented in this section, which resulted in a mud flow rate of 750 GPM for the entire section.
8.75″ (Curve)	• Well D kicked off at 13,861 ft with an estimated 85% sliding and 15% rotating. • An HC 405 bit was used throughout this section with a simulated downhole WOB of 25 klbs, resulting in an average ROP of 54 ft/hr. • Estimated averaged parameters were applied in rotating mode since prediction of sliding depths is impossible. • It was advised to maintain the same differential pressure in sliding mode as when rotating with the 25 klbs for the entire section. • A 0.2 rpg motor was also used throughout the section, which yielded a mud flow rate of 425 GPM.
8.5″	• An RH-713 bit with tier 1 cutters was used in the lateral with an estimated 95% rotating and 5% sliding. • Downhole WOB in rotating mode was simulated with 20 klbs at an RPM of 195, resulting in an average ROP of 72 ft/hr.

Table 5.3. PDS Finalized Detailed simulation Well D

Bit #	Bit Size	Bit ID	Nozzle Size	Depth In	Depth Out	Interval Section	WOB	Surface RPM	Motor RPM	Bit RPM	MW	GPM	Sim. ROP	Avg. ROP	Avg. IADC Wear Out	Bit Hours
1	17.5	Baker HC6055	7x12	335	620	285	8	70	0	70	8.4	800	204		0.3	
1	17.5	Baker HC6055	7x12	620	1520	900	20	100	0	100	8.4	800	158	167	1.6	7
2	12.25	Baker 506	6x16	1521	6610.5	5089.5	35	20	60	80	9.3	750	85		0.8	
2	12.25	Baker 506	6x16	6610.5	7530	919.5	35	20	60	80	9.3	750	63		0.9	
2	12.25	Baker 506	6x16	7530	7607	77	45	20	60	80	9.3	750	62		1	
2	12.25	Baker 506	6x16	7607	8400	793	45	15	60	75	9.3	750	48		1.1	
2	12.25	Baker 506	6x16	8400	10100	1700	35	20	60	80	9.3	750	48		1.4	
2	12.25	Baker 506	6x16	10100	10380	280	45	15	60	75	9.3	750	30		1.6	
2	12.25	Baker 506	6x16	10380	10400	20	45	25	60	85	9.3	750	29		1.6	
2	12.25	Baker 506	6x16	10400	11100	700	45	25	60	85	9.3	750	45		1.7	
2	12.25	Baker 506	6x16	11100	11700	600	50	20	60	80	9.3	750	27	58	1.9	175
3	12.25	Baker 506	6x16	11700	12471	771	50	20	60	80	9.3	750	35		0.8	
3	12.25	Baker 506	6x16	12471	12581	110	60	10	60	70	9.3	750	49		0.9	
3	12.25	Baker 506	6x16	12581	13600	1019	50	20	60	80	9.3	750	38	37	1.5	51
4	8.75	Baker 405	5x13	13600	15486	1886	25	20	85	105	10.3	425	54			
														54	0.6	35
5	8.75	Reed 713	5x13, 2x14	15486	24453	8967	20	110	85	195	10.3	425	72			
														72	2.2	125
														Avg Well ROP		61
														Time		394

5.1.2. Completion Offset Data Collection and Simulation

To obtain the necessary completion rock properties, drilling core and log data from various sources were collected. Core samples from Well C were subjected to rock mechanical testing at the University of Pittsburgh, with the results presented in Chapter 6. Additional core analysis and testing were conducted at the Chesapeake Laboratory Facility to determine the porosity and permeability of core samples from the Caney formation.

5.1.3. Determination of Properties from Core Plugs

The University of Pittsburgh conducted mechanical property testing on core plugs, which included UCS, indirect tensile strength, fracture toughness, triaxial testing, and creep testing. Details of these tests are provided in the University of Pittsburgh's part of Chapter 6. The rock properties derived from testing of Reservoir 3 were used to establish the geomechanical and petrophysical log formation constants for Well D. These formation constants are essential for the D-ROCK software to calculate geomechanical and petrophysical properties along the wellbore using drilling data. The D-ROCK module employs Equations 5.1 to 5.7 to generate a complete geomechanical and petrophysical property log while drilling a lateral well in an unconventional reservoir. The CCS is calculated from the inverted ROP model in D-ROCK and which includes operational parameters ROP, RPM and WOB, and specific functions for h_x (bit hydraulics), W_f, (bit wear) and B_x(bit design). The constants a_1 b_1, and c_1 are bit type specific constants (Nygaard and Hareland, 2007). To ensure accuracy for the specific reservoir formation as in this case, the Caney Shale formation constants must be calibrated. The constants a_E, b_E, a_S, and b_S are utilized for calculating UCS, and Young's Modulus (E) from the CCS. Similarly, the constants k_{por1}, k_{por2}, k_{prm3}, and k_{prm4} are used for determining porosity ($\emptyset$) and permeability(K_P) (Thameen et al., 2019),

$$CCS = \left(\frac{ROP}{K \times DWOB^{b_1} \times RPM^{c_1} \times h_x \times W_f \times B_x}\right)^{\frac{1}{a_1}} \quad (5.1)$$

The formation constants were derived through regression analysis. UCS and Young's modulus (E) can be defined as,

$$UCS = CCS/\left(1 + a_S \times P_C^{b_S}\right) \quad (5.2)$$

$$E = CCS \times a_E \times (1 + P_C)^{b_E} \quad (5.3)$$

The porosity (ϕ) and permeability (K_P) correlations (Cedola et al., 2017a and Cedola et al., 2017b) for the Caney formation were obtained from the core analysis shown below:

$$\emptyset = k_{por1} \times UCS^{-k_{por2}} \quad (5.4)$$

$$K_P = k_{prm3} \times \emptyset^{k_{prm4}} \quad (5.5)$$

Here, a_S, b_S, a_E, b_E, k_{por1}, k_{por2}, k_{prm3} and k_{prm4} are reservoir specific formation constants calculated using laboratory test data on Reservoir 3 core samples. Poisson's ratio is a crucial elastic property of reservoir rock that is essential for stimulation design, as it measures the material's compressibility in a direction perpendicular to the applied stress. The rock (Mohr) failure envelope method was employed to determine the angle of internal friction (β), which was then used to calculate friction angle (β) the coefficient of earth at rest (K_0) and Poisson's ratio (ν) (Hareland and Hoberock, 1993).

$$\beta = \sin^{-1}\left[1/\left(1+\left\{\frac{4\Delta}{UCS \times a_S \times \left[P_{e1}^{b_S} - P_{e2}^{b_S}\right]}\right\}\right)\right] \tag{5.6}$$

$$K_0 = 1 - \sin\beta;\ \ \nu = \frac{K_0}{1+K_0} \tag{5.7}$$

An example of the process used to calculate the reservoir constants is the correlation between porosity and UCS, as illustrated in Figure 5.3. This correlation is determined using Onyia's Equation 5.8 (Onyia, 1988), applied to Well C core samples from Reservoirs 1, 2, and 3.

$$\delta_{ult} = K_6 + \frac{K_7}{\Delta t_c} \tag{5.8}$$

The trendline for the data, represented by the equation $y = 231.57x^{-1.95}$ where y is the porosity (in percent) and x is the UCS (in ksi), represents Equation 5.4 above. In this case, 231.57 is k_1 and -1.95 is k_2.

To achieve a more accurate alignment with D-ROCK calculations and units including Chesapeake Laboratories petrophysical measurements, the constants were obtained as 41.03 for k_{por1} and -0.636 for k_{por2}. These revised constants are then input into the D-ROCK software to define formation constants for the Caney Shale. Another example of the process used to calculate the reservoir constants is permeability versus porosity as shown below in Figure 5.4.

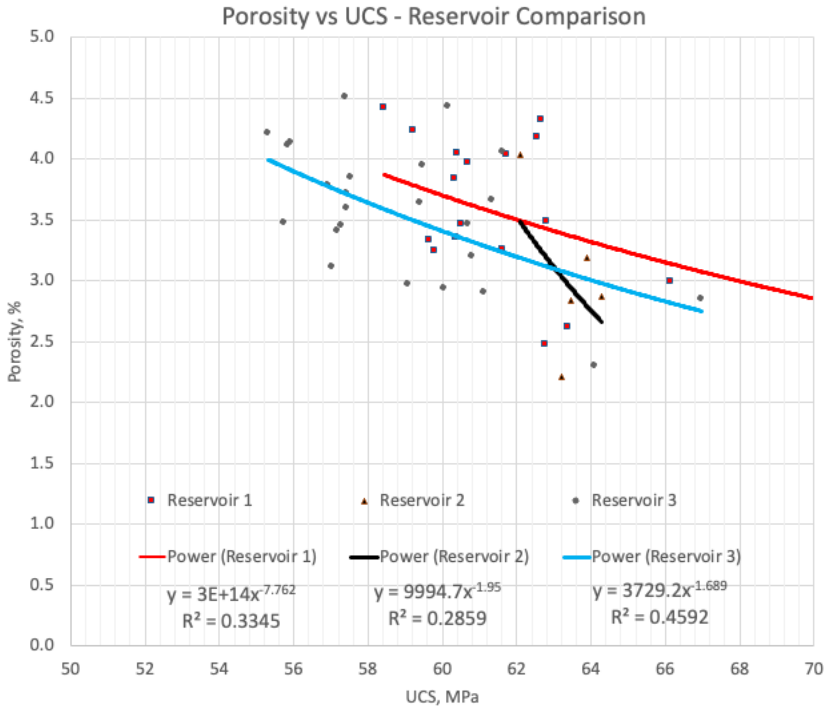

Figure 5.3. Porosity versus UCS - Well C (Reservoir 1, 2 and 3 Comparison).

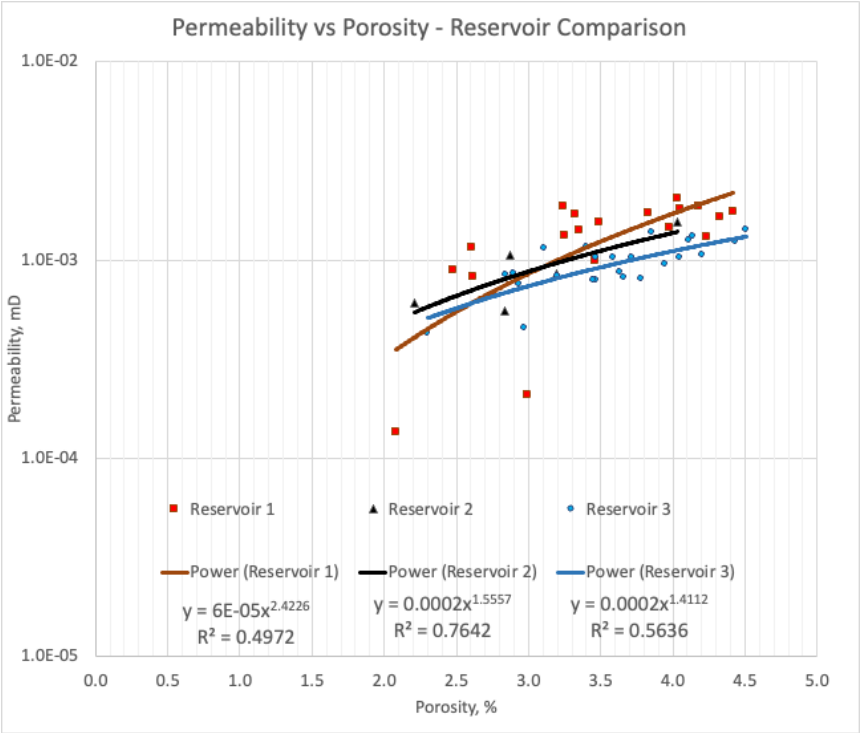

Figure 5.4. Permeability versus Porosity - Well C (Reservoir 1, 2 and 3 Comparison)

5.1.4. Determination of Properties from Drilling Data

After the D-WOB software derives the friction coefficient and DWOB along the wellbore, this information is formatted into the required data file and input into the D-ROCK software. Within D-ROCK, the correlation constants derived from uniaxial and triaxial tests are used to predict unconfined compressive strength (UCS), Young's Modulus (E), Poisson's Ratio, porosity, and permeability based on the compressive strength of cores (CCS) on a per-foot basis. D-ROCK generates a comprehensive geomechanical and petrophysical log profile for the lateral section of the well.

Using these correlations, as UCS increases, porosity, permeability, and Young's Modulus tend to decrease, while Poisson's Ratio increases. This indicates that zones with a higher Poisson's Ratio exhibit signs of increased rock brittleness and lower permeability compared to zones with higher UCS.

The formation constants, listed in Table 5.4, represent the correlations between UCS, CCS, E, K_P, $\emptyset$ extracted from core testing for Reservoir 3. A comparison with the Upper Eagle Ford Shale formation constants is also provided as a comparison.

Table 5.4. Formation Constants Compared to the Eagle Ford Shale

	Eagle Ford	**Caney**
Constant ID	Formation Constant	Formation Constant
as	0.04078	0.601
bs	1.0396	0.404
ae	0.4209	0.441
be	-0.16773	-0.16
kpor1	92.529	41.03
kpor2	0.636	0.636
kprm1	6.9302	23.08
kprm2	2.5313	1.586

By extrapolating drilling parameters across the lateral and inputting them into the D-WOB the DWOB for Well B was calculated and compared to the surface measured WOB (SWOB). To illustrate the importance and the difference between SWOB and DWOB, it can be observed from Figure 5.5 that as wellbore friction increases, especially in the build section, the difference between SWOB and DWOB can reach 5-10 klbf. However, as mud weight increases and the drill string settles

on the bottom throughout the lateral, the surface and downhole WOB converges to approximately 5 klbf, though a difference persists.

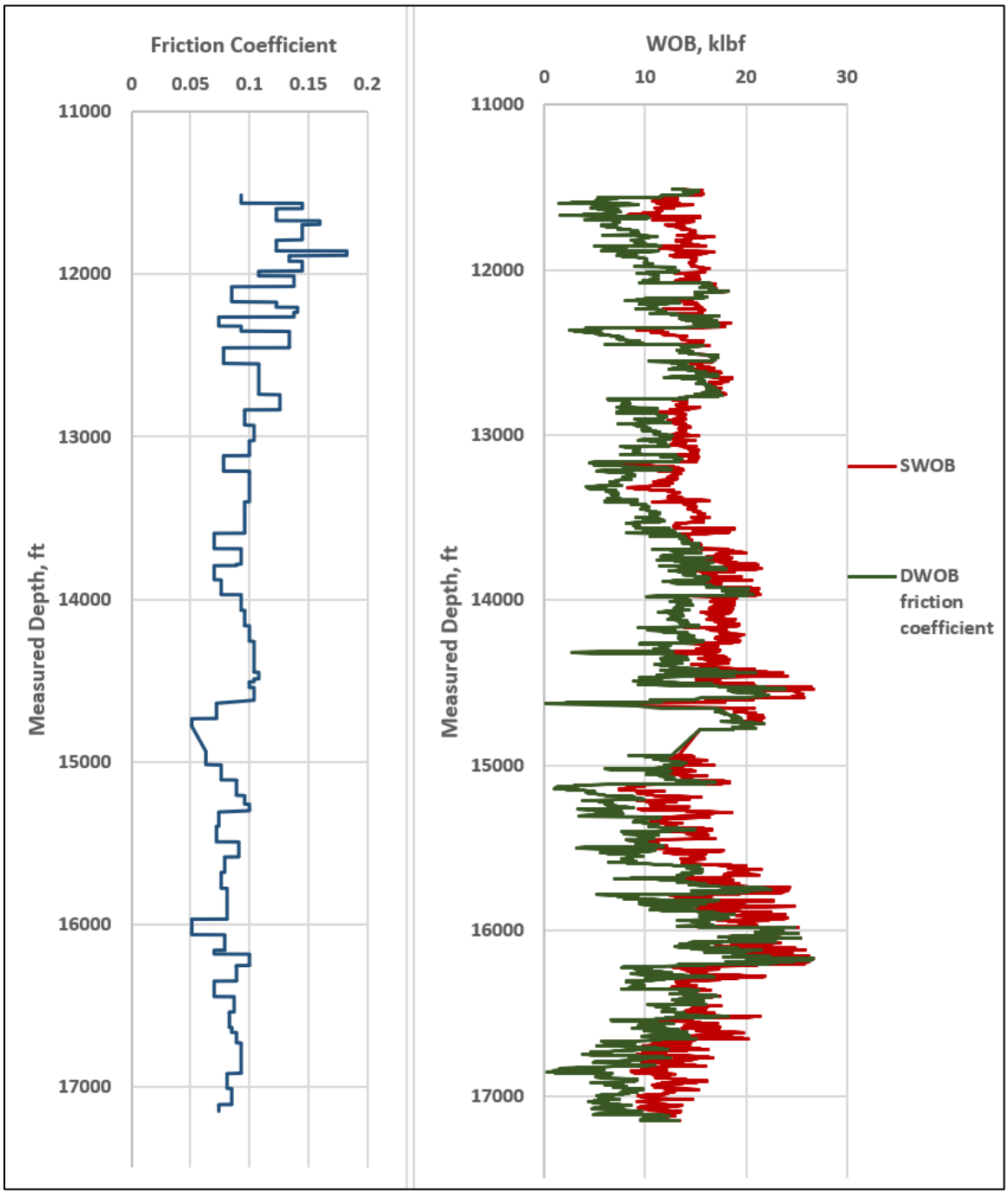

Figure 5.5. WOB and Friction versus Measured Depth for Well B

Figure 5.6 is a geomechanical log for Well B which was constructed using the correlations in Equations 5.2 to 5.7 and the constants for Reservoir 3.

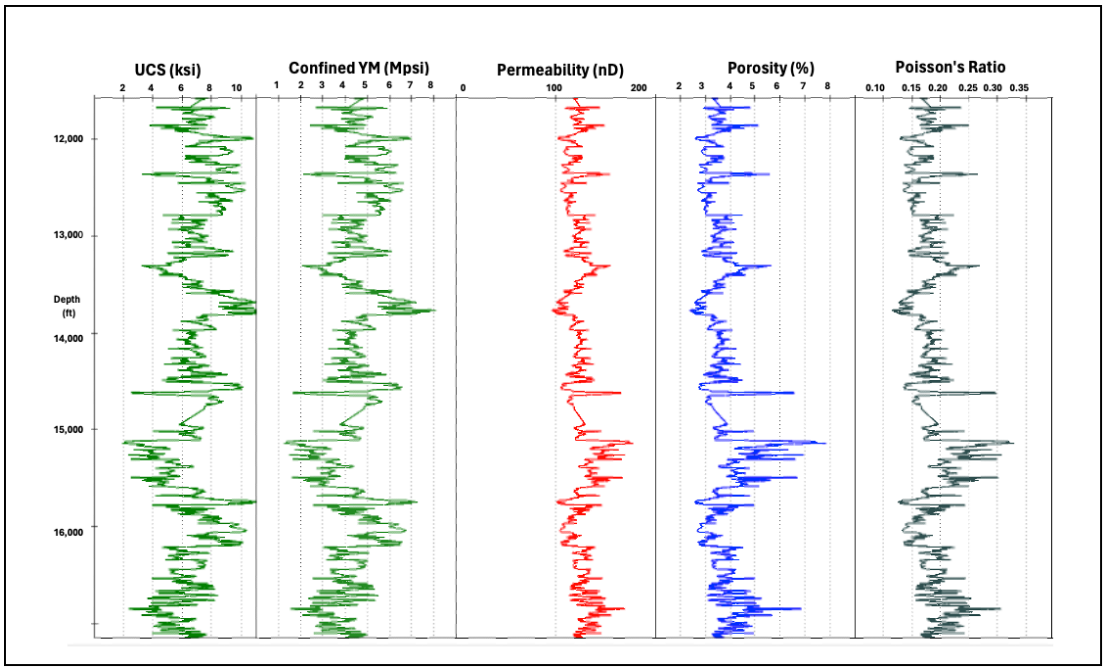

Figure 5.6. D-ROCK Output for Well B

5.1.5. Production Offset Data and Simulation

Optimization methods were evaluated to determine the highest impact on production from a completions standpoint to optimize the production. The study was two-fold, first data from the 97 horizontal wells from the Springer field in SW Oklahoma study were utilized. Within the study, lateral length and treatment volume were compared and evaluated to determine what had the largest impact on production. To evaluate the production, the top 5 wells for the years between 2014 and 2019 had their production averaged and each vintage of wells production was plotted. As displayed in Figure 5.7, the later drilled wells performed significantly better.

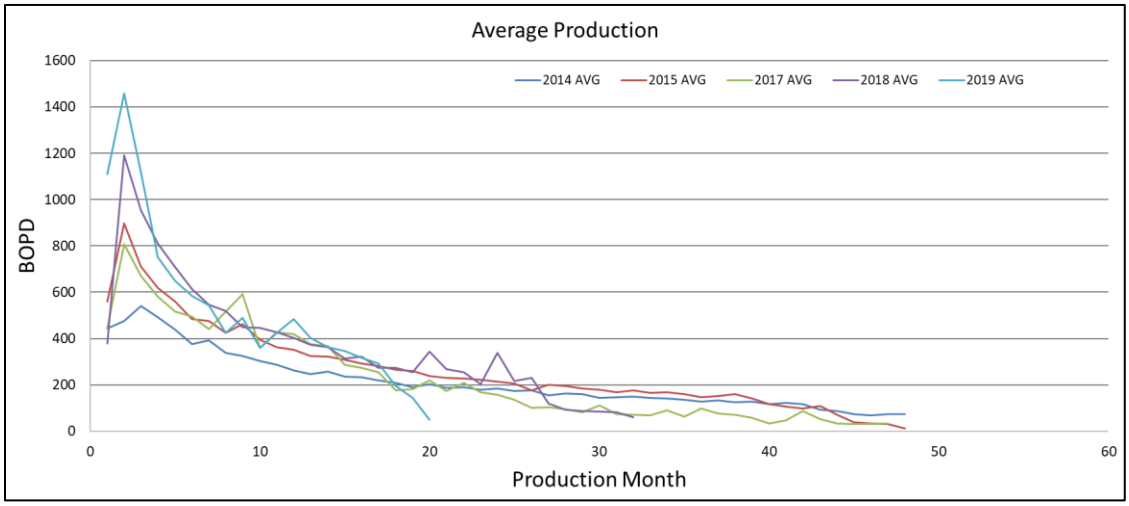

Figure 5.7. Top 5 Wells for Each Year 2014-2019 Production Averaged and Plotted Against Other Vintage Wells

As displayed in Figure 5.8, the treatment lengths became significantly longer and the treatment

volumes per foot increased as displayed in Figure 5.9.

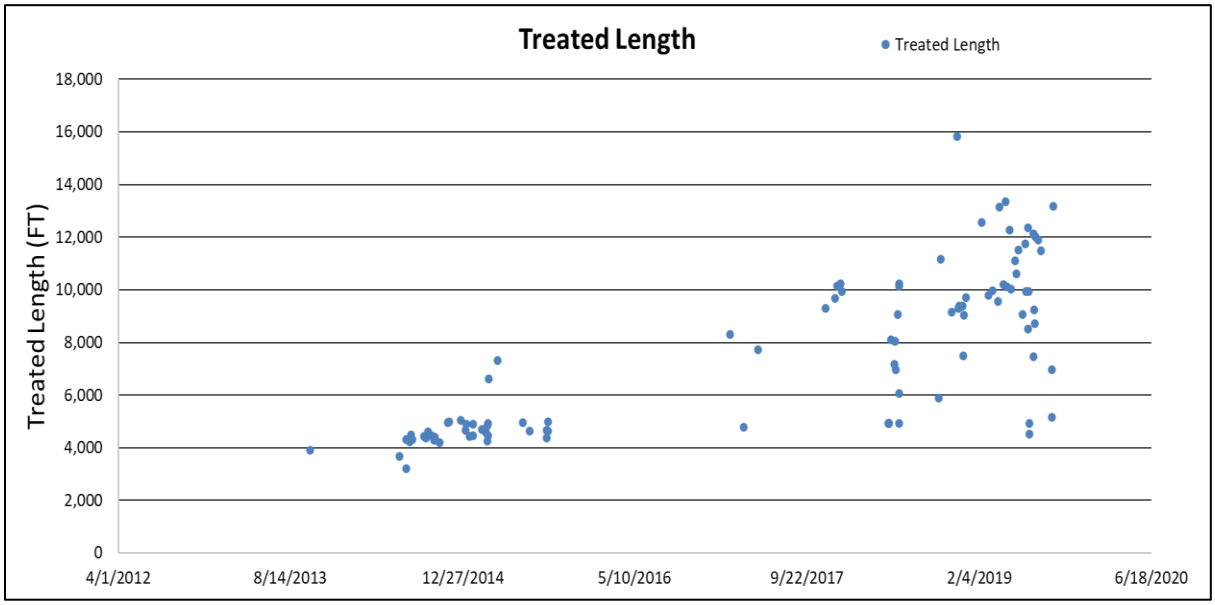

Figure 5.8. Springer Treatment Length versus Time

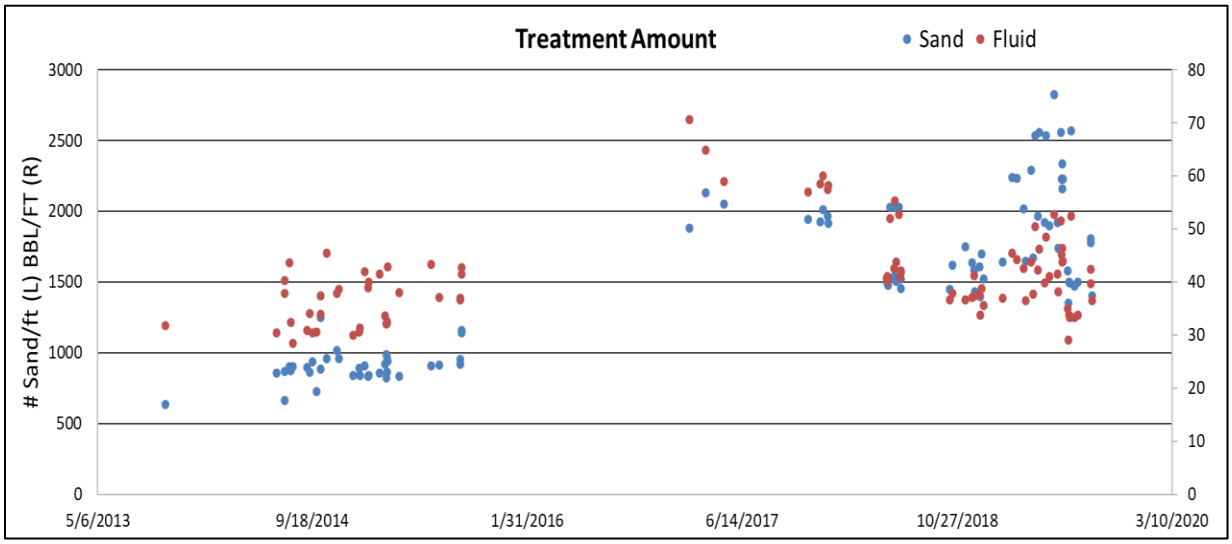

Figure 5.9. Springer treatment volume versus time

When the production of 1st year oil was broken down on a per foot basis, the wells did not seem to significantly improve due to treatment as displayed in Figure 5.10.

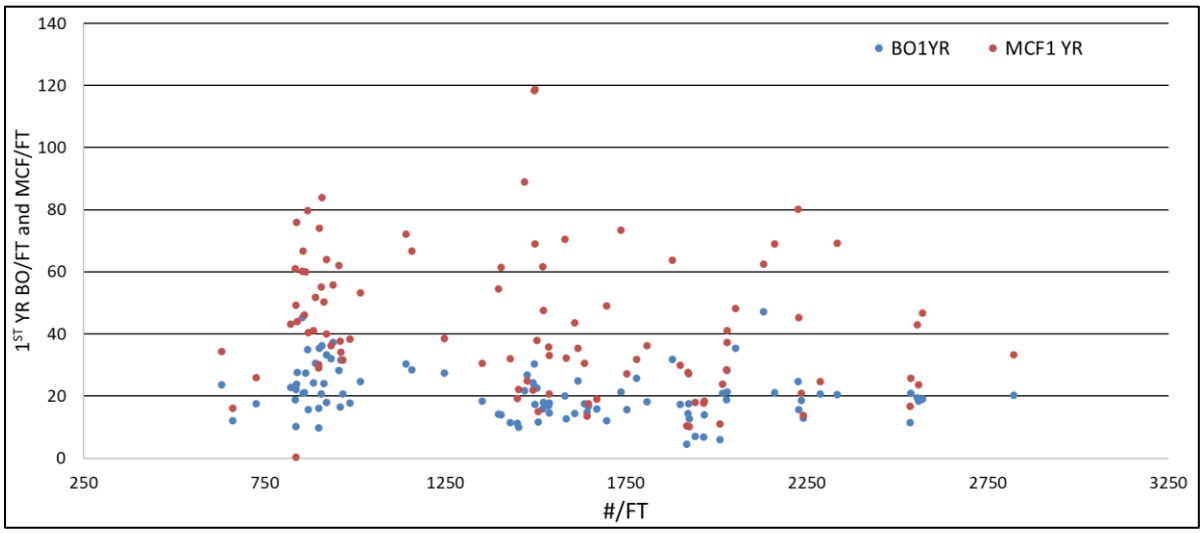

Figure 5.10. Springer first year oil and gas production versus proppant treatment per foot

This prompted an evaluation to investigate whether factors other than treatment volumes significantly impacted production. The second part of the study used GOHFER software (GOHFER, 2016) to measure the impact on cluster perforations and spacing because perforation data is not publicly available. Within the model, a treatment design was initially created using a 10-perforation setup. A modified version of this model was then developed, omitting three evenly spaced perforations to simulate scenarios where some perforations do not receive treatment fluid or are excluded from the design. Both designs had the production model with identical reservoir inputs and the output are listed in Table 5.5 below.

Table 5.5. Impacts on production with reduced cluster efficiency.

			Cumulative (BO/MCF)		Rates (BOPD/ MCFPD)		Cumulative (BO/MCF)		Rates (BOPD/ MCFPD)	
Design	IP Oil	IP Gas	1 YR Oil	1 YR Gas	1 YR Oil	1 YR Gas	5 YR Oil	5 YR Gas	5 YR Oil	5 YR Gas
Well 1 100% Perforation	805	2,817	83,747	293,114	148	520	201,079	703,776	44	155
Well 1 70% Perforation	595	2,082	71,200	249,201	137	178	187,578	656,525	48	168

Between the two studies it was determined that lateral length and perforation spacing had the largest impact on production and these points should be focused on going forward.

5.2. Post Analysis of Drilling and Completion of the Horizontal Well

Upon completion of the drilling of Well D well, a post-analysis procedure compared the simulated results with the actual drilling outcomes, including UCS, ROP and on bottom drilling time. The

analysis revealed that Well B had higher UCS values in sandstone formations, while Well D showed higher UCS in the Caney formation. The formation top depths encountered during drilling differed from those used in the simulation, necessitating adjustments in the PDS to better match the actual encountered UCS in Well D. Overall, the simulated on bottom drilling time matched well with the actual encountered on Well D.

Well D's production data, sourced from the Oklahoma Tax Commission (2023), was analyzed, revealing monthly oil and gas figures. Initial Production (IP) suggested that the actual performance closely matched the projected type curve for Reservoir 3. The gas-oil ratio (GOR)

began at approximately 3 MCF/BO and gradually increased to 6 MCF/BO over seven months, aligning with typical Reservoir 3 characteristics. The discrepancies were attributed to real-life operational challenges, such as weather-related shut-ins, and the time it took for the GOR to stabilize. Future gas production is expected to more closely align with the type curve as the well continues to produce.

5.2.1. Drilling Post Analysis

The post-drilling analysis for Well D involved a comparison of rock strength (UCS) between the simulated well, as generated by the PDS, and the actual drilled well. A detailed comparison of Well D's drilling results with the pre-drilling plan is presented in Table 5.6.

Table 5.6. Simulated vs Actual Well D Results

Simulated Well D Results					**Actual Well D Results**				
Hole Size (in)	Depth In (ft)	Depth Out (ft)	Avg. ROP (ft/hr)	Hours (hrs)	Hole Size (in)	Depth In (ft)	Depth Out (ft)	Avg. ROP (ft/hr)	Hours hrs)
17.5	335	1,520	167.1	7.0	17.5	208	1,528	335.5	3.9
12.25	1,520	13,600	53.4	226.5	12.25	1,528	13,660	59.1	205.2
8.75	13,600	24,453	67.8	159.5	8.75-8.50	13,660	22,708	60.3	149.7
Average Well ROP			61.4		**Average Well ROP**			62.7	
Total Rotating time				393.0	**Total Rotating time**				358.8

The post-analysis revealed that the well was drilled in close alignment with the simulated drilling parameters, particularly bottom hole hours. Key differences were observed in sand content and hardness, as well as the number of bit runs on Well D, which had less footage in the lateral section. While the average on-bottom ROP aligned well with the simulated results, Well D was drilled 34 hours faster than simulated. This difference is attributed to variations in section lateral lengths, the use of additional bits, and the presence of more and harder sand in certain formations. The lithology of Well B showed higher sandstone content than Well D. Gamma ray logs were used to determine the lithology contents, revealing Well B had more and harder sand compared to Well D. The average UCS for Well B was 11.5 kpsi and 10.5 kpsi for Well D. However, Well B exhibited higher UCS values in the Caney formation than Well D.

Well D's 17.5-inch section was drilled with a higher ROP and was completed 3 hours faster than pre-simulated due to the controlled drilling implemented in the simulation process. The 12.25-inch section of Well D was drilled 21.3 hours faster than the simulated time but with an additional bit and trip. Additionally, Well D encountered less sand, resulting in a lower apparent rock strength (ARS)

compared to Well B. For the 8.5-inch section, the simulation projected a total depth (TD) of 24,453 feet, but Well D reached only 22,708 feet, leading to a reduction in drilling time for this section due to the shorter lateral length.

The formation top depths used in the simulation process differed from the actual encountered formations. To accurately compare and analyze both strength logs, it was necessary to correlate Well B formation tops with the actual tops encountered in Well D. Some formations present in Well B were not encountered in well D and were therefore removed in the simulation process. Adjustments using PDS software involved entirely removing, thinning, or stretching certain formations to fit the actual formation tops. Table 5.7 shows the formations encountered in both wells with their corresponding top depths.

The second part of the post-drilling analysis involved a 'follow-up' comparison of the simulated ROPs to the actual ROPs observed in Well D. The 'follow-up' module within the PDS recalculates ROPs for a planned or simulated well using the actual field operational data.

The recalculated ROPs were then overlaid onto the actual field ROPs for comparison, as shown in Figure 5.11. The comparison, conducted on a foot-by-foot basis for every drilled formation, indicated similar ROP trends, with slight deviations observed in the Hoxbar/Deese formations where the simulated well had higher ROPs due to the observed higher and harder sand content in Well D. The drill bits used in the analysis are also depicted in Figure 5.11.

Table 5.7. Formations encountered in both wells.

Formations	WELL B	WELL D
HOXBAR	3,222 ft	2,995 ft
DEESE	5,505 ft	5,280 ft
TUSSY	6,935 ft	7,561 ft
ATOKA	9,092 ft	9,097 ft
DORNICK HILLS	9,928 ft	10,118 ft
SPRINGER	11,105 ft	11,222 ft
HUMPHRIES	11,275 ft	11,402 ft
SIMS	11,595 ft	11,701 ft
GOODWIN	12,471 ft	12,036 ft
CANEY	14,095 ft	13,411 ft

5.2.2. Completion Post Analysis

The following section analyzes Well D's production data, sourced from the Oklahoma Tax Commission (2023). Table 5.8 displays the monthly oil and gas production for Well D. It is important to note that this public data may differ slightly from the actual production data. In Oklahoma, oil production is reported by the purchaser rather than the operator, meaning the public records reflect the barrels of oil sold, not necessarily the barrels produced.

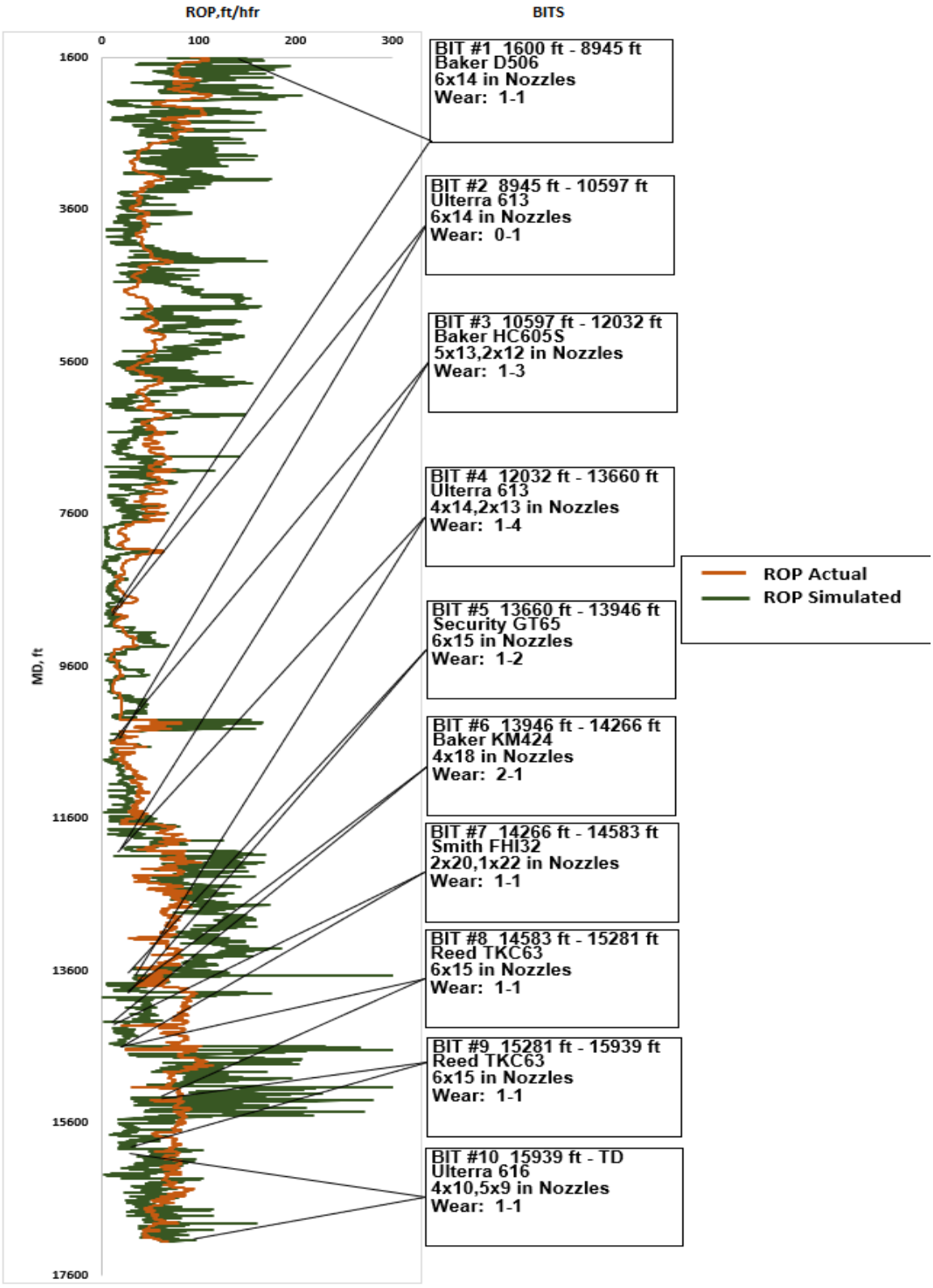

Figure 5.11. Follow-Up Analysis for Well D

Table 5.8. Well D's production obtained from the Oklahoma Tax Commission (Oklahoma Tax Commission, 2023)

Year	Month	Oil Prod (BBLS)	Gas Prod (MCF)	AVG Daily Oil Rate (BOPD)	AVG Daily Gas Rate (MCFPD)	EST Days	GOR	CUM Oil	CUM Gas
2021	November	1,845	7,240	185	724	10	3.9	1,845	7,240
2021	December	16,603	54,810	536	1,768	31	3.3	18,448	62,050
2022	January	12,861	47,235	415	1,524	31	3.7	31,309	109,285
2022	February	9,705	42,176	347	1,506	28	4.3	41,014	151,461
2022	March	11,246	56,975	363	1,838	31	5.1	52,260	208,436
2022	April	9,366	46,736	312	1,558	30	5.0	61,626	255,172
2022	May	8,799	49,490	284	1,596	31	5.6	70,425	304,662
2022	June	7,966	47,658	266	1,589	30	6.0	78,391	352,320
2022	July	7,025	42,788	227	1,380	31	6.1	85,416	395,108
2022	August	6,934	41,159	224	1,328	31	5.9	92,350	436,267
2022	September	6,251	38,082	208	1,269	30	6.1	98,601	474,349
2022	October	6,663	37,897	215	1,222	31	5.7	105,264	512,246
2022	November	5,455	35,044	182	1,168	30	6.4	110,719	547,290

Figure 5.12 displays the field production from Well D against the projected type curve for Reservoir 3. The GOPHER projected type curve (P50) is displayed with a black line, and the 20% high and low bounds are also displayed. To project the daily rates for Well D, the average daily rate was calculated, that rate was placed in the middle of the month, and the production day was referenced from the initial production (IP) date.

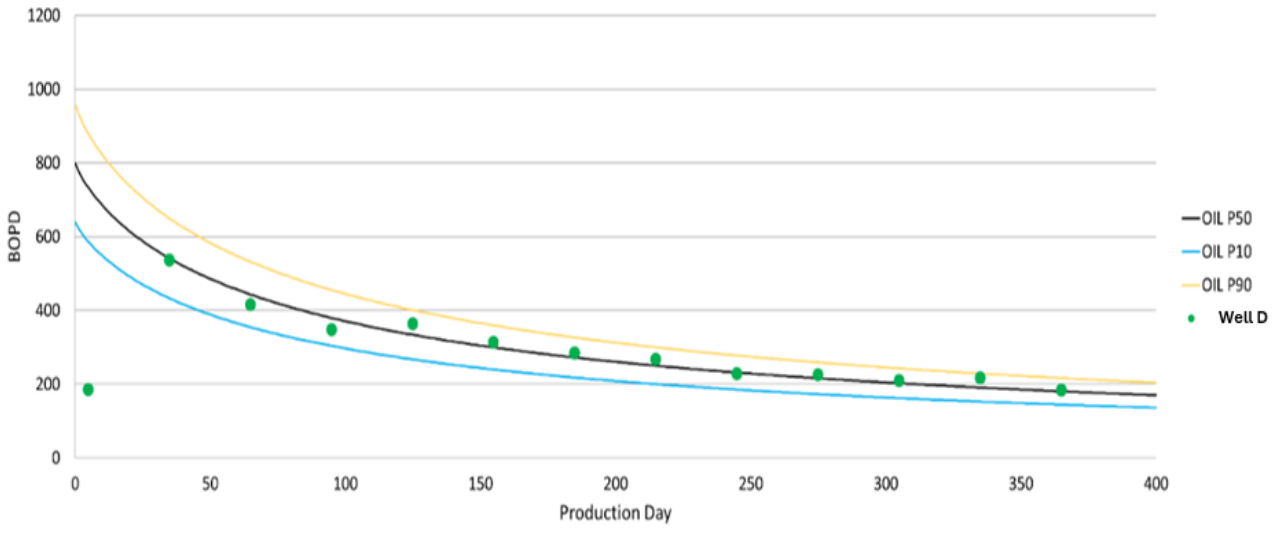

Figure 5.12. Well D field production (green dots) plotted against projected type curve

After completion fluids are cleaned up, additional monitoring is necessary to establish an accurate type curve for the well. However, the Initial Production (IP) oil volumes suggested that the projected type curve would closely match the actual performance. The gas-oil ratio (GOR) was initially projected to be 6 MCF/BO. In the first full month of production, the GOR of Well D was approximately 3 MCF/BO. Over time, as production continued, the GOR gradually increased, reaching nearly 6 MCF/BO by the end of the seventh month. This trend indicated that Well D was exhibiting the hydrocarbon characteristics typical of Reservoir 3 (Note: Reservoir 2 has a GOR of 4).

During the first 12 months of full production, Well D produced 108,874 barrels of oil (BO) and 540,050 thousand cubic feet (MCF) of gas. The type curve had projected production values of 117,840 BO and 707,065 MCF, resulting in percentage differences of 8% for oil and 24% for gas. The discrepancy in oil production is relatively minor and can be attributed to the type curve's assumption of ideal production conditions, which do not account for real-life operational challenges. In Oklahoma, ice storms and tornadoes can cause well shut-ins for up to a week, impacting actual production and, consequently, the type curve's accuracy. The gas production, however, showed a more significant deviation, primarily because the model assumed a consistent gas-oil ratio (GOR) throughout the well's life. It took nearly six months for the GOR to reach the anticipated 6 MCF/BO ratio. As the well continued to produce, the average GOR gradually aligned with the projection, and future gas volumes are expected to more closely match the type curve's estimates.

5.3. Design Drilling and Completion for Individual Areas

In continuation of the previous analysis of Well D, a ‘generic’ drilling strength log was used as the baseline scenario to evaluate various bits, pull depths, and drilling parameters through the PDS. This evaluation aimed to determine whether Well D could have been drilled more efficiently with different equipment and to also develop an optimized drilling plan for future wells in the Caney formation.

Stimulation design and well performance analysis have also demonstrated that completion design is critical in determining a well's production performance and estimated ultimate recovery. Key completion design metrics include cluster spacing, clusters per stage, sand volume, sand size, fluid volume, fluid type, and stimulation rate. In this evaluation, the original design proposed served as the baseline. The modeling process incorporated stage shadowing to ensure the fracture geometry was as accurate as possible. Various design modifications were then tested, and the modeled production responses were compared to the original design.

The design alterations did not deviate significantly from the original design, as it represents the current industry standard, and major changes would likely be irrelevant. However, the secondary stimulation optimization involved evaluating slightly modified designs against the proposed design to determine if any adjustments were worth pursuing.

5.3.1. Design Drilling

Two optimized scenarios were simulated:

- **Optimized Option 1:** This scenario utilized the same equipment and BHAs as the original well (Well D), specifically a combination of Conventional Bent Housing (CBH) and motor-driven Rotary Steerable System (RSS).
- **Optimized Option 2:** This scenario employed a Stand-Alone Rotary Steerable System (SA-

RSS) and incorporated a higher kick-off point (KOP) than in the original well (Well D). Figure 5.13 displays a depth versus time drilling curve comparing the non-optimized option from the PDS alongside the two optimized scenarios. Each curve accounts for the time spent on rotating and connections, tripping, circulating, rig service, cementing, nipple up, nipple down, rig up, and rig down. Among the scenarios, Option 2 achieved the shortest drilling time of 20.6 days, which is 18.3 days less than the non-optimized well and 37.4 days less than Well D.

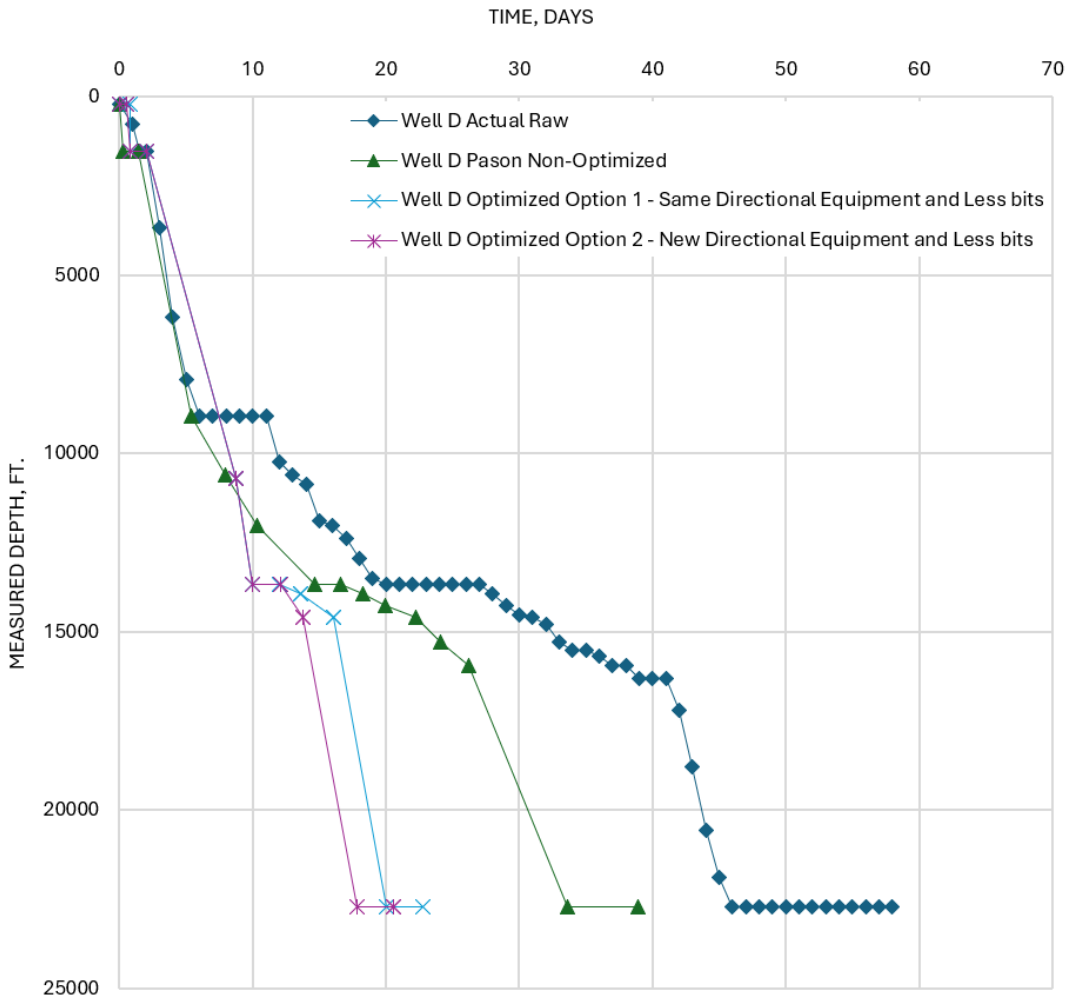

Figure 5.13. Optimized Simulation of Future Caney Wells based on Well D

For reference:

- Well D took 58 days to drill (excluding Non-Productive Time, or NPT the well took 38.3 days) and was drilled using a total of 11 drill bits.
- Using the same directional tools but with fewer bit changes and optimized drilling parameters, the drilling time was reduced to 22.7 days, utilizing a total of 6 bits.
- By employing a Rotary Steerable System (RSS) exclusively in the build and lateral sections and changing to an earlier kick-off point (KOP) by 300 feet (while remaining within the Caney formation), the drilling time was further reduced to 20.6 days, requiring only 5 bits.

Future Caney wells could potentially achieve a 30 to 40% reduction in drilling time compared to Well D. By utilizing the same directional tools with fewer bits and optimized parameters, drilling

time could be reduced by 15.6 days. Employing RSS exclusively in the build and lateral sections with a higher kick-off point (KOP) could further cut drilling time by 17.7 days.

5.3.2. Stimulation Design & Optimization

It is important to note that completion designs must be tailored on a well-by-well basis to account for geological variations. For instance, in Well D, the cluster spacing, and cluster count were adjusted during stimulation to better match the well's specific conditions. Table 5.9 presents the perforation design used in Well D.

Table 5.9. Well D perforation design

Section	Length of Lateral	Stage Length	Cluster Count	Cluster Spacing	Shots Per Cluster	Hole Count
Toe	1/3	240’	8	29’	4	32
Central	1/3	240’	9	27’	3	27
Heal	1/3	240’	10	23’	3	20

When developing and optimizing stimulation treatment, sand and fluid selection are two of the more critical components in the design. For this section, only the sand and fluid components are evaluated. During this evaluation, both the sand and fluids were evaluated separately and using the optimum combination of the two, a completed stimulation design can be created. The completion optimization and production analysis involved creating a production type curve, optimizing production using GOHFER, and conducting economic and sensitivity analyses. By varying stimulation parameters like cluster spacing, sand volumes, fluid volumes, and proppant size, an optimized completion design was developed. An economic sensitivity analysis identified the most impactful economic parameters on project viability.

During the sand selection process, the only evaluation conducted was grain size. Sand concentration was evaluated in the next section. The focal point of this study was to use the industry standard design of stimulation proppant of 100 mesh and 40/70 sand and compare it against a design that uses a much larger grain size of 20/40 sand. Table 5.10 displays the results of the altered sand design. All other variables within the stimulation design were held constant.

Table 5.10. Production output difference in replacing the 40/70 sand in the original design with 20/40 sand holding all other variables constant

			Cumulative (BO/MCF)		Rates (BOPD/ MCFPD)		Cumulative (BO/MCF)		Rates (BOPD/ MCFPD)	
Design	IP Oil	IP Gas	1 YR Oil	1 YR Gas	1 YR Oil	1 YR Gas	5 YR Oil	5 YR Gas	5 YR Oil	5 YR Gas
Original	802	2809	83,604	292,615	148	519	201,913	706,696	45	159
20/40 Original	761	2664	77,551	271,427	138	483	204,739	716,586	65	227

As shown, using larger grain size sand had minimal impact on the well's productivity. This outcome reinforces the understanding that the effective permeability of the fracture is significantly higher than that of the reservoir rock, meaning that increasing the fracture's width or permeability does not lead

to improved production. Furthermore, larger grain sizes are more prone to wedging within the fracture during stimulation, increasing the risk of a screen-out during the fracture job. Given the heightened risk of screen-out and the negligible productivity gains, the use of larger grain sand is not recommended. Future designs will therefore default to smaller grain sand following this evaluation.
During the fluid selection process, two fluid types were evaluated: slickwater and linear gel. The linear gel design is the standard approach used during stimulation, typically introduced towards the end of the process to ensure that higher proppant concentration sand is effectively carried into the fracture by slightly increasing the fracture width due to the fluid's higher viscosity. In the slickwater design, the linear gel portion was replaced with slickwater. Table 5.11 presents the results of these two design approaches.

Table 5.11. Production output difference in replacing the linear gel in the original design with slickwater holding all other variables constant

			Cumulative (BO/MCF)		Rates (BOPD/ MCFPD)		Cumulative (BO/MCF)		Rates (BOPD/ MCFPD)	
Design	IP Oil	IP Gas	1 YR Oil	1 YR Gas	1 YR Oil	1 YR Gas	5 YR Oil	5 YR Gas	5 YR Oil	5 YR Gas
Original	802	2,809	83,604	292,615	148	519	201,913	706,696	45	159
Slickwater	752	2,560	78,038	273,134	139	486	181,777	636,220	36	126

As shown, the linear gel and slickwater designs resulted in only a slight difference in well productivity, with the linear gel outperforming slickwater by approximately 10%. In addition to this modest performance advantage, linear gel also offers other benefits, such as reducing the risk of screen-outs during stimulation. Given these factors, a hybrid design incorporating both slickwater and linear gel is recommended.
Another fluid commonly used in the industry is crosslinked gel. However, previous research has demonstrated that crosslinked gels can negatively impact productivity, particularly in tight formations. Although crosslinked gels can break down, the residue they leave behind can clog the pore throats of tight reservoir rocks, hindering the flow of reservoir fluids into the fracture system and thus reducing production. Studies have shown that the average permeability damage from gel residue invasion can exceed 12% in low-permeability rock (Liang et al., 2020). Due to these detrimental effects, crosslinked gels were not evaluated in this study.

5.3.3. Sand Content

An investigation was conducted within GOHFER to determine how the pounds of sand per square foot within the fracture would impact production. Pounds of sand per square foot would have a correlation to the pounds per gallon of sand pumped during the fracture treatment. If more pounds per gallon are pumped, the pounds per square foot will increase. The test conducted took five different stimulation treatments in Reservoir 3 and evaluated the first year of oil production. Figure 5.14 displays the results of the test.

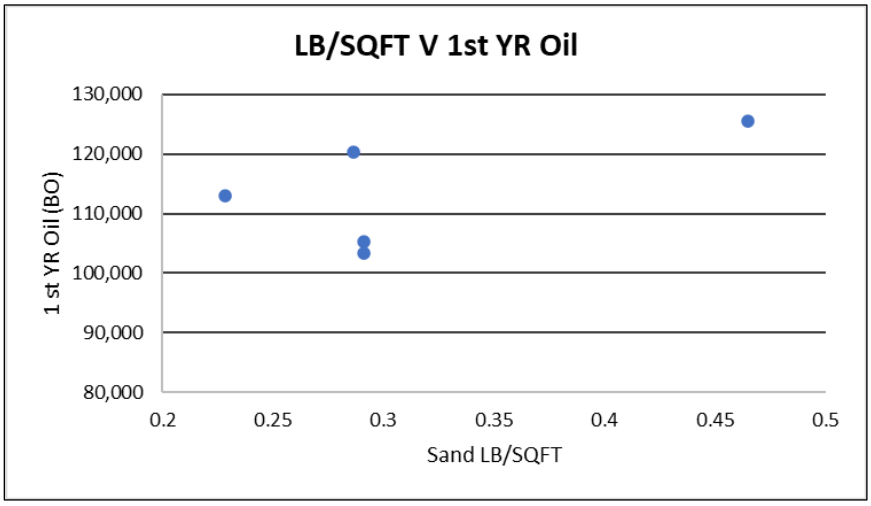

Figure 5.14. Pounds of sand per square foot in the fracture versus first-year oil production in Reservoir 3

As shown, the pounds per square foot of sand in the fracture did not correlate with the first year of oil production in the same reservoir test. This finding is consistent with the study by Briggs et al. (2014) in the Fayetteville Shale. It also aligns with the sand grain study, which confirmed that the fracture's effective permeability is significantly higher than that of the reservoir rock, meaning that increasing the fracture's width or permeability does not lead to improved production.

Finally, Dimensionless Fracture Conductivity (FCD), a relative measure of the difference between fracture and reservoir permeability, was compared to well performance. The primary methods to increase FCD include using larger proppant sizes and increasing the sand concentration in the treatment fluid, which results in more pounds of sand per square foot in the fracture. However, as demonstrated in the previous sections, these strategies do not significantly enhance well performance, indicating that FCD does not correlate strongly with well productivity.

5.3.4. Stage Shadowing

Stage shadowing is employed to ensure that stimulations accurately reflect true reservoir conditions. This technique adjusts the stresses in the reservoir based on the outcomes of a previous stage, using these updated stress values to inform the subsequent stage. Figure 5.15 illustrates the stress shadowing effect.

The top portion of Figure 5.15 represents a typical frac design, which assumes that all perforations are open, take an equal amount of fluid, and break down evenly. However, the middle figure shows a more realistic scenario during the first stage of a well, assuming identical lithology. Here, the outermost perforations absorb most of the fluid and create longer fractures. This occurs because the outer perforations experience stress only from the inner perforations, while the inner perforations face stress from both sides. As a result, the outer perforations can open wider, take in more fluid, and generate longer fractures. The bottom portion of Figure 5.15 demonstrates the effects of stress shadowing on subsequent fractures. The stresses generated by the previous stimulation stage cause the perforations near the plug to take in less fluid, while the perforations farther from the plug, which are closer to the near-virgin reservoir pressure, absorb more fluid. This results in a more complex and realistic fracture geometry, influenced by the stress shadowing from earlier stages.

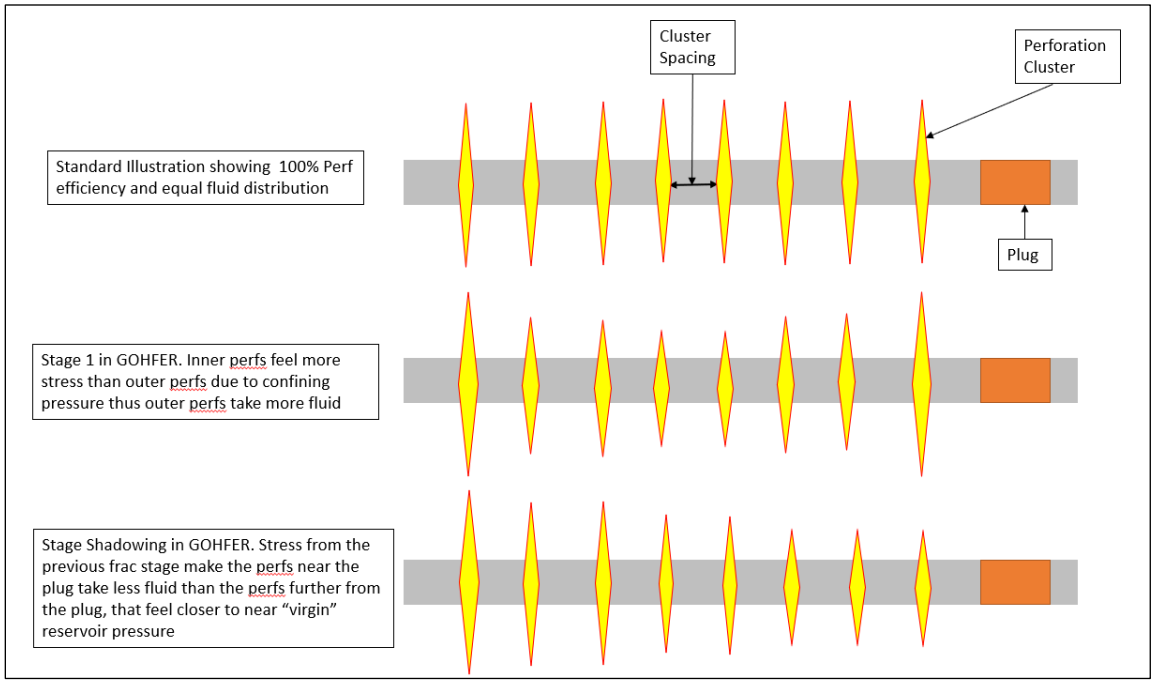

Figure 5.15. Stress shadowing effects on perforation clusters during stimulation and the resulting fracture geometry

A stage-shadowed fracture geometry represents the typical scenario for most stages in a horizontal well, as only the initial stage is free from the stress influences of previous stimulations. The effects of stage shadowing highlight that even when using the same stimulation design in the same reservoir, variations in fracture formation and geometry can occur. These differences can significantly influence the production curve, underscoring the importance of accounting for stage shadowing when evaluating well performance. Table 5.12 illustrates the impact on production values when comparing a well with no stage shadowing to one where stage shadowing effects were considered, with all other inputs held constant.

Table 5.12. Effect of stage shadowing on production.

			Cumulative (BO/MCF)		**Rates (BOPD/ MCFPD)**		**Cumulative (BO/MCF)**		**Rates (BOPD/ MCFPD)**	
Design	IP Oil	IP Gas	1 YR Oil	1 YR Gas	1 YR Oil	1 YR Gas	5 YR Oil	5 YR Gas	5 YR Oil	5 YR Gas
Original	802	2,809	83,604	292,615	148	519	201,913	706,696	45	159
Original Stage Shadow	805	2,817	83,747	293,114	148	520	201,079	703,776	44	155

As displayed, stage shadowing does not play a significant role in production. Although the fracture geometry varies between a "virgin pressure" reservoir versus the reservoir with a stimulation stage nearby, a similar rock volume is stimulated resulting in a near equivalent production profile. With this study completed, stage shadowing was not considered a concern for production value going

forward.

5.3.5. Cluster Efficiency

Finally, to model the effects of rock stress on perforation efficiency, a hybrid approach was taken to measure how the well would perform if all the perforations did not open. Within GOHFER, grid cells, as covered in previous sections, characterize the simulated fracture and reservoir flow. Although the collected foot-by-foot well data while drilling and this information can be used as input into GOHFER, creating grid cells that are only one foot wide would require computing power that does not exist yet.

To measure these effects of rock stress and determine if future work should be conducted on the subject, an alteration to the job design was conducted and compared against the original case to determine how much of an effect non-open or stimulated clusters would have on production. As covered in previous sections, perforation cluster spacing played the most significant role in enhancing production compared to sand and fluid volumes. Local operators confirmed these findings and how the industry has evolved in stimulation design. To test the hypothesis, the original design was loaded into GOHFER. Three of the 10 perforation clusters that were evenly spaced perforations were omitted and the stimulation was conducted without those perforations. Then the results were compared against the original design. Table 5.13 displays the cumulative oil production curve for both wells and daily oil rates.

Table 5.13. Impacts of reduced cluster efficiency on production

			Cumulative (BO/MCF)		**Rates (BOPD/ MCFPD)**		**Cumulative (BO/MCF)**		**Rates (BOPD/ MCFPD)**	
Design	IP Oil	IP Gas	1 YR Oil	1 YR Gas	1 YR Oil	1 YR Gas	5 YR Oil	5 YR Gas	5 YR Oil	5 YR Gas
Well 1 100% Perforation	805	2,817	83,747	293,114	148	520	201,079	703,776	44	155
Well 1 70% Perforation	595	2,082	71,200	249,201	137	178	187,578	656,525	48	168

Although the reduced perforation design had slightly higher daily rates at the end of the 5-year period, it will not produce nearly as much oil. The importance of increasing oil on the front end of production is much greater because of discounted cash flow. In the findings of this study, it is imperative to create as many flow paths as possible from the reservoir to the wellbore, and an engineered perforating design will help ensure that it is completed.

One crucial portion of modeling this effect and determining where to place the perforations is determining the method of perforating. In the US, the most common method of perforating is “plug and perf”. This method in horizontal wells involves lowering the plug and perforating guns to the horizontal portion of the well, then using the pumping equipment at the surface to pump the plug and perforating equipment to the desired lateral portion. When perforating, the guns are generally pulled at a constant rate out of the hole and fired at selected depths. The guns cannot stop moving when perforating due to the risk of tangling the eline and getting the eline tools stuck.

There will be some variance in the proposed perforating depth and what occurs in the field. The two main reasons for this are human error and changes in line tension. The eline used to pull the guns out of the hole and send the signal to fire the guns is generally 0.377" to 0.548" in diameter, so a slight 100-pound difference in line tension at the surface could have significant depth change effects downhole due to line stretch. When determining where to optimize perforations, finding a zone about 5' or longer is important so that any point in the zone will have similar rock property characteristics to the other perforated zones.

5.3.6. Selective Stimulation Potential

To evaluate the potential for selective stimulation in the Caney the rock mechanical and petrophysical property correlations to UCS developed in previous tasks for the Caney Reservoir 3 were used to obtain the needed inputs for parametric studies using GOHFER. 5-YR oil production was used to evaluate the changes in the GOHFER rock mechanical and petrophysical properties input parameters. Well D's pre-stimulation GOHFER estimated and proven production match type curve were used as the simulation starting point and from where the parametric studies were performed. The results from the study revealed the effect of the individual independent stimulation parameters. From a simulation test matrix, the correlations and trendline equations 5.9, 5.10 and 5.11 are given below in Figure 5.16 where UCS with the corresponding geomechanical and petrophysical properties, stage length and cluster spacing were changed on the x-axis and 5-YR oil production on the y-axis.

$$\text{5-YR Oil} = 11.721 \times \text{UCS} + 167.73 \quad (5.9)$$

$$\text{5-YR Oil} = -0.2895 \times \text{Stage Length} + 326.6 \quad (5.10)$$

$$\text{5-YR Oil} = -5.7635 \times \text{Cluster Spacing} + 394.01 \quad (5.11)$$

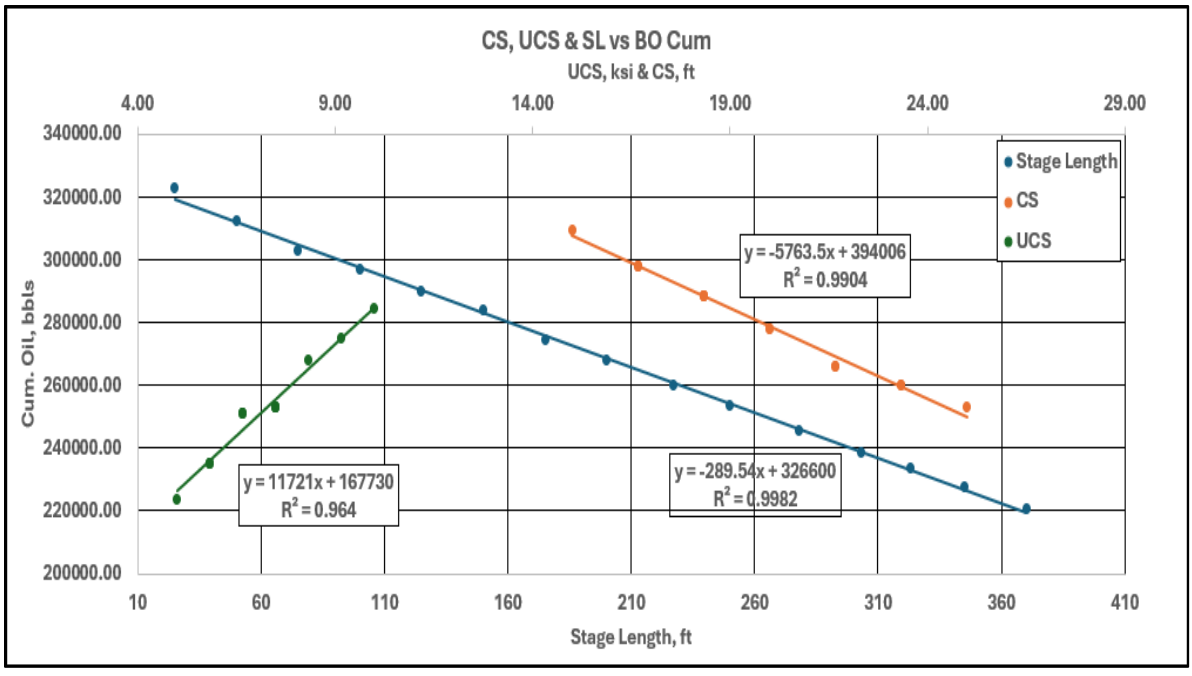

Figure 5.16. Cumulative 5-YR Oil per UCS, cluster spacing, and stage length trendlines.

A selective design algorithm was developed for selective stimulation which utilizes the unconfined compressive strength (UCS) values from D-ROCK on a foot-by-foot basis to determine corresponding permeability, porosity, Young's Modulus, Poisson's Ratio, and brittleness, based on the correlations developed for Reservoir 3. For the actual 34-stage design on Well D implemented by the operator, the selective stimulation algorithm was executed using the UCS data derived from D-ROCK. The results of this analysis are presented in Table 5.14.

Table 5.14. Selective Stimulation Algorithm Outputs for Well D Stage Design

Stg #	Plug Depth	UCS	Stage Length	Plug Depth	Stage Length	UCS	Grouping	Stage Length	Plug Depth	UCS	Final BO
1	22459	16	238	22570	127	17	180	180	22517	17	10855
2	22221	11	238	22416	154	14	180	180	22337	11	8972
3	21983	14	238	22228	188	11	180	180	22157	12	9088
4	21745	16	238	22056	172	12	180	180	21977	14	10030
5	21507	13	238	21926	130	16	180	180	21797	17	10814
6	21269	9	238	21799	127	17	180	180	21617	12	9233
7	21031	8	238	21626	173	12	180	180	21437	13	9595
8	20793	7	238	21465	161	13	180	231	21205	8	7413
9	20555	10	238	21221	244	9	240	231	20973	8	7279
10	20317	9	238	20944	277	7	240	231	20741	8	7435
11	20079	8	238	20698	246	8	240	231	20509	9	7836
12	19841	9	238	20475	223	9	240	231	20277	8	7553
13	19603	11	238	20230	245	8	240	231	20046	8	7475
14	19365	11	238	19977	253	8	240	231	19814	9	7575
15	19127	8	238	19749	228	9	240	180	19634	11	8919
16	18889	7	238	19567	182	12	180	180	19454	12	9152
17	18651	10	238	19373	194	11	180	231	19222	8	7494
18	18413	7	238	19123	250	8	240	231	18990	8	7315
19	18174	7	238	18817	306	7	360	231	18758	8	7438
20	17936	8	238	18620	197	11	180	335	18422	8	6456
21	17698	7	238	18304	316	6	360	231	18190	7	7063
22	17460	8	238	18036	268	8	240	231	17958	8	7361
23	17222	10	238	17746	290	7	240	335	17622	7	6254
24	16984	10	238	17485	261	8	240	231	17391	9	7591
25	16746	9	238	17262	223	9	240	231	17159	10	8030
26	16508	10	238	17053	209	10	240	231	16927	10	8000
27	16270	12	238	16833	220	10	240	231	16695	10	7967
28	16032	7	238	16619	214	10	240	231	16463	9	7732
29	15794	5	238	16424	195	11	180	180	16283	14	9772
30	15556	4	238	16213	211	10	240	335	15947	6	6087
31	15318	6	238	15911	302	7	360	335	15611	5	5548
32	15080	4	238	15465	446	4	360	335	15276	5	5769
33	14842	4	238	15058	407	5	360	335	14940	4	5425
34	14604	4	238	14604	454	4	360	335	14604	4	5358

From a lateral length of 8093 feet, the 34-stage design was geometrically spaced at 238 feet per stage, with plug depths of each isolation tool also shown. The UCS for each stage is compiled, which in

turn assists the algorithm in determining the criteria for adding or subtracting footage to each stage interval. Throughout each iteration, the stage lengths converge onto the minimum or maximum length bound as the UCS allows. For the end result, a barrel of oil per stage is equated where the summation equates to the 5-Year total oil recovery. As the iterative process continues, recovered barrel of oil from each stage increases along with greater UCS values.

The iterative process is imperative in the selective design as lower UCS values can be shown to have diminishing oil recovery and increasing stage lengths. A 3,500-feet section of the well is shown plotted in Figure 5.17. As expected, higher UCS values have shorter stage lengths and lower UCS values have longer stage lengths. Values of higher UCS have the minimum bounded stage length of 180 feet while the maximum does not exceed 400 feet set as bounded maximum stage length.

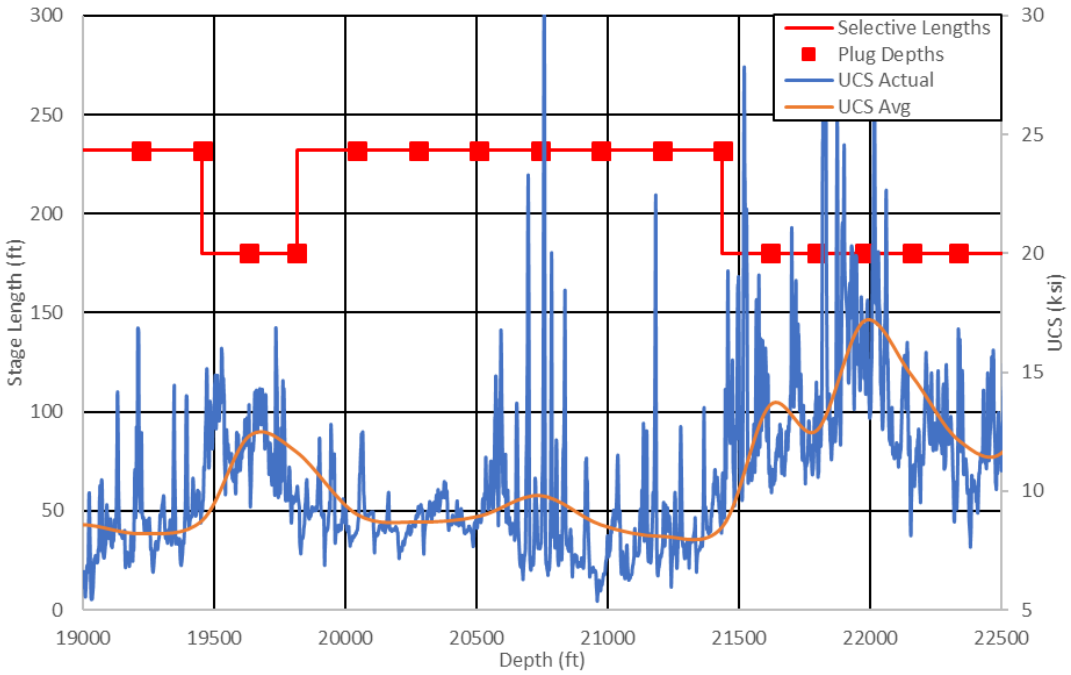

Figure 5.17. Well D UCS Profile and Selective Stage Lengths with Plug Depths Section from 19,000 to 22,500 ft for 34 Stage Selective Design

The 34-stage geometric spacing design resulted in 257,677 (Barrels of Oil) BO in the 5-Yr term for the comparative design of the actual Well D's UCS profile. In contrast, the selective stimulation resulted in 265,899, or a 3.2% increase, with varying stages between 180-feet and 400-feet. The inverse relationship between UCS and stage length is also shown in Figure 5.17 where higher UCS (with corresponding higher brittleness seen from the geomechanical derived correlations) has increased stage density as compared to the lower UCS values. For each selective stage within the lateral, a BO/stg is calculated and compared to the geometric design. As shown in Figure 5.18, the beginning stages at the toe show the greatest return of oil in the selective design whereas in the middle few stages, geometrically placed plugs show great return but with the cumulative stage return being higher for the selective design.

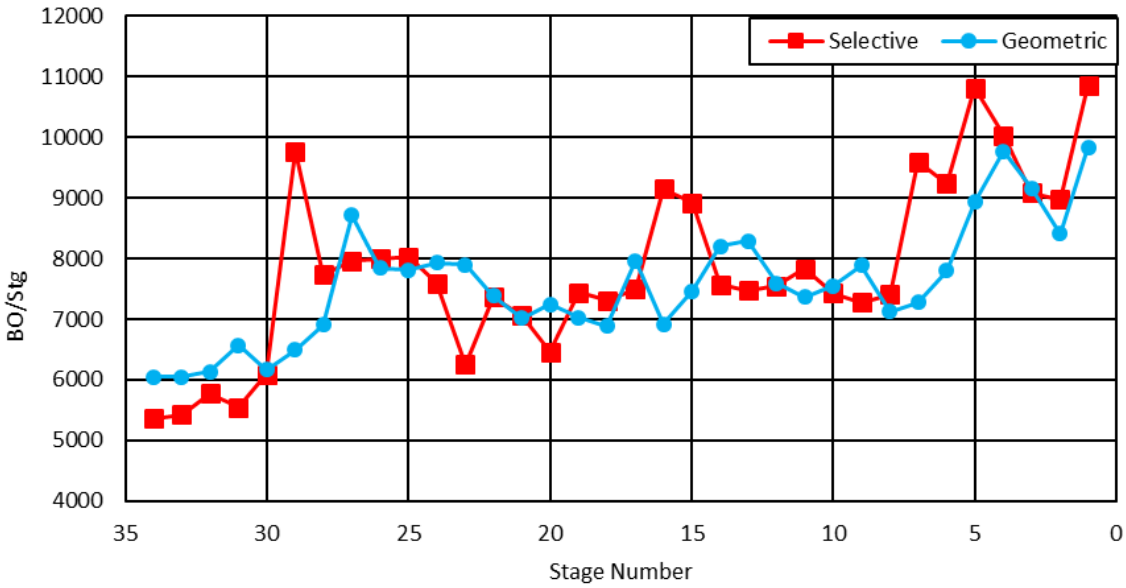

Figure 5.18. 34-Stages BO/stg for Individual Stages for Selective and Geometric Designs

Due to the stage length differential in the mid to lower UCS zones, geometric fracs are higher within the BO/stg curve while the overall cumulative oil recovery, displayed in Figure 5.19, result of the selective design being overall more beneficial in the 5-Year term.

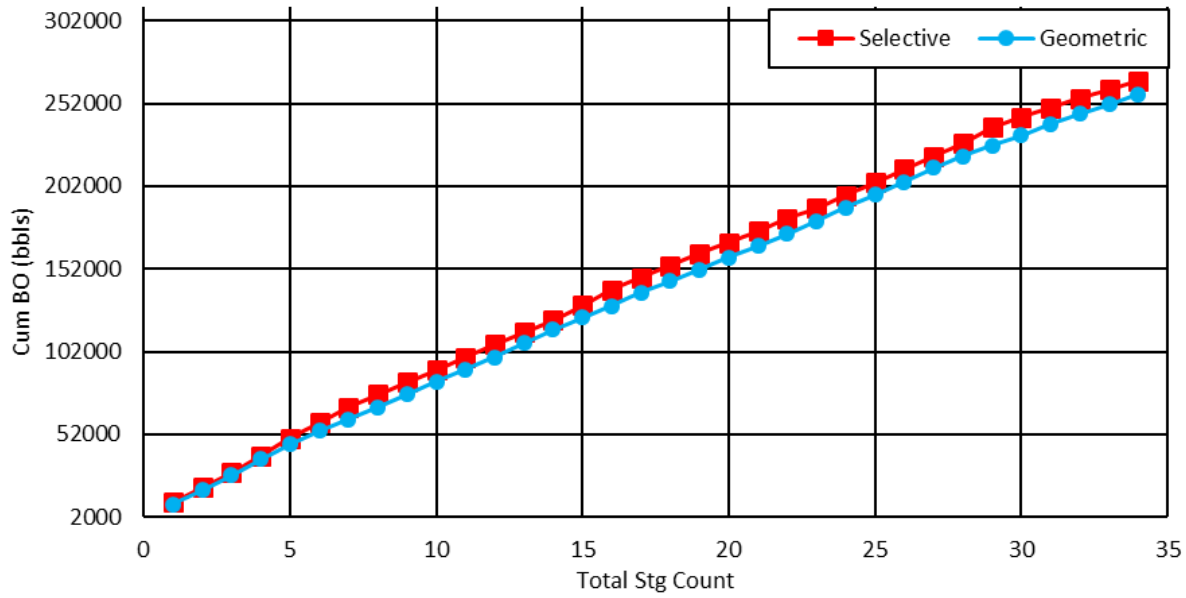

Figure 5.19. 34-Stages Cumulative Oil over Completed Length

Due to the stage length differential in the mid to lower UCS zones, geometric fracs are higher within the BO/stg curve while the overall cumulative oil recovery, displayed in Figure 5.19, result of the selective design being overall more beneficial in the 5-Year term.

5.4. Economic Analysis

5.4.1. Drilling Economic Analysis

Non-optimized and optimized curves explained in section 5.3.1 were used to conduct a detailed cost analysis for each scenario and compare to the actual Well D costs to show the potential cost savings of using the PDS and RSS. The four scenarios were plotted on a depth versus cost curve as shown in Figure 5.20.

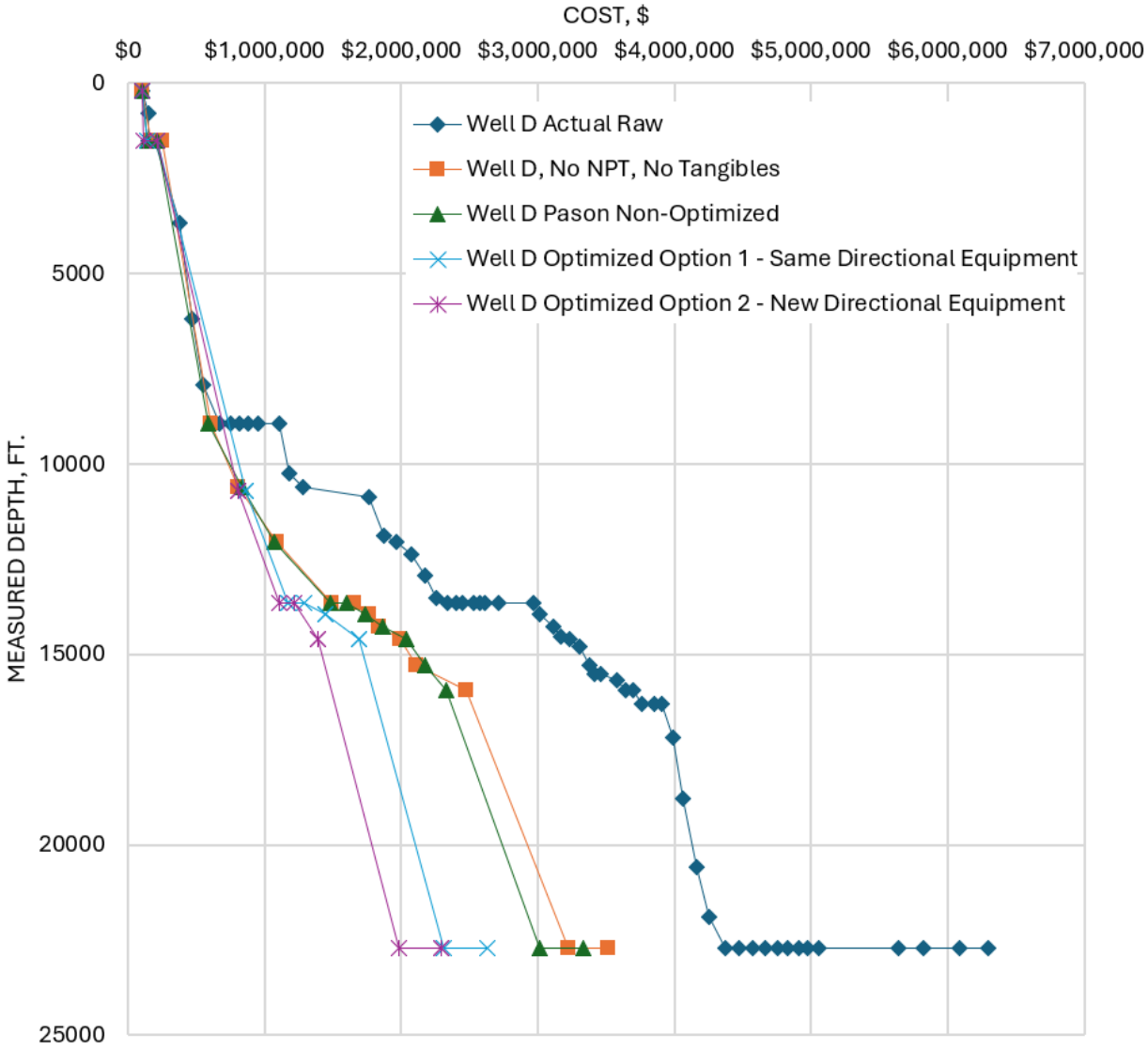

Figure 5.20. Well D Depth vs Cost Comparison.

The four cost scenarios are as follows:

1. Well D Actual Raw: The cost data for this curve was taken from Well D's daily drilling reports and includes the non-productive time (NPT) costs as well as tangible costs of $1,750,000.
2. Well D PDSD Non-Optimized No NPT: This cost curve was created from PDS data with no NPT costs and no tangible costs.

3. Well D Optimized Option 1 – This optimized cost curve was created using the same directional equipment as the original well but with the same but fewer bits using the PDS to optimize drilling parameters.
4. Well D Optimized Option 2 – This optimized cost curve was created using only SA-RSS directional equipment with different and fewer bits using the PDS to optimize drilling parameters.

The drilling costs for scenarios 2, 3 and 4 were calculated using the costs in Table 5.15 and Equation 5.12. The costs were calculated for each BHA run using Equation 5.12 and plotted against depth to generate Figure 5.20. In equation 5.12, the base day rate was multiplied by the total number of hours the BHA was run, plus the appropriate directional tool rate multiplied by the sum of rotating, circulating and tripping hours, plus the drill bit cost.

Table 5.15. Day Rate and Drill Bit Costs

Base Day Rate	$59,000
Day Rate: Conventional Bent Housing (CBH)	$8,000
Day Rate: Stand Alone Rotary Steerable System (SA-RSS)	$25,000
Day Rate: Motor Driven Rotary Steerable System (MD-RSS)	$32,000
Day 0: Prepare location, set conductor & Rig Move	$100,000
17.5" Drill Bit	$25,000
12.25" Drill Bit	$20,000
8.5" and *8.75" Drill Bit	$15,000

** One 8.75" hybrid PDC/Tricone drill bit cost of $35,000 was used for scenarios 2 and 3.*

$$\text{Cost per BHA} = (\text{Base Day Rate} * \frac{\text{BHA Hours}}{24}) + (\text{Directional Tool Rate} * \frac{\text{Rotating+Circulating+Tripping Hours}}{24}) + \text{Drill Bit Cost} \quad (5.12)$$

Table 5.16 presents a cost comparison for the four scenarios. The total cost of drilling Well D was $6,346,662, which includes approximately $1.75 million in tangible costs. For a more accurate comparison with the other three scenarios, these tangible costs were excluded, resulting in an adjusted drilling cost of $4,596,562. The tangible costs accounted for items such as surface casing and cement, intermediate casing and cement, logging, production casing and cement, and the final rig move at the end of the well.

Table 5.16. Drilling Cost Comparison

	Day Rate	CBH	SA-RSS	MD-RSS	Bit Cost	Total
Actual Raw						$6,346,562
Actual Raw no Tangible Costs						$4,596,562
Non-Optimized – No NPT	$2,395,780	$70,745		$646,991	$215,000	$3,328,516
Optimized Option 1	$1,846,129	$2,382		$651,019	$130,000	$2,629,531
Optimized Option 2	$1,731,830	$2,382	$464,889		$95,000	$2,294,101

The cost difference between the actual raw Well D, actual raw no tangible costs and the non-optimized scenario from PDS was $1,268,046, reflecting the cost of non-productive time (NPT) on the actual well. Optimized Option 1 resulted in a cost savings of $1,967,031 compared to the actual raw, no tangible costs case, while Optimized Option 2 provided a cost reduction of $2,302,461, representing a 50% decrease. These savings highlight the potential cost benefits of using the PDS software and the SA-RSS directional tool. In a full-field development scenario, where four wells are drilled per section, this could translate to a total savings of $9.2 million per section. Further economic analyses for full-field development will be covered in Chapter 7.

5.4.2. Completion Tier Economical Analysis

The baseline economic metrics for different Tier economics is summarized in Tables 5.17 to 5.19. The field development has 70 Reservoir 3 wells and 40 Reservoir 2 wells and the procedure to obtain the overall economic analysis includes a baseline analysis with commodity pricing of $65 WTI with a comparison to $75 WTI. The production of each well, reservoir and the field were presented for each WTI. In addition, the economic analysis will present the potential benefits of implementing the drilling optimization cost savings and the use of selective stimulation. As an example, the baseline input data required for reservoir 3 is shown in Table 5.17, the single well analysis outputs are shown for Tier 1, 2 and 3 wells in Table 5.18 and the field development analysis outputs for reservoir 3 is shown in Table 5.19. The analysis presented in Table 5.19 will be integrated for all wells in the field development for the different scenarios presented above.

Table 5.17. Baseline Input Data Required (Reservoir 3 well)

Reservoir 3	Input Data		
$10 MM	CAPEX	$10,000,000	
$65 WTI	Projected Online	44,562	
Enhanced Curve			
	Working Interest	100%	
	NRI	80%	
	State Tax	7%	
	Discount Rate NPV	10%	
	Depletion	N/A	Years
	MACRS	N/A	Years
	Gas Price	$3.00	USD
	Oil Price	$65.00	USD
	NGL	5	GPM
	NGL Price	$0.75	USD
	SWD	$1.50	$/BBL
	WOR	0.25	
	Reinvestment Rate	8%	
	LOE Gas Lift (>30 BOPD)	$180,000	$/Year
	LOE Beam Pump (<30 BOPD)	$42,000	$/Year
	Workover	$25,000	
	Workover Annual INC	1%	/Year

Table 5.18. Single Well Analysis for Tier 1, 2 and 3 Wells (Reservoir 3)

Single Well Output Data

Output Data	Teir 1	Teir 2	Teir 3	BFIT
NPV	$12,374,705	$10,083,950	$7,750,148	USD
IRR	57%	48%	38%	
MIRR	11%	11%	10%	
Payback	0.94	1.12	1.44	Years
Discounted Payback	1.10	1.41	1.80	Years
Discounted ROI	1.24	1.01	0.78	
Discounted Sum Earnings	$22,374,705	$20,083,950	$17,750,148	USD
NPV @ 8%	$14,044,703	$11,586,608	$9,074,442	USD
NPV @ 10%	$12,374,705	$10,083,950	$7,750,148	USD
NPV @ 13%	$10,374,929	$8,283,989	$6,162,357	USD
NPV @ 15%	$9,284,255	$7,302,305	$5,295,812	USD
NPV @ 20%	$7,122,894	$5,357,757	$3,578,505	USD
Total Oil	505,771	455,194	404,617	BBLS
Total Gas	3,186,359	2,867,723	2,549,087	MSCF

Table 5.19. Field Development Analysis (Reservoir 3)

Development			
Input Values		Year	Drill Type
Wells Per Year	10	1	Tier 1
Wells Per Section	3.5	2	Tier 1
Sections per Well	2	3	Tier 1
Drilling Years	7	4	Tier 2
Wells Drilled	70	5	Tier 2
Acreage Drilled	25600	6	Tier 3
SQ Miles Drilled	40	7	Tier 3
CAPEX	$10,000,000	8	NA
Discount Rate	0.1	9	NA
		10	NA
Output Data			
Total Cash Flow	$ 1,635,831,265		
CF per Well	$ 23,369,018		
Total DCF	$ 575,021,490		
Total DCF (AC)	$ 22,462	Per acre	
Years to Drill in FCF	3		
Years to Drill DFC	3		
MAX Outlay	$ (100,000,000)		

5.4.3. Stimulation Economical Analysis

Five data points were run for the selective spacing design to develop the type curve model fit using

an exponential decline correcting for differing b & D values common with increased stage count. When increasing the number of stages, b ranges from 1 – 1.3 while D ranges from 0.27 – 0.35, with the higher value of the two being the highest stage count. When contrasting the singular 40-stage design with other fracture designs from 30 to 50 stages, as displayed in Figure 5.21, visible trends emerge from the algorithm's selective allocation. A notable convergence is evident before the initial year, indicative of pronounced initial declines resulting from heightened rates and drawdowns associated with deploying more stages. Consequently, the variable approach yields escalated oil production within 3- to 5-years.

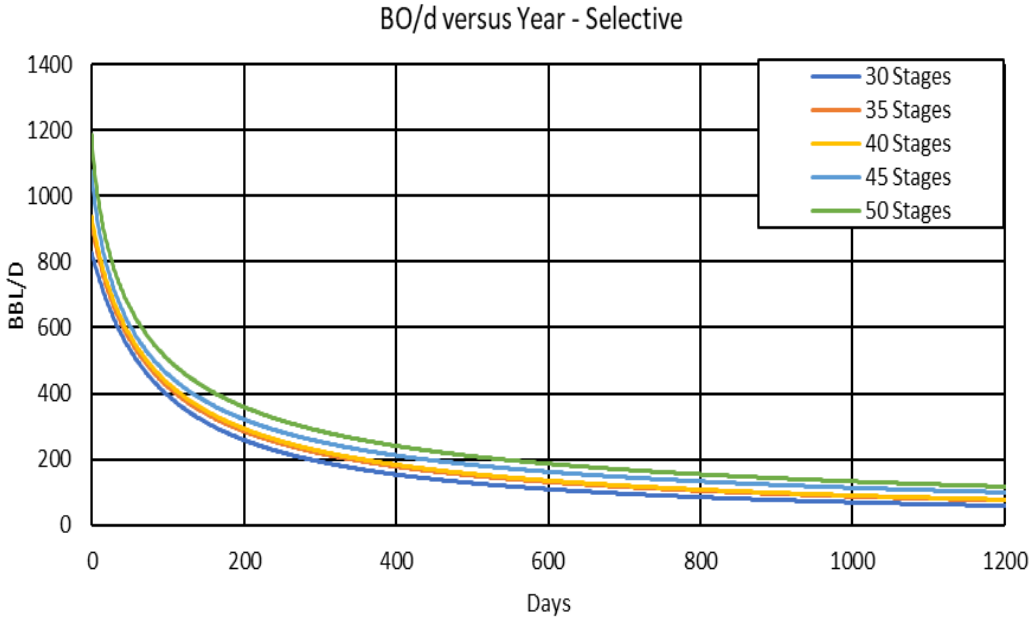

Figure 5.21. Decline Curves for Varying Number of Stages

Replicating this analysis for 30, 34, 35, 40, and 45 stages for both geometric and selective stimulation, Tables 5.20 and 5.21 are shown summarizing the algorithms expected yield and economic viability of each design.

Table 5.20. Geometric – Results for Different Stages.

GEOMETRIC					
STAGE	**30**	**34**	**35**	**40**	**45**
IP	715.00	811.00	834.00	954.00	1073.00
3 YR	183504	210862	216652	255776	288317
5 YR	210862	257677	267280	315309	363311
CAPEX	$8,750,000	$9,250,000	$9,375,000	$10,000,000	$10,625,000
NPV	$7,667,546	$10,743,969	$11,700,406	$15,196,236	$19,218,444
IRR	47.08%	55.21%	56.54%	66.27%	73.42%
MIRR	10.52%	11.07%	11.23%	11.66%	12.09%
PAYBACK	1.00	0.95	0.95	0.88	0.84
DIS SUM EARN	$16,417,546	$19,993,969	$21,075,406	$25,196,236	$29,843,444

Table 5.21. Selective – Results for Different Stages

SELECTIVE					
STAGE	**30**	**34**	**35**	**40**	**45**
IP	825.33	915.65	938.52	1075.77	1185.64
3 YR	193423	218899	225387	255776	287972
5 YR	229512	265899	274038	319449	364652
CAPEX	$8,750,000	$9,250,000	$9,375,000	$10,000,000	$10,625,000
NPV	$8,419,768	$11,321,119	$11,904,723	$15,899,390	$19,395,687
% INCREASE	8.84%	3.19%	2.53%	1.31%	0.36%
IRR	52.53%	59.37%	61.02%	67.30%	73.55%
MIRR	10.68%	11.17%	11.25%	11.78%	12.11%
PAYBACK	0.92	0.90	0.89	0.87	0.83
DIS SUM EARN	$17,169,768	$20,566,881	$21,279,723	$25,899,390	$30,020,687

For the 30-stage comparison, an Initial Production (IP) of 715 b/d and 210,862 BO in the 5-year for the geometric design, and 825 b/d and 229,512 BO for the selective design. An 8.84% increase in the 5-year oil is shown, with the same CAPEX, while an additional 5% IRR and 0.08-year payback differential. Evaluating the discounted sum earnings, the selective design generated approximately $800k more than the geometric design. For 35-stages, 834 b/d, 267,280 BO, for the geometric design versus 938 b/d, 274,038 BO in the 5-year term for the selective design, increasing overall oil recovery by 2.53%. with an NPV increase of nearly $200k, an IRR increase of 5%, and 0.06-year payback differential prove the selective design outweighs the geometric approach in all economic facets. While analyzing greater stage count, however, the metrics begin to converge. For 45-stages, the geometric design revealed 1073 b/d, 363,311 BO recovered, with a NPV of $19.2M. Alternatively, for the selection algorithm, 1185 b/d, 364,652 BO recovered, with a NPV of $19.4M for an overall 0.36% increase. With almost a $180k difference in discounted earnings, the designs are becoming increasingly similar with the growing stage count. The economic values converging is due to the similarity of greater stage count designs, where for a given lateral length, at some point, the geometric stage length will equal the selective stage length. Because of this, it is key to evaluate the total simulation length against number of stages and the variation in UCS. As laterals become longer, and number of stages are limited the value of selective stimulation increases especially where there is a large variation in UCS.

5.5. Results and Discussion

In conclusion, drilling and core data from the Caney Shale were utilized to develop a simulation platform incorporating detailed drilling, core, and log data. This platform was then used to predict drilling and completion performance for the upcoming Well D. The drilling simulation approach has the potential to further save approximately ~$1 million in drilling costs, reducing CAPEX to $9 million. Future Caney wells could benefit significantly from this approach, potentially achieving a 30-40% reduction in on bottom drilling time compared to Well D. Additionally, selective stimulation could increase production rates by up to 10% because as the completed reservoir length increases to two miles (10,560 feet) versus Well D's length of 8,093 feet the average stage spacing is larger for

the same number of stages which show more benefit of a selective stimulation in the Caney Shale. These scenarios will be further assessed in the overall field development strategy economics section to evaluate their impact on cost savings and overall economics of the Caney field.

6. Rock Mechanics

6.1. Estimating rock mechanical properties of Caney shale from the well log data

6.1.1. Approach

The objectives for this task were to (1) quantify the static-to-dynamic Young's modulus ratio (F_{ds}) for Caney shale under subsurface conditions, and (2) develop supervised machine learning (ML) models to predict the rock mechanical properties, including static Young's modulus, from the well log data of the Caney shale. For this task, ten subsurface cores were retrieved from various depths to represent different layers of the Caney shale and were utilized for acoustic velocity measurements. For the first objective, the ultrasonic P and S velocities were measured using a triaxial Hoek cell (Kholy et al., 2024) under triaxial conditions (axial stress = 7,000 psi, confining stress = 3,000 psi, and temperature = 204 °F), which are similar to the actual downhole conditions, except for the actual temperature of 240 °F due to the Hoek cell's limitation. The correction for temperature was incorporated by extrapolating the measurements taken at two temperatures—room temperature (70 °F) and the maximum cell temperature (204 °F). Also, due to the extremely low permeability of Caney samples, the saturation correction was applied using the measurements from dry and fully saturated Gray Berea sandstone samples, which have similar clay and quartz contents to those of Caney's reservoir layers.

The estimated dynamic Young's modulus and Poisson's ratio, with and without these corrections, were then compared to the dynamic properties derived from conventional well logs using equations from Nielsen and Kohlhaas (1979). To evaluate the impact of effective stress on the dynamic mechanical properties, three effective stress conditions were tested to indirectly assess the impact of pore pressure. Lastly, to quantify the static-to-dynamic Young's modulus ratio (F_{ds}) for Caney shale under subsurface conditions. The static Young's modulus (E_{stat}) measurements conducted by Benge et al. (2021) on five downhole samples from several depths along the same pilot well were compared to the corresponding derived dynamic Young's modulus (E_{dyn}) from well logs to quantify F_{ds}.

The second objective was achieved in two ways: (1) constructing the static Young's modulus (E_{stat}^{*}) profile by assuming that each of the five layers has constant F_{ds} values, and (2) developing ML models, specifically the random forest (RF) and extreme gradient boosting (XGBoost) models, to predict E_{stat} using conventional well logs, including TVD, GR, RHOB, PHIN, PEF, RDeep, and CALI. Then, SHapley Additive exPlanations (SHAP) were utilized to assess the importance of features in predicting E_{stat} for both models (Shapley and Roth, 1988; Lipovetsky and Conklin, 2001).

6.1.2. Results and Discussion

<u>Dynamic mechanical properties estimated from acoustic measurements and well logs</u>

Analysis of the laboratory measurements from the ten samples indicated a higher Young's modulus (E_{dyn}^{av}) and lower Poisson's ratio (υ_{dyn}^{av}) than those estimated from the well logs as illustrated. By incorporating the saturation and the temperature effects, as described earlier, the E_{dyn}^{av} and υ_{dyn}^{av} shifted closer to the properties derived from the well log data, significantly improving the match (Table 6.1).

Table 6.1. Summary of derived mechanical properties from the acoustic measurements with adjustments for temperature and saturation.

Sample TVD (ft)	Zone	Without Correction		With Correction		Well Logs	
		E_{dyn}^{av} (Mpsi)	υ_{dyn}^{av}	E_{dyn}^{av} (Mpsi)	υ_{dyn}^{av}	E_{dyn} (Mpsi)	υ_{dyn}
X030	Reservoir #1	5.86	0.14	5.38	0.22	5.94	0.26
X050		5.59	0.14	5.13	0.23	5.12	0.24
X061	Ductile #1	5.87	0.17	5.36	0.24	5.22	0.24
X145	Reservoir #2	6.65	0.05	6.34	0.15	7.07	0.25
X151		6.16	0.10	5.78	0.19	5.83	0.19
X158	Ductile #2	6.14	0.17	5.59	0.24	5.88	0.19
X212	Intermediate Zone	5.62	0.14	5.15	0.23	6.05	0.22
X259		5.02	0.12	4.61	0.21	4.65	0.21
X340	Reservoir #3	5.82	0.13	5.34	0.22	5.85	0.22
X450		6.80	0.09	5.77	0.26	4.71	0.2

Impact of effective stress on dynamic mechanical properties

Figure 6.1 indicates that the dynamic Young's modulus (E_{dyn}^{av}) increases with increasing effective stress for all samples, presumably due to the closure of microcracks. Whereas Poisson's ratio shows no clear correlation with effective stress (Figure 12D-2b), consistent with the findings discussed by McPhee et al. (2015).

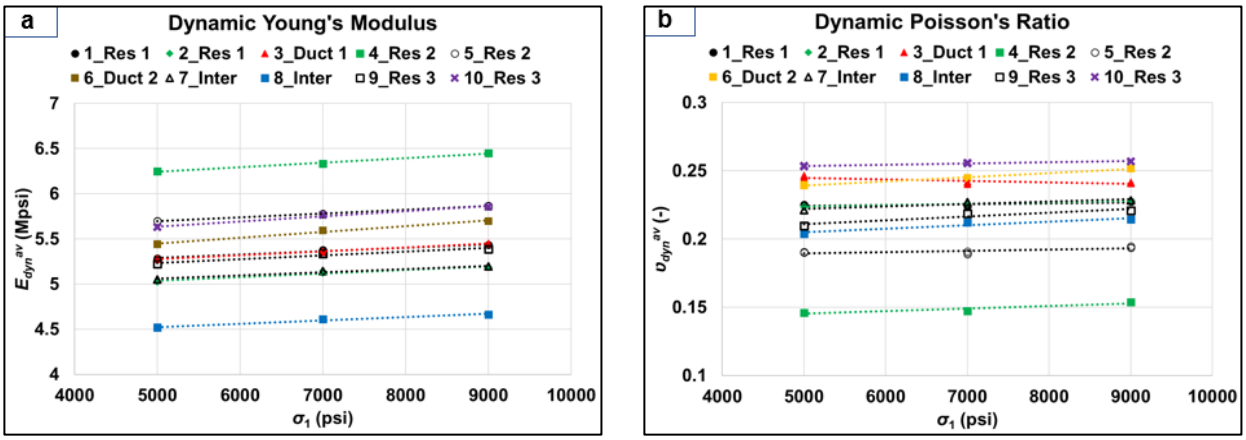

Figure 6.1. Estimated mechanical properties from laboratory ultrasonic measurements at constant differential stress (σ_{diff}): (a) E_{dyn}^{av}, and (b) υ_{dyn}^{av}.

Static-to-dynamic Young's modulus ratio quantification

The F_{ds} values were 0.95 and 0.83 for Reservoirs 1 and 3, respectively, and tend to be higher than the values in Ductile layers 1 and 2, which were 0.77 and 0.55. These high F_{ds} values occur in zones of high neutron porosity (PHIN), approximately 22%, and low bulk density (RHOB), approximately 2.48 g/cc, as illustrated in Figure 12D-3a, in contrast to other zones. Reservoir 2 showed a relatively low F_{ds} value of 0.47, lower than that of the other reservoirs and closer to the ductile layers. This is possibly due to the sample selection being near the depth where the well logs change dramatically around X150 ft within Reservoir 2, which coincides with the lowest PHIN for this entire interval.

Although the estimated F_{ds} may not perfectly represent Reservoir 2, the value is presented since it is the only E_{stat} value available from the triaxial test for comparison.

On the other hand, the measured static Poisson's ratio from Benge et al. (2021) were 0.318 and 0.212 for Reservoirs 1 and 2 samples, respectively which were higher than the corresponding dynamic Poisson's ratio values of 0.234 and 0.209, respectively yielding a static-to-dynamic ratio of greater than 1. Thus, we only focused on the prediction of static Young's modulus using ML models.

Static Young's modulus prediction from ML models

Due to the limited number of E_{stat} measurements along the depth, a constant F_{ds} was assumed for the same lithological layer, as shown in Figure 6.2.

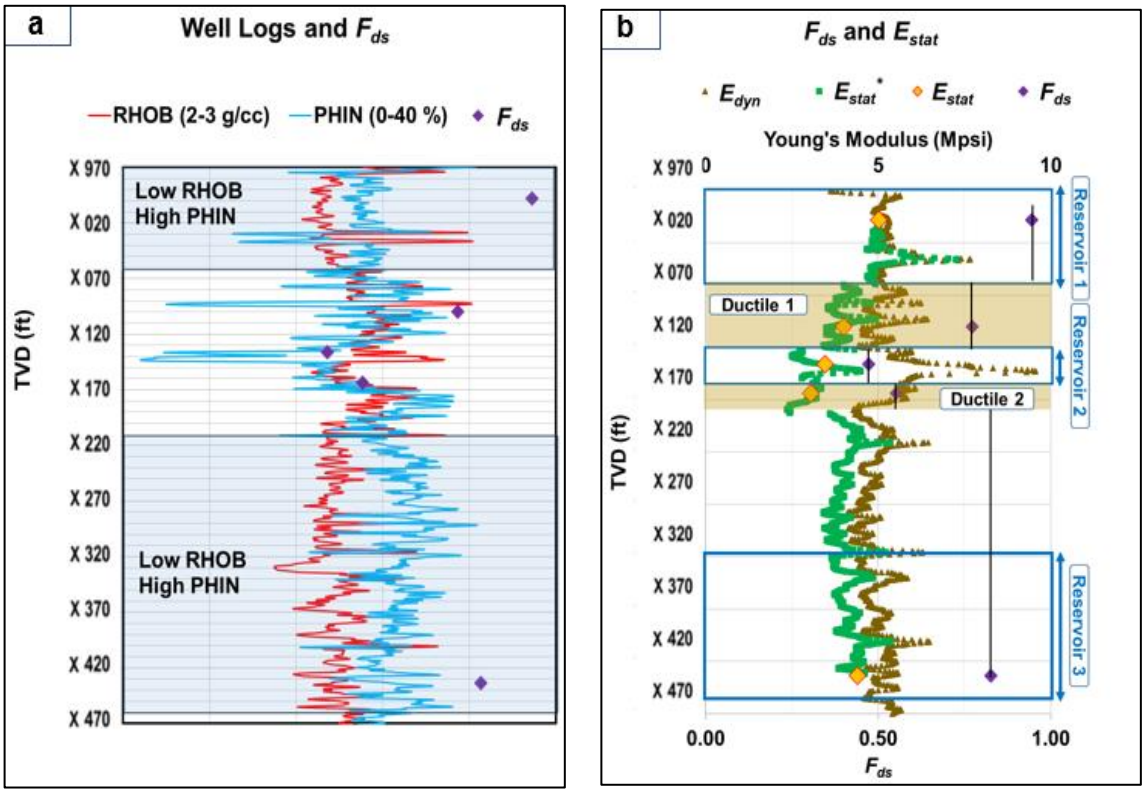

Figure 6.2. (a) The relationship between F_{ds}, neutron porosity (PHIN), and bulk density (RHOB), (b) Constant F_{ds} and E_{stat} profiles for Caney shale.

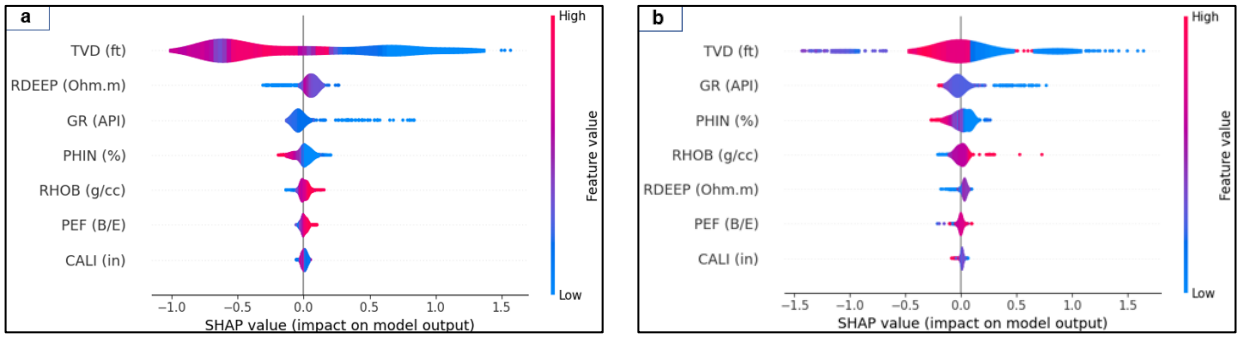

Figure 6.3. SHAP evaluation for the ML models predicting Estat: (a) RF, and (b) XGBoost.

Based on this assumption, the static Young's modulus (E_{stat}^{*}) profile was derived. The F_{ds} for the intermediate zone was analogous to that of Reservoir 3, as both zones tend to have similar average PHIN and RHOB values. The RF and XGBoost ML models have been trained to predict E_{stat} using conventional well logs. The predictions from XGBoost model showed a better agreement with lower RMSE of 0.00115 compared to 0.0696 of RF model (Kholy et al., 2024). The SHAP evaluation of the RF model ranked features for E_{stat} in the following order: TVD, RDEEP, GR, PHIN, and RHOB (Figure 6.3). In the XGBoost, the results indicated that TVD, GR, PHIN, RHOB, and RDeep are the most influential features for predicting E_{stat} (Figure 12D-4b). Interestingly, both models indicated that PHIN and RHOB are the key features in predicting E_{stat}, as discussed above. In addition, GR was a key feature for both models, showing an inverse correlation with E_{stat}. This is because E_{stat} tends to be low for shale formations with high clay content (Benge et al., 2021), which is reflected as a high GR.

6.2. Characterization of Geomechanical Properties

Mechanical properties testing was completed for the Caney plug samples. Testing included unconfined compressive strength, indirect tensile strength, fracture toughness using a semi-circular bending specimen, triaxial testing, and creep testing. Results from unconfined and triaxial testing demonstrated the nominally ductile zones are mechanically weaker than the nominally brittle reservoir zones. However, there was no significant difference in properties beyond the change in strength. Creep testing revealed a more comprehensive demonstration of the difference in behavior between the two zones, specifically with respect to the long-term deformation of the samples. The ductile samples experienced significantly more long-term deformation than the reservoir samples. By testing samples drilled perpendicular, parallel, and at 45° relative to bedding planes, it was demonstrated most of the creep occurs in the bedding planes themselves. Furthermore, the properties and amount of creep is related to the orientation of the bedding planes, with the vertical samples drilled perpendicular to bedding experiencing the greatest amount of creep.

6.2.1. Approach

To determine the mechanical properties of the Caney shale samples, unconfined and confined testing was performed on 30 mm diameter by 60 mm long cylindrical samples.

Unconfined Testing

Unconfined compressive strength testing was completed at an external laboratory. However, both indirect tensile testing and fracture testing were conducted at the University of Pittsburgh.

For tensile and fracture testing, the 30 mm by 60 mm samples were cut using a tile saw into four pieces, resulting in smaller samples approximately 15 mm in length and 30 mm in diameter. While this completed the preparation of the tensile samples, the fracture samples were additionally cut in half along the diameter of each sample. A notch was created in the fracture samples using a coping saw to create a 6 mm notch in the semi-circular bending samples.

Tensile testing was conducted using a load frame with a piston controlled by an ISCO pump. The flow rate of the pump was controlled to allow for failure within the five-minute recommendation provided in ASTM D3967-08 (2008).

Fracture toughness was conducted on the semi-circular bending specimens using a Test Resources load frame. A constant displacement rate of 0.02 mm/minute was chosen to match the loading rate used in triaxial testing. Samples were loaded in a three-point bending method until failure.

Triaxial Testing

Triaxial testing was conducted on the 30 mm by 60 mm cylindrical samples. To prepare the samples for testing, four strain gauges were adhered to the surface of the sample. These were located in the approximate middle of the sample along the outer surface. Two were oriented vertically to measure the axial strain and two were oriented radially to capture the radial strain. The two pairs of strain gauges were positioned opposite each other to compensate for any possible differential displacement of the sample.

Samples were loaded into a Hoek triaxial cell. The sample is placed in a polymer sleeve which is open to the atmosphere at the ends, and the sleeve is placed in the cell. The top and bottom surface of the sample are exposed to the environment while hydraulic oil placed in the cell provides a radial confining pressure. Spacers were used to position the sample in the middle of the cell and semi-hemispherical loading platens were used to ensure uniform application of an axial load.

Triaxial testing was conducted at 90°C. This temperature was achieved by wrapping the cell with heating tape. A maximum temperature of 90°C was chosen to simulate downhole conditions as closely as possible while not allowing the pore fluid in the sample to boil. Because the Hoek cell does not have a method to control pore pressure, the temperature must be kept below the boiling point of any pore fluids.

Using an external ISCO pump, the confining pressure was set to 50, 500, 1500, or 3000 psi. These pressures were predetermined before testing, and the 50 psi case acts as an analogue for an unconfined sample at temperature.

After loading the sample into the cell, the cell was loaded into an INSTRON load frame. For the 50 psi test, the sample was placed under hydrostatic loading at 250 psi as the cell reached temperature. A higher hydrostatic pressure of 500 psi was applied for the samples tested at 1500 or 3000 psi. For the 50 psi confined case, the hydrostatic pressure was set to 50 psi and remained constant throughout the test. Once the cell reached temperature, measured from a thermocouple located just above the sample, the sample was brought to the test pressure. The sample was allowed to equalize for one hour before the axial load was increased using a constant displacement rate of 0.02 mm/minute until the sample failed.

Creep Testing

Preparation of the creep samples was almost identical to the preparation of the triaxial samples. The only difference was the four strain gauges were all oriented axially, as it was found the amount of radial deformation during testing was negligible.

For creep testing, the sample was loaded into a MTS 810 load frame, as this equipment provided more precise load control. Additionally, it was found the adhesive for the strain gauges would experience deformation during the six days of testing. To still provide a reliable deformation measurement of the sample, three LVDTs were placed equidistant around the sample to measure axial displacement during creep testing.

All creep testing was conducted at 90°C and 3000 psi. As with the triaxial testing procedure, the samples were first placed under a 500 psi hydrostatic load while the temperature was increased. The sample was then brought up to the 3000 psi hydrostatic pressure for the test. As the creep samples were found to need additional time to equalize, the samples remained at the 3000 psi of pressure for 24 hours before testing started.

Creep testing consisted of several load/unload cycles. For each load cycle, the axial load was increased to 30% of the expected failure stress of the sample at 3000 psi confining pressure. These load/unload cycles allow for identification of the elastic and plastic components of the viscoelastic behavior. The first cycle consisted of a 20-minute load and 20-minute unload cycle. Next, a 12-hour load cycle with an equally long unload cycle. Next, a second 12-hour load cycle and a final 2-hour unload cycle marked the end of the load/unload testing phase. To determine the long-term creep deformation, the axial load was increased and held for 72 hours before the sample was unloaded.

6.2.2. Results and Discussion

A summary of results from unconfined testing is presented in Figure 6.4. Interestingly, the samples identified as nominally more ductile are markedly weaker than the zones identified as nominally brittle. This is true for unconfined compressive strength, indirect tensile strength, and fracture toughness. The Irwin length, calculated using the tensile strength and fracture toughness, does not adhere to the same trend as the other metrics. This difference indicates while the ductile zones are weaker this is not necessarily a correlation to behavior.

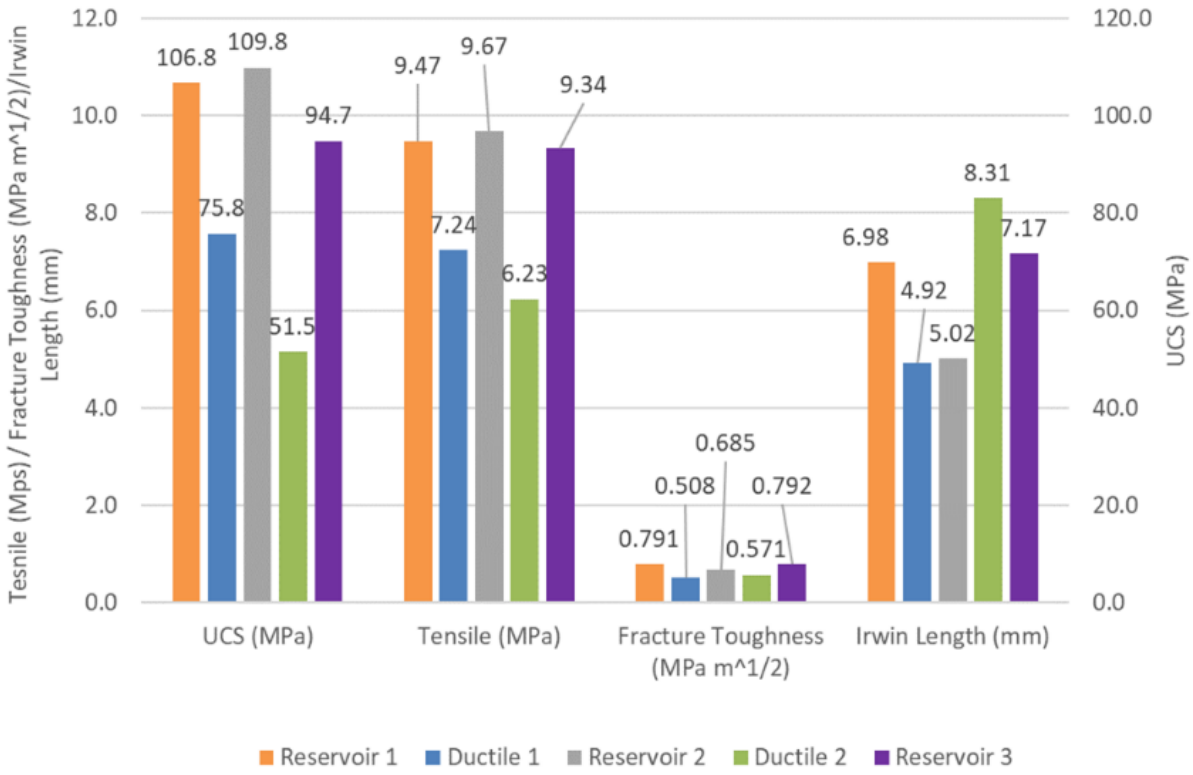

Figure 6.4. Summary of unconfined testing results (from Benge et al, 2021a)

Triaxial results are presented in Figure 6.5 (a) for each confining pressure, and 6.5 (b) compare the properties at 3000 psi confining pressure to the calculated friction angle and cohesion. As with the unconfined testing, the ductile zones are again weaker than the reservoir zones in terms of failure stress. However, there is not a clear difference between the Young's modulus and Poisson's ratio values of the two sets of samples. A ductile material would be expected to have a lower Young's modulus and higher Poisson's ratio, but this is not the case. There is no clear differentiation between the zones in terms of these parameters, and similarly the friction angle and cohesion are similar for all five zones.

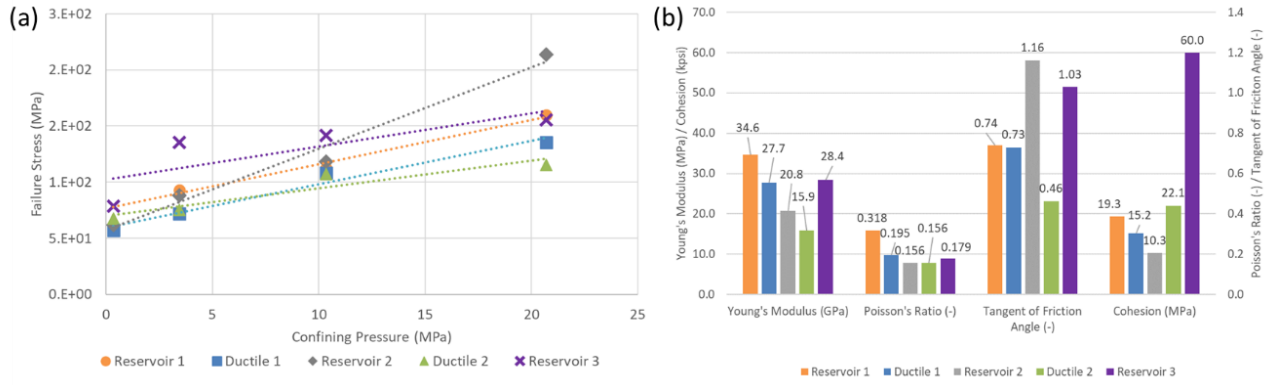

Figure 6.5. (a) Failure envelopes from triaxial testing and (b) Properties obtained from triaxial testing at 3000 psi confining pressure (from Benge et al, 2021a)

Unlike the other tests performed on the samples, creep testing shows a clear difference in behavior between the ductile and reservoir zones. Figure 6.6 (a) provides the creep compliance, which is the axial strain normalized by the applied axial stress, as a function of time for the load/unload cycles of creep testing. Note the time scale is logarithmic to better show the 20-minute and 12-hour cycles against the final 72-hour loading stage.

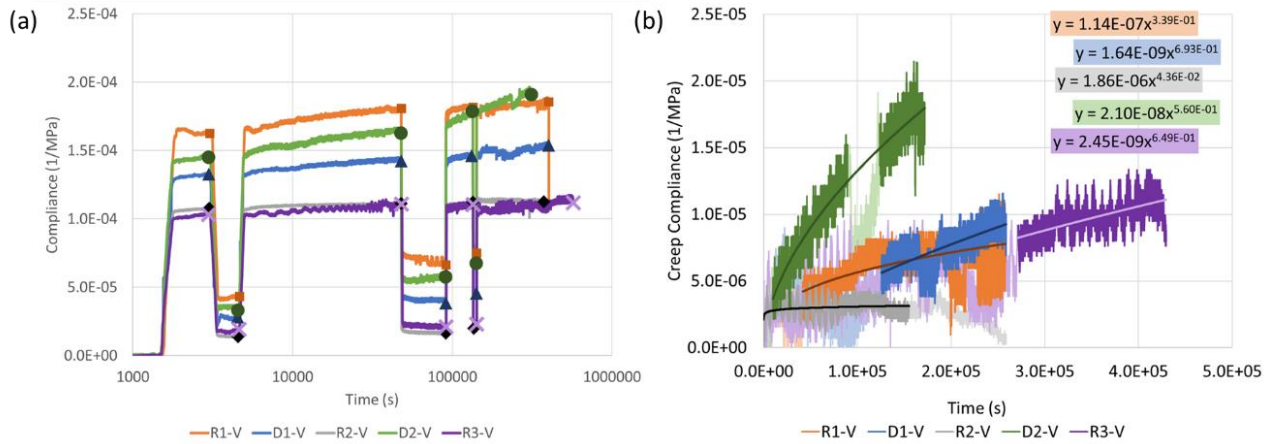

Figure 6.6. (a) Compliance over time and (b) Power-law description of creep for vertical samples (from Benge et al, 2023)

The ductile zones clearly show a greater amount of deformation over time compared to the reservoir zones. When examining the long-term deformation of the 72-hour loading stage, as shown in figure 6.6 (b), the difference in behavior is even more apparent. Note in this figure the reference point for

the strain is at the start of the 72-hour loading stage, where previously it was at the end of the 24-hour hydrostatic stage. A power-law fit to the deformation further emphasizes the difference in behavior between the ductile and reservoir zones, as the exponent on the time parameter is significantly higher for the ductile zones, demonstrating they will experience more long-term deformation than their reservoir counterparts.

Because the properties of the formation are dependent on the orientation of the bedding planes in the formation, horizontal and 45° samples were also tested. Figure 6.7 provides the results for the horizontal samples, drilled parallel to bedding planes, for both the load/unload cycles and the 72-hour loading stage. The relative behavior of the ductile and reservoir zones remains the same as for the vertical samples, where the ductile zones experience significantly more deformation. However, all creep compliance values are lower, indicating the horizontal samples will experience significantly less deformation than their vertical counterparts.

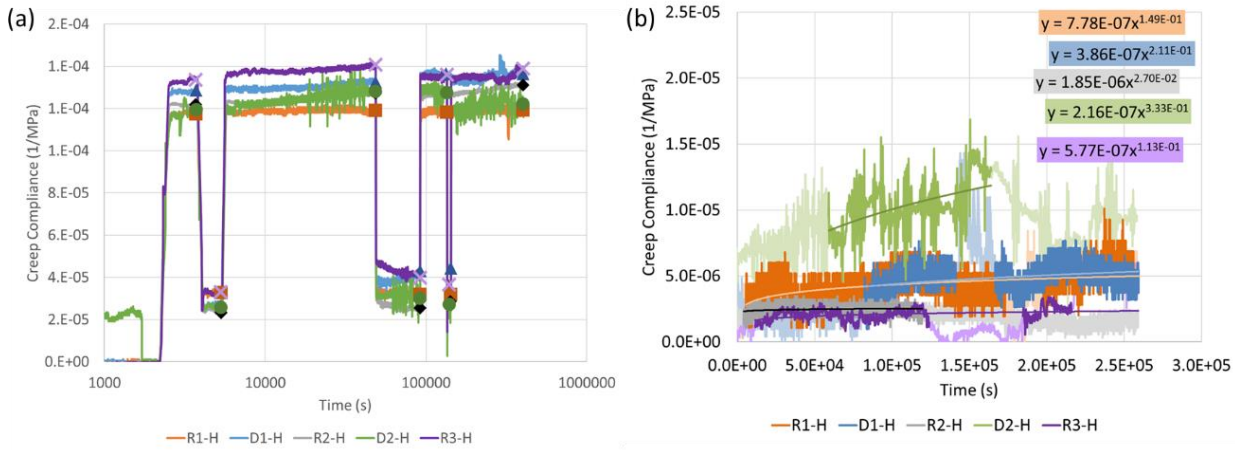

Figure 6.7. (a) Compliance over time and (b) Power-law description of creep for horizontal samples (from Benge, 2023)

6.2.3. Conclusions

Mechanical characterization of the Caney shale was completed using unconfined and confined testing. These tests consisted of unconfined compressive strength, indirect tensile strength, fracture toughness using a semi-circular notched bending specimen, confined triaxial testing at 90°C, and creep testing at 90°C and 3000 psi confining pressure.

Unconfined testing results demonstrated the nominally ductile zones are mechanically weaker than the nominally brittle reservoir zones. This behavior was confirmed in the triaxial testing results. However, triaxial testing did not indicate a clear difference between the Young's modulus, Poisson's ratio, or failure envelope between the reservoir and ductile zones.

Finally, creep testing revealed the nominally ductile zones undergo significantly greater creep deformation than the reservoir zones. The amount of creep deformation a given sample will undergo depends on the orientation of the bedding planes, as most of the deformation occurs in the bedding planes themselves.

7. Development Strategy Plan

7.1. Approach

When evaluating the development of an oil and gas field, multiple variables and inputs are used to risk assessing the project. The basics of this evaluation are determining the type of curve and economics for a single well, determining how much commercial reservoir acreage is available, how many wells can be drilled, and risking the production curves in potentially lower-yielding reservoir areas. All the metrics, calculations and conclusions for the Caney Reservoirs 2 and 3 are covered in this section to determine the net asset value of the play.

7.1.1. Single Well Economics

The first process in determining the assets' net value is understanding a single well's economics. Production curves and economic data are input into the OSU in-house developed Petroleum Fiscal Analysis Program (PFAP) model (Hareland, 2022) to calculate the well's economics, and these variables are listed in both Reservoir 2 and Reservoir 3 sections. A post-modeling drilled well matches the projected type of curve for Reservoir 3 as covered in the field results section, so the projected type curve for Reservoir 3 was used in the analysis, and the projected type curve for Reservoir 2 was assumed to be correct. The curves in this analysis are the Tier 1 reservoir curves, and the lower tier curves are covered in future sections.

7.1.2. Reservoir 2

Reservoir 2 type curve was projected using an IP value of 915 Barrels of Oil per Day (BOPD), a ‘d’ value of 0.310, a ‘B’ Value of 1.190, and a GOR of 3800 MCF/BO. Table 7.1 displays the Economic Inputs for the well, and Table 7.2 displays the Economic Outputs generated in PFAP. The baseline commodity price was held at $65 West Texas Intermediate (WTI), $3 Henry Hub (HH), and $0.75 per gallon for (Natural Gas Liquids) NGL, and the model assumes 5 gallons of liquids per thousand cubic feet of natural gas. The model did not have any negative cashflow years, so the model was run through the entire 30-year period. Figure 7.1 displays the single well cumulative undiscounted and discounted cash flows for a Tier 1, or base case Reservoir 2 well.

With the baseline economics conducted for Reservoir 2, a sensitivity analysis was evaluated to determine what inputs have the largest impacts on Net Present Value (NPV) and Internal Rate of Return (IRR). The inputs that were tested were Capital Expenditure (CAPEX), Operating Expenditure (OPEX), Oil Price, Gas Price, and NGL price. One factor to note is that for each of the commodity pricing sensitivities, production sensitivity would have the same effect, meaning a 10% increase in oil price would have the same impact as a 10% increase in oil production. Figure 7.2 displays the sensitivity analysis on NPV, and Figure 7.3 displays the sensitivity analysis on IRR.

Table 7.1. Economic inputs for Reservoir 2 economic model

Input Data		
CAPEX	$10,000,000.00	
Projected Online	Jan 1, 2022	
Working Interest	100%	
NRI	80.00%	
State Tax	7.0%	
Discount Rate NPV	10%	
Depletion	N/A	Years
MACRS	N/A	Years
Gas Price	$3.00	USD
Oil Price	$65.00	USD
NGL	5	GPM
NGL Price	$0.75	USD
SWD	1.5	$/BBL
WOR	0.25	
Reinvestment Rate	8%	
LOE Gas Lift (>30 BOPD)	180000	$/Year
LOE Beam Pump (<30 BOPD)	42000	$/Year
Workover	25000	Year
Workover Annual INC	1%	

Table 7.2. Economic outputs for Reservoir 2 generated by PFAP

Output Data	BFIT	
NPV	$8,822,707.54	USD
IRR	41.02%	
MIRR	10.58%	
Payback	1.36	Years
Discounted Payback	1.69	Years
Discounted ROI	88%	
Discounted Sum	$18,822,707.54	USD
NPV @ 8%	$10,299,307.14	USD
NPV @ 10%	$8,822,707.54	USD
NPV @ 13%	$7,070,436.90	USD
NPV @15%	$6,122,363.26	USD
NPV @ 20%	$4,259,508.76	USD
Total Oil	529311	BBLS
Total Gas	2011382	MSCF

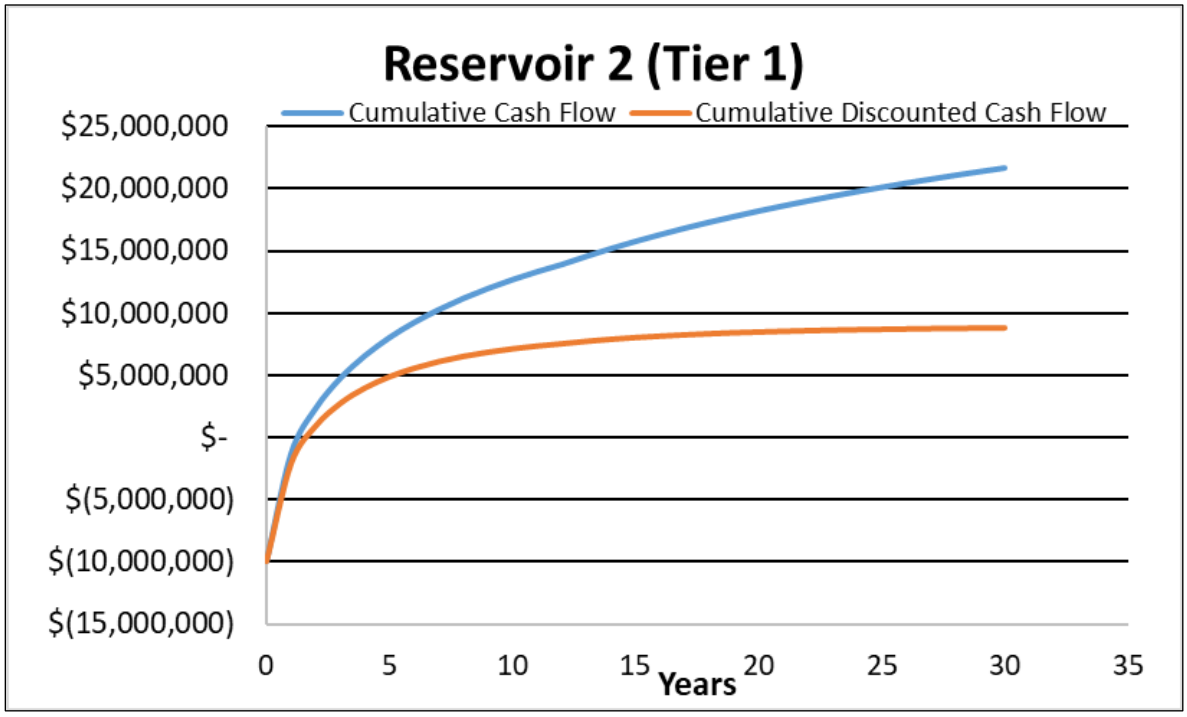

Figure 7.1. Single well cumulative undiscounted and discounted cash flows for the base case Reservoir 2 well.

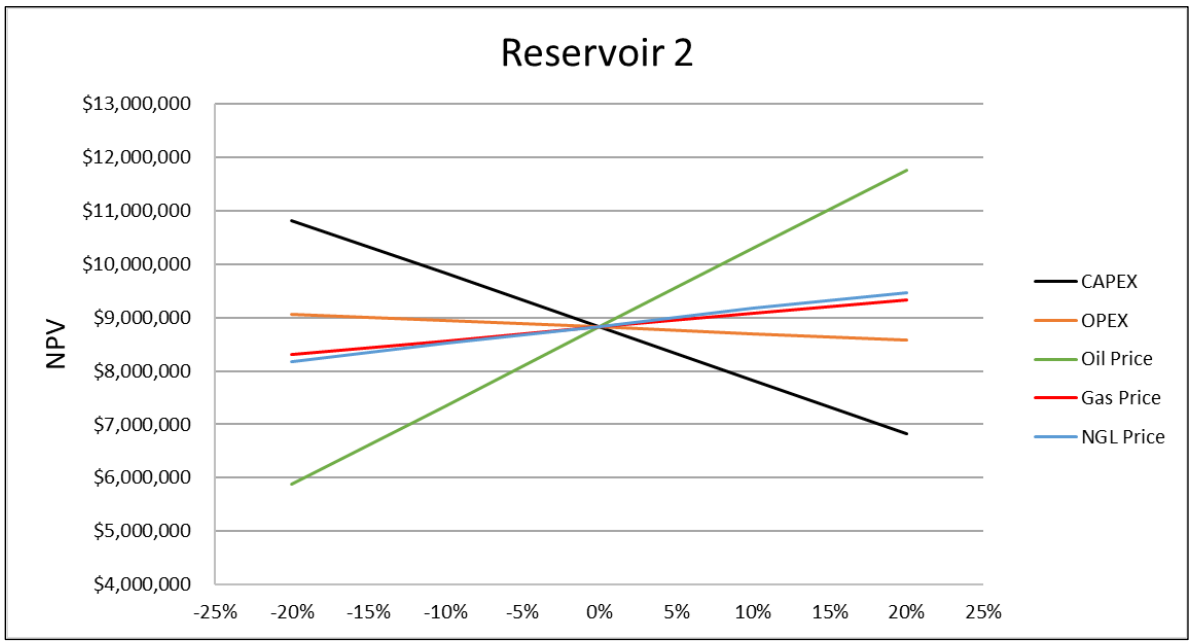

Figure 7.2. NPV sensitivity analysis for Reservoir 2

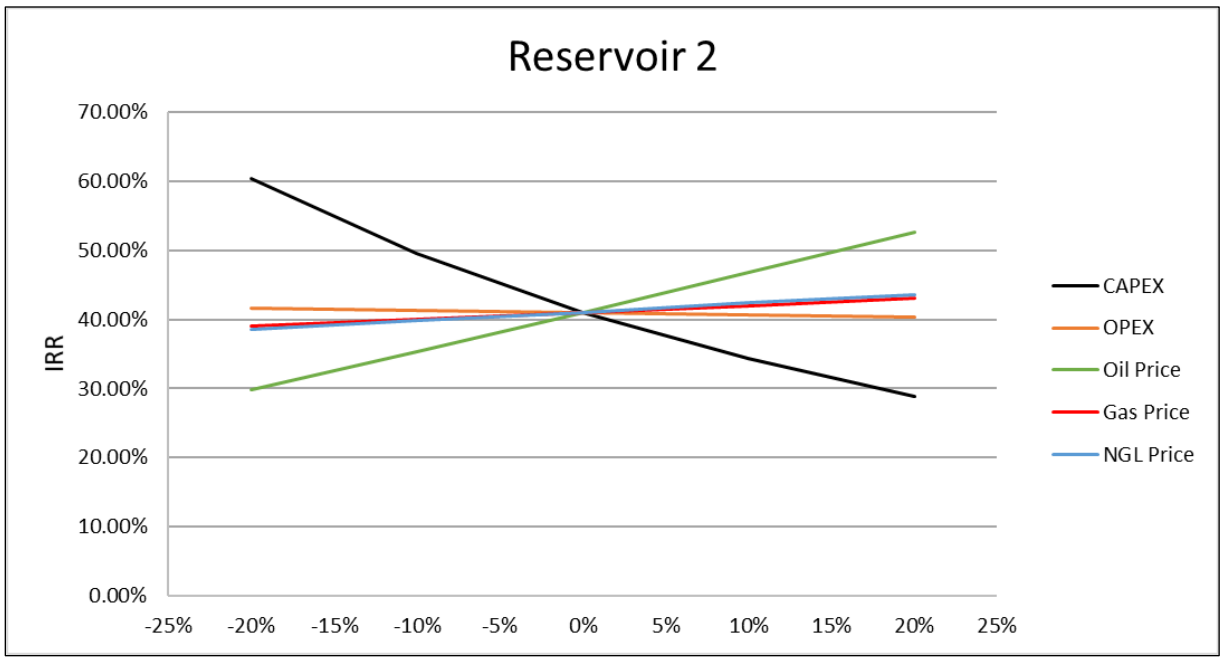

Figure 7.3. IRR sensitivity analysis for Reservoir 2

As displayed, CAPEX and oil price significantly impact NPV and IRR for Reservoir 2. For risk analysis, the lowest NPV comes from a 20% drop in oil price but still generates a ~$5.8MM NPV. The lowest IRR comes from a 20% increase in CAPEX but still generates a 29% IRR. These values indicate that the economics of Reservoir 2 can be stressed and still produce an economic well.

7.1.3. Reservoir 3

Reservoir 3 type curve was projected using an Initial Production (IP) value of 800 BOPD, a d value of 0.300, a B Value of 1.19, and a Gas Oil Ratio (GOR) of 6300 MCF/BO. Table 7.3 displays the Economic Inputs for the well, and Table 7.4 displays the Economic Outputs generated in PFAP. The baseline commodity price was held at $65 WTI, $3 HH, and $0.75 per gallon for NGL liquids, and the model assumes 5 gallons of liquids per thousand cubic feet of natural gas. The model did not have any negative cashflow years, so the model was run through the entire 30-year period. Figure 7.4 displays the single well cumulative undiscounted and discounted cash flows for a Tier 1, or base case, Reservoir 3 well. With the baseline economics conducted for Reservoir 3, a sensitivity analysis was evaluated to determine what inputs have the largest impact on NPV and IRR. Figure 7.5 displays the sensitivity analysis on NPV, and Figure 7.6 displays the sensitivity analysis on IRR. As displayed, CAPEX and oil price significantly impact NPV and IRR for Reservoir 3. For risk analysis, the lowest NPV comes from a 20% drop in oil price but still generates a ~$7.5MM NPV. The lowest IRR comes from a 20% increase in CAPEX but still generates a 32% IRR. These values indicate that the economics of Reservoir 3 can be stressed and still produce an economic well.

Table 7.3. Economic inputs for Reservoir 3 economic model

Input Data		
CAPEX	$10,000,000.00	
Projected Online	Jan 1, 2022	
Working Interest	100%	
NRI	80.00%	
State Tax	7.0%	
Discount Rate NPV	10%	
Depletion	N/A	Years
MACRS	N/A	Years
Gas Price	$3.00	USD
Oil Price	$65.00	USD
NGL	5	GPM
NGL Price	$0.75	USD
SWD	1.5	$/BBL
WOR	0.25	
Reinvestment Rate	8%	
LOE Gas Lift (>30 BOPD)	180000	$/Year
LOE Beam Pump (<30 BOPD)	42000	$/Year
Workover	25000	Year
Workover Annual INC	1%	

Table 7.4. Economic outputs for Reservoir 3 generated by PFAP

Output Data	BFIT	
NPV	$10,134,465.59	USD
IRR	45.56%	
MIRR	10.83%	
Payback	1.21	Years
Discounted Payback	1.52	Years
Discounted ROI	101%	
Discounted Sum	$ 20,134,465.59	USD
NPV @ 8%	$11,742,211.89	USD
NPV @ 10%	$10,134,465.59	USD
NPV @ 13%	$8,229,289.05	USD
NPV @15%	$7,200,239.13	USD
NPV @ 20%	$5,183,223.21	USD
Total Oil	473465	BBLS
Total Gas	2982827	MSCF

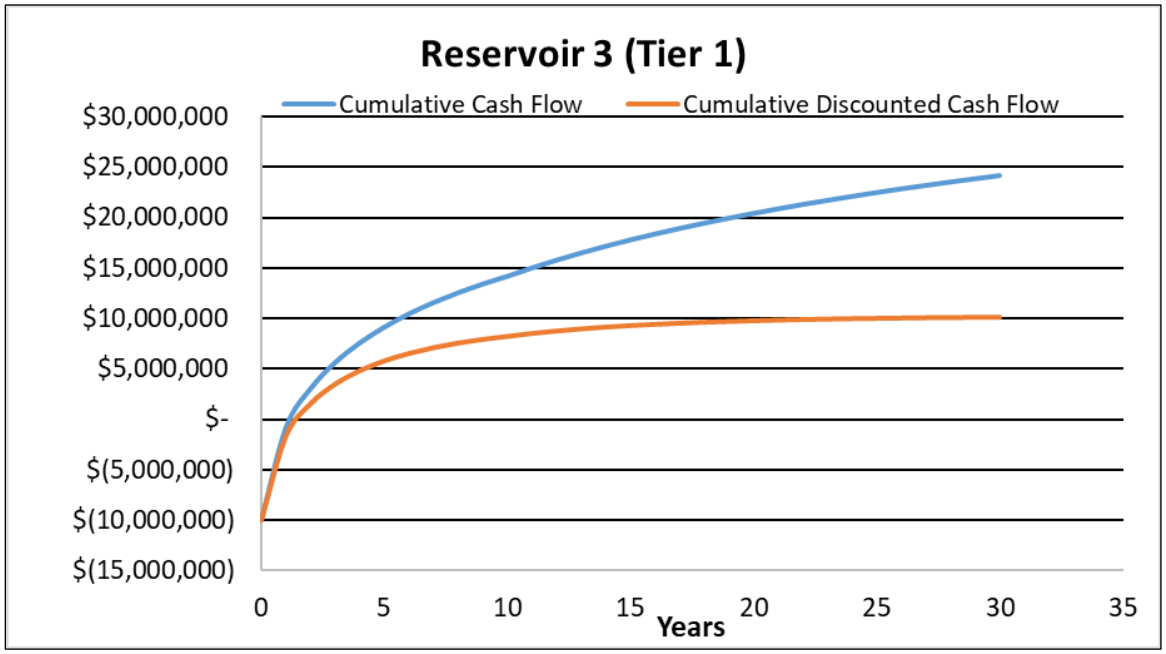

Figure 7.4. Single well cumulative undiscounted and discounted cash flows for the base case Reservoir 3 Well.

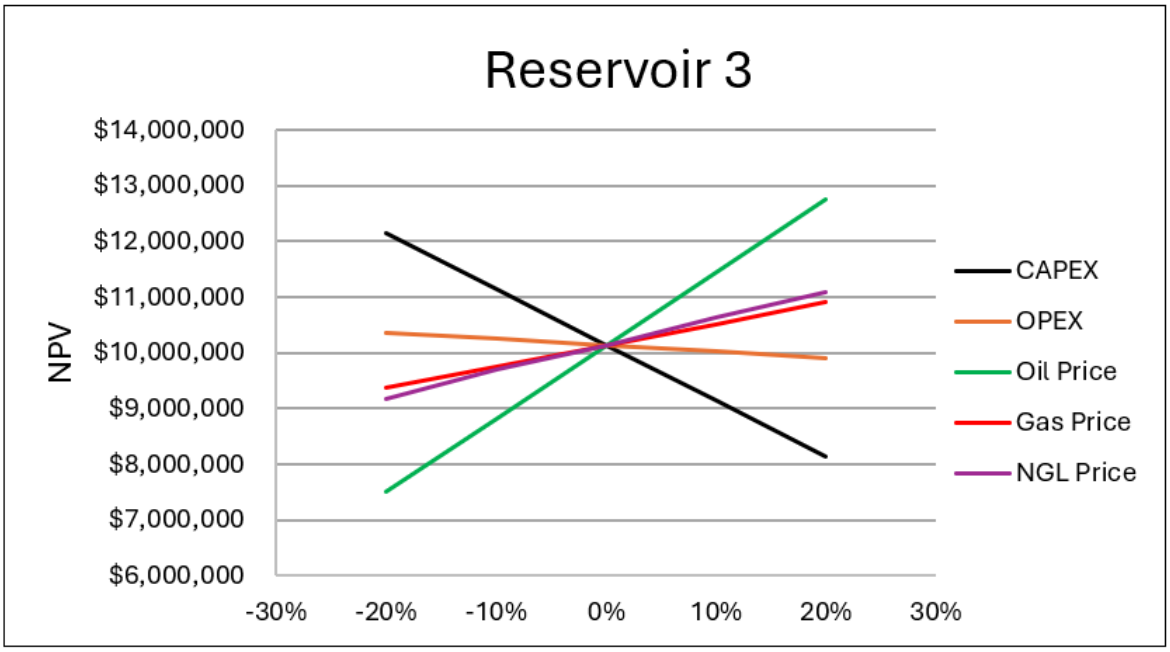

Figure 7.5. NPV sensitivity analysis for Reservoir 3

Figure 7.6. IRR sensitivity analysis for Reservoir 3

7.1.4. Price Deck Analysis

The economics of a project must analyze how the project will perform under various commodity price scenarios. All other variables were held constant to generate the commodity price analysis, with only the oil price, gas price, and NGL price fluctuating. Table 7.5 displays the results.
Additionally, the oil breakeven price was evaluated. In this evaluation, multiple natural gas prices and NGL prices were set, and the oil price was adjusted downwards to the point at which the NPV 10 was zero, and the IRR value was 10%. Table 7.6 displays the oil breakeven pricing scenarios. As realized above, Reservoir 2 does not have the gas volume; thus, the NGL volume of Reservoir 3 is much more dependent on the price of oil to be economic. During full-field development, economics are calculated using tiered production. Tiered production is a means that allows an operator to classify certain areas predicated on their realized or anticipated production. When an operator purchases a leasehold, certain areas are expected to perform better than other areas within the leasehold or project area.

Generally, tiered production is determined in an area by offset wells type curves to help project future well's type curves. Tiers are created by project area and reservoir thickness, whereas in a small area, the thicker the reservoir, the better the production curve. Tiering production helps an operator offset risk. An example would be if one well were drilled in the best reservoir area, an operator may overpay for offset acreage, assuming all wells in the area will produce as well as the first well. After overpaying for acreage, if offset wells do not produce as well as the first well, the project may become uneconomic and a loss for the company. Since there are no other wells in the area, the economic assumptions for Reservoirs 2 and 3 will be as follows in the full field model.

Table 7.5. Commodity price deck analysis for Reservoir 2 and Reservoir 3

Commodity Pricing			RESV 2			RESV 3	
WTI ($/BBL)	NG ($/MCF)	NGL ($/g)	NPV	IRR		NPV	IRR
$ 55.00	$ 3.00	$ 0.75	$ 6,558,020	32.41%		$ 8,112,930	37.81%
$ 65.00	$ 3.00	$ 0.75	$ 8,822,708	41.02%		$ 10,134,466	45.56%
$ 75.00	$ 3.00	$ 0.75	$ 11,087,395	49.86%		$ 12,156,001	53.47%
$ 85.00	$ 3.00	$ 0.75	$ 13,352,083	58.89%		$ 14,177,536	61.52%
$ 55.00	$ 5.00	$ 0.85	$ 8,709,473	40.58%		$ 11,296,848	50.09%
$ 65.00	$ 5.00	$ 0.85	$ 10,974,161	49.42%		$ 13,318,384	58.09%
$ 75.00	$ 5.00	$ 0.85	$ 13,238,849	58.43%		$ 15,339,919	66.19%
$ 85.00	$ 5.00	$ 0.85	$ 15,503,537	67.59%		$ 17,361,455	74.39%
$ 55.00	$ 7.00	$ 0.95	$ 10,860,927	48.97%		$ 14,480,767	62.74%
$ 65.00	$ 7.00	$ 0.95	$ 13,125,615	57.98%		$ 16,502,302	70.90%
$ 75.00	$ 7.00	$ 0.95	$ 15,390,303	67.13%		$ 18,523,838	79.14%
$ 85.00	$ 7.00	$ 0.95	$ 17,654,991	76.39%		$ 20,545,373	87.44%

Table 7.6. Oil price breakeven pricing at a PV10 using various natural gas and NGL pricing for Reservoir 2 and Reservoir 3

Commodity Pricing		RESV 2		RESV 3
NG ($/MCF)	NGL ($/g)	Breakeven WTI ($/BBL)		Breakeven WTI ($/BBL)
$3.00	$0.55	$30.00		$ 21.50
$3.00	$0.65	$28.00		$ 18.50
$3.00	$0.75	$26.50		$ 15.00
$3.00	$0.85	$24.50		$ 12.00
$5.00	$0.55	$22.50		$ 9.00
$5.00	$0.65	$20.50		$ 5.50
$5.00	$0.75	$18.50		$ 2.50
$5.00	$0.85	$17.00		$ -
$7.00	$0.55	$15.00		$ -
$7.00	$0.65	$13.00		$ -
$7.00	$0.75	$11.00		$ -
$7.00	$0.85	$9.00		$ -

The model assumes three tiers of production. The first tier will be the projected type curve developed from the Springer evaluation. Tier 2 production will reflect a 10% reduction in the oil and gas production model from the Tier 1 curve. To accomplish this, only the annual oil and gas production will be reduced by 10%, and all other variables in the economic calculator will remain constant. The final economics from the Tier 2 production is then inserted into the full field economic calculator. Tier 3 production will reflect a 20% reduction in the oil and gas production model from the Tier 1 curve. Tier 3 economics will be conducted the same as Tier 2 economics by holding all other variables constant.

7.1.5. Tiered Production

After the production curves were constructed for the various tiers of production, an economic analysis was conducted for each tier in both Reservoir 2 and 3 to ensure that all tiers were economically viable to develop. To run the economics, all the input variables covered in Section 7.1 for single well economics were applied to the lower tier production curves. Table 7.7 displays the economic output for a Tier 2 Reservoir 2 well and Table 7.8 displays the economic output for a Tier 3 Reservoir 2 well. As displayed, both Tier 2 and Tier 3 wells in Reservoir 2 are economic. The most stressed case, Tier 3, still generates ~$4.9 NPV 10 and a ~26% IRR. Additionally, a Tier 3 well will payout in ~2 undiscounted years with conservative commodity pricing environments. These economics will pass the majority of operators' hurdle rates. Table 7.9 displays the economic output for a Tier 2 Reservoir 3 well and Table 7.10 displays the economic output for a Tier 3 Reservoir 3 well.

Table 7.7. Economic outputs for Tier 2 Reservoir 2 well generated by PFAP.

Output Data	BFIT	
NPV	$6,873,521.88	USD
IRR	33.31%	
MIRR	10.18%	
Payback	1.67	Years
Discounted Payback	2.13	Years
Discounted ROI	69%	
Discounted Sum Earnings	$16,873,521.88	USD
NPV @ 8%	$8,201,152.88	USD
NPV @ 10%	$6,873,521.88	USD
NPV @ 13%	$5,297,946.17	USD
NPV @ 15%	$4,445,707.00	USD
NPV @ 20%	$2,772,352.74	USD
Total Oil	476380	BBLS
Total Gas	1810244	MSCF

Table 7.8. Economic outputs for Tier 3 Reservoir 2 well generated by PFAP

Output Data	BFIT	
NPV	$4,885,201.98	USD
IRR	25.92%	
MIRR	9.72%	
Payback	2.11	Years
Discounted Payback	2.94	Years
Discounted ROI	49%	
Discounted Sum Earnings	$14,885,201.98	USD
NPV @ 8%	$6,052,931.79	USD
NPV @ 10%	$4,885,201.98	USD
NPV @ 13%	$3,498,294.93	USD
NPV @ 15%	$2,747,706.88	USD
NPV @ 20%	$1,273,433.73	USD
Total Oil	423449	BBLS
Total Gas	1609106	MSCF

Table 7.9. Economic outputs for Tier 2 Reservoir 3 well generated by PFAP

Output Data	BFIT	
NPV	$8,024,203.81	USD
IRR	37.31%	
MIRR	10.42%	
Payback	1.51	Years
Discounted Payback	1.88	Years
Discounted ROI	80%	
Discounted Sum Earnings	$ 18,024,203.81	USD
NPV @ 8%	$9,461,099.08	USD
NPV @ 10%	$8,024,203.81	USD
NPV @ 13%	$6,320,533.97	USD
NPV @ 15%	$5,399,996.95	USD
NPV @ 20%	$3,595,337.83	USD
Total Oil	426118	BBLS
Total Gas	2684545	MSCF

Table 7.10. Economic outputs for Tier 3 Reservoir 3 well generated by PFAP

Output Data	BFIT	
NPV	$5,919,262.52	USD
IRR	29.40%	
MIRR	9.97%	
Payback	1.88	Years
Discounted Payback	2.55	Years
Discounted ROI	59%	
Discounted Sum Earnings	$ 15,919,262.52	USD
NPV @ 8%	$7,185,099.92	USD
NPV @ 10%	$5,919,262.52	USD
NPV @ 13%	$4,417,063.81	USD
NPV @ 15%	$3,604,871.50	USD
NPV @ 20%	$2,011,910.01	USD
Total Oil	378772	BBLS
Total Gas	2386262	MSCF

As displayed, both Tier 2 and Tier 3 wells in Reservoir 3 are economic. The most stressed case, Tier 3, still generates ~$5.9 NPV 10 and a ~29% IRR. Additionally, a Tier 3 well will payout in under 2 undiscounted years with conservative commodity pricing environments. These economics will also pass the majority of operators' hurdle rates. A summary table of the tiers NPV10 and IRR for both reservoirs is listed in Table 7.11.

Table 7.11. Summary of tier economics for Reservoir 2 and Reservoir 3

		NPV 10	IRR
RESV 2	Tier 1	$ 8,822,708	41.02%
RESV 2	Tier 2	$ 6,873,522	33.31%
RESV 2	Tier 3	$ 4,885,202	25.92%
RESV 3	Tier 1	$ 10,134,466	45.56%
RESV 3	Tier 2	$ 8,024,204	37.31%
RESV 3	Tier 3	$ 5,919,263	29.40%

Within the economic model, a near-even distribution of wells will be categorized by each tier. This means roughly one-third of all PUDs for each reservoir will be Tier 1, a third will be Tier 2, and a

third will be Tier 3. Table 7.12 displays the well count for each tier, and the appendix covers the tiers' projected annual production values.

Table 7.12. Tier well count calculations

	Drill Type		Wells per Year		Well Types Drilled		
Year	Reservoir 2	Reservoir 3	Reservoir 2	Reservoir 3	Type	Reservoir 2	Reservoir 3
1	Tier 1	Tier 1	10	10	Tier 1	20	30
2	Tier 1	Tier 1	10	10	Tier 2	10	20
3	Tier 2	Tier 1	10	10	Tier 3	10	20
4	Tier 3	Tier 2	10	10	***Total***	***40***	***70***
5		Tier 2		10			
6		Tier 3		10			
7		Tier 3		10			

There are three important notes to cover on the tiering of production. First is a sequence, as will be covered in future sections. The timing of which the different tiers of wells are drilled will have an impact on the economics of the development program. Different areas, thus different tiers, will be drilled simultaneously, but the PFAP software currently only allows one tier to be drilled at a time. Second, each tier reflects what would become the P50 curve for each area. This means the wells drilled in Tier 2 rock may reflect a Tier 1 or Tier 3 curve, but the averaged curves between the wells are projected to fit the Tier 2 curve. Third, this evaluation covers the entire mapped area of the Caney Shale and has preset well-spacing assumptions. As well spacing is refined, the tiers may change, as would the well count. Additionally, as the Caney Shale is developed, certain project areas will be mapped, and they will have their own subdivision of tiers. This, in total, means as the reservoir is developed, these well counts and tier valuations will be refined. This refinement is covered in the future work and discussion sections.

7.1.6. Evaluation of Reservoir Vastness

To quantify a prospect, an operator needs to know the individual well economics and the scale of the play. The scale of the play matters because it is directly linked to how many drilling locations are available, and that will determine the assets' net value. To determine the scope of the play, geologists will generally use one of two techniques. The first is seismic; this method involves using large machines on a surface that vibrate the ground or explosives creating a seismic wave through the earth. Monitors are set in the general area and collect the wave data. Geologists use seismic data to create formation layer models and try to determine if oil and gas traps are below. This method is typically used in "wildcat" areas where no other wells are drilled that could be used as a reference point. The second method is using control wells, this method was used to quantify the thickness of the Caney Shale. Control wells are either offset wells drilled through the target formation or pilot wells operators

drill in an area to map and characterize formations. When enough control wells are available, cross-sections can be constructed along with isopach maps to estimate the thickness of a formation and subunits by interpolating values between points and extrapolating values outside of the control area.

Three principal reservoirs were mapped within the Caney Shale. Using the geologist's metrics, the general scale of the play can be noted for full-field development. The figures that follow (Figures 7.7 to 7.9) show the geologist's isopach maps of the drilled thickness of the principal reservoirs in the Caney Shale. To determine if the reservoir would have commercial production, the team determined that Reservoir 1 needed at least 30 feet of thickness, Reservoir 2 needed at least 20 feet, and Reservoir 3 needed 60 feet of thickness. After completion, the geology team determined that Reservoir 1 has 27 square miles of pay, Reservoir 2 has 26 square miles of pay, and Reservoir 3 has 42 square miles of pay. These values were used in the full field economic section to determine how many locations are available for the operator to drill and then estimate the net asset value. The final assumption within geology is that the operator has all the acreage that the geology team mapped leased or held by production.

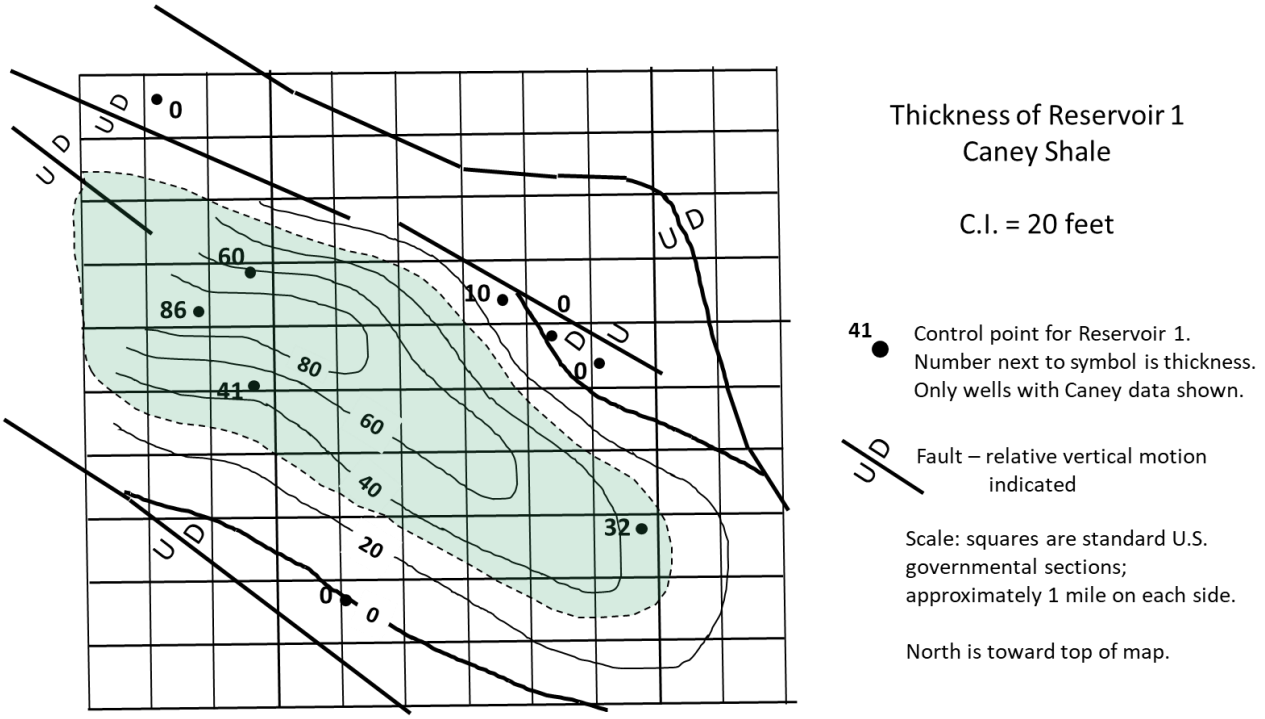

Figure 7.7. Isopach map of Reservoir 1, showing that reservoir >30 feet thick is distributed for 27 square miles (Provided by Oklahoma State University School of Geology)

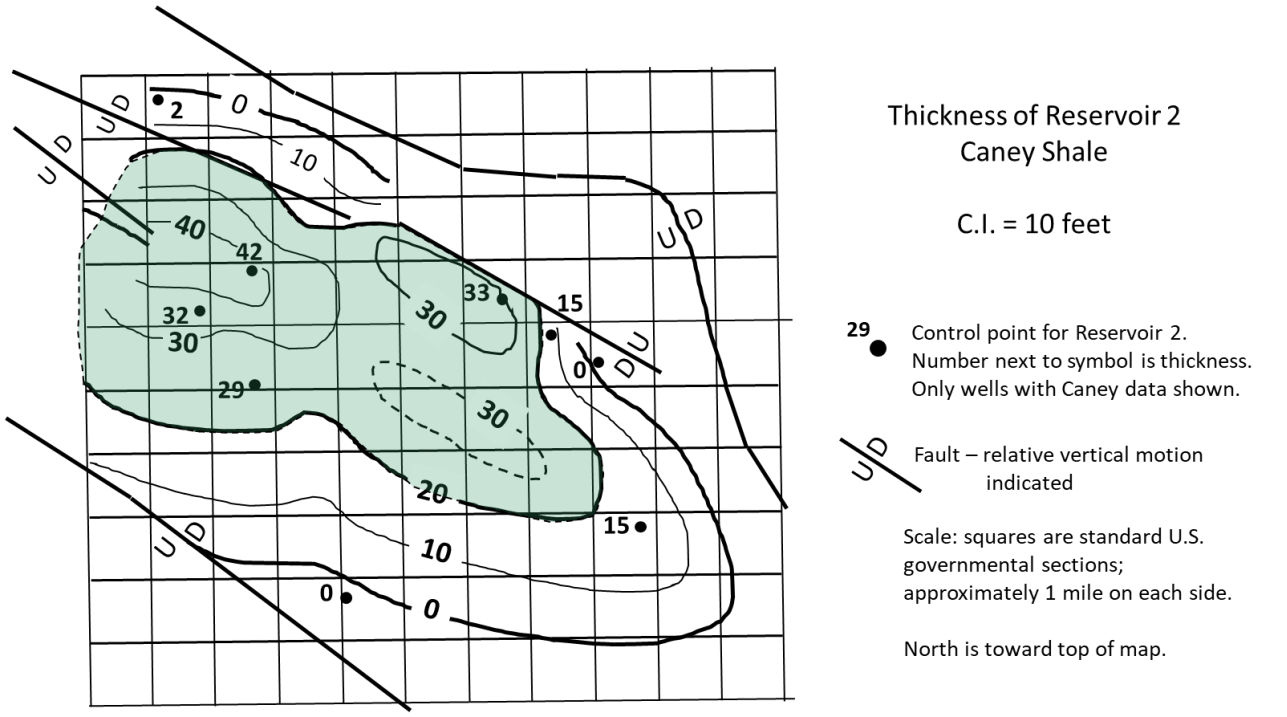

Figure 7.8. Isopach map of Reservoir 2, showing that reservoir >20 feet thick is distributed for 26 square miles (Provided by Oklahoma State University School of Geology)

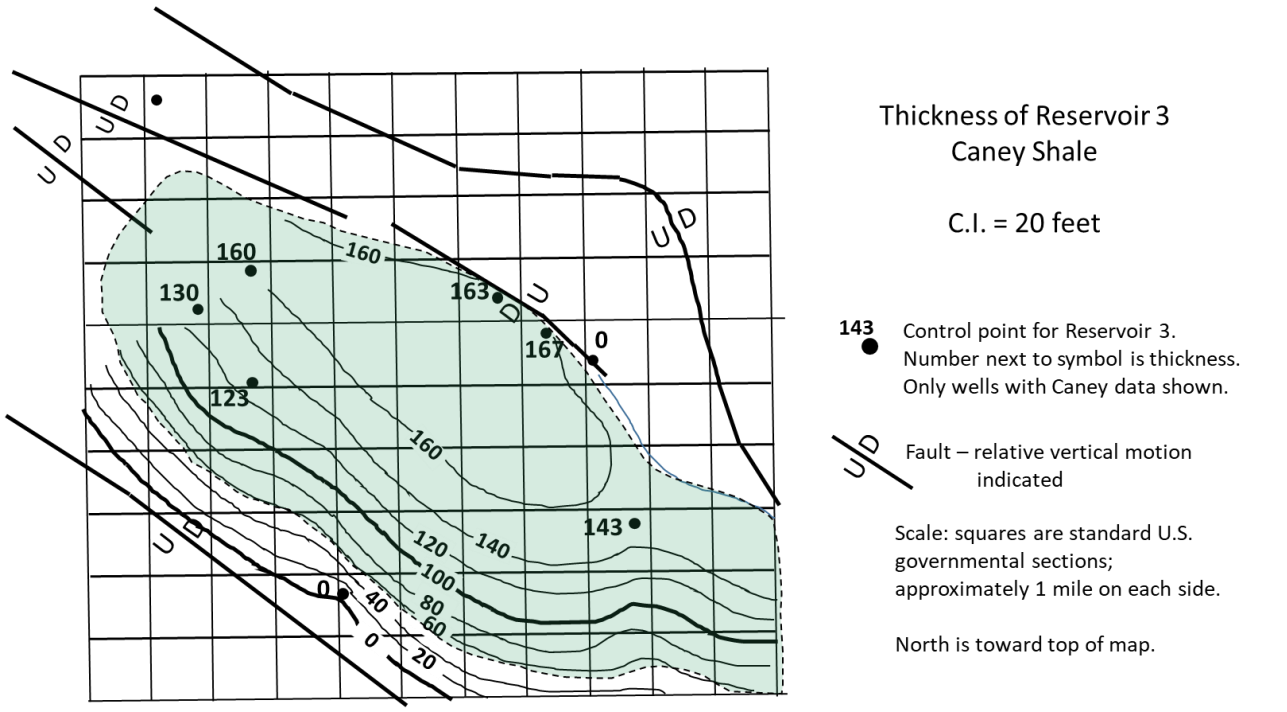

Figure 7.9. Isopach map of Reservoir 3, showing that reservoir >60 feet thick is distributed for 42 square miles (Provided by Oklahoma State University School of Geology)

7.1.7. Determining Quantity of Drilling Locations Based on Well Spacing

The distance wells are spaced can play a critical role in how the wells will perform. The well spacing also plays a key role in determining the net asset value. To perform the well spacing analysis, two scenarios must be considered, that is, if one or more reservoirs are present. In the case that only one reservoir is present, a single-pay bench analysis will be conducted. Six wells in an area where only Reservoir 3 is present in commercial quantities were evaluated to perform this task. Figure 7.10 displays the evaluation. Under standard spacing, each well would be 880' apart. Reservoir 3 is approximately 125' thick, so the alternate scenario will have wells wine racked throughout Reservoir 3 to increase the distance between wells to reduce fracture interference. By wine racking the wells throughout Reservoir 3, the wells would increase to approximately 890' of spacing or a 10' increase in distance between wells.

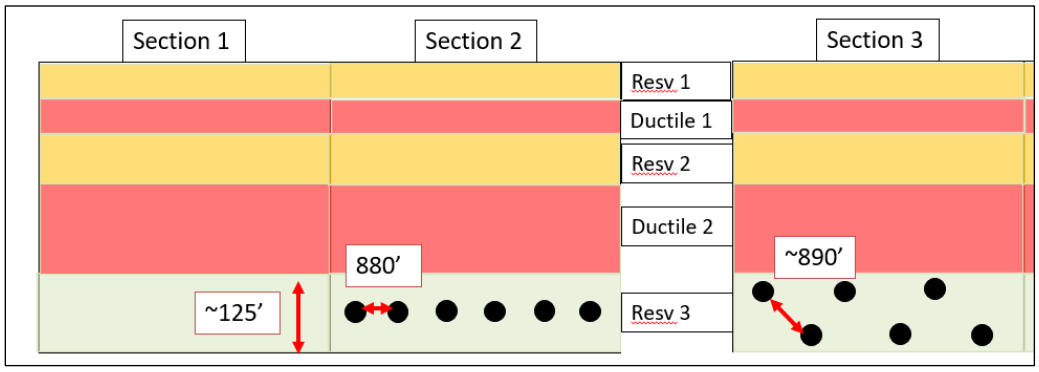

Figure 7.10. Gunbarrel view of well stacking in Reservoir 3 measuring the distance between wells that are landed linear versus a wine-rack configuration

An additional 10' of spacing in a reservoir is negligible, so it would be best to drill the wells in the highest quality portion of the reservoir when only a single pay bench is available. For areas that have multiple pay benches, an additional investigation was conducted. Knowing that ~880' well spacing was the minimum acceptable spacing between wells for a single pay bench, the same distance between wells was applied to wells in different pay benches. Figure 7.11 displays various wine-racking methods between Reservoir 2 and Reservoir 3 and their respective well-spacing distances.

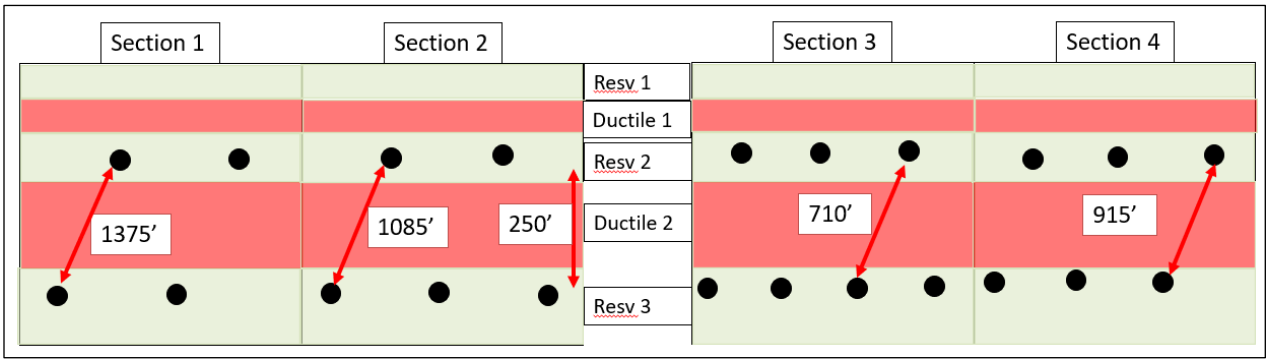

Figure 7.11. Various well-spacing distances when wells are wine racked between Reservoir 2 and Reservoir 3.

With the various configurations that can be applied, a means to project what configuration would create the highest value was analyzed. To perform the analysis, the NPV for various tiers was evaluated, and the probability of the performance was predicated upon the spacing results used in the previous studies. The key example was 880' of well spacing with 1750 PSI of offset depletion resulted in approximately 10% production reduction. For this case, wells spaced farther apart were anticipated to have 90-100 % of Tier 1 production values and wells spaced closer together were anticipated to have Tier 3 production or a 20% reduction in production from a Tier 1 well. The higher probability scenarios have green highlights indicating a higher probability of occurring, yellow marked cells have a moderate chance of occurring and red marked cells are very unlikely scenarios. To assess the value, the assumption is that all the wells are drilled and completed simultaneously or within a few months of each other, and the NPV is determined by adding all the NPVs of the developed well together. The wells were calculated as 2-mile laterals to determine the acreage value, so two sections would be required to drill the wells. With two sections being drilled, the total NPV was divided by 1280 acres (640 acres per section times 2 sections = 1280 acres) to determine the value per acre. Last, the total NPV was divided by the total well count to determine the average value per well, giving the study 3 different value metrics to evaluate. The results of this study are displayed in Table 7.13.

Table 7.13. Value calculations predicted upon well spacing, including a probabilistic evaluation of scenario likelihood

Scenario	NPV	NPV/AC	AVG Value/ Well	Rough Spacing	Comment
4 R3/ 3 R2 100%	$ 67,005,985	$ 52,348	$ 9,572,284	710	Too tight Fracture Interference Likely to Occur
6 R3 100%	$ 60,806,794	$ 47,505	$ 10,134,466	880	Too tight Fracture Interference Likely to Occur
3 R3/ 3 R2 100%	$ 56,871,519	$ 44,431	$ 9,478,587	915	Reasonable Probability
4 R3/ 3 R2 90%	$ 52,717,381	$ 41,185	$ 7,531,054	710	Too tight Fracture Interference Likely to Occur
5 R3 100%	$ 50,672,328	$ 39,588	$ 10,134,466	1050	Reasonable Probability
6 R3 90%	$ 48,145,223	$ 37,613	$ 8,024,204	880	Reasonable Probability
3 R3 2 R2 100%	$ 48,048,812	$ 37,538	$ 9,609,762	1085	Reasonable Probability
3 R3/ 3 R2 90%	$ 44,693,177	$ 34,917	$ 7,448,863	915	High Probability
4 R3 100%	$ 40,537,862	$ 31,670	$ 10,134,466	1320	High Probability
5 R3 90%	$ 40,121,019	$ 31,345	$ 8,024,204	1050	High Probability
4 R3/ 3 R2 80%	$ 38,332,656	$ 29,947	$ 5,476,094	710	Reasonable Probability
2 R3 2 R2 100%	$ 37,914,346	$ 29,621	$ 9,478,587	1375	High Probability
3 R3 2 R2 90%	$ 37,819,655	$ 29,547	$ 7,563,931	1085	High Probability
6 R3 80%	$ 35,515,575	$ 27,747	$ 5,919,263	880	Reasonable Probability
3 R3/ 3 R2 80%	$ 32,413,394	$ 25,323	$ 5,402,232	915	Reasonable Probability
5 R3 80%	$ 29,596,313	$ 23,122	$ 5,919,263	1050	Probably too degrated

From the evaluation, when Reservoirs 2 and 3 are present, drilling three Reservoir 2 and three Reservoir 3 wells with a projected Tier 2 type curve creates the highest NPV per acre under the high likelihood filter. Drilling two Reservoir 2 wells and two Reservoir 3 wells with Tier 1 production increases the average well value but reduces total NPV and NPV per acre. When only Reservoir 3 is present, four Reservoir 3 wells at Tier 1 production (100%) are better for acreage value and average well value than five Reservoir 3 wells at Tier 2 (90%) level, knowing that at 1050' spacing there will be interference, four wells per section would likely be the better value. To confirm these spacing values against industry standards, a shale well unit spacing the industry partner employs in Oklahoma was referenced as an analog. As Figure 7.12 shows, the industry partner will drill 2 to 6 wells per

unit depending on the reservoir thickness and quality. The proposed development plan proposes 4 to 6 Caney wells per section, or unit with 2-mile laterals, and falls well within industry and operator standards.

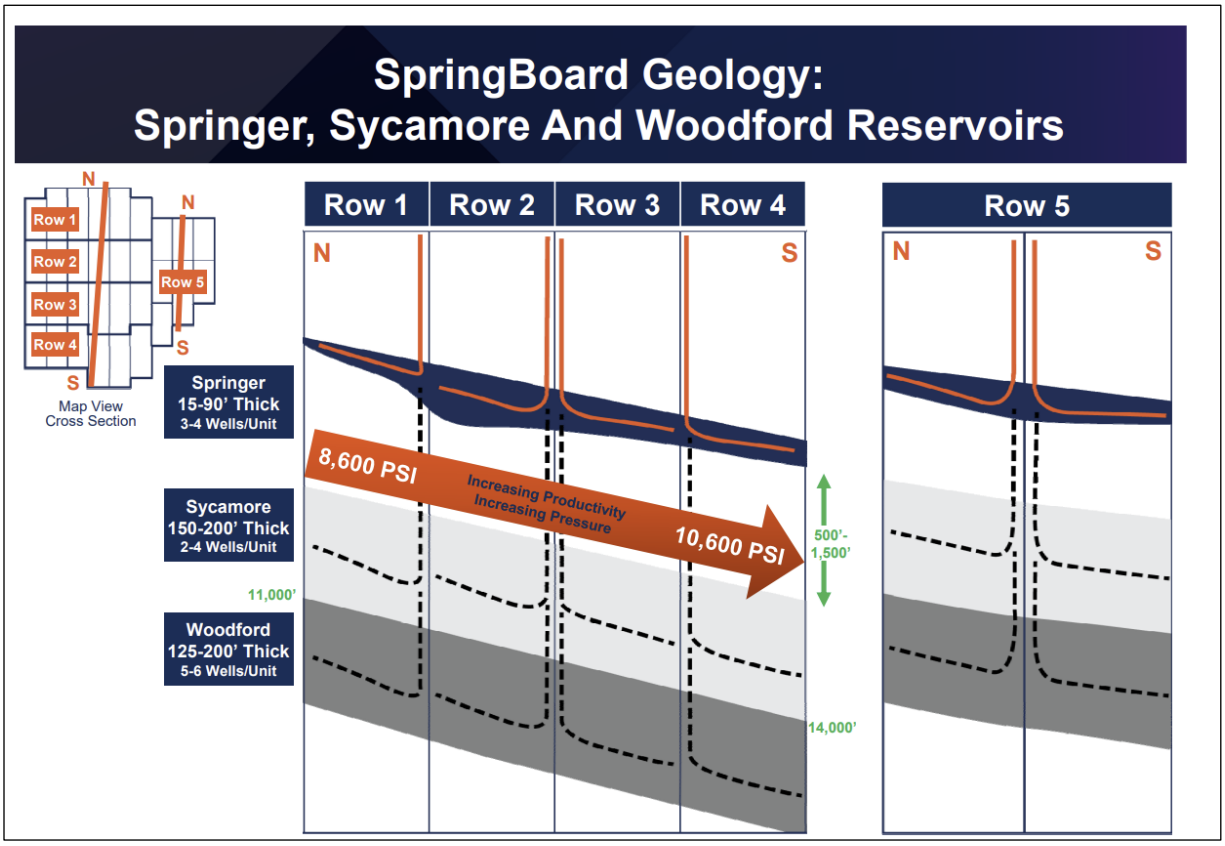

Figure 7.12. Well count per drilling unit (The industry partner, 2023).

The number of drillable locations can be determined using the well spacing analysis and the geological mapping of the Caney reservoir. These locations will, in essence, sum up the net asset value of the project due to the fact each wells' economic valuation will sum to the NAV.

To set the baseline, each drilling unit is approximately 2 square miles, one-mile-wide by two miles long. When conducting the spacing analysis, the well spacing was evaluated per drilling unit, meaning it was determined how many laterals could be placed within a mile stretch. The 2-mile-long portion of the drilling unit is a function of the lateral length for the Caney wells, which is roughly 2 miles. The geologic evaluation determined that Reservoir 2 is present in approximately 26 square miles, and Reservoir 3 is present in approximately 42 square miles. Additionally, in sections where Reservoir 2 is present, Reservoir 3 is also present.

In the 26 square miles where Reservoirs 2 and 3 are present, the well spacing analysis determined that three Reservoir 2 wells and three Reservoir 3 wells per drilling unit was the optimum configuration. Twenty-six square miles is equivalent to 13 drilling units meaning that within these 13 drilling units, there will be thirty-nine Reservoir 2 wells (3 wells per unit * 13 drilling units) and thirty-nine Reservoir 3 wells (3 wells per unit * 13 drilling units).

In the area where just Reservoir 3 is present is approximately 16 square miles. This is the 42 square miles of Reservoir 3 being present less the 26 square miles where Reservoirs 2 and 3 are present, which was already covered. The well spacing analysis determined that four Reservoir 3 wells per drilling unit was the optimum configuration when only Reservoir 3 was present. Sixteen square miles is equivalent to 8 drilling units meaning that within these eight drilling units, there will be 32 Reservoir 3 wells (4 wells per unit * 8 drilling units). The analysis shows approximately 39 drillable locations for Reservoir 2 and 71 drillable locations for Reservoir 3. The total drillable locations for the Caney prospect are 110. These values will be used in the full field analysis to determine the asset's net value predicated upon a predetermined drilling schedule.

7.1.8. Wells Per Section and Acreage Value

When calculating net asset value or value per section, understanding how many wells can be drilled in the leased acreage is the cornerstone of value assessment. The basics of the Oklahoma grid system are the state is sectioned off into townships and ranges using the Public Land Survey System. Each township and range is broken down into 36 sections. Each section, under most circumstances, is one mile by one mile. Within each section are 16 unit letters; each unit letter is 40 acres and the 16-unit letters in a section add up to 640 acres. Figure 7.13 displays the Public Land System Survey grid methods.

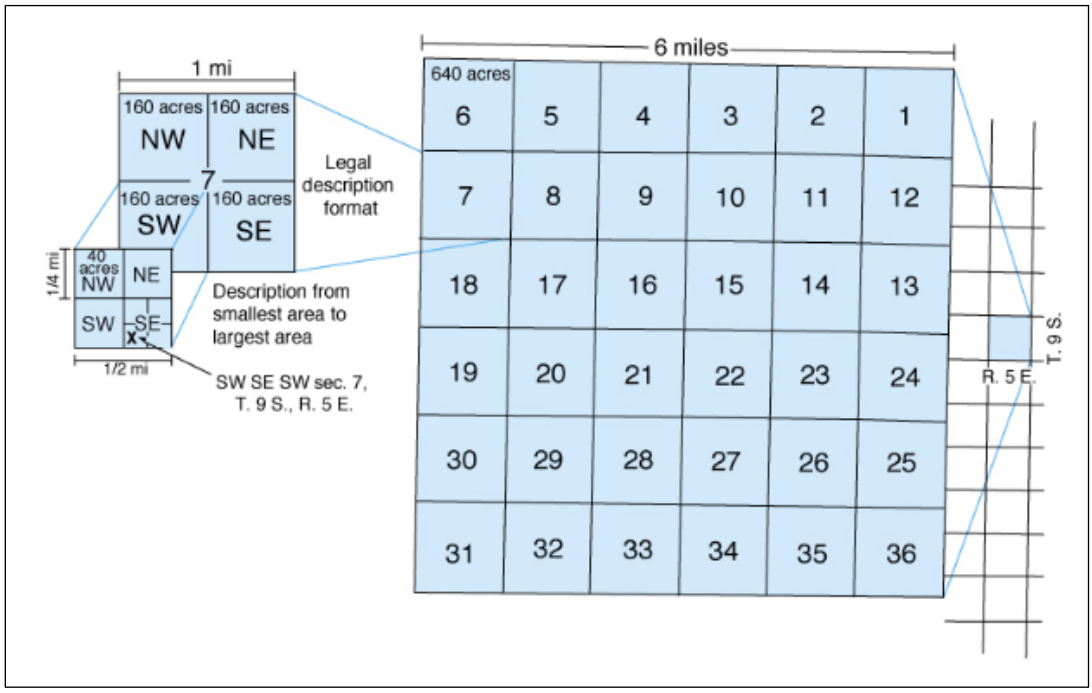

Figure 7.13. Public Land Survey System (Geokansas, 2023)

As stated, a section is 1 mile (5280') by 1 mile long, so the Caney laterals drilled true north-south or east-west would cover two sections, as shown in Figure 7.14. After knowing the distance of a well, the distance that wells are spaced will help calculate how many wells can fit into a section. Current industry practice spaces horizontals shale well at ~880' apart. The reason that wells are not spaced

closer is the fracture interference resulting in parent-child degraded type curve issues. By spacing wells farther apart, many of the economic reserves in the reservoir are left behind. Using an 880' well spacing, six wells per zone can be landed in one section. Using a one-reservoir scenario, it takes two sections to drill six wells. Two sections equal 1280 acres, so each well will require approximately 213 acres to drill. Assuming acreage leases at $20,000/acre, an additional $4,200,000 (213 * $20,000) would need to be added to the well cost.

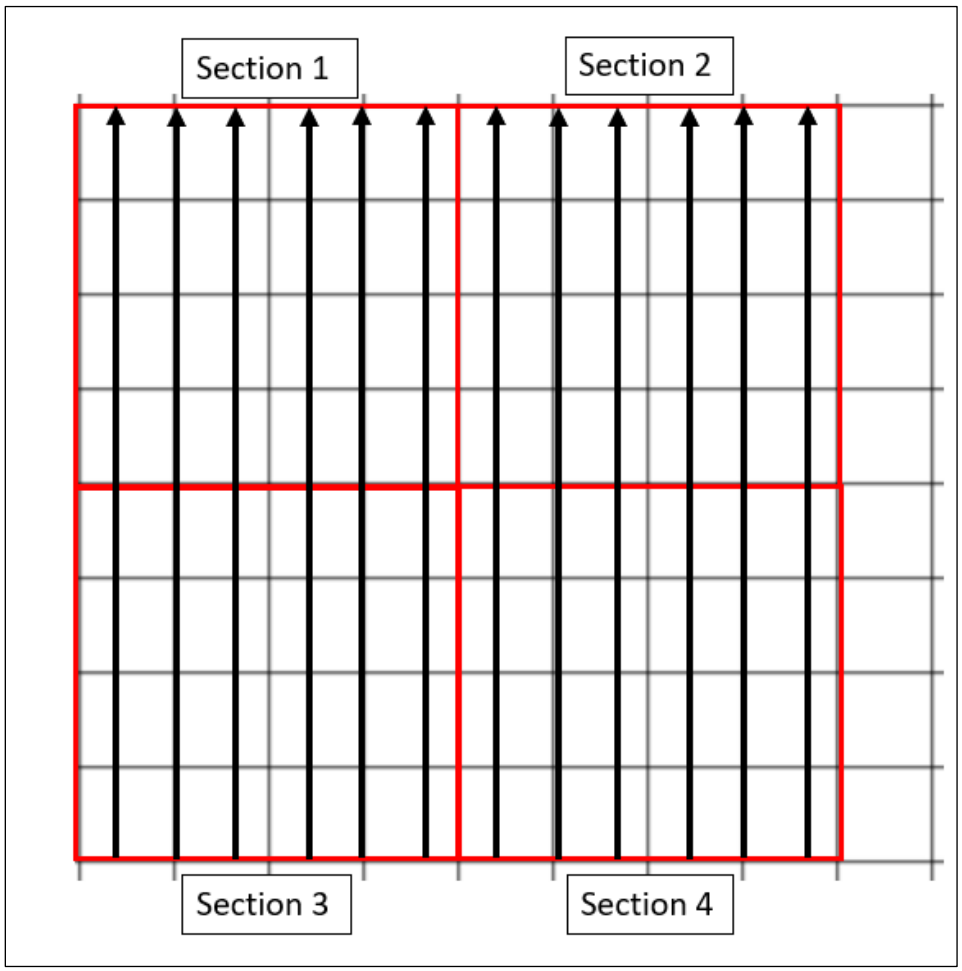

Figure 7.14. Six horizontal wells fitting a pay bench using a six well per section and 2 sections per well orientation, fit to a true north and south drill on a township range section grid configuration

7.1.9. Development Plan

With the analysis of the depletion study landing 6 Reservoir 3 wells in a drilling unit will likely result in production degradation of greater than 10% per well or effectively drilling a drilling unit full of Tier 2 wells. Where 3 Reservoir 2 wells and 3 Reservoir 3 wells are drilled in a drilling unit, the model predicts minimal inference between the wells, which in turn would lead to a better value for the unit. Table 7.14 displays the economics per unit with listed development scenarios.

Table 7.14. Single well NPV and drilling unit NPV

		NPV10				
Well Type	Production Curve	RESV 2	RESV 3		Wells per Drilling Unit	**NPV10**
Tier 1	Base	$8,822,708	$10,134,466		6 Tier 2 RESV 3	$48,145,223
Tier 2	-10%	$6,873,522	$8,024,204		3 Tier 1 RESV 2 and 3 Tier 1 RESV 3	$56,871,519
Tier 3	-20%	$4,885,202	$5,919,263			

With the information given, having three wells in each reservoir is recommended going forward when both reservoirs are present. In the case the ductile zone thins, these metrics will need to be reevaluated.

When only Reservoir 3 is present, 4 Tier 1 Reservoir 3 wells have roughly the same value as 5 Tier 2 Reservoir 3 wells, as displayed in Table 7.15. Predicated upon the depletion study, it is likely that wells spaced 1050’ apart will have more depletion impact than wells spaced 1320’ apart. This infers that the two well configurations will create similar NPV per Drilling Unit, but the four well design creates more value per well. With the information given, having four wells in Reservoir 3 is recommended going forward when only Reservoir 3 is present.

Table 7.15. NPV comparison of 4 Tier 1 wells versus 5 Tier 2 wells in Reservoir 3

Wells per Drilling Unit	NPV	NPV/ Well
4 Tier 1 RESV 3	$ 40,537,862	$ 10,134,466
5 Tier 2 RESV 3	$ 40,121,019	$ 8,024,204

The model assumes ~1/3 of the drilling locations are Tier 1, ~1/3 Tier 2, and ~1/3 Tier 3. Figure 7.15 displays what a typical generic tiered production map would look like. In the example tiered production map, the tier 1 or best productive rock is in the middle of the project area, and as you get closer to the edges of the play, the rock is not as productive. When operators develop a play, they generally try to develop the best rock first, then move towards the lesser quality rock. In the model, the assumption is the projected type curve for all tiered rock is quantified, so there is no need to develop lesser grade rock for testing and that the geologic extent of the reservoir is leased by the operator and the leases are held by legacy production in different reservoirs allowing the operator to develop the reservoir in the most economically beneficial manner.

Additionally, the model does not assume cost inflation in the CAPEX portion or strip pricing in commodity pricing. Commodity prices were held constant to evaluate the performance of the asset at various price points. The CAPEX pricing will not have as large of an effect on the final economics of the project because the development calculator discounts all future cash flows starting from time

zero. This means when capital expenditure pricing escalates in the future, they will have more minor effects due to the discounting effect creating smaller variances in projected economics and field economics.

The development model assumes that the drilling units will be drilled sequentially. The reason for sequential drilling or drilling each unit to completion before drilling the next unit will help minimize the depletion impact of offset wells on the new drills. If wells were drilled randomly throughout the leasehold, depletion impacts could vary significantly between wells. Additionally, drilling sequentially will allow the operator to slowly step out into new rock and find if there are uneconomic areas to drill by noting trends in the production curves as the step out occurs. Figure 7.16 shows the 110 well final field development plan.

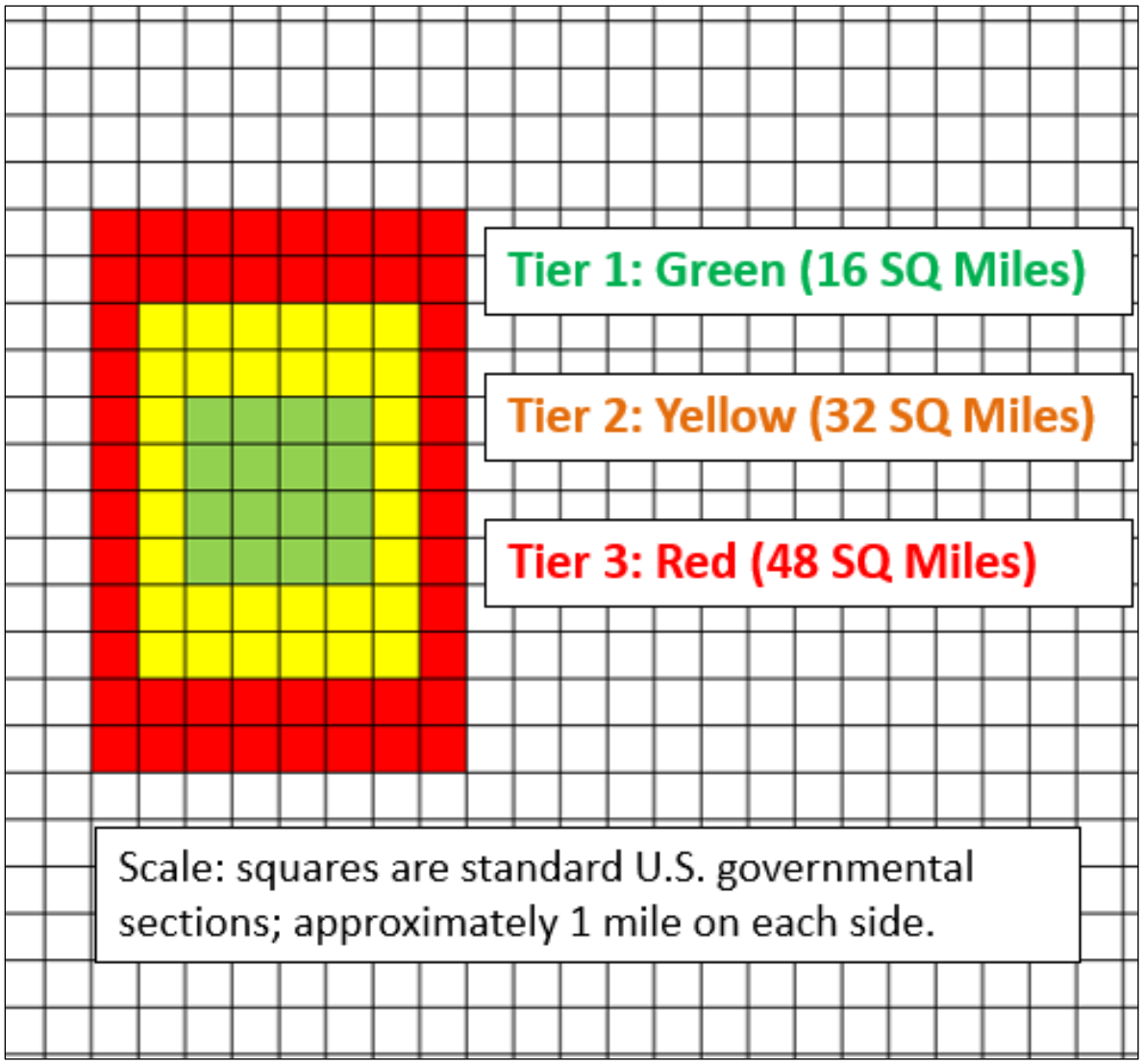

Figure 7.15. Generic tiered acreage.

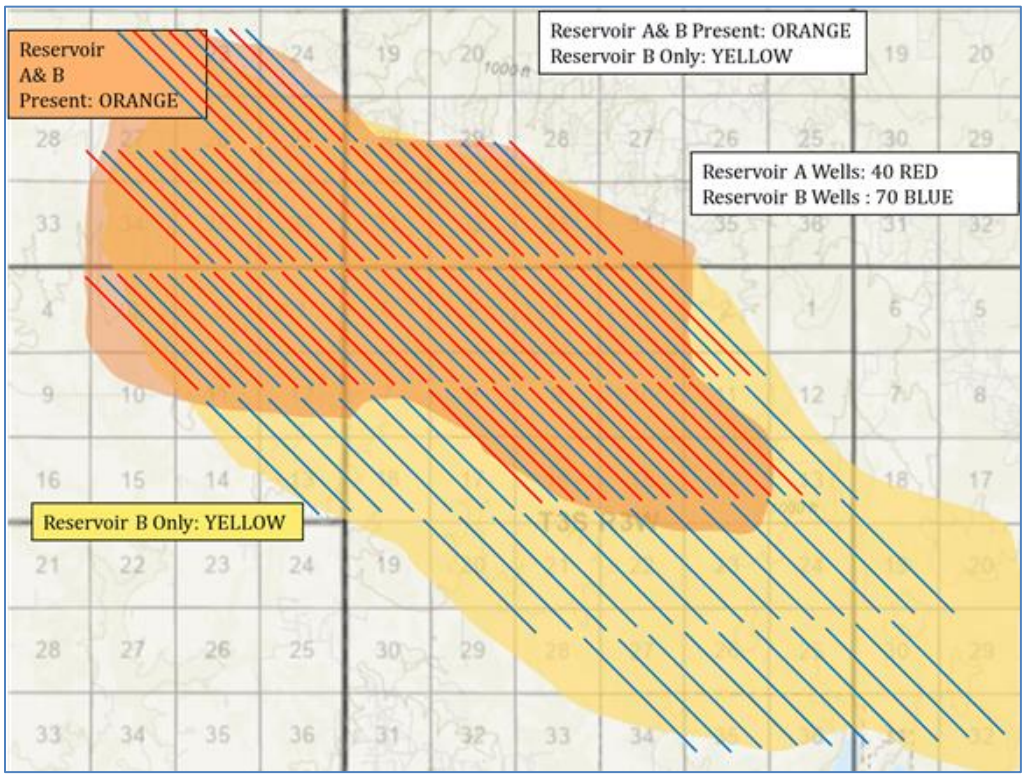

Figure 7.16. Proposed final field development plan for Caney Shale

Lastly, the economic development model assumes the Reservoir 2 and Reservoir 3 wells will be drilled simultaneously. The development economic model evaluates one pay bench. To combine the two reservoirs, the assumption is that they are drilled as separate programs but are assumed to combine the values of the two reservoirs. Additionally, drilling the reservoirs simultaneously will help minimize the depletion impact of offset wells in the other reservoir on the new drills. Table 7.16 displays the proposed drilling program and the assumption of the well curve. The drilling program calls for ten Reservoir 2 wells and ten Reservoir 3 wells to be drilled annually until the reservoir is completely developed. The program assumes Reservoir 2 to be drilled in 4 years (40 wells) and Reservoir 3 to be drilled in 7 years (70 wells).

Table 7.16. Development program and years to complete

	Drill Type		**Wells per Year**		**Well Types Drilled**		
Year	Reservoir 2	Reservoir 3	Reservoir 2	Reservoir 3	Type	Reservoir 2	Reservoir 3
1	Tier 1	Tier 1	10	10	Tier 1	20	30
2	Tier 1	Tier 1	10	10	Tier 2	10	20
3	Tier 2	Tier 1	10	10	Tier 3	10	20
4	Tier 3	Tier 2	10	10	***Total***	***40***	***70***
5		Tier 2	0	10			
6		Tier 3	0	10			
7		Tier 3	0	10			

7.1.10. Net Asset Value

This portion will evaluate the entire Net Asset Value (NAV) of the Caney Shale. To conduct this, all the single well economics, well spacing analysis, and development planning will be used to calculate the values. The field development calculator will also consider the discounted value of the wells predicted upon the development plan, meaning the acreage value and NAV will have reductions due to the length of time it will take to complete the project to its entirety. Each reservoir is calculated separately, and the combined values will then be used to calculate various economic metrics to evaluate NAV and incorporate other metrics such as ROI, maximum outlay, total cash flow, etc. The last important note to consider is since the reservoirs are evaluated separately within the PFAP software, the assumption is parallel development, meaning that if ten Reservoir 2 wells and ten Reservoir 3 wells are drilled in year one, a total of 20 wells will be drilled which will increase the NAV but also increase value such as maximum outlay. This program assumes a few test wells have been drilled, and full field development has begun. To evaluate Reservoir 2, the input value for Reservoir 2 is listed in Table 7.17, and the output values for the development are listed in Table 7.18. Figure 7.17 displays the development cumulative undiscounted and discounted cash flows for Reservoir 2 wells.

Table 7.17. Input data for Reservoir 2 development

Input Values		Year	Drill Type
Wells Per Year	10	1	Tier 1
Wells Per Section	3	2	Tier 1
Sections per Well	2	3	Tier 2
Drilling Years	4	4	Tier 3
Wells Drilled	40	5	NA
Acreage Drilled	17067	6	NA
CAPEX	$10,000,000	7	NA
Discount Rate	10%	8	NA
		9	NA
		10	NA

Table 7.18. Output data for Reservoir 2 development

Output Data		
Total Cash Flow	$768,980,872	
CF per Well	$19,224,522	
Total DCF	$261,942,719	
Total DCF (AC)	$15,348	per acre
Years to Drill in FCF	3.4	
Years to Drill in DFCF	3.6	
MAX Outlay	$(112,947,290)	

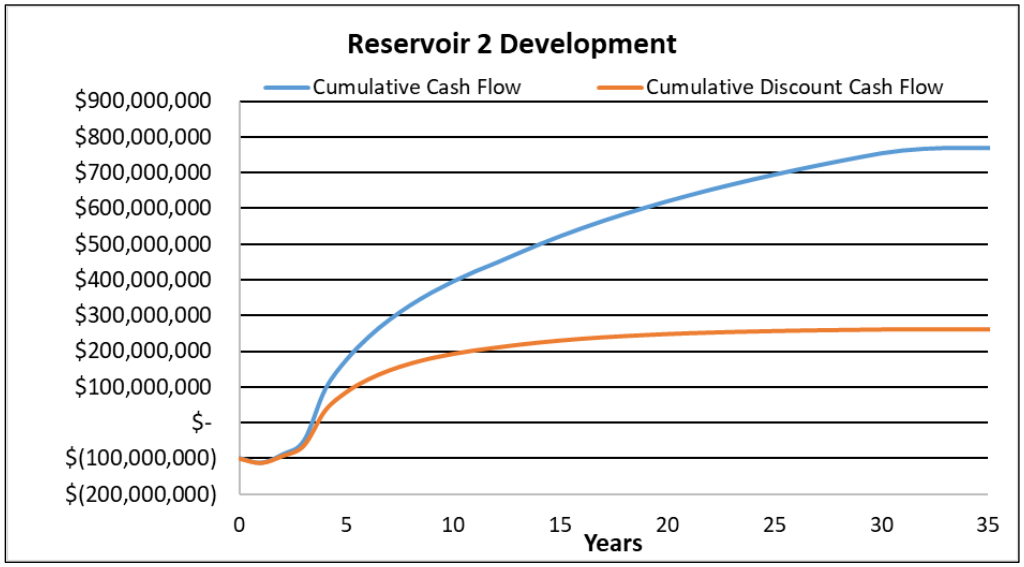

Figure 7.17. Cumulative undiscounted and discounted cash flows for the development of Reservoir 2 wells

Reservoir 2 drill plan will develop approximately 17,000 acres which is within 3% of the proposed acreage position outlined by geology. There will be 40 wells drilled in total over a four-year period. 50% of the wells are Tier 1, 25% Tier 2, and 25% Tier 3. The model has a discount rate of 10% and assumes a $10 million CAPEX per well. The total cash flow over the 34-year economic run is ~$837 million. The discount cash flow (DCF) over the 34-year economic run is ~$260 million. This creates a discounted acreage value for the Reservoir 2 bench at $15,300 per acre. The development plan will be able to drill within a free cash flow (FCF) in approximately 3.4 years. The maximum outlay is estimated to be ~$110 million, but $100 million will be spent after drilling in the first year, meaning the maximum exposure point occurs during the drilling of the first year. To evaluate Reservoir 3, the input value for Reservoir 3 is listed in Table 7.19, and the output values for the development are listed in Table 7.20. Figure 7.18 displays the development cumulative undiscounted and discounted cash flows for Reservoir 3 wells.

Table 7.19. Input data for Reservoir 3 development

Input Values		Year	Drill Type
Wells Per Year	10	1	Tier 1
Wells Per Section	3.5	2	Tier 1
Sections per Well	2	3	Tier 1
Drilling Years	7	4	Tier 2
Wells Drilled	70	5	Tier 2
Acreage Drilled	25,600	6	Tier 3
SQ Miles Drilled	40	7	Tier 3
CAPEX	$10,000,000	8	NA
Discount Rate	10%	9	NA
		10	NA

Table 7.20. Output data for Reservoir 3 development

Output Data		
Total Cash Flow	$1,475,340,027	
CF per Well	$21,076,286	
Total DCF	$462,492,155	
Total DCF (AC)	$18,066	per acre
Years to Drill in FCF	3.3	
Years to Drill in DFCF	3.9	
MAX Outlay	$(108,218,222)	

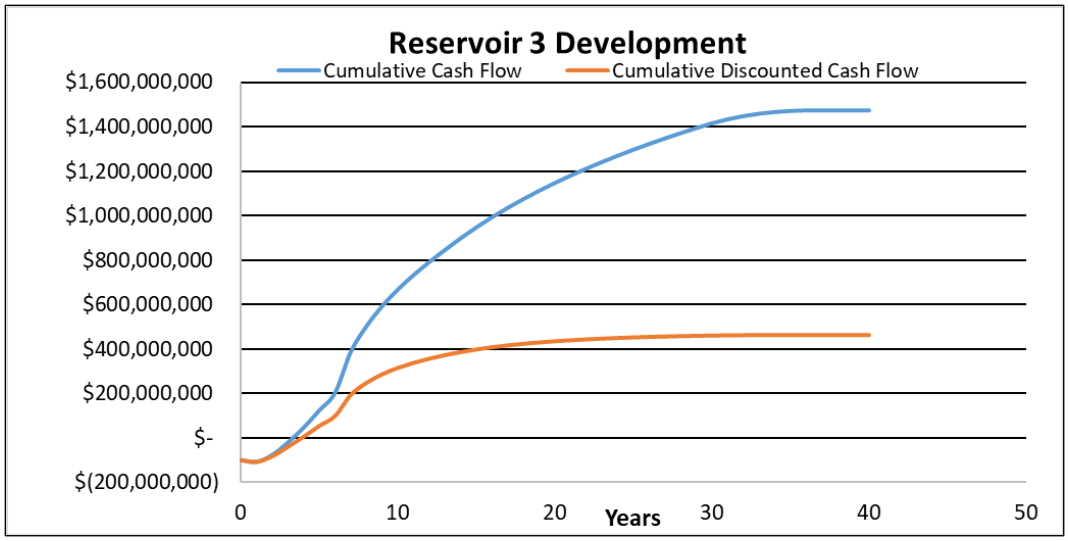

Figure 7.18. Cumulative undiscounted and discounted cash flows for the development of Reservoir 3 wells

The Reservoir 3 drill plan will develop approximately 25,600 acres which is within 5% of the proposed acreage position outlined by geology. There will be 70 wells drilled in total over a seven-year period. 43% of the wells are Tier 1, 28% Tier 2, and 28% Tier 3. The model has a discount rate of 10% and assumes a $10 million CAPEX per well. The total cash flow over the 37-year economic run is ~$1.475 billion. The discount cash flow over the 37-year economic run is ~$460 million. This creates a discounted acreage value for the Reservoir 3 bench at $18,060 per acre. The development plan will be able to drill within a free cash flow is approximately 3.3 years. The maximum outlay is estimated to be ~$108 million, but $100 million will be spent after drilling in the first year, meaning the maximum exposure point occurs during the drilling of the first year. To value the Caney asset completely, the assumption will be made that an operator has all ~26,000 acres leased and or held by production and will develop the entire asset. It is important to note the acreage values are calculated to reflect the Caney formation only and do not include pay above or below this formation. The output data values will be combined to conduct the analysis, and various economic metrics can then be calculated. The only variable that will be partially combined is the value per acreage because Reservoir 2 and Reservoir 3 have different reservoir expanses. Various economic metrics can be

considered for NAV by combining the output values. Table 7.21 displays the combined output values. Figure 7.19 displays the development cumulative undiscounted and discounted cash flows for the combined economics of Reservoir 2 and Reservoir 3 wells.

Table 7.21. Combined development output values for Reservoirs 2 and 3

Output Data	Reservoir 2	Reservoir 3	Combined	
Total Cash Flow	$768,980,872	$1,475,340,027	$2,244,320,900	
CF per Well	$19,224,522	$21,076,286	$40,300,808	
Total DCF	$261,942,719	$462,492,155	$724,434,874	
Total DCF (AC)	$15,348	$18,066	$33,414	per acre
Years to Drill in FCF	3.4	3.3	3.33	AVERAGE
Years to Drill in DFCF	3.6	3.9	3.77	AVERAGE
MAX Outlay	$(112,947,290)	$(108,218,222)	$(221,165,512)	

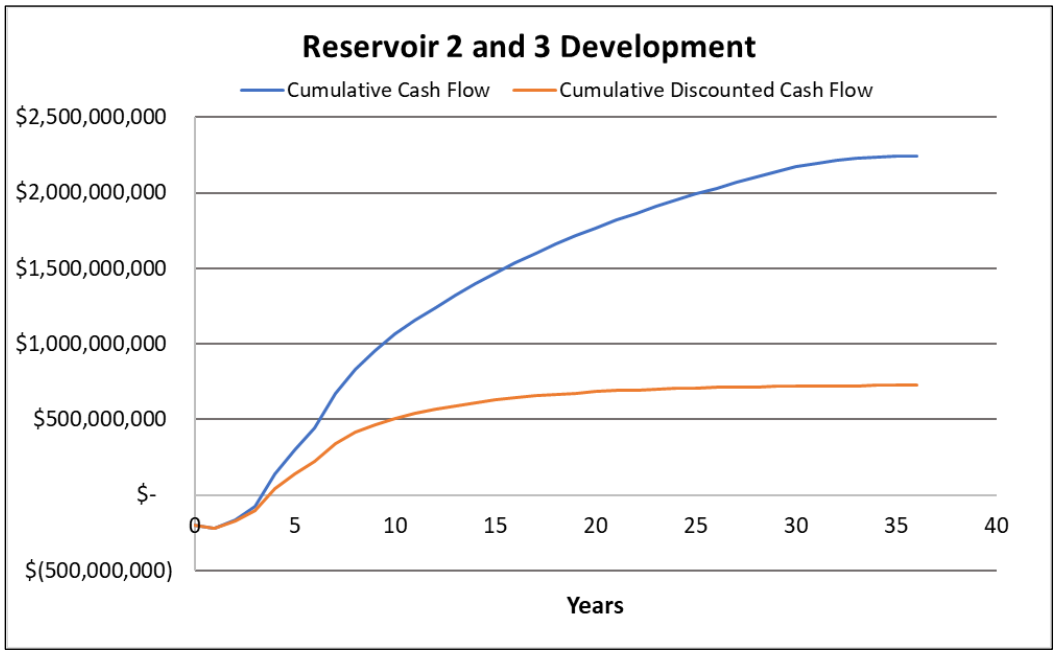

Figure 7.19. Cumulative undiscounted and discounted cash flows for the development of Reservoir 2 and 3 wells

There are various metrics that can be determined from this, which are as follows. The Net Asset Value of this asset, at a PV10, is $724 million. Committing to a full drilling plan, the field will start to drill within cash flow at three years. The discounted acreage value, or acreage value at a PV10, is ~$33,000 per acre in areas where Reservoirs 2 and 3 are present. To expand, in the areas where only

Reservoir 3 is present, the acreage value is still only ~$18,000 per acre. To calculate the average acreage value of the play, the ~17,000 acres of an area where Reservoir 2 and Reservoir 3 are present is averaged against the ~8500 acres where only Reservoir 3 is present. Equation 7.1 below displays how the average acreage value of ~$29,800 per acre was calculated.

(($36,414*17,067 acres) + ($18,066* 8533 acres))/ 25,600 acres= $28,298 per acre (7.1)

The total return on investment was calculated by taking the maximum outlay value, which would reflect the highest amount of capital invested at a single point and the total cash flow of the asset generating a non-discounted return on investment. The non-discounted Return on Investment (ROI) comes to a value of $2.244 billion divided by $220 million or 10.2 NON-discounted ROI. The discount ROI will divide the total discounted CF by the maximum outlay for a value of ($724 million/ $220 million) ~3.3 discounted ROI.

Additionally, an investigation was conducted in assessing the value of the Caney assuming the CAPEX of the wells could be reduced to $9MM instead of the proposed $10MM CAPEX through drilling and completion efficiencies. Within the study, all other variables were held constant and the only value that was adjusted was CAPEX. The output data values were combined in the same method as the $10MM CAPEX to conduct the analysis. Table 7.22 displays the combined output values. Figure 7.20 displays the development cumulative undiscounted and discounted cash flows for the combined economics of Reservoir 2 and Reservoir 3 wells using a $9MM CAPEX for each well.

Table 7.22. Combined development output values for Reservoirs 2 and 3 with a $9MM CAPEX

Output Data	Reservoir 2	Reservoir 3	Combined	
Total Cash Flow	$808,980,872	$1,545,340,027	$2,354,320,900	
CF per Well	$20,224,522	$22,076,286	$42,300,808	
Total DCF	$296,811,239	$516,044,762	$812,856,001	
Total DCF (AC)	$17,391	$20,158	$37,549	per acre
Years to Drill in FCF	3.1	2.7	2.90	AVERAGE
Years to Drill in DFCF	3.3	3.1	3.19	AVERAGE
MAX Outlay	$(92,947,290)	$(90,000,000)	$(182,947,290)	

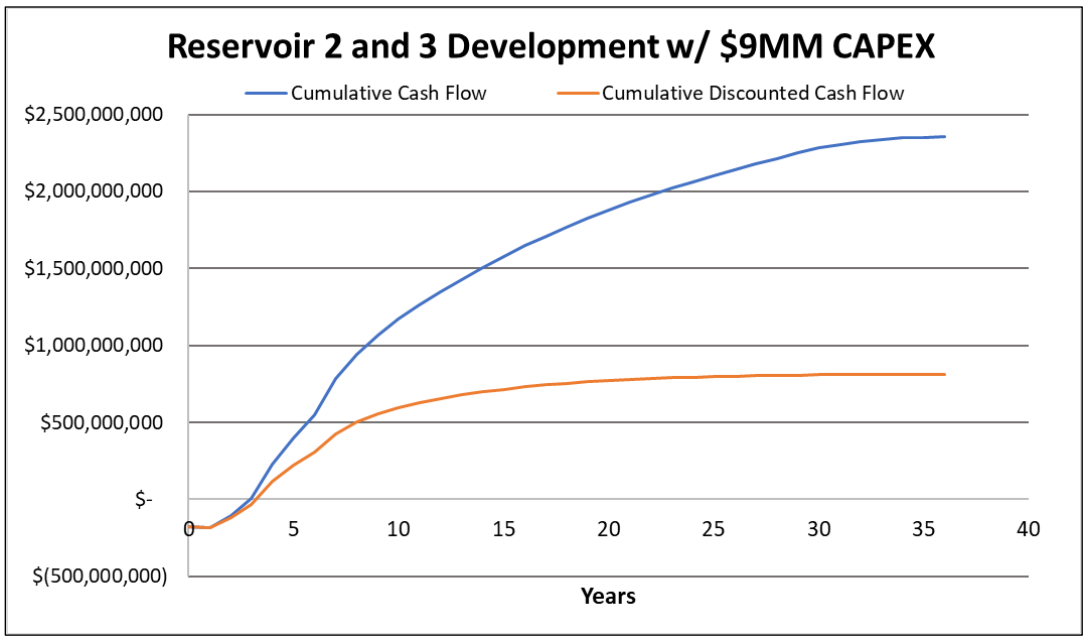

Figure 7.20. Cumulative undiscounted and discounted cash flows for the development of Reservoir 2 and 3 wells using a $9MM CAPEX.

As demonstrated by the table above, reducing CAPEX by 10% or $1MM per well will result in an increase of ~$110MM in total cash flow over the life of the project. The discounted cash flow add is ~$88MM which increases the combined discounted acreage value by ~$4000/ per acre. Additionally, the maximum outlay will be reduced by ~$38MM. These values demonstrate the value add created by engineering enhancements to improve well operation efficiencies and reducing well cost. Lastly, an investigation was conducted in assessing the value of the Caney assuming the CAPEX of the wells could be reduced to $9MM instead of the proposed $10MM CAPEX through drilling and completion efficiencies and all production was Tier 1 indicating the potential maximum value of selective stimulation as discussed in Chapter 5. Using Tier 1 production would make the average curve ~10% better because since all the tiers were given roughly equal value in the original analysis, the average curve would be a Tier 2 curve which is a 10% reduction of a Tier 1 curve. Within the study, all other variables were held constant. The output data values were combined in the same method as the $10MM CAPEX to conduct the analysis. Table 7.23 displays the combined output values. Figure 7.21 displays the development cumulative undiscounted and discounted cash flows for the combined economics of Reservoir 2 and Reservoir 3 wells using a $9MM CAPEX and Tier 1 production for each well. As demonstrated by the table above, reducing CAPEX by 10% or $1MM per well and having Tier 1 production or ~10% production increase will result in an additional ~$427MM of total cash flow over the life of the project. The discounted cash flow adds ~$214MM which increases the combined discounted acreage value by ~$10,000/ per acre. Additionally, the maximum outlay will be reduced by ~$38MM. These values demonstrate the value add created by engineering enhancements to improve well operation efficiencies and reducing well cost.

Table 7.23. Combined development output values for Reservoirs 2 and 3 with a $9MM CAPEX and Tier 1 production

Output Data	Reservoir 2	Reservoir 3	Combined	
Total Cash Flow	$908,581,339	$1,763,253,801	$2,671,835,141	
CF per Well	$22,714,533	$25,189,340	$47,903,874	
Total DCF	$342,503,274	$596,279,660	$938,782,934	
Total DCF (AC)	$20,069	$23,292	$43,361	per acre
Years to Drill in FCF	3.0	2.7	2.9	AVERAGE
Years to Drill in DFCF	3.2	3.1	3.1	AVERAGE
MAX Outlay	($92,947,290)	($90,000,000)	($182,947,290)	

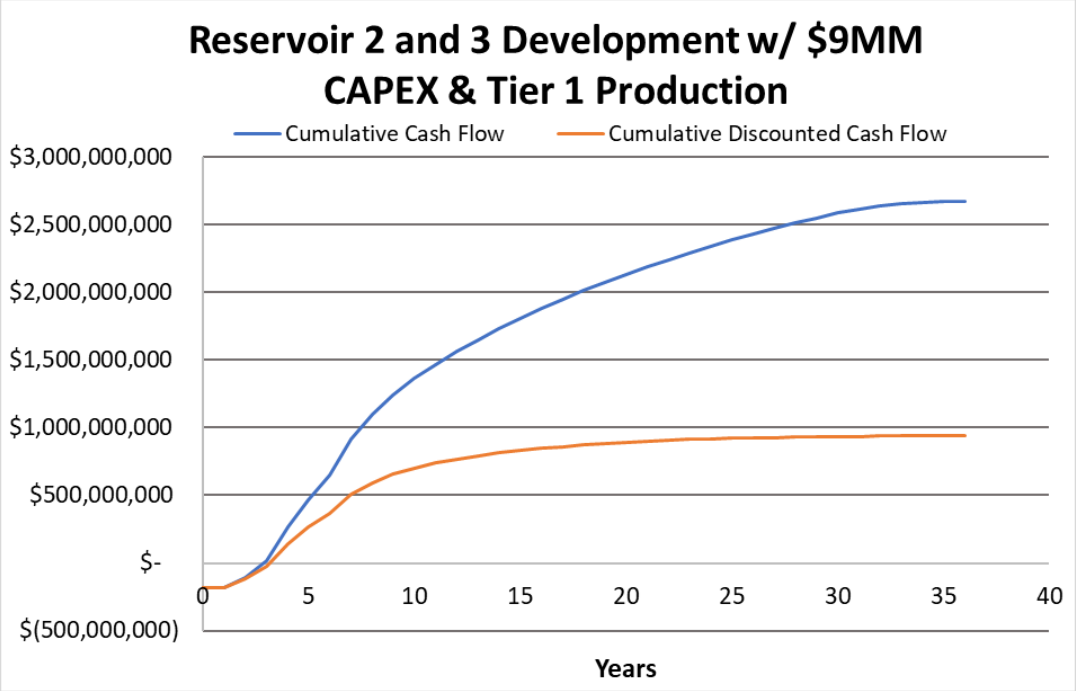

Figure 7.21. Cumulative undiscounted and discounted cash flows for the development of Reservoirs 2 and 3 wells using a $9MM CAPEX and Tier 1 production.

As demonstrated by the table above, reducing CAPEX by 10% or $1MM per well and having Tier 1 production or ~10% production increase will result in an additional ~$427MM of total cash flow over the life of the project. The discounted cash flow adds ~$214MM which increases the combined discounted acreage value by ~$10,000/ per acre. Additionally, the maximum outlay will be reduced by ~$38MM. These values demonstrate the value add created by engineering enhancements to improve well operation efficiencies and reducing well cost.

An important detail to note on both the maximum outlay and ROI calculations is how the outlay is generated. PFAP runs annual cash flows, meaning the CAPEX will be deployed and all the oil and gas revenue for the first 12 months of production is summed up and set as year 1 cash flow whereas CAPEX is year 0. This is not how cash is distributed in oil and gas, but rather on a month-by-month basis. Generally, an operator will sell a load of oil and receive payment for the oil the following month. This means as wells are being drilled each month, there will be incoming cash from the production of wells drilled and completed earlier in the year. This in summary means that the maximum outlay number calculated is significantly higher than what would happen in a real-world month-by-month cash flow basis and reduces the maximum outlay. As the maximum outlay is reduced the ROI values will be significantly enhanced.

From these economic performance metrics, the Caney Shale is proven to be a highly economic project. After a thorough risk analysis of both Reservoir 2 and Reservoir 3, the results have proven this play is economically viable under various commodity pricing and well production scenarios. As more wells are drilled, the drilling and completion knowledge will increase and due to the enhanced understanding of the formation and reduced infrastructure requirements for future drills, the economics for single wells will likely improve and raise the net asset value of the Caney Shale during development.

7.2. Results and Discussion

This study evaluated the economic viability of the Caney Shale in Stephens and Carter County, Oklahoma and determined that the reservoir is both productive and economic under stressed commodity pricing. This project was conducted in conjunction with the Department of Energy (DOE) and the reserves projected were estimated for DOE and represent the entire Caney reservoir. The study concluded the economic reserves within the Caney Shale and believes this process can be applied in other United States resource plays that were once deemed uneconomic with older horizontal and hydraulic fracturing technology.

The study has concluded that nearly 50 MMBO and 265 BCF are present in the reservoir predicted on the models used within the study. The study determined the single well economics for Reservoir 2 and Reservoir 3, giving the NPV, IRR, and payback periods for various tiers of production for both reservoirs.

The results of the study determined that increased stage count and tighter perforation cluster spacing, compared to historic designs, would result in a production increase via optimized stimulated reservoir rock volume, justifying the increase in capital expenditure. Due to the lack of permeability in shale rock, the tighter cluster spacing creates enhanced access for the reservoir fluid to enter the wellbore. Additionally, the study determined that larger proppant sizes did not significantly improve production because the fracture is substantially more permeable than the reservoir rock.

Last, the study found that Reservoir 2 wells generate a NPV of $8.8MM and an IRR value of 41%. Reservoir 3 wells generate a NPV of $10.1MM and an IRR value of 46%. These values are for Tier 1 wells with commodity pricing of $65 WTI, $3 Natural Gas, and $0.75 NGL. These commodity

price values are moderately conservative indicating that the Caney Shale can be developed in a stranded commodity price environment. The base case conservate values generate $33,000 per acre value when both Reservoir 2 and Reservoir 3 are present and $18,000 per acre when only Reservoir 3 is present. With Reservoir 2 projected to have 26 square miles of development and Reservoir 3 projected at 42 square miles of development, over $700MM in total discounted cash flow is estimated for the Caney Shale in the project area.

8. Summary of Project Publication

JOURNAL PAPERS

1. Xiong, F., Wang, Y., Puckette, J., Grammer, M., Awejori, G. and Radonjic*, M., (2024). Geochemical and Microstructural Characterization of Shale Rock: A Workflow for Site Evaluation for Energy–Fluids Storage. Energy & Fuels. https://doi.org/10.1021/acs.energyfuels.4c03197 https://pubs.acs.org/doi/full/10.1021/acs.energyfuels.4c03197
2. Awejori, G. A., Dong, W., Doughty, C., Spycher, N., & Radonjic*, M. (2024). Mineralogy and Reactive Fluid Chemistry Evolution of Hydraulically Fractured Caney Shale of Southern Oklahoma. Gas Science and Engineering, 205458. https://doi.org/10.1016/j.jgsce.2024.205458 https://www.sciencedirect.com/science/article/pii/S2949908924002541
3. Cox, I.A., and Pashin, J.C., 2024, Burial and thermal history modeling of basins in convergent oblique-slip mobile zones: A case study of the Ardmore Basin, southern Oklahoma: International Journal of Coal Geology, p. 104486. https://doi.org/10.1016/j.coal.2024.104486.
4. Awejori, G. A., Dong, W., Doughty, C., Spycher, N., Radonjic*, M. (2024). Mineral and fluid transformation of hydraulically fractured shale: case study of Caney Shale in Southern Oklahoma. Geomechanics and Geophysics for Geo-Energy and Geo-Resources, 10(1), 128. https://doi.org/10.1007/s40948-024-00835-0 https://link.springer.com/article/10.1007/s40948-024-00835-0
5. Katende, A., Rutqvist, J., Massion, C., Radonjic*, M. (2023). Experimental flow-through a single fracture with monolayer proppant at reservoir conditions: A case study on Caney Shale, Southwest Oklahoma, USA, Energy, (273,127181). https://doi.org/10.1016/j.energy.2023.127181 https://www.sciencedirect.com/science/article/pii/S0360544223005753?via%3Dihub
6. Benge, M., Katende, A., Rutqvist, J., Radonjic, M., & Bunger*, A. (2023). Creep Properties of Shale and Predicted Impact on Proppant Embedment for the Caney Shale, Oklahoma. Rock Mechanics and Rock Engineering, 56 (8), 5903-5921. https://doi.org/10.1007/s00603-023-03362-8 https://link.springer.com/article/10.1007/s00603-023-03362-8
7. Katende, A., Allen, C., Rutqvist, J., Nakagawa, S., and Radonjic*, M. (2023). Experimental and numerical investigation of proppant embedment and conductivity reduction within a fracture in the Caney shale, Southern Oklahoma, USA. Fuel, (341, 127571). https://doi.org/10.1016/j.fuel.2023.127571 https://www.sciencedirect.com/science/article/abs/pii/S0016236123001849?via%3Dihu
8. Xiong, F., Rother, G., Radonjic*, M., (2022), Insights into controls of mineralogy and pore structure on the density of adsorption phase in shales under supercritical conditions, Energy Fuels 36, 17, 10110–10122. https://doi.org/10.1021/acs.energyfuels.2c01847 https://pubs.acs.org/doi/10.1021/acs.energyfuels.2c01847
9. Awejori, G.A., Doughty, C., Xiong, F., Paronish, T., Spycher, N., Radonjic*, M. (2022) Integrated experimental and modeling study of geochemical reactions of simple fracturing fluids with Caney Shale. Energy Fuels 36, 17, 10064–10081. https://doi.org/10.1021/acs.energyfuels.2c01739 https://pubs.acs.org/doi/10.1021/acs.energyfuels.2c01847

10. Rupom Bhattacherjee, Prem Bikkina (2022), Preparation of Illite Coated Geomaterial Microfluidic Surfaces: Effect of Salinity and Heat Treatment, Journal of Petroleum Science and Engineering, 216, 110805. https://doi.org/10.1016/j.petrol.2022.110805 https://www.sciencedirect.com/science/article/pii/S0920410522006660
11. Katende, A., O'Connell, L., Rich, A., Rutqvist, J., Radonjic*, M. (2021), A comprehensive review of proppant embedment in shale reservoirs: Experimentation, Modeling, and prospects. Journal of Natural Gas Science and Engineering 95, 104143. https://doi.org/10.1016/j.jngse.2021.104143 https://www.sciencedirect.com/science/article/pii/S1875510021003449?via%3Dihub
12. Katende, A., Rutqvist, J., Benge, M., Seyedolali, A., Bunger, A., Puckette, J.O., and Radonjic*, M. (2021), Convergence of micro-geochemistry and micro-geomechanics towards understanding proppant shale rock interaction: a Caney shale case study in southern Oklahoma, USA. Journal of Natural Gas Science and Engineering 96, 104296, December 2021. https://doi.org/10.1016/j.jngse.2021.104296 https://www.sciencedirect.com/science/article/pii/S1875510021004935?via%3Dihub
13. Wang, Y., Luo, G., Achang, M., Cains, J., Wethington, C., Katende, A., Grammer, G.M., Puckette, J., Pashin, J., Castagna, M., Chan, H., King, G.E., and Radonjic*, M. (2021). Multiscale Characterization of the Caney Shale - An Emerging Play in Oklahoma, Midcontinent Geoscience 2, 33-53. https://doi.org/10.17161/mg.v2i.15911 https://journals.ku.edu/mg/article/view/15911

PROFESSIONAL JOURNALS AND REPORTS

1. Paronish*, T. J. Schmitt R, Moore J. E., Crandall*, D., Rihn, A., Renk, J., Doughty, C., Bunger, A., Wang, Y., Katende, A. Seyedolali, A., Puckette, J., & Radonjic, M. (2021). Computed tomography scanning and geophysical measurements of the Caney Shale Formation from the T# 1-35-34-27 Well. DOE. NETL-2021. 2654. August 2021. https://doi.org/10.2172/1812176 https://www.osti.gov/biblio/1812176

SHORTER WORKS: BOOK CHAPTERS

1. Awejori, G.A. & Radonjic*, M. (2021). Hydraulic Fracturing: Review of Geochemical and Geo-mechanical Impact of Formation Clay-Fluid Interactions: Focus on Hydraulic Fracturing. IntechOpen. July 2021. Book Chapter. https://doi.org/10.5772/intechopen.98881 https://www.intechopen.com/chapters/77571

PEER REVIEWED CONFERENCE PAPERS and EXTENDED ABSTRACTS:

1. Awejori, G.A., Dong, W., Doughty, C., Radonjic*, M. (2024). Geochemically driven Petrophysical Transformations in Caney Shale and its Impact on Reservoir Productivity. Unconventional Resources Technology Conference 2024. Houston, TX. https://doi.org/10.15530/urtec-2024-4042958 https://onepetro.org/URTECONF/proceedings/24URTC/2-24URTC/D021S038R001/546990

2. Elkholy, S., Radonjic, M., and Lee*, H.P., Integrating experiments and well logs to predict Caney shale static mechanical properties during production with supervised machine learning. Unconventional Resources Technology Conference, 2024. https://doi.org/10.15530/urtec-2024-4038060 https://onepetro.org/URTECONF/proceedings/24URTC/3-24URTC/D031S067R002/546937
3. Xiong, F., Awejori, G.A., Radonjic*, M. (2024). Effects of interactions between produced formation fluid and rock matrix on pore structure of Caney Shale, southern Oklahoma. 58th American Rock Mechanics Association (ARMA) Conference 2024. Golden, CO. https://doi.org/10.56952/ARMA-2024-0837 https://onepetro.org/ARMAUSRMS/proceedings/ARMA24/ARMA24/D041S053R002/549088
4. Dje, L.B., Awejori G.A., and Radonjic*, M. (2024). Comparison of Geochemical Reactivity of Marcellus and Caney shale based on effluent analysis. 58th American Rock Mechanics Association (ARMA) Conference 2024. Golden, CO. https://doi.org/10.56952/ARMA-2024-1079 https://onepetro.org/ARMAUSRMS/proceedings/ARMA24/ARMA24/D041S053R004/549102
5. Awejori, G.A., Xiong, F., Massion, C., Radonjic*, M. (2023). Produced Fluid Induced Mineralogy and Elemental Alterations of Caney Shale, Southern Oklahoma. 57th American Rock Mechanics Association Symposium. Atlanta, GA. https://doi.org/10.56952/ARMA-2023-0881 https://onepetro.org/ARMAUSRMS/proceedings/ARMA23/All-ARMA23/ARMA-2023-0881/532138
6. Hayes, J., Dionne Mayibeki, M. Al Dushaishi, and G. Hareland. Analysis of Rotary Steerable Systems versus Conventional Mud Motors for Vertical and Horizontal Wells in the Caney Formation, Southwest Oklahoma. ARMA 23-763, 57th U.S. Rock Mechanics/Geomechanics Symposium, Atlanta, GA, 25-28 June 2023. https://doi.org/10.56952/ARMA-2023-0763 https://onepetro.org/ARMAUSRMS/proceedings/ARMA23/All-ARMA23/ARMA-2023-0763/532560?searchresult=1
7. Katende, A., Awejori, G., Benge, M., Nakagawa, S., Wang, Y., Xiong, F., Puckette, J., Grammer, Rutqvist, J., Doughty, C., M., Bunger, A., Paronish, T., Crandall, D., Renk, J., and Radonjic*, M. (2023). Multidimensional, experimental, and modeling evaluation of permeability evolution, the Caney Shale Field Lab, OK, USA. Unconventional Resources Technology Conference, Denver, CO. https://doi.org/10.15530/urtec-2023-3869822 https://onepetro.org/URTECONF/proceedings/23URTC/2-23URTC/D021S040R002/520718
8. Radonjic*, M., Massion. C., Xiong, F., Awejori, G.A., Katende, A., Whitworth, L., Puckette, J., Wang, Y., Grammer, G.M., Rutqvist, J. Nakagawa, S., Binge, M., Lu. L, Bunger, A., Paronish, T., Crandall, D., Renk. J. (2022) Applying lessons from shale hydraulic fracturing to shale caprock integrity: experimental and modeling comparison of ductile and brittle samples from Caney Shale, Oklahoma. CouFrac 2022 conference, Berkeley, CA. November 14-16, 2022.
9. Awejori, G.A., Whitworth, L., Paronish, T., Xiong, F., Katende, A., Radonjic*, M. (2022). Fluid Induced Elemental and Mineralogy Alterations of Caney Shale. American Rock Mechanics Association Conference (ARMA), Santa Fe, NM. https://doi.org/10.56952/ARMA-2022-0763 https://onepetro.org/ARMAUSRMS/proceedings/ARMA22/All-ARMA22/ARMA-2022-0763/510538
10. Katende, A., Allen, C., Massion, C., Awejori, G.A., Xiong, F., Rutqvist, J., Nakagawa, S., Radonjic*, M. (2022). Experiments and modeling of proppant embedment and fracture

conductivity for the Caney Shale, Oklahoma, USA. American Rock Mechanics Association Conference (ARMA), Santa Fe, NM.
https://doi.org/10.56952/ARMA-2022-0805
https://onepetro.org/ARMAUSRMS/proceedings/ARMA22/All-ARMA22/ARMA-2022-0805/510470

11. Awejori, G.A., Barnett, L., Al Dushaishi, M.F., Massion, C., Radonjic*, M. (2022). Chemical and Mechanical Stability of Cement during Fluid Invasion in Hydraulic Fractured Geothermal Wells. Geothermal Rising Conference (GRC), Reno, NV. (46, 1399-1415)
12. Awejori, G.A., Jupudi, H., Massion, C., Radonjic*, M. (2022). Study on Advanced Cementing Practices using Inert Graphene Nanoplatelets and Hydraulic Fracturing Fluids for Wellbore Integrity and Sustainability. The Minerals, Metals & Materials Society, TMS 2023 152nd Annual Meeting & Exhibition Supplemental Proceedings, The Minerals, Metals & Materials Series, https://doi.org/10.1007/978-3-031-22524-6_117
https://link.springer.com/chapter/10.1007/978-3-031-22524-6_117
13. Awejori, G.A., Luo, G., Grider, C., Katende, A., Radonjic*, M. Doughty, C., Spycher, N. Paronish, T. O'Connell, L. Rihn, A. (2021). Fracturing Fluid-Induced Mineralogy Changes and Impact on Elastic Properties for the Caney Shale, Oklahoma. 55th U.S. Rock Mechanics/Geomechanics Symposium, Virtual, June 2021.
https://onepetro.org/ARMAUSRMS/proceedings/ARMA21/All-ARMA21/ARMA-2021-2004/468308
14. Benge, M., Lu, Y., Katende, A., Rutqvist, J., Crandall, D., Haecker, A., ... & Bunger*, A. (2021, July). Connecting geomechanical properties with potential for proppant embedment and production decline for the emerging caney shale, oklahoma. In SPE/AAPG/SEG Unconventional Resources Technology Conference (p. D011S002R001). URTEC.
https://doi.org/10.15530/urtec-2021-5084
https://onepetro.org/URTECONF/proceedings/21URTC/1-21URTC/D011S002R001/465258
15. Kolmer, H., Dionne Mayibeki, and G. Hareland. Using Drilling Data of Offset Wells and Core Data to Optimize Perforation Selection for the Caney Shale. ARMA 21-1934, 55th U.S. Rock Mechanics/Geomechanics Symposium, Houston, TX, USA, 20-23 June 2021.
16. Benge, M., Lu, Y., Jones, J., Bunger, A., Haecker, A., Rihn, A., Crandall, D., Luo, G., and Radonjic, M. 2021. Mechanical Properties of Nominally Ductile and Brittle Zones Within the Caney Shale Formation. American Rock Mechanics Association. 55th US Rock Mechanics/Geomechanics Symposium, Houston, Texas, June 20-23.
17. Radonjic*, M., Luo, G., Wang, Y., Achang, M., Cains, J., Katende, A., ... & King, G. E. (2020, December). Integrated microstructural characterisation of caney shale, OK. In Unconventional Resources Technology Conference, 20–22 July 2020 (pp. 2157-2174). Unconventional Resources Technology Conference (URTEC).
https://doi.org/10.15530/urtec-2020-2947
https://onepetro.org/URTECONF/proceedings/20URTC/2-20URTC/D023S039R003/450534

PRESENTATIONS & POSTERS: Conferences, Workshops, Forums, And Symposia

1. Awejori, G.A., Dong, W., Doughty, C., Radonjic, M., Geochemically driven Petrophysical Transformations in Caney Shale and its Impact on Reservoir Productivity. Presented in person at the Unconventional Resources Technology Conference 2024. Houston, TX. June 17-19, 2024.
2. Xiong, F., Awejori, G.A., Radonjic, M., Effects of interactions between produced formation fluid and rock matrix on pore structure of Caney Shale, southern Oklahoma. Presented in person at the American Rock Mechanics Association (ARMA) Conference 2024. Golden, CO. June 23-26.
3. Dje, L.B., Awejori G.A., and Radonjic M. Comparison of Geochemical Reactivity of Marcellus and Caney shale based on effluent analysis. Presented at the American Rock Mechanics Association (ARMA) Conference 2024. Golden, CO. June 23-26.
4. Dje, L.B., Carpenter, K.C., Awejori, G.A., Achang M., Radonjic, M. Environmental Impact of Hydraulic Fracturing: A Comparative Analysis of the Marcellus and Caney Shales. School of Chemical Engineering, Oklahoma State University. May 02, 2024.
5. Dje, L.B., Awejori, G.A., and Radonjic, M. Geochemical Interactions of Synthetic Hydraulic Fracturing Fluids with Marcellus and Caney Shales: A Comparative Batch-Scale Laboratory Investigation. International Meeting for Applied Geoscience & Energy (IMAGE) in Houston, Texas, August 26-29, 2024 (Abstract accepted for oral presentation).
6. Dje, L.B., Carpenter, K.C., Awejori, G.A., Achang M., Radonjic, M. Hydraulic Fracturing Fluids and Shale Interactions as Sources of Critical Elements: A Comparative Batch-Scale Laboratory Investigation of Caney and Marcellus Shale Flowback Waters. American Institute of Chemical Engineers (AICHE) Annual Meeting and Topical Conference. San Diego, October 27-31, 2024 (Abstract submitted).
7. Katende, A., Awejori, G., Benge, M., Nakagawa, S., Wang, Y., Xiong, F., Puckette, J., Grammer, Rutqvist, J., Doughty, C., M., Bunger, A., Paronish, T., Crandall, D., Renk, J., and Radonjic, M. Multidimensional, experimental, and modeling evaluation of permeability evolution, the Caney Shale Field Lab, OK, USA. Presented at the Unconventional Resources Technology Conference, Denver, CO, June 13-15, 2023.
8. Awejori, G.A., Dong, W., Doughty, C., Spycher, N., Xiong, F., Dje, L. B., & Radonjic, M. Subsurface Geochemical Rock-Fluid Reactions in Caney Shale of southern Oklahoma. Accepted for the American Geographical Union (AGU) 2023 Annual Meeting, San Francisco, CA, December 11-15, 2023, presentation, MR41A-05: Geochemical, Geomechanical and Hydraulic Properties of Unconventional Reservoir Rocks at Laboratory, Modeling and Field Temporal and Spatial Scales.
9. Xiong, F., Rother, G., Awejori, G.A., & Radonjic, M. Controls of matrix on natural gas storage in Caney Shale, an emerging unconventional play, southern Oklahoma. Accepted for the American Geographical Union (AGU) 2023 Annual Meeting, San Francisco, CA, December 11-15, 2023, presentation, MR41A-05: Geochemical, Geomechanical and Hydraulic Properties of Unconventional Reservoir Rocks at Laboratory, Modeling and Field Temporal and Spatial Scales.
10. Xiong, F., Rother, G., Awejori, G.A., Dje, L. B., & Radonjic, M. Insights into rock-gas interactions under reservoir conditions: A case study from the late Mississippian Caney Shale, southern Oklahoma, USA. Accepted to American Chemical Society (ACS) Southwest Reginal Meeting 2023, Oklahoma City, OK, November 15-18, 2023 (accepted for oral presentation).
11. Awejori, G.A., Dong, W., Doughty, C., Spycher, N., Xiong, F., & Radonjic, M. Subsurface geochemical rock-fluid interactions in Caney Shale, South-Central Oklahoma Oil Province. Presented at International Meeting for Applied Geoscience & Energy (IMAGE) 2023, Houston, TX, August 28-September 1, 2023 (oral presentation).

12. Awejori, G.A., Dong, W., Doughty, C., Spycher, N., Xiong, F., Dje, L. B., & Radonjic, M. Impacts of geochemical rock-fluid interactions on production and carbon storage in Caney Shale of southern Oklahoma. Accepted to ACS Southwest Reginal Meeting 2023, Oklahoma City, OK, November 15-18, 2023 (Accepted for oral presentation).
13. Dje, L.B., Awejori G.A., Carpenter K.C., Xiong F., Achang M. and Radonjic M. (2023). Comprehensive Geochemical Analysis of Rock-fluid Interactions in Marcellus Shale. An oral presentation at the American Chemical Society Southwest Regional Meeting, Oklahoma City, November 17, 2023
14. Awejori, G.A., Dong, W., Doughty, C., Xiong, F., Radonjic, M., Subsurface Geochemical Rock-Fluid Reaction in Caney Shale of Southern Oklahoma. American Geophysical Union (AGU) Conference 2023. San Francisco, CA. December 13 – 15, 2023.
15. Awejori, G.A., Xiong, F., Massion, C., Radonjic, M., Geochemical, Geo-mechanical, and Petrophysical Studies of Impacts of Rock-Fluid Interactions in Caney Formation in South Central Oklahoma. Orally presented in person at the 57th American Rock Mechanics Association Symposium. Atlanta, GA. June 21-29, 2023.
16. Xiong, F., Rother, G., Radonjic, M., Potential of Natural Gas Storage in Caney Shale, the Ardmore Basin, southern Oklahoma. Orally presented in person at SPWLA Oklahoma City Carbon Capture Technical Exposition 2023, Oklahoma City, OK. April 21, 2023.
17. Xiong, F., Rother, G., Awejori, G., Radonjic, M., Characterization and potential gas adsorption of the late Mississippian Caney Shale, southern Oklahoma, USA. Poster, presented in person at SPWLA Oklahoma City Carbon Capture Technical Exposition 2023, Oklahoma City, OK. April 21, 2023.
18. Awejori, G., Dong, W., Xiong, F., Radonjic, M., Hydraulic fracturing induced geochemical evolution of Caney Shale. Poster, presented in person at SPWLA Oklahoma City Carbon Capture Technical Exposition 2023, Oklahoma City, OK. April 21, 2023.
19. Cox, I.A., and Pashin, J.C., 2023, Mississippian Black Shale in an Oblique Slip Mobile Zone: The Caney Shale in the Ardmore Basin, southern Oklahoma. Oral Presentation at GSA Connects in October 2023
20. Cox, I.A., and Pashin, J. C., Integrated analysis of the burial and thermal history of the Ardmore Basin, southern Oklahoma, presented at the 2023 AAPG Southwest Section Meeting in Wichita Falls, Texas. Poster presentation at APG Southwest Section in May 2023
21. Radonjic group, Field Evaluation of the Caney Shale as an Emerging Unconventional Play, Southern Oklahoma: Task 6A/12A: Rock-Proppant/Fluid Interactions. Orally presented in person at Caney Symposium 2023, Oklahoma City, OK. April 14, 2023.
22. Awejori, G., Dong, W., Xiong, F., Radonjic, M., Hydraulic fracturing induced geochemical evolution of Caney Shale. Poster, presented in person at Caney Symposium 2023, Oklahoma City, OK. April 14, 2023.
23. Xiong, F., Rother, G., Awejori, G., Radonjic, M., Characterization and potential gas adsorption of the late Mississippian Caney Shale, southern Oklahoma, USA. Poster, presented in person at Caney Symposium 2023, Oklahoma City, OK. April 14, 2023.
24. Xiong, F., Rother, G., Awejori, G.A., Katende, A., Whitworth, L., Johnson B., Radonjic, M. Potential Carbon Dioxide Storage in Caney Shale, Southern Oklahoma. Presented at AGU 2023, San Francisco, CA, December 11-15, 2023.
25. P Bikkina, EOR Technologies via Microfluidics, Federation of Indian Petroleum Industry Student Chapter, Pandit Deendayal Energy University, India, Dec 14, 2023.
26. Xiong, F., Wang, Y., Puckette, J., Rother, G., Grammer, M., Awejori, G., Katende, A., Whitworth, L., Johnson, B., Massion, C., & Radonjic, M. Application of integrated visual observations on characterization of Caney Shale at micro-nano scales, a poster presentation at

The International Meeting for Applied Geoscience & Energy 2023, Houston, TX, August 28-September 1, 2023.

27. Awejori, G.A., Wenming, D., Doughty, C., Spycher, N., Radonjic, M., Subsurface Geochemical Rock-Fluid Interactions in Caney Formation, South-Central Oklahoma Oil Province (SCOOP). Presented at IMAGE 2023, Houston, TX, August 28-September 1, 2023.
28. Wang, Y. and Xiong, F. session chaired Geological Society of America 2023 South-Central Section Meeting with faculty advisors, Radonjic, M., Grammer, M., and Puckette, J. Session T16, Shale Lab and Field Projects: Sciences and Techniques on Unconventional Resources, Stillwater, OK, March 13-14, 2023.
29. Xiong, F., Rother, G., Radonjic, M., Petrological controls on density of adsorption phase in shales under reservoir conditions: A case study from the late Mississippian Caney Shale, southern Oklahoma, USA. Presented in person (oral talk) at Geological Society of America 2023 South-central section meeting, Stillwater, OK, March 13-14, 2023.
30. Katende, A., Radonjic, M. The use of Raman spectroscopy in assessing thermal maturity of the Caney Shale in southeastern Oklahoma, USA. Presented to Geological Society of America 2023 South-central section meeting, Stillwater, OK, March 13-14, 2023.
31. Awejori, G.A., Whitworth, L., Spycher, N., Doughty, C., Xiong, F., Katende, A., Radonjic, M. Geochemical and petrophysical transformations during rock-fluid interactions in Caney formation, south-central Oklahoma. Presented in person at Geological Society of America 2023 South-central section meeting, Stillwater, OK, March 13-14, 2023.
32. A Joshi, P Bikkina, Influence of Brine Salinity, First Contact Liquid, and Aging on Wettability of Untreated and Illite-coated Glass Surfaces - A Microfluidics-based Study, 1st Annual College of Engineering, Architecture, and Technology (CEAT) Graduate Research Symposium, Oklahoma State University, Stillwater, Feb 25, 2023.
33. A Joshi, P Bikkina, Investigation of rock-fluid interactions using geomaterial microfluidics, Caney Symposium, Hamm Institute, Oklahoma City, April 18, 2023.
34. A Joshi, P Bikkina, Investigation of rock-fluid interactions using geomaterial microfluidics, Carbon capture technical exposition, Hamm Institute, Oklahoma City, April 21, 2023.
35. Awejori, G.A., Jupudi, H., Massion, C., Radonjic, M. (2023). Study on Advanced Cementing Practices using Inert Graphene Nanoplatelets and Hydraulic Fracturing Fluids for Wellbore Integrity and Sustainability. Presented in person at The Minerals, Metals & Materials Society, TMS 2023 152nd Annual Meeting & Exhibition Supplemental Proceedings**,** San Diego, CA. March 19-23, 2023.
36. P. K. Bikkina, Recent Developments in the Application of Microfluidics in Oil & Gas Industry, International Conference on Petroleum, Hydrogen and Decarbonisation, IIT Guwahati, India, Nov 3-5, 2023.
37. Awejori, G.A., Barnett, L., Al Dushaishi, M.F., Massion, C., Radonjic, M. (2022). Chemical and Mechanical Stability of Cement during Fluid Invasion in Hydraulic Fractured Geothermal Wells. Presented in person at Geothermal Rising Conference (GRC), Reno, NV. August 28-31, 2022.
38. Awejori, G.A., Xiong, F., Katende, A., Radonjic, M., Whitworth, L., Paronish, T, (2022). Fluid induced elemental and mineralogy alterations of Caney Shale. Presented in person at 56th American Rock Mechanics Association (ARMA) Symposium. Santa Fe, NM, June 26-29, 2022.
39. Katende, A., Allen, C., Massion, C., Awejori, G.A., Xiong, F., Radonjic, M, Rutqvist, J. Nakagawa, S. (2022). Experiments and Modeling of Proppant Embedment and Stress-dependent Conductivity of Sand-Propped Fractures in the Caney Shale, Oklahoma, 56th American Rock Mechanics Association (ARMA) Symposium. Santa Fe, NM, June 26-29, 2022.
40. Radonjic, M., and Puckette, J., (2022) Presented Caney Shale Field Lab Project Report at the DOE Resource Sustainability Annual Project Review Meeting, Pittsburgh, (October 25-27,

2022).

41. Puckette, J., Wang, Y., Xiong, F., and Radonjic, M., presented (oral talk) in person at Caney Shale Field Lab Workshop with Continental. Gary Stewart Core Facility, Stillwater, Oklahoma. October 14, 2022.
42. Awejori, G.A., Massion, C. and Jupudi, H., Radonjic, M. Oklahoma Oil and Gas Expo, Oklahoma City, OK. October 13, 2022.
43. Awejori, G.A., Spycher, N.F., Paronish, T.J., Radonjic, M. (2022). Geochemical Compositional Changes due to Fracturing Fluid Interaction with Caney Shale, South Central Oklahoma, USA. Presented virtually at Goldschmidt 2022, Honolulu HI, July 10-15, 2022.
44. Allen, C., Katende, A., Xiong, F., Massion, C., Krumm, R., Radonjic, M., Subsurface Engineering of Conductive Fractures in Caney Shale, Southern Oklahoma: A Step Towards Energy Transition, Presented virtually (oral talk) at Goldschmidt Conference, Honolulu HI, July 10-15, 2022.
45. Katende, A., Allen, C., Rutqvist, J., Nakagawa, S., Massion, C., Awejori, G.A., Xiong, F., and Radonjic, M., Experiments and Modeling of Proppant Embedment and Fracture Conductivity for the Caney Shale, Oklahoma, USA. Presented virtually at the July 2022 proppant consortium meeting hosted by Core Labs Inc at Colorado School of Mines.
46. Allen, C., Krumm, R., Katende, A., Massion, C., Xiong, F., Radonjic, M., Subsurface Engineering of Conductive Fractures in Caney Shale, Southern Oklahoma: A Step Towards Energy Transition, poster presented in person at Undergraduate Research Symposium, Stillwater OK, April 19, 2022.
47. Roubik, A., Dean, B., Radonjic, M., Impact of Fluid & Proppant Volumes on Oil & Natural Gas Returns in the Caney Shale of Oklahoma, poster presented in person at Undergraduate Research Symposium, Stillwater OK, April 19, 2022.
48. Radonjic, M., Massion. C., Xiong, F., Awejori, G.A., Katende, A., Whitworth, L., Puckette, J., Wang, Y., Grammer, G.M., Rutqvist, J. Nakagawa, S., Binge, M., Lu. L, Bunger, A., Paronish, T., Crandall, D., Renk. J. Applying lessons from shale hydraulic fracturing to shale caprock integrity: experimental and modeling comparison of ductile and brittle samples from Caney Shale, Oklahoma. CouFrac 2022 conference, Berkeley, CA. November 14-16, 2022.
49. Katende, A., Rutqvist, J., Benge, M., Seyedolali, A., Bunger, A., Puckette, J.O., and Radonjic, M. (2021). Micro-geochemistry and Micro-geomechanics towards understanding proppant shale rock interaction: A Caney Shale case study, USA. Abstract presented virtually at the 2021 American Geophysical Union.
50. Awejori, G.A., Katende, A., Xiong, F., Radonjic, M. (2021). Geochemical and Geo-mechanical Responses of Caney Shale to Fracturing Fluid Compositions and Reservoir Conditions. Presented virtually at Geological Society of America (GSA-Connect), Portland OR, October 10-13, 2021.
51. Xiong, F., Jiang, Z., Lu, H., Moortgat, J., Radonjic, M., Observation and modeling of kinetic emission of shale gas using canister desorption testing, presented at GSA (virtual oral talk), Portland OR, (October 10-13, 2021).
52. Cox, I.A., and Pashin, J.C., 2021, Integrated Stratigraphic, Structural, Tectonic, and Petroleum Systems Analysis of the Mississippian Caney Shale, Ardmore Basin, Southern Oklahoma. Poster prestation at AAPG ACE in September 2021:
53. Xiong, F., Rother, G., Gong, Y., Moortgat, J., Radonjic, M., Application of supercritical gas adsorption theories in assessment of adsorbed gas in shales under geological conditions. presented at GSA (virtual oral talk), Portland OR, (October 10-13, 2021). P. K. Bikkina, Application of Nano- and Micro-fluidics in Petroleum Industry, Graduate Seminar Series, McDougall School of Petroleum Engineering, The University of Tulsa, Tulsa, Sep 17, 2021.
54. Katende, A., Rutqvist, J., Benge, M., Seyedolali, A., Bunger, A., Puckette, J.O., and Radonjic,

M. (2021). Convergence of micro-geochemistry and micro-geomechanics towards understanding proppant shale rock interaction: a Caney shale case study in southern Oklahoma, USA. Presented virtually at the July 2021 proppant consortium meeting hosted by Core Labs Inc.

55. Awejori, G.A., Luo, G., Grider, C., Katende, A., Radonjic, M. Doughty, C., Spycher, N. Paronish, T. O'Connell, L. Rihn, A., (2021), Fracturing Fluid-Induced Mineralogy Changes and Impact on Elastic Properties for the Caney Shale, Oklahoma, Presented virtually at 55th American Rock Mechanics Association (ARMA), Houston TX. June 18-25, 2021.
56. Katende, A., Grider C, Awejori. G and Radonjic, M. Application of correlative Raman microscopy and micro-indentation for proppant shale rock interaction: a Caney Shale case study. Presented virtually at the February 2021 proppant consortium meeting hosted by Core Labs Inc.
57. Awejori, G.A., and Radonjic, M. (2021). Chemical Reactivity of Caney Shale to KCl-Brines at Elevated Temperature and Pressure. Presented virtually at American Institute of Chemical Engineers (AIChE) Annual Meeting. Boston, MA. November 15-19, 2021.
58. P K. Bikkina, Application of Nano- and Micro-fluidics in Petroleum Industry, Petroleum Engineering Graduate Seminar, University of Wyoming, WY, Virtual, Mar 11, 2021.
59. R Bhattacherjee, P Bikkina, Functionalizing glass micromodels with illite clay: Effect of salinity and heat treatment, ACS Spring 2021, Virtual, Apr 14, 2021.
60. P K. Bikkina, Application of Nano- and Micro-fluidics in Petroleum Industry, SPE Student Chapter, Department of Petroleum Engineering & Petrochemical Engineering, University College of Engineering Kakinada (A), JNTUK, Virtual, Apr 9, 2021.
61. P K. Bikkina, Application of Nano- and Micro-fluidics in Petroleum Industry, Graduate Seminar Series, McDougall School of Petroleum Engineering, The University of Tulsa, Tulsa, Sep 17, 2021.
62. Katende, A. and Radonjic, M. (2020). Application of correlative Raman microscopy and micro-indentation for proppant shale rock interaction: a Caney Shale case study. Presented virtually at the July 2020. Clay Minerals Society Conference hosted by Pacific Northwest National Laboratory.
63. R. Bhattacherjee, S Pradhan, P Bikkina, Preparation of Illite-coated Geomaterial Surface for Microfluidic Studies, 57th Annual Meeting, Clay Minerals Society (CMS), Virtual, Oct 18-23, 2020.
    https://doi.org/10.15530/urtec-2020-2947
64. Radonjic Group, STIM-Lab Annual Workshop on Proppant, Testing, Virtual presentation, (June 2020).
65. P. K. Bikkina, Application of Nano- and Micro-fluidics in Petroleum Industry, Luncheon Meeting, Society of Petroleum Engineers Oklahoma City Section, OK, Jun 18, 2020.
66. Radonjic, M., Lou, G., Wang, Y., Achang, M., Cains, J., Katende, A., Puckette, J., Grammer, M., and King, G.E. (2020). Integrated Microstructural Characterization of Caney Shale, OK. Unconventional Resources Technology Conference (URTEC), 2020.

List of Postdocs and Students Who Contributed to the Project

POST-DOCTORAL RESEARCHERS

1. Yulun Wang, Grammer Group
2. Mercy Achang, Radonjic Group
3. Cody Massion, Lab Manager, Radonjic Group
4. Yunxing Lu, Bunger Group
5. Guofan Lu, Radonjic Group
6. Fengyang Xiong, Radonjic Group
7. Ali Ettehadi, Radonjic Group

PhD and MS GRADUATE STUDENTS

1. Haden P. Kolmer MS: The Use of Core and Drilling Data for Selective Stimulation Selection in the Caney Shale. (Graduated May 2021).
   Advisor/Chair: G. Hareland; MS Committee: M. Al Dushaishi, P. Bikkina.
2. Dionne M. Mayibeki MS: Drilling Optimization of a Caney Shale Well Using Offset Well Drilling Data. (Graduated December 2021).
   Advisor/Chair: G. Hareland; MS Committee: M. Al Dushaishi, P. Bikkina.
3. Rupom Bhattacherjee MS: Preparation of Clay-Coated Glass Surfaces for Microfluidics-Based Study on Clay-Fluid Interaction. (Graduated Summer 2021).

   Advisor/Chair: P. Bikkina; MS Committee: J. Puckette

4. Allan Katende PhD: Impact of lithology and microstructural properties on proppant embedment and fracture conductivity: A case study of the Caney shale, Southern Oklahoma, USA. (Graduated December 2022). Advisor/Chair: M. Radonjic; PhD Committee: J. Puckette, H. Lee, J. Rutqvist
5. Ian Cox MS: Integrated stratigraphic, structural, tectonic, and petroleum systems analysis of the Mississippian Caney Shale, Ardmore Basin, southern Oklahoma (Graduated December 2022).
6. Lauren Brown MS: Petrophysical and geochemical characterization of the Caney Shale, Ardmore Basin, southern Oklahoma (Graduated December 2022).
   Advisor/Chair: M. Hileman; Committee: J. Puckette, J. Pashin.

7. Ayush Joshi MS: Investigation of Rock-Fluid Interactions using Geomaterial Microfluidics (Graduated Summer 2023).
   Advisor/Chair: P. Bikkina
8. Margaret Benge PhD: From Well Log to Formation Model: A Novel Methodology with Demonstration (Graduated December 2023).
   Advisor/Chari: A. Bunger; PhD Committee: J. Brigham, J. Lin, B. Harber
9. Clark Cunningham PhD: Caney Shale: A Potential Resource Play; (Graduated December 2023).
   Advisor/Chair G. Hareland; PhD Committee: M. Al Dushaishi, J. Puckette, P. Bikkina.
10. John P. Hayes MS: Drilling Analysis and Optimization in the Caney Field, SW Oklahoma; (Graduated December 2023).
11. Haden P. Kolmer PhD: Selective versus Geometric Completions Analysis in the Caney Shale: A Prescriptive Analytical Approach; (Graduated December 2023).
    Advisor/Chair: M. Al Dushaishi, PhD Committee: G. Hareland, J. Puckette, H. Lee.
12. Gabriel Awejori PhD: Subsurface Geochemical Reactions and their Impact on Long-term Hydrocarbon Production in Caney Shale, South-Central Oklahoma Oil Province (SCOOP), USA; (estimated graduation December 2024)
    Advisor/Chair: M. Radonjic; PhD Committee: H. Lee, M. Al Dushaishi, C. Doughty, J. Puckette,
13. Sherif Elkholy PhD: Investigation of acoustic wave velocities under subsurface conditions to improve the predictions of rock mechanical properties and natural fracture characteristics (estimated graduation 2024).
    Advisor: H. Lee; Chair: M. Radonjic; PhD Committee: M. Al Dushaishi, D. Lao Davila
14. Dionne M. Mayibeki PhD: Evaluation and Optimization Simulation of Different Caney Shale Drilling Plans for Field Development; (estimated graduation 2024).
    Advisor/Chair: G. Hareland; PhD Committee: J. Puckette, M. Al Dushaishi, H. Lee.
15. Izabelle Buentello MS: Implications for Unconventional Reservoir Quality: Pore System Architecture and Analysis of the Caney Shale; (estimated graduation 2024)
    Advisor/Chair: G. M. Grammer, MS Committee: J. Puckette, D.Lao Davila, M. Radonjic
16. Mitchell Craig MS: Hydraulic Fracturing Optimization of the Caney Shale in Southern Oklahoma; (estimated graduation 2024)
    Advisor/Chair: G. Hareland; MS Committee: M. Al Dushaishi, P. Bikkina.

17. Ian Cox PhD: The effects of structural geometry and kinematics on petroleum source rock maturity in convergent oblique-slip mobile zones.

Advisor/Chair: J. Pashin; Ph.D. Committee: TBD.

18. Loic Bethel Dje, PhD: CO2 Storage Potential Evaluation of Caney Shale (working title)

Advisor/Chair: M. Radonjic; PhD Committee: TBD

UNDERGRADUATE STUDENT RESEARCHERS

1. Canaan Ferguson, **UGS,** Radonjic Group
2. Vaughn Berkheiser, **UGS,** Radonjic Group
3. Madolyn Hugasian, **UGS,** Radonjic Group
4. Connor Allen, **UGS,** Radonjic Group and Rob Krumm, Baker Hughes
5. Alexander Roubik, **UGS**, Radonjic Group
6. Ben Emmert, **UGS**, Puckette
7. Julia Jones, **PITT**, Bunger Group

Nomenclature:

MS – Master Student

PhD – PhD Student

UGS – Undergraduate Student

* Corresponding author

Bibliography

ASTM D3967-08. 2008. Standard Test Method for Splitting Tensile Strength of Intact Rock Core Specimens. ASTM International.

Allen, R.W., 2000, Stratigraphy, mountain building and complex geological structures of the Ardmore Basin: Oklahoma City Geological Society, Shale Shaker, v. 51, p. 11-21.

Amati, L., and Westrop, S.R., 2006, Sedimentary facies and trilobite biofacies along an Ordovician shelf to basin gradient, Viola Group, South-Central Oklahoma: PALAIOS, v. 21, p. 516–529, doi: 10.2110/palo.2006.p06-069.

Anselmetti, F.S., Luthi, S., and Eberli, G.P. 1998. Quantitative characterization of carbonate pore systems by digital image analysis. AAPG bulletin, v. 82, p. 1815-1836.

Aydin, A. and A. Basu, 2005. The Schmidt hammer in rock material characterization: Engineering Geology, v. 81, p. 1-14.

Barree & Associates, LLC. GOHFER (Version 8.4.x.x) [Software]. 2016. Lakewood, CO. Retrieved from http://gohfer.com/.

Barree and Associates. GOHFER. Accessed 13 Sept. 2023. https://barree.net/2-general/5-gohfer-software.html.

Benge, M., Lu, Y., Katende, A., Rutqvist, J., Crandall, D., Haecker, A., King, G., Renk, J.B., Radonjic, M., Bunger, A., 2021. Connecting Geomechanical Properties with Potential for Proppant Embedment and Production Decline for the Emerging Caney Shale, Oklahoma. Presented at the SPE/AAPG/SEG Unconventional Resources Technology Conference, p. D011S002R001. https://doi.org/10.15530/urtec-2021-5084

Bickford, M.E., and Lewis, R.D., 1979, U-Pb geochronology of exposed basement rocks in Oklahoma: Geological Society of America Bulletin, v. 90, p. 540-544.

Briggs, K., A. D. Hill, D. Zhu, and K. Olson. "The Relationship Between Rock Properties and Fracture Conductivity in the Fayetteville Shale." All Days. 2014. https://doi.org/10.2118/170790-MS.

Bouma, A. H., 1962, Sedimentology of some flysch deposits: a graphic approach to facies interpretation: Amsterdam, Elsevier, 168 p.

Bouma, A. H., 2000, Fine-grained, mud-rich turbidite systems: model and comparison with coarse-grained, sand-rich systems, in A. H. Bouma and C. G. Stone, eds., Fine-grained turbidite systems, American Association of Petroleum Geologist (AAPG) Memoir 72/Society for Sedimentary Geology (SEPM) Special Publication 68, p. 9-20.

Bourget, J., S. Zaragosi, T. Mulder, J. L. Schneider, T. Garlan, A. Van Toer, V. Mas, and N. Ellouz-Zimmermann, 2010. Hyperpycnal-fed turbidite lobe architecture and recent sedimentary processes: A case study from the Al Batha turbidite system, Oman margin: Sedimentary Geology, v. 229, p. 144-159.

Bowring, S.A., Hoppe, W.J., 1982, U−Pb zircon ages from Mount Sheridan Gabbro, Wichita Mountains, in Gilbert, M.C., Donovan, R.N., eds., Geology of the Eastern Wichita Mountains, Southwestern Oklahoma: Oklahoma Geological Survey Guidebook, 21, p. 54–59.

Brown, A., 2002, Petroleum charge to the Mill Creek Syncline and adjacent areas, southern Oklahoma: Oklahoma Geological Survey Circular 107, p. 17–36.

Burke, K., and Dewey, J.F., 1973. Plume-generated triple junctions: Key indicators in applying plate tectonics to old rocks: Journal of Geology, v. 81, p. 406–433. https://doi.org/10.1086/627882.

Campos, C., O. Guzmán, A. Pilloud, R. Uzcátegui, A. Cabrera, and M. Toro, 2011, Gravelly and sandy facies of Rio Guache Formation, Venezuelan Andes: evidence for transformation of gravity flows in deep-marine water, in R. M. Slatt and C. Zavala, eds., Sediment transfer from shelf to deep water – revisiting the delivery system: American Association of Petroleum Geologist (AAPG) Studies in Geology 61, p. 117–128.

Cardott, B.J., 2012. Thermal maturity of Woodford Shale gas and oil plays, Oklahoma, USA: International Journal of Coal Geology, v. 103, p. 109–119.

Cardott, B.J., and J.B. Comer, 2021, Woodford Shale (Upper Devonian to Lower Mississippian): From hydrocarbon source rock to reservoir: Oklahoma Geological Survey, Bulletin 152, 108 p.

Comer, J. B., 1992. Organic geochemistry and paleogeography of Upper Devonian formations in Oklahoma and western Arkansas, in K.S. Johnson and B.J. Cardott, (Eds.), Source rocks in the southern Midcontinent, 1990 symposium: OGS Circular 93, p. 70-93.

Cox, I.A., 2021. Integrated stratigraphic, structural, tectonic, and petroleum systems analysis of the Mississippian Caney Shale, Ardmore Basin, southern Oklahoma (M.S. thesis): Stillwater, Oklahoma State University, 159 p.

Cox, I.A., and Pashin, J.C., 2024. Burial and thermal history modeling in convergent oblique-slip mobile zones: A case study of the Ardmore Basin, southern Oklahoma: International Journal of Coal Geology, v. 285, paper 104486, 24 p., https://doi.org/10.1016/j.coal.2024.104486.

Cunningham, C. M., and R. W. C. Arnott, 2021. Systematic organization of thin-bedded turbidites in ancient deep-marine levees: possible evidence of rhythmic pulsing in turbidity currents: Journal of Sedimentary Research, v. 91, p. 1257-1274.

Dunham, R. J., 1962. Classification of carbonate rocks according to their depositional texture, in W. E. Ham, ed., Classification of Carbonate Rocks – a symposium: American Association of Petroleum Geologists (AAPG) Memoir 1, p. 108-121.

Embry, A. F. and J. E. Klovan, 1971. A Late Devonian reef tract on northeastern Banks Island, N.W.T.: Bulletin of Canadian Petroleum Geology, v. 19, p. 730-781.

Feinstein, S., 1981. Subsidence and thermal history of Southern Oklahoma Aulacogen-Implication for petroleum exploration: AAPG Bulletin, v. 65, p. 2521–2533. https://doi.org/10.1306/03b599f9-16d1-11d7-8645000102c1865d.

Fritz, R.D., Patrick M., Kuykendall, M.J., and Wilson, J.L., 2012. The geology of the Arbuckle Group in the midcontinent: Sequence stratigraphy, reservoir development, and the potential for hydrocarbon exploration, in Derby, J.R., Fritz, R.D., Longacre, S.A., Morgan, W.A., and Sternbach, C.A., (Eds.), The great American carbonate bank: The geology and economic resources of the Cambrian-Ordovician Sauk megasequence of Laurentia: AAPG Memoir 98, p. 203–273.

Gale, J. F., R. M. Reed, and J. Holder, 2007. Natural fractures in the Barnett Shale and their importance for hydraulic fracture treatments: American Association of Petroleum Geologist (AAPG) Bulletin, v. 91, p. 603-622.

Gale, J. F., S. E. Laubach, J. E. Olson, P. Eichhubl, and A. Fall, 2014. Natural fractures in shale: a review and new observations: American Association of Petroleum Geologist (AAPG) Bulletin, v. 98, p. 2165-2216.

Gani, M. R., 2004. A Straightforward approach to sediment gravity flows and their deposits: The Sedimentary Record, v. 2, p. 4-8.

Geokansas. "Public Land Survey System." Webpage. 2023. https://geokansas.ku.edu/public-land-survey-system.

Grammer, G. M. and R. N. Ginsburg, 1992. Highstand versus lowstand deposition on carbonate platform margins: insight from Quaternary foreslopes in the Bahamas: Marine Geology, v. 103, p. 125-136.

Granath, J.W., 1989. Structural evolution of the Ardmore Basin, Oklahoma: Progressive deformation in the foreland of the Ouachita collision: Tectonics, v. 8, p. 1015–1036. https://doi.org/10.1029/tc008i005p01015.

Ham, W.E., 1969. Regional geology of the Arbuckle Mountains, Oklahoma: Oklahoma Geological Survey Guidebook 17, 52 p.

Hanson, R.E., Puckett, R.E., Keller, G.R., Brueseke, M.E., Bulen, C.L., Mertzman, S.A., Finegan, S.A., and Mccleery, D.A., 2013. Intraplate magmatism related to opening of the southern Iapetus Ocean: Cambrian Wichita igneous province in the southern Oklahoma rift zone: Lithos, v. 174, p. 57–70. https://doi.org/10.1016/j.lithos.2012.06.003.

Harding, T.P., 1985, Seismic characteristics and identification of negative flower structures, positive flower structures, and positive structural inversion: American Association of Petroleum Geologists Bulletin, v. 69, p. 582-600.

Harding, T.P., Gregory, R.F., and Stevens, L.H., 1983, Convergent wrench fault and positive flower structure, Ardmore Basin, Oklahoma in Balley, A.W., ed., Seismic Expression of Structural Styles: AAPG Studies in Geology, no. 15, v. 3, p 4.2–13–4.1-17.

Hareland, G., and L. L. Hoberock. "Use of Drilling Parameters to Predict In-Situ Stress Bounds." All Days. 1993. https://doi.org/10.2118/25727-MS.

Hareland, G., PFAP spreadsheet well model used in PETE 5363, Petroleum Economics and Investments Course. Oklahoma State University. Stillwater, OK, 2022.

Heran, W.D., Green, G.N., Stoeser, D.B., 2003. A digital geologic map database for the state of Oklahoma. U.S. Geological Survey open-file report 97–23, U.S. Geological Survey, Oklahoma City, http://pubs.usgs.gov/of/2003/ofr-03-247/ (accessed 20 October 2020).

Hoffman, P., Dewey, J.F., and Burke, K., 1974. Aulacogens and their genetic relation to geosynclines, with a Proterozoic example from Great Slave Lake, Canada: SEPM Special Publication 19, p. 38–55. https://doi.org/10.2110/pec.74.19.0038.

Huffman, G.G., Bridges, K.F., Ganser, R.W., Holtzman Jr., A.M., Merritt, M.L., 1987. Geology and Mineral Resources of Marshall County, Oklahoma. Oklahoma Geological Survey Bulletin,142.

Huffman, G.G., Hart, T.A., Olson, L.J., Currier, J.D., and Ganser, R.W, 1978. Geology and mineral resources of Bryan County, Oklahoma: Oklahoma Geological Survey Bulletin 126, 113 p.

Hurd, G. S., C. Kerans, E. L. Frost, J. A. Simo, and X. Janson, 2018. Sediment gravity-flow deposits and three-dimensional stratigraphic architectures of the linked Cutoff, upper Bone Spring, and upper Avalon system, Delaware Basin: American Association of Petroleum Geologist (AAPG) Bulletin, v. 102, p. 1703-1737.

Ingram, W. C., D. C. Mosher, and S. W. Wise, Jr., 2011. Biostratigraphy of an Upper Miocene mass-transport deposit on Demerara Rise, northern South American margin, in R. C. Shipp, P. Weimer, H.

W. Posamentier, eds, Society for Sedimentary Geology (SEPM) Special Publication 96: Mass-transport deposits in deepwater settings, p. 475-498.

Jablonska, D., C. N. Di Celma, G. I. Alsop, and E. Tondi, 2018. Internal architecture of mass-transport deposits in basinal carbonates: a case study from southern Italy: Sedimentology, v. 65, p. 1246-1276.

Johnson, K.S., 1989. Geologic evolution of the Anadarko Basin, in Johnson, K.S., (Ed.), Anadarko Basin symposium, 1988: Oklahoma Geological Survey Circular 90, p. 3–12.

Johnson, K.S., 2008. Geologic history of Oklahoma, in Johnson, K.S., and Luza, K.V., (Eds.), Earth sciences and mineral resources of Oklahoma: Oklahoma Geological Survey Educational Publication 9, p. 3–5.

Johnson, K.S., and B.J., Cardott, 1992, Geologic framework and hydrocarbon source rocks of Oklahoma, in K.S. Johnson and B.J. Cardott, eds., Source rocks in the southern Midcontinent, 1990 symposium: Oklahoma Geological Circular 93, p. 21–37.

Kholy, S.M., Lee, H.P., Radonjic, M., 2024. Integrating Experiments and Well Logs to Predict Caney Shale Static Mechanical Properties During Production with Supervised Machine Learning, in: The Unconventional Resources Technology Conference. Presented at the The Unconventional Resources Technology Conference, American Association of Petroleum Geologists, Houston, TX USA. https://doi.org/10.15530/urtec-2024-4038060

Kneller, B. C. and M. J. Branney, 1995. Sustained high-density turbidity currents and the deposition of thick massive sands: Sedimentology, v. 42, p. 607-616.

Kneller, B. C. and W. D. McCaffrey, 2003. The interpretation of vertical sequences in turbidite beds: the influence of longitudinal flow structure: Journal of Sedimentary Research, v. 73, p. 706-713.

Kvale, E. P., C. M. Bowie, C. Flenthrope, C. Mace, J. M. Parrish, B. Price, S. Anderson, and W. A. DiMichele, 2020. Facies variability within a mixed carbonate–siliciclastic sea-floor fan (upper Wolfcamp Formation, Permian, Delaware basin, New Mexico): American Association of Petroleum Geologists (AAPG) Bulletin, v. 104, p. 525-563.

Latham, J. W., 1968. Petroleum geology of Arbuckle Group (Ordovician), Healdton Field, Carter County, Oklahoma: AAPG Bulletin, v. 52, p. 3-20.

Lee, Y., and Deming, D., 1999. Heat flow and thermal history of the Anadarko Basin and the western Oklahoma Platform: Tectonophysics, v. 313, no. 4, p. 399–410.

Liang, X., F. Zhou, T. Liang, C. Wang, and Y. Li. "Experimental Quantification of Formation Damage Caused by the Cross-Linked Gel in Tight Gas Reservoirs." Journal of Natural Gas Science and Engineering 84 (2020). https://doi.org/10.1016/j.jngse.2020.103608.

Liang, X., Zhou, F., Liang, T., Wang, C. and Li, Y., “Experimental quantification of formation damage caused by the cross-linked gel in tight gas reservoirs.” Journal of Natural Gas Science and Engineering, Volume 84, 2020. https://doi.org/10.1016/j.jngse.2020.103608.

Lipovetsky, S., Conklin, M., 2001. Analysis of regression in game theory approach. Applied Stochastic Models in Business and Industry 17, 319–330. https://doi.org/10.1002/asmb.446

Lo, H.B., and B.J. Cardott, 1994, Detection of natural weathering of Upper McAlester coal and Woodford Shale, Oklahoma, U.S.A.: Organic Geochemistry, v. 22, p. 73-83.

Lorenz, J. C., J. L. Sterling, D. S. Schechter, C. L. Whigham, and J. J. Jensen, 2002. Natural fractures in the Spraberry Formation, Midland Basin, Texas: the effects of mechanical stratigraphy on fracture

variability and reservoir behavior: American Association of Petroleum Geologist (AAPG) Bulletin, v. 86, p. 505–524.

Loucks, R.G., Reed, R.M., and Ruppel, S.C. 2009. Morphology, genesis, and distribution of nanometer-scale pores in siliceous mudstones of the Mississippian Barnett Shale. Journal of Sedimentary Research, v. 79, p. 848-861.

Loucks, R. G., C. Kerans, X. Janson, and M. Alfredo Marhx Rojano, 2011. Lithofacies analysis and stratigraphic architecture of a deep-water carbonate debris apron: Lower Cretaceous (Latest Aptian to Latest Albian) Tamabra Formation, Poza Rica Field area, Mexico, in R. C. Shipp, P. Weimer, H. W. Posamentier, eds, Society for Sedimentary Geology (SEPM) Special Publication 96: Mass-transport deposits in deepwater settings, p. 367-390.

Loucks, R. G., R. M. Reed, S. C. Ruppel, and U. Hammes, 2012. Spectrum of pore types and networks in mudrocks and a descriptive classification for matrix-related mudrock pores: American Association of Petroleum Geologists (AAPG) Bulletin, v.96, p.1071-1098, doi: 10.1306/08171111061.

Marrett, R., O. J. Ortega, and C. M. Kelsey, 1999. Extent of power-law scaling for natural fractures in rock: Geology, v. 27, p. 799-802.

McPhee, C., Reed, J., Zubizarreta, I., 2015. Chapter 12 - Geomechanics Tests, in: McPhee, C., Reed,

Miser, H.D., 1954. Geologic Map of Oklahoma: Norman, Oklahoma, Oklahoma Geological Survey, scale 1:500,000.

Mulder, T. and J. Alexander, 2001. The physical character of subaqueous sedimentary density flows and their deposits: Sedimentology, v. 48, p. 269-299.

Mutti, E., D. Bernoulli, F. R. Lucchi, and R. Tinterri, 2009. Turbidites and turbidity currents from Alpine ‘flysch’ to the exploration of continental margins: Sedimentology, v. 56, p. 267-318.

Nelson, R. A., 2001. Geological analysis of naturally fractured reservoirs, 2nd edition: New York, Elsevier, 332 p.

Nielsen, R.M., Kohlhaas, C.A., 1979. Acoustic And Biaxial Measurement Of Rock Mechanical Properties For Interpretation Of Logs For Design Of Well-Completion Operations. Presented at the SPE Annual Technical Conference and Exhibition, p. SPE-8238-MS. https://doi.org/10.2118/8238-MS

Norbisrath, J. H., Grammer, G. M., Vanden Berg, B., Tenaglia, M., Eberli, G. P., and Weger, R. J. 2017. Nanopore imaging in Vaca Muerta mudrocks to evaluate controls on complex resistivity spectra in unconventional reservoirs. SPE Reservoir Evaluation & Engineering, v. 20, p. 1028-1044.

Northcutt, R.A., and J.A. Campbell, 1998, Geologic provinces of Oklahoma, in J.P. Hogan and M.C. Gilbert, eds., Basement tectonics 12, central North America and other regions: Boston, Kluwer Academic Publishers, Proceedings of the 12th International Conference on Basement Tectonics, p. 29–37.

Nygaard R. and G. Hareland, “Calculating Unconfined Rock Strength from Drilling Data”, 1st Canada-U.S. Rock Mechanics Symposium, Vancouver, British Colombia, Canada, 27-31 May, 2007. https://doi.org/10.2118/106573-MS

Oklahoma State Geology Department: Boone Pickens School of Geology. "105 Noble Research Center Stillwater, OK 74078." Webpage. https://geology.okstate.edu/.

Oklahoma Tax Commission. "OKTAP." Webpage. 2023.

https://www.ok.gov/triton/more_information.php?id=281#.

Onyia, E. C. "Relationships Between Formation Strength, Drilling Strength, and Electric Log Properties." All Days. 1988. https://doi.org/10.2118/18166-MS.

Payros, A. and V. Pujalte, 2008. Calciclastic submarine fans: an integrated overview: Earth-Science Reviews, v. 86, p. 203-246.

Perry, W.J., 1989. Tectonic evolution of the Anadarko Basin region, Oklahoma: US Geological Survey Bulletin 1866-A, p. A1–A19. https://doi.org/10.3133/b1866a.

Schlager, W., J. J. Reijmer, and A. Droxler, 1994. Highstand shedding of carbonate platforms: Journal of Sedimentary Research, v. 64, p. 270-281.

Siwek, P., A. Waśkowska, and M. Wendorff, 2023. Mud-rich low-density turbidites in structurally controlled intraslope mini-basin: the influence of flow containment on depositional processes and sedimentation patterns (Szczawa, Oligocene, Polish Outer Carpathians): Sedimentology, doi: 10.1111/sed.13095

Shapley, L.S., Roth, A.E., 1988. The Shapley value: essays in honor of Lloyd S. Shapley. Cambridge University Press.

Shatski, N.S., 1946. The great Donets Basin and the Wichita System; Comparative tectonics of ancient platforms: Akademiya Nauk SSSR Izvestiya, Seriya Geologicheskaya 6, p. 57–90.

Stow, D. A. and M. Johansson, 2000. Deep-water massive sands: nature, origin and hydrocarbon implications: Marine and Petroleum Geology, v. 17, p. 145-174.

Spears, J. D, and Pashin, J. C., 2022. The Goddard Shale in the eastern Anadarko Basin: Understanding a highly productive mudrock reservoir with fluid-sensitive clay: American Association of Petroleum Geologists Bulletin, v. 106, p. 1453-1477. https://doi.org/10.1306/02072219255.

Stanley, T.M., and Chang, J.M., 2012. Preliminary geologic map of the Ardmore 30′ × 60′ quadrangle and the Oklahoma part of the Gainesville 30′ × 60′ quadrangle, Carter, Jefferson, Love, Murray, and Stephens Counties, Oklahoma: Oklahoma Geological Survey, scale 1:100,000.

Suneson, N., 2020. Roadside Geology of Oklahoma: Missoula, MT, Mountain Press Publishing Company 385 p.

Suneson, N.H., and T.M. Stanley, 2017, The age of Oklahoma's mountain ranges: Oklahoma Geological Survey, Oklahoma Geology Notes, v. 76, p. 4-19.

Suppe, J., and Medwedeff, D. A., 1990. Geometry and kinematics of fault-propagation folding: Eclogae Geologicae Helvetiae, v. 83, p. 409-454.

Tahmeen, M., et al. "Geomechanical Properties from Drilling Data to Optimize Stimulation Design." AADE 2019 NTCE-036. https://www.aade.org/application/files/1615/7132/0392/AADE-19-NTCE-036_-_Tahmeen.pdf.

Talling, P. J., L. A. Amy, R. B. Wynn, J. Peakall, and M. Robinson, 2004. Beds comprising debrite sandwiched within co-genetic turbidite: origin and widespread occurrence in distal depositional environments: Sedimentology, v. 51, p. 163-194.

Thomas, W.A., 1977. Evolution of Appalachian-Ouachita salients and recesses from reentrants and promontories in the continental margin: American Journal of Science, v. 277, p. 1233–1278. https://doi.org/10.2475/ajs.277.10.1233.

Thomas, W. A., 1991, The Appalachian-Ouachita rifted margin of southeastern North America: Geological Society of America Bulletin, v. 103, p. 415-431.

Thomas, W.A., 2014. The southern Oklahoma transform-parallel intracratonic fault system in Suneson, N.H., (Ed.), Igneous and Tectonic History of the Southern Oklahoma Aulacogen, Oklahoma Geological Survey Guidebook 38, p. 375–387.

Turko, M., and B. Tapp, 2021, A structural analysis of the Washita Valley Fault in the southeast Anadarko Basin: Interpretation, v. 9, no. 1, p. T183-T200.

Turko, M., and Mitra, S., 2021. Macroscopic structural styles in the southeastern Anadarko Basin, southern Oklahoma: Marine and Petroleum Geology, v. 125, paper 104863. https://doi.org/10.1016/j.marpetgeo.2020.104863

U.S. Dept. of Energy. "Field Evaluation of the Caney Shale as an Emerging Unconventional Play, Southern Oklahoma—Project Number DE-FE-0031776." Webpage. 2020. https://netl.doe.gov/sites/default/files/2020-11/NETL-DOE-GranteesConference-Caney-Field-Lab-2020.pdf.

Van der Gracht, W.A.J.M. van Waterschoot, 1931. Permo-Carboniferous orogeny in south-central United States: AAPG Bulletin, v. 15, p. 991-1057. https://doi.org/10.1306/3d9329f2-16b1-11d7-8645000102c1865d.

Vanden Berg, B. and G. M. Grammer, 2016. 2-D pore architecture characterization of a carbonate mudrock reservoir: insights from the Mid-Continent “Mississippi Lime”, in T. Olson, eds, American Association of Petroleum Geologist (AAPG) Memoir 112, p. 185-231.

Van Daele, M., I. Meyer, J. Moernaut, S. De Decker, D. Verschuren, and M. De Batist, 2017. A revised classification and terminology for stacked and amalgamated turbidites in environments dominated by (hemi)pelagic sedimentation: Sedimentary Geology, v. 357, p. 72-82.

Walker, W.M., 2006. Structural analysis of the Criner Hills, south-central Oklahoma (unpublished M.S. thesis): Waco, Baylor University, 64 p.

Wang, Y., T. Thompson, and G. M. Grammer, 2019. Fracture characterization and prediction in unconventional reservoirs of the “Mississippian Limestone”, North-Central Oklahoma, USA, in G. M. Grammer, J. M. Gregg, J. Puckette, P. Jaiswal, S. J. Mazzullo, M. J. Pranter, R. H. Goldstein, eds, American Association of Petroleum Geologist (AAPG) Memoir 122, p. 271-299, DOI: 10.1306/13632151M1163789.

Wang, Y., G. M. Grammer, G. Eberli, R. Weger, and R. Nygaard, 2021. Testing rebound hardness for estimating rock properties from core and wireline logs in mudrocks: U.S. Midcontinent (“Miss Lime”/STACK) and Argentina (Vaca Muerta Formation), Journal of Petroleum Science and Engineering, Journal of Petroleum Science and Engineering, v. 210, 109973, DOI: 10.1016/j.petrol.2021.109973.

Wang, Y., Luo, G., Achang, M., Cains, J., Wethington, C., Katende, A., Grammer, G.M., Puckette, J., Pashin, J., Castagna, M., Chan, H., King, G.E. and Radonjic, M. 2021, Multiscale characterization of the Caney Shale—A case study from southern Oklahoma: Midcontinent Geoscience, v. 2, p. 33-53, https://doi.org/10.17161/mg.v2i.15911.

Wavrek, D.A., 1992. Characterization of oil types in the Ardmore and Marietta basins, southern Oklahoma aulacogen, in Johnson, K.S., and Cardott, B.J., (Eds.), Source rocks in the southern Midcontinent, 1990 Symposium: Oklahoma Geological Survey Circular 93, p. 185–195.

Weger, R.J., G.P. Eberli, G.T. Baechle, J.L. Massaferro, and Y.F. Sun. 2009. Quantification of pore structure and its effect on sonic velocity and permeability in carbonates: American Association of Petroleum Geologists (AAPG) Bulletin, v. 93, p.1297-1317.

Ye, H., Royden, L., Burchfiel, C., and Schuepbach, M., 1996. Late Paleozoic deformation of interior North America: The greater Ancestral Rocky Mountains: AAPG Bulletin, v. 80, p. 1397–1432. https://doi.org/10.1306/64ed9a4c-1724-11d7-8645000102c1865d.